THÈSE

Pour obtenir le grade de

DOCTEUR DE L'UNIVERSITÉ GRENOBLE ALPES

École doctorale : PHYS - Physique
Spécialité : Nanophysique
Unité de recherche : Spintronique et Technologie des Composants

Skyrmion magnétiques contrôlés par une tension de grille

Gate voltage control of magnetic skyrmions

Présentée par :

Capucine GUENEAU

Direction de thèse :

Hélène BEA MAITRESSE DE CONFERENCES HDR, UNIVERSITE GRENOBLE ALPES	Directrice de thèse
Claire BARADUC DIRECTRICE DE RECHERCHE, CEA CENTRE DE GRENOBLE	Co-directrice de thèse

Rapporteurs :

DIETER SUESS
FULL PROFESSOR, UNIVERSITÄT WIEN
LIZA HERERRA DIEZ
DIRECTRICE DE RECHERCHE, CNRS DELEGATION ILE-DE-FRANCE SUD

Thèse soutenue publiquement le **25 novembre 2025**, devant le jury composé de :

SOPHIE DE BRION, PROFESSEURE DES UNIVERSITES, UNIVERSITE GRENOBLE ALPES	Présidente
DIETER SUESS, FULL PROFESSOR, UNIVERSITÄT WIEN	Rapporteur
LIZA HERERRA DIEZ, DIRECTRICE DE RECHERCHE, CNRS DELEGATION ILE-DE-FRANCE SUD	Rapporteure
NICOLAS REYREN, CHARGE DE RECHERCHE, CNRS DELEGATION ILE-DE-FRANCE SUD	Examinateur
ALEXANDRA MOUGIN, DIRECTRICE DE RECHERCHE, CNRS DELEGATION ILE-DE-FRANCE SUD	Examinatrice

Ackowledgments

Je tiens tout d'abord à remercier les membres de mon jury: Dieter Suess, Liza Herrera Diez, Nicolas Reyren, Alexandra Mougin et Sophie De Brion d'avoir accepté d'en faire partie. Je les remercie également pour l'intérêt qu'ils ont porté à mon travail, pour leur bienveillance ainsi que pour leurs remarques pertinentes et les échanges scientifiques enrichissants.

Évidemment, je tiens à remercier chaleureusement Hélène et Claire de m'avoir permis d'intégrer le laboratoire, d'abord pour mon stage, puis de m'avoir accordé leur confiance pour poursuivre en thèse. Hélène, merci pour ton soutien tout au long de ces trois années, mais aussi pour ton optimisme et ta bonne humeur communicative. Tu m'as beaucoup aidé et encouragé, toujours présente lorsque c'était nécessaire, tout en me laissant la liberté de gagner en autonomie. Johanna, merci pour ton énergie et ta bonne humeur en toutes circonstances. Tu es toujours disponible, toujours là pour me conseiller et me guider quand j'en ai besoin.Dès le début de cette thèse, j'ai eu la chance d'intégrer une superbe équipe. Un grand merci à toi, Charles, tu m'as beaucoup aidé à m'intégrer, et tu as toujours été présent pour moi au début de cette aventure. Ta bienveillance et ton sourire ont beaucoup compté. Merci également à Lucia, Thomas, Samuel et Suraj pour la bonne ambiance, que ce soit pendant les réunions ou en dehors.

J'ai rencontré énormément de personnes durant ces trois années de thèse, et tout cela n'aurait pas été possible sans la plupart d'entre elles. J'aimerais particulièrement remercier Mair et Fatima pour leur aide et leur bienveillance tout au long de ma thèse. Mair, merci pour toutes les histoires que tu nous racontes. Tu es très inspirant par l'étendue de tes connaissances. J'aimerais également remercier Olivier et Gilles pour toutes les discussions, scientifiques ou non, que nous avons eues au cours de mon stage et de ma thèse. Votre aide a été très précieuse. Merci aussi à Laurent pour m'avoir permis d'utiliser la précieuse machine de wire bonding, mais surtout pour l'ambiance que tu apportes au quotidien dans le laboratoire. Enfin, évidemment, j'aimerais remercier Stefania pour m'avoir permis de participer à mon premier run synchrotron, mais également pour t'être toujours rendue disponible pour m'aider avec mes dépôts d'ALD, l'article, ou encore mon manuscrit. Merci à Liliana, Vincent et Kévin pour les discussions que nous avons eues et pour l'aide que vous m'avez apportée, que ce soit tout au long de ma thèse ou pour mon manuscrit. Et bien évidemment, un grand merci à tous les autres permanents du laboratoire qui se rendent disponibles au quotidien pour nous aider.

Un grand merci également à Stéphane et Jérôme pour les dépôts et leur aide précieuse. C'est toujours un plaisir d'échanger avec toi, Stéphane. Tu prends le temps d'expliquer les procédés avec clarté et patience, toujours accompagnées d'une touche d'humour et de bonne humeur. Et

bien sûr, merci à toi, Jérôme, de veiller à ce que les membres de Spintec suivent un régime strict composé exclusivement de gâteaux !

Spintec is an amazing lab because it give us the opportunity to share so much with so many people that became really important in my life now.
First of all, of course, Théo. Thanks for sharing a flat with me, I would probably not have survived this years without knowing you would always be here for me, listen to my problem or my shitty jokes, supporting me after a long and tiring day in the lab when nothing seemed to want to works. You make me see things differently on many subject and you make me evolves in so many point in my life.

At my arrival in PhD I have been assigned to the 433C office, without knowing I will share it with amazing people: I can't start by someone else than Hanna. Being in the office with you removed so much stress. You always made me feel understood, and I would definitely not have achieved all of this without you. We have to be honest, maybe we were not the quietest one, but I will always remember these moments in the office together. Speaking about this, I have, of course, to thanks Sergi (eeeegiiii). Always there to listen to us, and never the last to do shitty jokes. You have been a real support for me both in and out the lab. I will always been grateful to have meet you. I miss you a lot but I know we will share many more moments and hopefully many more lunchy lunchy. And to finish with the "best office gang": Marco, a.k.a Marcolino, thanks for the moments we share in the office or outside and for the mood you bring even only with one good sentence. But above all thanks for the meow meow meow ... meow meow. Andréa, even if you were not coming often in this office your presence here was always reconforting. We never knew when you will be here, but when it was the case I knew it would be a good day, not the most productive one but for sure a good one.

I shared this office with many people and I would like to thanks the ones that was already there when I arrived: Joseba, Pedro, Matheo, Kamal, thanks for all the help you were always happy to give and for your support. You all have been an example for me. And of course Fatima, the mom of this office, thanks once again for your incredible kindness and for all the support you gave me. I also want to thanks the one that was there at the end: Noé, Joao, Davide. We did not had a lot of time together but I appreciate every moment, discussions and coffee with you.

These three years has been made of up and down, especially at the end, so of course I would like to thanks really a lot the writters team. Ilaria, thanks for always be there when it is needed, thanks for all the dinners and discussions we have, thanks for the reassurance you are always able to give me and to always be the attentive ear that everybody needs. Subham, thank you for all the laughter and joy you bring with you. Talking to you always makes my life feel lighter. You seem to understand everything so naturally, and you showed me how much easier life can be when we stop being anxious (especially about trains and planes). Thank you as well for your constant support and for introducing me to the Indian churros.

Everyone made Spintec special to me, but if I had to thank someone in particular for welcoming me from the very beginning, it would be you, Javi. Above all, thank you for your constant good mood, for always making me feel supported and listened to and thanks for all the advice

you gave me, especially valuable coming from someone as old as you, it made me grow as a person. In the same way, I would also like to thank Aurélie for being there from the very beginning as well. The long walk to your office was always worth it to spend time with you. And thanks a lot to have been patient enough to run with me when 5km seemed to be insurmountable for me. Coline, since you arrived at Spintec, you have brightened up my daily life with your personality. You have always been there for me. Our coffee/tea breaks and the little chats in your office were a big part of what helped me get through this thesis. I have always found you incredibly strong and intelligent. Rodri, thank you to have been a real support throughout these years. You taught me how to see things from different perspectives and helped me grow both scientifically and as a person and I will always remember it. Natalia, thank you for always caring about everyone and for being so genuinely interested in people. Kuldeep, thank you for your incredible for your incredible kindness, humour, and constant smile. But also for welcoming me so many times into your office and for never making me feel like I was too much. Thanks Léna for always lifting others up with your energy and to always find the positive part in everything. Lucia, for sharing the sensor meeting with me, always being up for everything and always happy to help around. Thomas, thank you for being here since the internship, and for going through all the meetings together with me. Also, a big thank you Giovanni for your humour, which never fails to make me laugh.

Jonathan, thankS god we met. Thank you for supporting me despite my not-so-perfect English and never commenting on it. Thank you for always making me feel comfortable sharing difficult subjects, and for being a steady support over the past year (even on one leg). Simone, Chloé, Arthur, thanks for always welcoming me in your office, to discuss about life, to talk of science or just to annoy you. Paolo, thank you for always welcoming me and for sharing a part of your knwoledge with me (even if the story about the eye operation was a bit too much for me!). Thanks Maxime for your light mood, for accepting me in your office maybe more than necessary, and always following me in my weird idea to annoy Théo. Thank you also to Corrado for your calm, your kindness, and your reassuring way of always understanding people. I would like to thanks the older generation: Miina, Hasan, Louis to have welcoming me and make me feel naturally included in the lab either by your jokes or the discussions we had. Nuno, my office neighbor, to always find the joke and the words when it was needed and for all the instagram reel exchange even after you left.

But also the new generation in Spintec: Alvaro for all your stories that definitively make every coffee break more interesting and fun. You quickly became someone I am always happy to see and discuss with, walking past your office was always a spike of hapinness. Giannis for your enthousiasm and jokes, despite the multiple coffee betrayals it was always nice to know someone would be in Spintec to take a coffee early-morning. Neha for your kindness and warmth since you arrive. Noé for the multiple memes, weird songs or pictures your shared with me quite randomly. Lucìa, for your calm in the middle of the jungle that is Spintec. And Selu, for bringing a new era to the lab, you always have the smart and funny sentence to say, yet we can always have deep and serious conversations.

I would also like to thank the unofficial Spintec members, who are not formally part of the lab but very much part of its spirit. Andres, thank you for your constant energy, for always being enthusiastic and available, and above all for your kindness and the genuine consideration

you show to everyone. Alice, you are like a little sunshine to me. Always smiling, you bring such a positive aura, and every time you enter the room, you make it a brighter and happier place. And finally David, my catalan queen/diva. Thanks to always welcoming me in your place but also in your life. You are such a refreshing human with your personality, your humour and your incredible culture. I am always looking forward to see you, you make every problem light, even when a phone get stolen in the middle of the night in Barcelona.

I would also like to thank my ESM mates. Inès, thank you for your energy and your constant good mood. I am sure that every time our paths cross, we will share a wonderful time together. I would also like to thank Matteo for all the discussions we have had, whether by message or when I randomly come to Barcelona and you always manage to make yourself available to share a drink. Both the scientific insights and the personal support you have given me over these years have been truly valuable to me.

Au cours de cette thèse, j'ai eu la chance de rencontrer énormément de personnes. Mais rien de tout cela n'aurait été possible sans le soutien de mes amis en dehors du laboratoire. Je pense évidemment très fort à Romy, Léna et Mathilde. Depuis la L1, nous parlons de cette thèse, et nous y voilà : quasiment toutes docteures (ou sur le point de l'être). Je suis très fière de vous, les filles, et de notre évolution au fil de ces années, qui nous ont soudées et fait grandir ensemble. Merci du fond du cur pour votre présence, votre écoute et votre soutien sans faille. Merci également à Antoine et Maxime pour toutes les soirées, les discussions et les bières partagées, quand le changement et le stress du stage et du début de thèse se faisaient ressentir. Que ce soit par la course, en regardant un Grand Prix ou avec un peu de ski, vous réussissez toujours à me changer les idées.

Je ne peux pas ne pas remercier les personnes avec qui j'ai grandi : Amélie, Emma, Énimie et Fiona. Merci à vous quatre pour votre soutien constant tout au long de ma vie. Je vous ai rencontrées il y a maintenant plus de 15 ans, et depuis, vous avez toujours été présentes pour moi, dans les bons comme dans les mauvais moments. On a grandi ensemble, on a évolué ensemble, et on vieillira ensemble. Je vous aime. Je pense également à Valentin, survivant dans ce groupe et nous supportant malgré tout, toujours à écouter d'une oreille les potins.

J'aimerais terminer en remerciant ma famille. Papa, Maman, merci pour le soutien que vous m'avez toujours apporté, pour m'avoir sans cesse encouragée à me dépasser, et bien sûr pour l'amour inconditionnel que vous me donnez depuis toujours. Elisa, je peux affirmer (en toute objectivité, bien sûr) que tu es la meilleure sur du monde. Je ne serais pas la personne que je suis sans toi, alors merci pour tout, et pour le soutien que tu m'apportes au quotidien. Mamie, merci pour ta douceur et ta bienveillance constantes, qui m'ont toujours accompagnée, même de loin. Merci pour nos discussions au téléphone, pour tes messages, et pour tous ces petits moments partagés qui m'ont toujours fait du bien. Et enfin, Papi, merci. Tu n'es malheureusement plus là pour lire ces lignes, mais tu m'as soutenue tout au long de cette thèse, jusqu'à l'écriture de ce manuscrit. Je chéris profondément tous les souvenirs que j'ai partagés avec toi. On me dit souvent que tu étais fier de moi, mais je le suis encore plus d'avoir eu un papi comme toi. Je vous aime.

Contents

Ackowledgments **3**

List of Figures **10**

Acronyms **15**

Abstract **19**

Résumé **21**

Introduction and Outline **23**

I Background 27

1 Magnetism **29**
1.1 Introduction to magnetism . . . 29
1.1.1 Diamagnetism . . . 31
1.1.2 Paramagnetism . . . 31
1.1.3 Ferromagnetism . . . 32
1.1.4 Antiferromagnetism . . . 32
1.1.5 Ferrimagnetism . . . 33
1.2 Magnetism in a tri-layer system . . . 33
1.2.1 The energies . . . 33
1.2.2 The spin textures . . . 43
1.3 Conclusion . . . 51

2 Control of the magnetic properties in a tri-layer system **53**
2.1 Material dependence . . . 54
2.1.1 Influcence of the oxidation state . . . 54
2.1.2 Influence of the ferromagnetic thickness . . . 57
2.2 Gate voltage control of magnetic energies . . . 60
2.2.1 Voltage control of magnetic anisotropy (VCMA) . . . 60
2.2.2 Voltage control of Dzyaloshinskii-Moriya interaction (VCDMI) . . . 63
2.3 Dynamic of spin textures . . . 67
2.3.1 Motion under an external magnetic field . . . 69
2.3.2 Motion under an electrical current . . . 73
2.3.3 Motion of magnetic skyrmions - Thiele equation . . . 77
2.4 Conclusion . . . 81

II Process and Characterization techniques 83

3 Experimental techniques **85**

3.1 Sample fabrication . . . 86
3.1.1 Tri-layer deposition . . . 86
3.1.2 Patterning process for gate voltage control . . . 90
3.2 Characterization Techniques . . . 92
3.2.1 Magneto-Optical Kerr Effect . . . 92
3.2.2 MOKE magnetometer . . . 93
3.2.3 MOKE microscope . . . 94
3.2.4 HAXPES measurements . . . 96

III Results 99

4 Material dependence of the DMI sign 101
4.1 Introduction . . . 101
4.2 Experimental Observation . . . 101
4.3 *Ab initio* study . . . 107
4.4 Conclusion . . . 114

5 Hard X-ray photoelectron spectroscopy measurements on gated Pt/Co/AlOx trilayers 117
5.1 Introduction . . . 117
5.2 Magnetic properties . . . 118
5.3 The HAXPES measurements . . . 124
5.4 Conclusion . . . 128

6 Chirality reversal by gate voltage 129
6.1 Introduction . . . 129
6.2 The sample: choice of the optimal parameters . . . 130
6.3 Gate voltage application on domain walls in track . . . 133
6.4 Gate voltage application on skyrmions in track . . . 138
6.4.1 Optimization of the process . . . 138
6.4.2 Attempt to reverse the chirality of a single skyrmions and problems encounter 141
6.5 Conclusion . . . 146

7 Micromagnetic analysis of skyrmion trajectories in systems with weak Dzyaloshinskii-Moriya interaction 149
7.1 Introduction . . . 149
7.2 Micromagnetic simulation parameters and initial state . . . 150
7.3 Motion of skyrmions under small current . . . 157
7.3.1 Trajectories . . . 157
7.3.2 Large Skyrmion Approximation . . . 163
7.3.3 Effect of the damping on the trajectories . . . 166
7.4 Motion of skyrmions under high current . . . 169
7.5 Conclusion . . . 176

8 Conclusion and perspectives **179**
8.1 General Conclusion 179
8.2 Perspectives 180

9 Supplementary **183**
9.1 Supplementary 1: Thickness conversion 183
9.2 supplementary 2: Inter and intralayer contribution to the DMI 184
9.3 Supplementary 3: Bloch and Néel domain wall energy and profile 185
9.4 Supplementary 4: Thiele equation - the velocities 188
9.5 Supplementary 5: Analytical model of the helicity as a function of the DMI coefficient D 189

List of Figures

Figure 1 History of artificial intelligence 23

Figure 1.1 Electron motion around a nucleus 30
Figure 1.2 Diamagnetism behavior 31
Figure 1.3 Paramagnetism behavior 31
Figure 1.4 Ferromagnetism behavior 32
Figure 1.5 Antiferromagnetism behavior 32
Figure 1.6 Ferrimagnetism behavior 33
Figure 1.7 Source of demagnetizing field in a ferroamgnetic material 35
Figure 1.8 Magnetization in a magnetic thin film 37
Figure 1.9 Evolution of the effective anisotropy coefficient $K_{eff} \times t_{FM}$ with respect to the thickness of the ferromagnet t_{FM}. 39
Figure 1.10 Convention relating chirality to the DMI sign 41
Figure 1.11 Fert-Levy DMI 42
Figure 1.12 Rashba DMI 43
Figure 1.13 Scheme of a Clockwise Néel and Bloch domain wall 44
Figure 1.14 Geometry and coordinates systems used to described the magnetization in a skyrmion 47
Figure 1.15 Evolution of the different energies with the radius of the skyrmion . . . 49
Figure 1.16 Topological soliton energy E_s for the three different DMI values 50
Figure 1.17 Topological soliton phase diagram. 51

Figure 2.1 Domain wall velocity and DMI sign study in Pt/Co/AlOx and Pt/Co/GdOx system 55
Figure 2.2 Evolution of the DMI coefficient with the oxidation state at the interface CoFe/TaOX 56
Figure 2.3 DMI coefficient in the tri-layer Ta/FeCoB/TaOX 57
Figure 2.4 Evolution of the effective anisotropy constqant with respect to the thickness of the ferromagnet 58
Figure 2.5 DMI study in the tri-layer Pt/CoFeB/AlOx and Pt/Co/TaOx systems . 59
Figure 2.6 Chirality study in the Ta/FeCoB/TaOX system 60
Figure 2.7 Summary of the VCMA efficiencies at a FM/MOx interfaces and in magnetic tunnel junction (MTJ) 62
Figure 2.8 TEM cross section of a Ta/Pt/Co/GdOx sample and EELS analysis of the oxide and cobalt quantity 63
Figure 2.9 BLS measurement of the DMI coefficient D in Pt/Co/AlOX system . . 65

Figure 2.10 VCDMI efficiencies and the equivalent normalized coefficients η_{DMI} . . 66
Figure 2.11 Chirality control by gate Voltage 67
Figure 2.12 Precession of the magnetization $\overrightarrow{m}$ in a constant effective field $\overrightarrow{H_{eff}}$ . . 68
Figure 2.13 Effect of torques generated by an applied magnetic field on Bloch domain walls 70
Figure 2.14 Domain wall velocity with respect to the external magnetic field 71
Figure 2.15 Evolution of the domain wall velocity with respect to the external magnetic field for different value of DMI coefficient D 72
Figure 2.16 Domain wall velocity with respect to the applied external magnetic field in Pt/Co/Pt and Pt/Co/AlOx 72
Figure 2.17 Scheme of the spin Hall effect 76
Figure 2.18 Drift velocity of skyrmions as a function of the current density 79
Figure 2.19 Modelisation of the motion of skyrmions inside a magnetic track 79
Figure 2.20 Phase diagram of the skyrmion Hall angle with respect to the current density 80

Figure 3.1 On-axis magnetron sputtering technique 86
Figure 3.2 Off-axis magnetron sputtering technique 87
Figure 3.3 3D and 2D scheme of the Off-axis deposition and resulting iso-thickness deposition lines 87
Figure 3.4 Variation of thickness deposited on an off-centered wafer 88
Figure 3.5 Error % between the linear approximation and the polynomial distribution 88
Figure 3.6 Scheme of the deposition of the tri-layer system step-by-step 89
Figure 3.7 Schematic cross-section of the tri-layer system along the y-axis for a given FeCoB thickness 89
Figure 3.8 Scheme of the process of the sample describe step-by-step 90
Figure 3.9 Full layout of one Hall cross device 92
Figure 3.10 Scheme of the different configurations for the Magneto-Optic Kerr Effect 93
Figure 3.11 Hysteresis curves obtained with a MOKE magnetometer for in the PM, PMA and IPA regions 94
Figure 3.12 Iso-thickness deposited lines in the spatial plane and the thickness space 95
Figure 3.13 Scheme of the operation of the MOKE microscope and resulting MOKE differential images 95
Figure 3.14 Comparison of the soft and hard X-Ray Photeoelectron Spectroscopy . 97

Figure 4.1 Remanence map of tri-layer system Ta/FeCoB/TaOx measured by MOKE magnetometry with hysteresis curves measured along both wedges . . . 102
Figure 4.3 DMI sign map in the perpendicular magnetic anisotropy region 105
Figure 4.4 The Fe_m/Ta_3 system for *ab initio* calculations 106
Figure 4.5 DMI energy of Fe_7Ta_3 and Fe_7Ta_5 systems 108
Figure 4.6 Energy of the DMI with varying distance between the first layer of Fe at the interface and the oxygen atoms. 109
Figure 4.7 *ab initio* DMI map for different number of oxygen atoms in ther interfacial Ta monolayer 110

Figure 4.8 *ab initio* DMI map for a change of the oxygen distance from the Ta/Fe interface . . . 111
Figure 4.9 Layer-resolved and 5D orbital resolved SOC energy in the Fe_m/Ta_3 . . 112
Figure 4.10 Spin dependent d-orbital occupations in Fe_3Ta_3 and Fe_5Ta_3 114
Figure 4.11 Decrease of interatomic distance with Fe monolayer thickness at the Fe_mTa_3 interface . . . 114
Figure 4.12 Layer resolved magnetic moment of the system Fe_mTa_3 115
Figure 4.13 Summary of the joint experimental and *ab initio* study 116

Figure 5.1 3D and 2D representation of the tri-layer system Pt/Co/AlOX 119
Figure 5.2 Remanence map of tri-layer system Pt/Co/AlOx 120
Figure 5.3 Hysteresis curves of the reference samples measured by p-MOKE 121
Figure 5.4 Capacitor-like devices for HAXPES measurements 121
Figure 5.5 Hysteresis curves of the capacitor-like devices measured by p-MOKE . . 122
Figure 5.6 Anisotropy state evolution with the oxidation state of the Co layer . . . 123
Figure 5.7 Co *2p* HAXPES spectra of reference and capacitor-likes samples 125
Figure 5.8 Summary of the Co *2p* HAXPES spectra evolution along the Al wedge . 126
Figure 5.9 Oxidation percentage of the Cobalt layer measured in reference and gated samples . . . 127

Figure 6.1 Remanence map of tri-layer system Ta/FeCoB/TaOx measured by MOKE magnetometry . . . 131
Figure 6.2 2D cut of the full system along the top Ta wedge 132
Figure 6.3 Layout and MOKE imaging of Hall crosses device 133
Figure 6.4 Comparison of I-V curves of an electronic insulator and a conducting one 134
Figure 6.5 P-MOKE map of the tri-layer Ta/FeCoB/TaOx 135
Figure 6.6 MOKE microscope setup 136
Figure 6.7 Chirality reversal of magnetic domain wall in a track using gate voltage 137
Figure 6.8 Change of anisotropy due to gate voltage 138
Figure 6.9 P-MOKE differential image of one Hall cross before and after rotation . 139
Figure 6.10 Shadow effect during the ferromagnetic layer deposition 140
Figure 6.11 Iso-thickness lines before and after rotation of the cross 140
Figure 6.12 Remanence map of tri-layer system Ta/FeCoB/TaOx measured by MOKE magnetometry before and after zoom . . . 141
Figure 6.13 Sample color difference between good and defective ALD depositions . . 142
Figure 6.14 Irreversible change of anisotropy due to gate voltage 143
Figure 6.15 Skyrmions to domain walls transformation by gate voltage 144
Figure 6.16 Manipulation of the skyrmions size and density by gate voltage 144
Figure 6.17 Non-uniform application of the gate voltage on the Ta/FeCoB/TaOx system 146

Figure 7.1 Demagnetizing field applied to simulate a single skyrmion in an infinite thin film . . . 151
Figure 7.2 Helicity evolution as a function of the DMI coefficient value 152
Figure 7.3 Clockwise and counter clockwise channel for the stabilization of a single skyrmion . . . 153

Figure 7.4 Evolution of the radius and domain wall width s a function of the DMI coefficient value . . . 153
Figure 7.5 Profile of the z-component of the magnetization m_z of a Bloch and a Néel skyrmion . . . 154
Figure 7.6 Analytical model studying the helicity as a function of the DMI . . . 156
Figure 7.7 Comparison of the helicity calculated using the analytical model and extracted from the simulations as a function of the DMI . . . 157
Figure 7.8 Evolution of the trajectory and helicity of the simulated skyrmions with the DMI value . . . 158
Figure 7.9 Geometry and coordinates systems used to described the magnetization in a skyrmion . . . 159
Figure 7.10 Trajectory with respect to the helicity of the simulated skyrmions . . . 162
Figure 7.11 Comparison of the skyrmion Hall angle extracted from the model and simulated . . . 163
Figure 7.12 Comparison of the β_0 exchange integral calculated from the model and approximated . . . 164
Figure 7.13 Simulated radius and domain wall width of skyrmion with respect to the helicity . . . 164
Figure 7.14 Comparison of the skyrmion Hall angle extracted from the approximation and simulated . . . 165
Figure 7.15 Trajectories of skyrmions driven by an electrical current density with a damping of $\alpha = 0.05$ . . . 166
Figure 7.16 Trajectories of skyrmions driven by an electrical current density with a damping of $\alpha = 1$ . . . 167
Figure 7.17 Damping effect of the skyrmion Hall angle: simulation vs model . . . 168
Figure 7.18 Deformation of a skyrmion under high current density . . . 169
Figure 7.19 Trajectories of the simulated skyrmions under high current density for different value of DMI . . . 170
Figure 7.20 Polar representation and evolution of the radius with the angle around the skyrmion edge: initial vs final state . . . 171
Figure 7.21 Polar representation and evolution of the domain wall width with the angle around the skyrmion edge: initial vs final state . . . 172
Figure 7.22 Polar representation and evolution of the helicity ξ with the angle around the skyrmion edge: initial vs final state . . . 173
Figure 7.23 Evolution of the difference measured between the initial and the final state for the trajectory, the radius, the domain wall width δ_{DW} and the helicity ξ as a function of the DMI value . . . 175
Figure 7.24 Average helicity as a function of the DMI: initial vs final state . . . 176
Figure 7.25 Evolution of the average radius R, average domain wall width δ_{DW} and average helicity ξ as a function of the time of current injection fro two critical skyrmions. . . . 176

Figure 8.1 LiPON-based solid-state ionic supercapacitor structure . . . 181

Figure 9.1 Off-axis deposition: geometry of the technique . . . 184

Figure 9.2 Inter and intralayer contribution to the DMI 185

List of Acronyms

ALD Atomic layer deposition.

BLS Brillouin light scattering.

CCW Counter Clock-Wise.

CIDWM Current induced domain wall motion.

CIM Current induced motion.

CW Clock-Wise.

DL Damping-like.

DMI DzyaloshinskiiMoriya interaction.

DW Domain wall.

FL Field-like.

FM Ferromagnet.

FMR Ferromagnetic resonance.

HAXPES Hard X-ray photoelectron spectroscopy.

HM Heavy metal.

IPA In-plane anisotropy.

ITO Indium Tin Oxide.

LLG Landau-Lifshitz-Gilbert.

MOKE Magneto-optical Kerr effect.

MOx Metal oxide.

MRAM Magnetic random access memory.

MTJ Magnetic tunnel junction.

OOP Out-of-plane.

PM Paramagnetic.

PMA Perpendicular magnetic anisotropy.

REE RashbaEdelstein effect.

SHE Spin Hall effect.

SIA Structural inversion asymmetry.

SkHA Skyrmion Hall angle.

SkHE Skyrmion Hall effect.

SOC Spinorbit coupling.

SOT Spinorbit torque.

STT Spintransfer torque.

VCDMI Voltage control of the DzyaloshinskiiMoriya interaction.

VCMA Voltage control of magnetic anisotropy.

XPS X-ray photoelectron spectroscopy.

Abstract

Skyrmions are chiral swirling magnetic spin textures that exhibit many characteristics: they can be small, they are stable at room temperature, we can create and annihilate them using a gate voltage and they are efficiently manipulated using an electrical current. These properties make skyrmions promising candidates for many applications such as skyrmion racetrack memories, skyrmion based logic devices or neuromorphic computing.

Realizing these technologies, however, requires precise control over the creation, stability, and motion of skyrmions. Recent studies have shown that gate voltages can not only nucleate and delete skyrmions but also modulate the DzyaloshinskiiMoriya interaction (DMI), a key factor responsible for their stabilization and their chirality, ie. the sense of rotation of spins within their domain wall.

In this PhD work, we investigated the evolution of the DMI chirality as a function of material parameters in a Ta/FeCoB/TaOx trilayer system, with the two top layers deposited in a wedge to tune interfacial properties. In addition, to better understand the interaction at the origin of the stabilization of skyrmion, we discovered, using ab initio calculations a new mechanism possibly explaining the inversion of the DMI chirality with respect to the thickness of the ferromagnetic layer, linked to structural relaxation in the ultrathin regime.

Then, we also experimentally demonstrate the magneto-ionic origin of the non-volatile and strong anisotropy variation induced by gate voltage in a Pt/Co/AlOx system, which is similar to the Ta/FeCoB/TaOx stack but exhibits larger DMI and magnetic anisotropy. A comparison between reference and gated samples showed the evolution of the oxidation state at the Co/Oxide interface a result further supported by Hard X-ray Photoelectron Spectroscopy (HAXPES) measurements.

Additionally, we focused on the gate voltage control of skyrmion chirality, with the goal of achieving single-skyrmion manipulation and detection. Skyrmion stabilization in patterned tracks was thus achieved, where their behavior under gate voltage control was subsequently studied.

Finally, to better understand skyrmion dynamics under electrical currents, we conducted micromagnetic simulations under small ($10^{10} A/m^2$) and large ($10^{11} A/m^2$) current. We have in particular observed that for large currents, the type of skyrmions, ie Néel, Bloch or intermediate, is modified. It induces a bending of their trajectory so that, in the stationary regime, initially

nearly-Bloch skyrmions move under current similar to Néel skyrmions. This is of importance since the current induced motion is very often used to deduce skyrmion type.

Résumé

Les skyrmions sont des textures magnétiques chirales qui présentent de nombreuses propriétés remarquables : ils peuvent être de taille nanométrique, ils sont stables à température ambiante, nous pouvons les créer et les annihiler à l'aide d'une tension de grille et ils peuvent être déplacés efficacement à l'aide d'un courant électrique. Ces propriétés font des skyrmions des candidats prometteurs pour de nombreuses applications telles que les mémoires à piste magnétique contenant des skyrmions, les dispositifs logiques basés sur les skyrmions ou le calcul neuromorphique.

La mise en uvre de ces technologies nécessite toutefois un contrôle précis de la création, de la stabilité et du déplacement sous courant des skyrmions. Des études récentes ont montré quune tension de grille peut non seulement créer ou supprimer des skyrmions, mais également moduler l'interaction Dzyaloshinskii-Moriya (DMI), un facteur clé responsable de leur stabilisation et de leur chiralité, c'est-à-dire du sens de rotation des spins dans la paroi de domaine du skyrmion.

Durant cette thèse, nous avons étudié l'évolution de la chiralité de la DMI en fonction des paramètres matériaux dans un système tricouche Ta/FeCoB/TaOx, les deux couches supérieures étant déposées avec un gradient dépaisseur (épaisseur de FeCoB et degré doxydation de TaOx) afin de moduler progressivement les propriétés magnétiques. De plus, ayant pour objectif de mieux comprendre l'interaction à l'origine de la stabilisation des skyrmions, nous avons découvert, en utilisant des calculs ab initio, un nouveau mécanisme pouvant expliquer l'inversion de la chiralité de la DMI en fonction de l'épaisseur de la couche ferromagnétique, liée à une relaxation structurelle dans le régime ultra-mince.

Nous avons ensuite démontré expérimentalement lorigine magnéto-ionique de la forte variation non volatile de lanisotropie induite par la tension de grille dans le système Pt/Co/AlOx, similaire à la tri-couche Ta/FeCoB/TaOx mais présentant un DMI et une anisotropie magnétique plus élevés. La comparaison entre les échantillons de référence et ceux soumis à une tension de grille a mis en évidence une évolution de létat doxydation à linterface Co/oxyde, un résultat confirmé par des mesures de spectroscopie photoélectronique à rayons X de hautes energies (HAXPES).

Par ailleurs, nous avons étudié le contrôle de la chiralité des skyrmions par tension de grille, avec pour objectif la manipulation et la détection d'un skyrmion unique. La stabilisation des parois de domaine dans des pistes lithographiées a ainsi été réalisé et leur contrôle par la tension de la grille a ensuite été étudié.

Enfin, pour mieux comprendre la dynamique des skyrmions sous l'effet de courants électriques, des simulations micromagnétiques ont été menées à différentes densités de courant ($10^{10}A/m^2 - 10^{11}A/m^2$). Celles-ci ont révélé que sous fort courant, le type de skyrmion (Néel, Bloch ou intermédiaire) peut évoluer dynamiquement, modifiant sa trajectoire. Ainsi, des skyrmions initialement de type Bloch peuvent se comporter dynamiquement comme des skyrmions de Néel. Cette observation est importante, car lanalyse du mouvement est souvent utilisée comme critère indirect pour déterminer la nature du skyrmion.

Introduction and Outline

Spintronics, which stands for spin transport electronics, is the study and the use of the electron's spin degree of freedom in addition of its charge as in conventional electronic. In the 1950s, N. Mott proposed that conduction in ferromagnets occurs through two spin channels with different scattering rates. Several decades later, Johnson and Silsbee (1985) demonstrated spin-polarized electron injection from a ferromagnetic metal into a normal metal. Soon after, the discovery of giant magnetoresistance (GMR) by Albert Fert and co-workers [1], and independently by Peter Grünberg and colleagues (1988) [2], constitutes for many people the starting point of the spintronics as a field of research.

Nowadays, our society is in a continuous increase. Always looking for progress and efficiency. The biggest example is the large emergence of the artificial intelligence in these past few years. While the AI subject was already studied in the 50's, it is only in the early 2000's that the machine learning and later deep learning emerged both in academia and industry. The figure 1(a) shows that artificial intelligence as a subject of research boomed in the 2020s but the general public also takes up the subject as shown with the evolution over the years of the number of research in google about AI presented in figure 1(b).

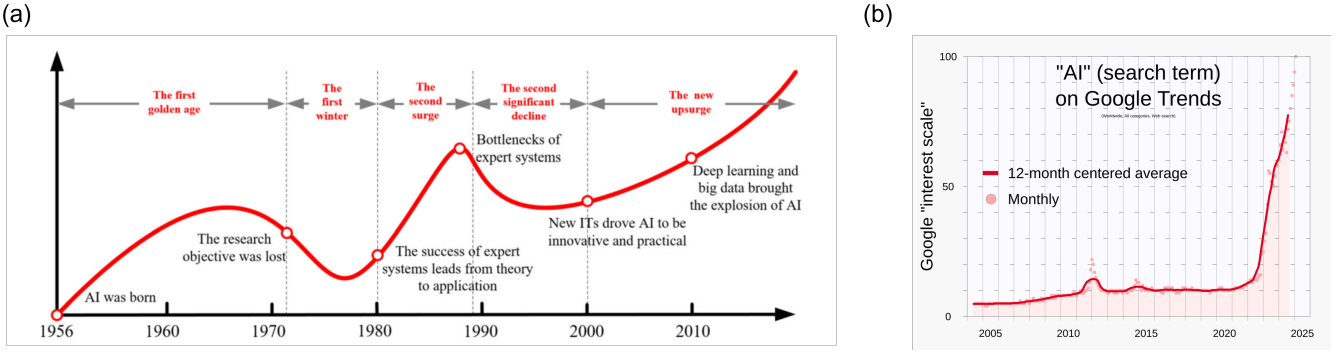

Figure 1: (a) (Taken from [3] History of the artificial intelligence highlighting the biggest advancement in the field over the year.(b) (Taken from Wikipedia) Google trends of the term 'AI' over the years.

At the same time, the environment should stand at the heart of societal priorities. This never ending growth comes at the cost of severe and often irreversible environmental damage. In this context, spintronics emerges as a promising solution, combining efficiency with low power consumption across a wide range of applications. Spintronic sensors, for example, offer the advantage of high sensitivity together with small dimensions and reduced energy cost. Another

major breakthrough is magnetic random-access memory (MRAM). Unlike conventional volatile memories, MRAM stores data in magnetic domains, providing non-volatility and representing a significant step forward in terms of energy efficiency compared to static or dynamic RAM.

In the von Neumann architecture, a fundamental limitation, the so-called von Neumann bottleneck, arises from the restricted data transfer rate between the central processing unit (CPU) and memory, which limits the effective processing speed. Inspired by the functioning of the human brain, unconventional computing seeks to overcome this limitation by integrating memory and processing within the same unit (called in memory-computing), thereby reducing energy losses. Neuromorphic computing, in particular, has emerged as a promising candidate in this field [4].

In this thesis we focus our work on a promising 2D magnetic object: the skyrmion. A skyrmion is a chiral swirling magnetic spin texture which can measure from few nanometers to few μm. These past few years, skyrmions appeared to be of particular interest for spintronics application. Particularly, skyrmions were envisioned as information carriers in memory computing or logic devices, since their presence or absence can be electrically detected and encoded as a '1' or a '0'[5], [6]. Associated with their small size and their ability to be manipulated efficiently using an electrical current make them promising also for logic devices and neuromorphic computing [7] [8].

But in order to be able to use skyrmions in these applications, we need to understand their behavior and to control them individually and collectively. This is in this context that this manuscript stands. First I studied the interaction at the origin of the stabilization of skyrmions: the Dzyaloshinskii-Moriya interaction (DMI) in Heavy Metal/ Ferromagnet/ Metal-Oxide (HM/FM/MOx) trilayers system. In this type of system the DMI depends both on the ferromagnetic thickness and the oxidation state at the interface. Following this, a promising, low power and versatile technique to control skyrmion motion is the gate voltage control of interfacial DMI. I explored the oxygen migration induced by the gate using synchrotron Hard X-Ray Photoelectron Spectroscopy (HAXPES) technique. In this thesis we experimentally demonstrate a static and dynamic way to control respectively collectively and individually the skyrmions. In addition, I performed micromagnetic analysis of the DMI impact on skyrmion properties and trajectories under current associated with a study on the effect of the mechanism of the damping.

This manuscript is organized as follows:

Outline

Part I: Background

Chapter 1 is a large overview on magnetism with a brief description of the different magnetic properties of matter. Then, I focus on the magnetism inside the tri-layer system used in mu studies, Ta/FeCoB/TaOx and more specifically on the energies and interactions inside the ferromagnetic layer. Finally, I discuss the magnetic spin textures stabilized in such system by the competitions of all the energies.

Chapter 2 is a state of the art chapter, dedicated to explain the different ways to control the magnetic properties in a tri-layer system, first in a static way by material dependence, then

dynamically using a gate voltage. Finally I describe the effect of the control of these energies on the spin textures and particularly on their dynamic.

Part II: Process and Characterization techniques

Chapter 3 explains the experimental techniques employed for the fabrication of the samples with a step-by-step detailed description of the process. Then, in a second part I present the characterization instruments used to investigate their properties.

Part III: Results

Chapter 4 presents a complete study of the DMI in the tri-layer system Ta/FeCoB/TaOx. First, we explain the experimental measurement of the DMI sign and the corresponding DMI sign map. The second part cover the ab initio calculations of the DMI, together with a comparison with the experimental results. Lastly, we explore the phenomena responsible for the observed reversal of the DMI sign.

Chapter 5 demonstrates experimentally the magnetoionic origin of the non-volatile strong anisotropy variation using gate voltage in a Pt/Co/AlOx/HfO2 system, similar to the Ta/FeCoB/TaOx tri-layer. First we compared magnetic properties between reference and gated samples to highlight the evolution of the oxidation rate at the Co/AlOx interface. Then this study is supported by hard x-rays spectroscopy measurements that we performed in the synchrotron.

Chapter 6 investigates the gate-voltage control of the DMI sign and spin-texture motion inside micro-metric tracks. After presenting the optimization of the sample parameters we show the reversal of domain wall chirality and discuss the control of a single skyrmion chirality using a gate voltage.

Chapter 7 studies the motion of skyrmion under a small ($10^{10} A/m^2$) and high ($10^{11} A/m^2$) electrical current, numerically, using micromagnetic simulations. I first describe the dependence of the skyrmions parameters with the DMI then study the skyrmion trajectories as a function the DMI, their helicity and the damping.

Chapter 8 gives a summary on the work performed during the thesis and described in this manuscript as well as an overview on the future projects connected to this work.

Part I

Background

Chapter 1

Magnetism

1.1 Introduction to magnetism 29
1.1.1 Diamagnetism 31
1.1.2 Paramagnetism 31
1.1.3 Ferromagnetism 32
1.1.4 Antiferromagnetism 32
1.1.5 Ferrimagnetism 33
1.2 Magnetism in a tri-layer system 33
1.2.1 The energies 33
1.2.2 The spin textures 43
1.3 Conclusion 51

1.1 Introduction to magnetism

Magnetism is a physical phenomenon describing the ability of certain materials to attract or repel each other through a magnetic field. This field, responsible for the magnetic forces, arises from the motion of electric charges and magnetic moments in the material.
Magnetic moments are a key property in magnetism. They represent the strength of the interaction with the magnetic field of the electrons in the materials.
A charged particle, such as an electron, moving around the nucleus of an atom is an easy picture allowing us to understand the two origins of a magnetic moment, as illustrated in the figure 1.1:

Orbital magnetic moment

The motion of an electron around the nucleus forms a current loop, which, according to Ampère's law, generates a magnetic field. The orbital magnetic moment is the dipole associated with this current loop. It can be written as:

$$\overrightarrow{m_L} = \frac{q}{2m}\overrightarrow{L} \tag{1.1}$$

With q the charge of the particle, m the mass of the particle, $\overrightarrow{L}$ the electron orbital angular momentum.
In this case the charged particle is an electron, we can then write :

$$\overrightarrow{m_L} = \frac{-e}{2m_e}\overrightarrow{L} = \gamma_e \overrightarrow{L} \tag{1.2}$$

With $e \approx 1.602 \times 10^{-19} C$, $m_e \approx 9.109 \times 10^{-31} kg$ and $\gamma_e = \frac{-e}{2m_e}$ the gyromagnetic ratio of the electron, it quantifies how much magnetic moment is produced per unit of angular momentum.

Spin magnetic moment

The spin magnetic moment $\overrightarrow{m_S}$ is an intrinsic property of a particle. It arises from their intrinsic angular momentum $\overrightarrow{S}$. For the electron, it is expressed as:

$$\overrightarrow{m_S} = -2\mu_B \frac{\overrightarrow{S}}{\hbar} \tag{1.3}$$

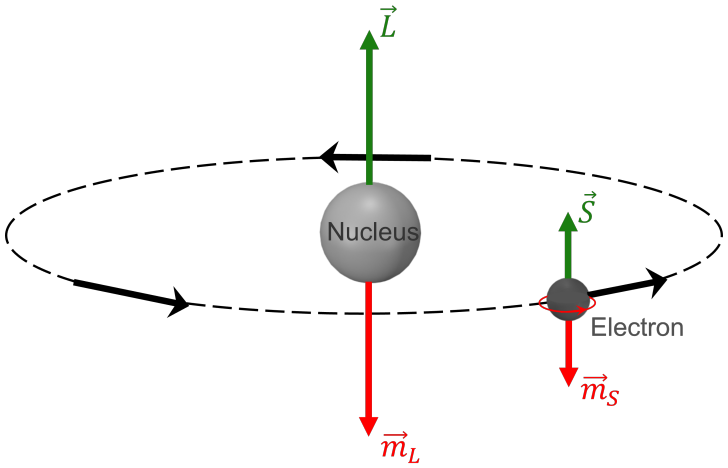

Figure 1.1: (Not at scale) An electron moving around a nucleus with orbital angular moment $\overrightarrow{L}$ creating a magnetic moment $\overrightarrow{m}_L$. In addition, electron have an intrinsic quantum property, the spin, described by the vector operator $\overrightarrow{S}$ and creating a magnetic moment $\overrightarrow{m}_S$.

Finally, materials can be considered as assemblies of numerous magnetic moments, making them responsive to magnetic fields. Thus, they can be classified according to this response to an external magnetic field $\overrightarrow{H}$. We call $\overrightarrow{M}$ the magnetization which represents the volume density of the magnetic moment, $\overrightarrow{\mu}$, within a magnetic material. The magnetic susceptibility, defined as $\chi = \left|\frac{dM}{dH}\right|_{H=0}$ quantifies the extent to which a material becomes magnetized in the presence of a magnetic field.

1.1.1 Diamagnetism

Diamagnetism is a property exhibited by all the materials in some extents. When no external magnetic field is applied, paired electrons produce no net magnetic moment, since both their spin and orbital contributions cancel. However, the application of an external magnetic field modifies the electronic orbital motion, inducing a magnetic moment opposite to the applied field in accordance with Lenzs law. The order of magnitude of the magnetic susceptibility $\chi \simeq -10^{-6}$ to -10^{-5} making the diamagnetism behavior negligible as compared to other magnetic behaviors that materials can adopt in response to an external magnetic field.

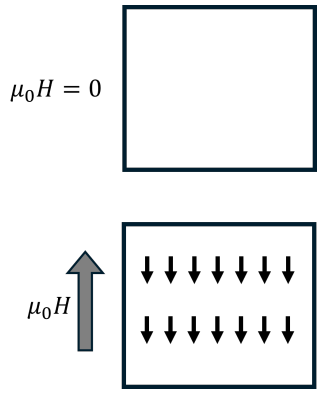

Figure 1.2: Diamagnetic behavior under a magnetic field $\mu_0 H$

1.1.2 Paramagnetism

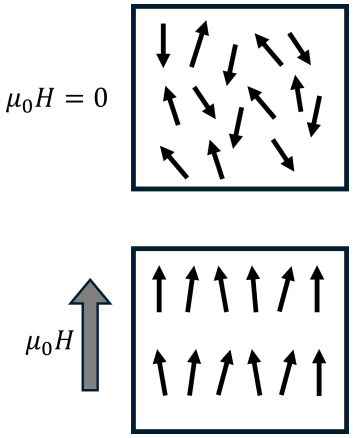

Figure 1.3: Paramagnetic ordering under a magnetic field $\mu_0 H$

Paramagnetism originates from the magnetic moments of unpaired electrons, which are typically found in atoms with partially filled atomic orbitals. In the absence of an external magnetic field, the magnetic moments on the atoms are randomly oriented due to thermal fluctuations. However, when an external magnetic field $\mu_0 H$ is applied, these magnetic moments tend to partially align parallel to the field resulting in a net magnetization. The magnetic susceptibility χ is then positive, in the order of 10^{-5} in metals. In ferromagnet the magnetic susceptibility follows the Curie-Weiss law as $\chi = \frac{C}{T - T_C}$ where C is a material-specific Curie constant, T is the temperature and T_C is the Curie temperature. The Curie temperature is the temperature above which certain material lose their permanent magnetic properties.

1.1.3 Ferromagnetism

Among all the types of magnetism, the ferromagnetism is the strongest one ($\chi = 10^4$ to 10^6). It is responsible for most of the common phenomena of everyday magnetism. The origin of the ferromagnetism is the same as paramagnetism however an exchange interaction between magnetic moments force them to align and makes the thermal agitation negligible unlike paramagnetism. The exchange energy coming from this interaction is written $E_{exchange} = -2J\overrightarrow{S}_i \cdot \overrightarrow{S}_j$. With J the exchange constant, positive in the case of ferromagnetism, $\overrightarrow{S}_i$ and $\overrightarrow{S}_j$ two neighboring spins.
In this case magnetic moments can be fully aligned without the application of an external magnetic field. But if the temperature increases until a certain threshold, called Curie temperature T_C, which is intrinsic to every material, the thermal agitation will increase and overcome the ferromagnetism property, the material will become paramagnetic [9] [10].

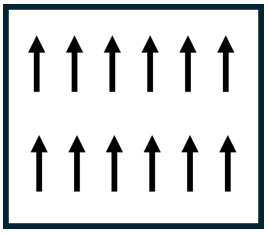

Figure 1.4: Ferromagnetic arrangement of a material

1.1.4 Antiferromagnetism

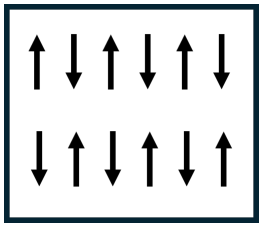

Figure 1.5: Antiferromagnetic arrangement

With no external magnetic field applied, an antiferromagnetic material exhibits no net magnetization. The exchange constant J is negative, favoring opposite alignment of magnetic moments in the two sublattices, thereby canceling each other's effect. As for ferromagnetism it exists a threshold temperature value, called Néel temperature T_N, above which the antiferromagnetic characteristic is lost and the material become paramagnetic.

1.1.5 Ferrimagnetism

The magnetic moments in a antiferromagnetic material are arranged in the same way as in an antiferromagnet. The difference is the magnitude of the moments pointing in opposite direction, due to different atoms or different valences of the same atoms in the two sublattices, resulting in a net magnetization. Above the Curie temperature, ferrimagnets become as well paramagnetic.

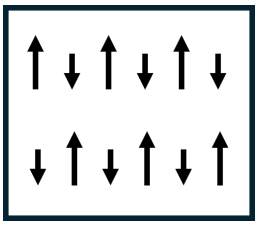

Figure 1.6: Ferrimagnetism behavior

In the context of this study, we focus on ferromagnetism and particularly on ferromagnetic ultrathin films within a tri-layer system composed of Heavy-Metal/ Ferromagnet/ Metal-Oxide (HM/FM/MOx). The reduced dimensionality of ferromagnetic thin film brings different properties and physics compared to bulk material. The film thickness, which is in the order of $\simeq 0.5-10$ nm, strongly influences magnetic behavior. In this ultrathin regime, many properties arise not only from the ferromagnetic layer itself but also from both top FM/MOx and bottom HM/FM interfaces and can change the magnetic configuration inside the ferromagnet.

1.2 Magnetism in a tri-layer system

Let's first introduce the different interactions, and their associated energy terms, that act on the magnetization inside the ferromagnetic layer. More detailed about all the energies can be found in [11],[12], [13], [14]. The magnetic configuration of the sample corresponds to a (local) minimum of the total free energy.

1.2.1 The energies

The Zeeman energy:
The Zeeman interaction describes the interaction between a magnetic moment and an external magnetic induction $\overrightarrow{B}$ leading to a potential energy expressed as :

$$E_{zeeman} = -\overrightarrow{\mu} \cdot \overrightarrow{B}_{ext} \tag{1.4}$$

With μ the magnetic moment

In the context of a magnetic material, the energy is typically expressed per unit volume as the Zeeman energy density:

$$\varepsilon_{Zeeman} = -\mu_0 \overrightarrow{M} \cdot \overrightarrow{H_{ext}} (J/m^3) \tag{1.5}$$

With $\mu_0 = 4\pi \times 10^{-7} H/m$ the vacuum permeability
$\overrightarrow{M}$ the magnetization vector (A/m)

$\overrightarrow{H_{ext}}$ the external magnetic field (A/m).

The Zeeman energy tends to favor alignment of the magnetization $\overrightarrow{M}$ with the external field $\overrightarrow{H_{ext}}$, minimizing the system's energy. The energy depends on the angle between the two vectors, influencing the formation and evolution of magnetic domains and textures.

At the macroscopic scale, the Zeeman interaction governs the behavior of magnetization curves (e.g., hysteresis loops) under applied fields. It plays a critical role in phenomena such as domain wall motion, skyrmion dynamics, and magnetic switching, where the balance between Zeeman and other magnetic energies determines the systems configuration.

The exchange energy:

The exchange interaction is a quantum mechanical interaction between neighboring magnetic moments due to the Pauli exclusion principle and the Coulomb interaction between electrons.

The Pauli exclusion states that two electrons cannot occupy the same quantum state. As a consequence if two electrons are in the same spatial region (orbital) their spins has to be opposite. Inversely, if they have the same spin they must occupy different orbitals.

The Coulomb interaction describes the electrostatic repulsion of two electrons due to their negative charges. This repulsion is stronger when electrons are closer together and decreases as their separation increases.

The competition between the spatial distribution imposed by the Pauli principle and the minimization of Coulomb repulsion gives rise to the exchange interaction. Depending on the system, this interaction may favor either parallel (ferromagnetic) or antiparallel (antiferromagnetic) spin alignment depending on the exchange constant J sign. Indeed at the atomic scale the interaction is governed by the Heisenberg model describing the energy for two interacting spins $\overrightarrow{S_i}$ and $\overrightarrow{S_j}$ of amplitude S, in a discrete form as:

$$E^{ij}_{exchange} = -J_{ij}\overrightarrow{S_i}.\overrightarrow{S_j} \tag{1.6}$$

With J_{ij} the exchange integral. The dot product $\overrightarrow{S_i}.\overrightarrow{S_j}$ determines whether the energy is minimized when the spins are parallel or antiparallel. J is a quantum constant that quantifies the strength and nature of the exchange interaction, its sign will depend on the overlap of the magnetic moment wavefunctions. If the constant J is positive (resp.negative) the system minimizes energy when the spins are parallel (resp. antiparallel) leading to ferromagnetism (resp. antiferromagnetism).

In the micromagnetic continuous approximation we consider the magnetization as a continuous vector field $\overrightarrow{M}(\overrightarrow{r})$. In this case the exchange energy density will represent the energy cost of a non-uniform magnetization (e.g in the case of magnetic domain walls or skyrmion where the magnetic moments rotates). We write:

$$\varepsilon_{exch} = A(\overrightarrow{\nabla}\cdot\overrightarrow{m})^2(J/m^3) \tag{1.7}$$

$\overrightarrow{m} = \frac{\overrightarrow{M}}{M_S}$ the normalized magnetization vector and the exchange stiffness constant $A = JS^2\frac{n}{a}$ (J/m) with the lattice parameter, n depending on the number of magnetic atoms per unit cell. The exchange energy will be minimum (=0) for uniform magnetization. The more rapidly and sharply the magnetization varies in space, the higher the associated exchange energy will be.

The dipolar energy:

The dipolar interaction arises from the classical magnetic dipole-dipole interaction between magnetic moments. Every magnetic moment in the material generates a magnetic field that influences other moments which is an analogy to electric dipoles interacting via the electric field they generates. This is why we often use the Coulombian approach and use virtual magnetic charges to calculate magnetic field created by a magnetized material.
We refer to the dipolar interaction inside the material as the demagnetizing field, and the dipolar interaction outside the material as the stray field.

This long-range interaction tends to minimize the dipolar field generated by virtual surface and volume magnetic charges. Surface magnetic charges occur wherever the magnetization has a component normal to a surface and are described by the surface charge density $\sigma_m = \overrightarrow{M} \cdot \hat{n}$, where $\hat{n}$ is the outward normal unit vector to the surface. Volume magnetic charges, on the other hand, appear in regions where the magnetization has a non-zero divergence (e.g within domain walls) and are given by the charge density $\rho_m = -\overrightarrow{\nabla} \cdot \overrightarrow{M}$. Both types of charges are sources of the demagnetizing field $\overrightarrow{H}_{\text{demag}}$, which opposes the magnetization. This is schematized in the figure 1.7.

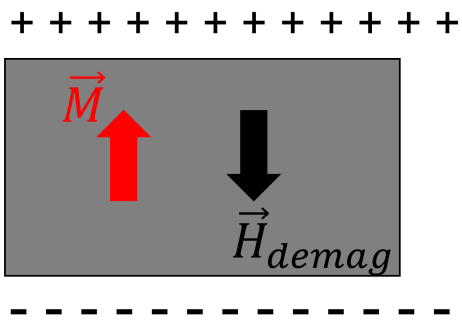

Figure 1.7: Scheme of a ferromagnetic material. The charge '+' and '-' are represented. The magnetization $\overrightarrow{M}$ is in red and the opposite demagnetizing field $\overrightarrow{H}_{demag}$ is in black.

To reduce the associated energy, both surface and volume magnetic charges are minimized and pushed away from each other. As a result, the magnetization tends to align along surfaces and edges to avoid generating normal components. This alignment is strongly dependent on the shape of the magnetic material. For example, in nanowires, dipolar interactions favor a magnetization along the wire axis, while in thin films, an in-plane configuration is energetically preferable to minimize magnetic charges.

For a homogeneous magnetization $\overrightarrow{M}$, the average demagnetizing field can be expressed as :

$$\overrightarrow{H}_{demag} = -\overline{\overline{N}} \cdot \overrightarrow{M} \tag{1.8}$$

$\overline{\overline{N}}$ being the demagnetizing tensor that depends on the geometry of the object.
The demagnetizing energy can then be written :

$$\varepsilon_{demag} = -\frac{1}{2}\mu_0 \overrightarrow{M} \cdot \overrightarrow{H}_{demag} \tag{1.9}$$

With μ_0 the vacuum permeability
$\overrightarrow{M}$ the magnetization vector (A/m)
$\overrightarrow{H}_{demag}$ the demagnetizing field (A/m).

In the case of a magnetic thin film laying in the (x,y) plane as represented in the figure 1.8, $N_z = 1$ and $N_x = N_y = 0$ [15]. Then,

$$\overrightarrow{H}_{demag} = -\begin{pmatrix}0\\0\\1\end{pmatrix} . \begin{pmatrix}M_s sin(\theta)cos(\varphi)\\M_s sin(\theta)sin(\varphi)\\M_s cos(\theta)\end{pmatrix} = -M_S cos(\theta)\hat{z} \tag{1.10}$$

M_S being the saturated magnetization and θ the angle between the magnetization and the out-of-plane direction, z here. By injecting it in the equation 1.9 we obtain:

$$\varepsilon_{Dipolar} = \frac{\mu_0}{2}\begin{pmatrix}M_s sin(\theta)cos(\varphi)\\M_s sin(\theta)sin(\varphi)\\M_s cos(\theta)\end{pmatrix} . \begin{pmatrix}0\\0\\M_s cos(\theta)\end{pmatrix} = \frac{\mu_0 M_S^2}{2} cos^2(\theta) = \frac{\mu_0 M_S^2}{2}(1 - sin^2(\theta)) \tag{1.11}$$

finally,

$$\varepsilon_{Dipolar} = K_d - K_d sin^2(\theta) \tag{1.12}$$

with $K_d = \frac{\mu_0 M_S^2}{2}$ the dipolar anisotropy constant (J/m^3).

In general, we are interested in how the energy varies, so we use its derivative. As a result, constant terms are typically neglected, and we write:

$$\varepsilon_{Dipolar} = -K_d sin^2(\theta) \tag{1.13}$$

The demagnetizing energy has two main consequences: (1) it gives rise to shape anisotropy, which favors the alignment of magnetization along specific directions depending on the geometry of the sample, and (2) it promotes the formation of magnetic domains: while the exchange interaction tends to align neighboring magnetic moments parallel over short distances, the demagnetizing interaction favors anti-parallel alignment over longer ranges. This competition leads to the formation of magnetic domains that are oriented in different directions to minimize the total energy of the system.

The anisotropy energy:

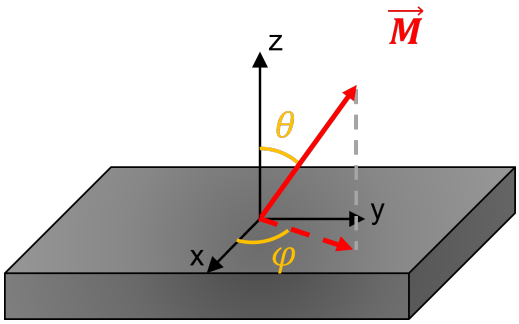

Figure 1.8: Scheme of a magnetic thin film. The magnetization $\overrightarrow{M}$ is represented by the red arrow. The polar angle (between the out-of-plane direction z and the magnetization) is θ and the azimuthal angle (between the x-axis and the magnetization projection in the (x,y) plane) is φ.

Magnetic anisotropy energy refers to the energy associated with the directional dependence of the magnetization. We speak about "easy" or "hard" axis depending if the energy favors or not the alignment of the magnetization along this crystallographic or geometric axis. Different types of anisotropic energy exists. In the context of the dipolar energy we already speak about the shape anisotropy favoring the alignment of the magnetization along edges and surface to reduces magnetic charges. Here we will detail two others anisotropy energies: The magnetocrystalline and the interfacial magnetic anisotropy.

Magnetocrystalline anisotropy

Anisotropy originates from the interaction between the electron spins and the crystal lattice (spinorbit coupling). With the lorentz transformation, in the electron's frame, the electric field transform into a magnetic field that will therefore interact with the spin magnetic moment. The energy is minimized if the magnetization is aligned with certain crystallographic directions. It will be minimum along easy axis/planes and maximum along the hard ones.
The expression of this energy depends on the symmetry of the crystals structure.
The most frequent case is for uni-axial anisotropy occurring for instance in hexagonal crystals where

$$E_{magnetocryst} = K_1 sin^2(\theta) + K_2 sin^4(\theta) \tag{1.14}$$

K_1 and K_2 are called first and second order anisotropy constants, expressed in J/m^3 and θ the angle between the magnetization and the crystal high symmetry axis. Very often higher order term can be ignored and the only term remaining is:

$$E_{magnetocryst} = K_1 sin^2(\theta) \tag{1.15}$$

Interfacial magnetic anisotropy

Interfacial anisotropy arises at the interface between a ferromagnet and another material (heavy metal, oxide or insulator). It is particularly significant in the case of ultra thin film for which surface and interfaces effect dominates over the volume contribution. Therefore, as the layer becomes thinner, the anisotropy increases.

In ultra thin film system the interfacial anisotropy is induced by the difference in the environment of the interface with respect to the bulk. This broken structural symmetry enhances the spin-orbit coupling effects which links the direction of an electrons spin to its orbital motion. At interfaces with heavy metals or oxides, this coupling is stronger and can favor an out-of-plane orientation of magnetization [16].

The interfacial anisotropy energy is written as:

$$\varepsilon_{interf} = \frac{K_s}{t_{FM}} sin^2(\theta) \tag{1.16}$$

With K_s the surface anisotropy constant (J/m^2) and t_{FM} the thickness of the ferromagnetic layer.
The $1/t_{FM}$ accounts for the interfacial nature of this term, being larger for thinner film.

Effective anisotropy energy:

The total effective anisotropy is the competition of the three anisotropy contributions :dipolar, magnetocrystalline and interfacial. As visible in equation 1.13,1.15 and 1.16 these anisotropy energies have the same dependence on θ in the case of z being the high symmetry axis of the magnetocrystalline anisotropy. Therefore, we can write:

$$\varepsilon_{aniso}^{eff} = -K_d sin^2(\theta) + K_{mc} sin^2(\theta) + \frac{K_s}{t_{FM}} sin^2(\theta) = K_{eff} sin^2(\theta) \tag{1.17}$$

With,

$$K_{eff} = \frac{K_s}{t_{FM}} + K_{mc} - K_d \tag{1.18}$$

In ultrathin Fe or Co films, the magnetocrystalline anisotropy energy is typically negligible compared to the dipolar anisotropy, except in textured films where both contributions can be of similar magnitude. Given that magnetocrystalline anisotropy depends on crystal orientation and crystalline quality, and that our sputtered films are polycrystalline, its contribution is negligible in our samples. Therefore, for our thin films, the effective anisotropy constant is

$$K_{eff} = \frac{K_s}{t_{FM}} - K_d \tag{1.19}$$

From Equation 1.17, the minimum of the effective anisotropy energy is reached at different magnetization orientations depending on the sign of the effective anisotropy constant K_{eff}. When $K_{eff} > 0$, the energy is minimized for a perpendicular magnetic anisotropy (PMA), i.e., $\theta = 0° or 180°$ Conversely, if $K_{eff} < 0$, the lowest energy corresponds to an in-plane (IP) magnetization, where $\theta = 90°$. The sign of K_{eff} is itself dependent on the thickness t_{FM} of the ferromagnetic layer. As shown in Equation 1.19, at small thicknesses, the interfacial anisotropy contribution dominates over the demagnetizing (dipolar) energy, leading to a positive K_{eff}. In this regime, the system favors PMA, primarily due to strong spin-orbit coupling at the interface, which drives interfacial anisotropy. This interaction can overcome the demagnetizing effects associated with magnetic charges induced by PMA. As the ferromagnetic layer's thickness increases, the demagnetizing energy contribution grows more significantly than the interfacial anisotropy one, which decreases. At a certain critical thickness t_c, the two contributions become equal, and beyond this point, K_{eff} becomes negative. The system then minimizes its energy by

aligning the magnetization in-plane, reducing both surface and volume magnetic charges. The evolution of the effective anisotropy constant with respect to the thickness of the ferromagnetic layer is schematized in the figure 1.9. For a too thin layer of ferromagnet the system becomes paramagnetic due the dead layer, the ferromagnet is too thin to have a magnetization at measuring temperature [17] [18].

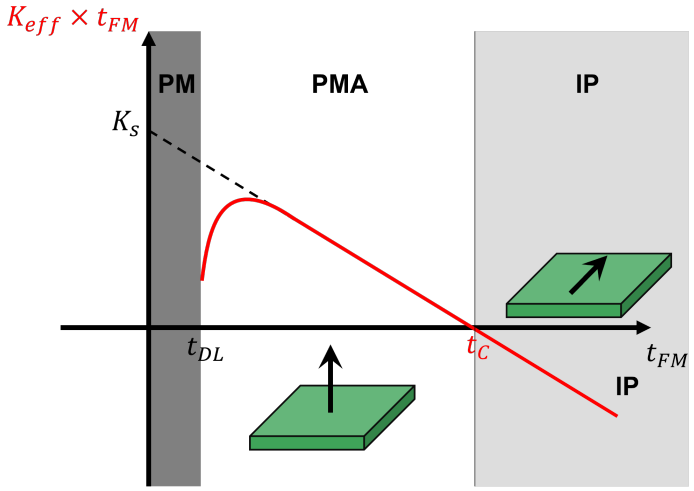

Figure 1.9: Evolution of the effective anisotropy coefficient $K_{eff} \times t_{FM}$ with respect to the thickness of the ferromagnet t_{FM}. Three regions can be distinguished: The paramagnetic region (represented by the dark gray area) when the ferromagnet is too thin to be ferromagnetic at the measuring temperature. The perpendicular magnetic anisotropy (PMA) region when t_{FM} increases until reaching the critical thickness t_C for which the anisotropy becomes in-plane (light gray region).

The Dzyaloshinskii-Moriya interaction (DMI):

In a system with strong spin-orbit coupling and a broken inversion symmetry, another interaction arises, the Dzyaloshinskii-Moriya interaction. This interaction was first introduced by I. Dzyaloshinskii in 1958 to explain the weak ferromagnetism observed in the antiferromagnetic α-Fe_2O_3 crystals [19]. Since the symmetric Heisenberg exchange interaction was unable to explain this phenomenon, Dzyaloshinskii provided the evidence that this weak ferromagnetism was due to the spin lattice and magnetic dipole interactions and proposed an antisymmetric exchange interaction as its origin. In 1960, T. Moriya calculated it by considering spin-orbit coupling in materials with broken inversion symmetry [20].

Spin Orbit Coupling (SOC):

SOC is a quantum interaction in which the electrons spin couples to its orbital motion in the potential of atoms or the crystal lattice. It can be understood as an electron moving with a velocity $\overrightarrow{v}$ in an electric field $\overrightarrow{E}$ due to the nucleus. With the Lorentz transformation, in the electron's rest frame, the electric field transform into an effective magnetic field is given by :

$$\mu_0 \overrightarrow{H} = \overrightarrow{E} \times \frac{\overrightarrow{v}}{c^2} \tag{1.20}$$

Where c is the speed of light. This magnetic field interacts with the spin magnetic moment, $\overrightarrow{m}_s = 2\mu_B \frac{\overrightarrow{S}}{\hbar}$, through a Zeeman interaction, giving an energy of :

$$E_{SOC} = -\mu_0 \overrightarrow{H} \cdot \overrightarrow{m}_s = -2\frac{\mu_B}{\hbar c^2} \overrightarrow{S}(\overrightarrow{E} \times \overrightarrow{v}) \tag{1.21}$$

Where $\overrightarrow{S}$ is the spin angular momentum, μ_B the Bohr magneton and $\hbar$ the reduced Planck constant.

The electric field responsible for the spin orbit coupling can have different origins. First, it can arises from the nucleus in the bulk. In that case the strength of the SOC is proportional to Z^4 [21],[22],[23], Z being the atomic number of the material we see that SOC is much larger for metal composed of heavy atoms (called heavy metals). Two main phenomena originates from the SOC in the bulk, the magnetocrystalline anistropy and the spin Hall effect.
Second, in tri-layer system as HM/FM/MOx that have a structural inversion asymmetry (SIA), the electric field responsible of the SOC originates from the interfaces. The inversion symmetry is broken at the interfaces between two different materials creating an interfacial electric field acting on the magnetization. This is one of the origin of the antisymmetric exchange interaction called the Dzyaloshinskii-Moriya interaction (iDMI).

In the microscopic form the DMI energy density for two neighboring spins is expressed as :

$$E_{DMI}^{ij} = \overrightarrow{d}_{ij} \cdot (\overrightarrow{S_i} \times \overrightarrow{S_j}) \tag{1.22}$$

With $\overrightarrow{d_{ij}}$ the Dzyaloshinskii-Moriya vectors which depends on the symmetry breaking axis and $\overrightarrow{S}_i / \overrightarrow{S}_j$ are the two spins.

The minimum of energy is reached when the cross product of the two spins $(\overrightarrow{S_i} \times \overrightarrow{S_j})$ is antiparallel to the vector $\overrightarrow{d}_{ij}$. This interaction thereby favors the canting of spins with a preferred sense of rotation, called chirality, determined by the direction of $\overrightarrow{d}_{ij}$. The DMI plays a key role in the stabilization of chiral spin textures such as domain walls or skyrmions.

Two types of DMI can appear, namely bulk DMI and interfacial DMI, depending on the symmetry in the system. In some magnetic crystalline materials the atomic arrangement lacks of inversion symmetry, as a consequence the spin-orbit coupling in the crystal creates DMI. This favors chiral spin arrangement inside the material. The type of DMI depends on how inversion symmetry is broken: if the symmetry is broken inside the crystal lattice itself, it is referred to as bulk DMI. If the broken inversion symmetry arise at a surface or interface it is referred to as interfacial DMI, expressed as[24]:

$$\varepsilon_{DMI}^{interf} = D[m_z(\nabla \cdot \overrightarrow{m}) - (\overrightarrow{m} \cdot \nabla)m_z] \tag{1.23}$$

In thin film system with broken inversion symmetry, as in a HM/FM/MOx system, the DMI arises from both interfaces: HM/FM and FM/MOx [25].

In our Ta/FeCoB/TaOx system, the broken symmetry arises from the oxidation of the top Ta layer. Combined with the strong spinorbit coupling (SOC) of Ta, this leads to the emergence of

an interfacial DMI. Considering that the symmetry is broken along the z axis, see the geometry in Figure 1.10, two conventions exists for the DMI vector: (1) $\overrightarrow{d_{ij}} = A(\overrightarrow{z} \times \overrightarrow{r_{ij}})$ or (2) $\overrightarrow{d_{ij}} = A(\overrightarrow{r_{ij}} \times \overrightarrow{z})$ with $A \propto D$ the DMI coefficient, $\overrightarrow{z}$ the axis along which the symmetry is broken and $\overrightarrow{r_{ij}}$ the unit vector that links the two spins $\overrightarrow{S_i}$ and $\overrightarrow{S_j}$. The direction of the DMI vector $\overrightarrow{d_{ij}}$ determines the chirality. It depends on both the sign of the coefficient D and of the cross product between $\overrightarrow{z}$ and $\overrightarrow{r_{ij}}$. For our studied we take as convention (1), $\overrightarrow{z} \times \overrightarrow{r_{ij}}$, see figure 1.10. This convention is the one used in micromagnetic simulations using Mumax[3] software, however studies using Brillouin light scattering (BLS) measurements generally used the opposite convention (2). Now that the cross product is set it is the sign of coefficient A and therefore of D that determines the preferred sense of rotation of the neighboring spins. $D > 0$ leads to minimize the DMI energy, equation 1.22, the cross product between the two spins as to be antiparallel to $\overrightarrow{d_{ij}}$, this favors counter clockwise rotation. Inversely if $D < 0$ it favors a clockwise rotation of the spins as shown in the figure 1.10.

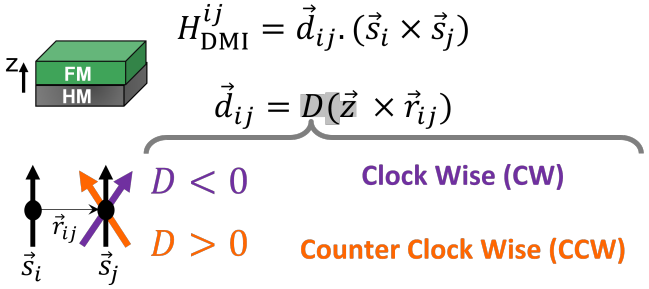

Figure 1.10: Expression of the DMI field H_{DMI} at the HM/FM interface. The convention used in our studies is defined: For a positive DMI coefficient D the rotation is clockwise (CW), for a negative coefficient the rotation is counter clockwise (CCW).

Also, the electric field responsible of the spin-orbit coupling essential for the DMI can have two different origins. This leads to two different DMI mechanisms:

- **Fert-Levy DMI**

At an HM/FM interface the heavy-metal material exhibits a strong spin-orbit coupling due to the HM high atomic number. At the interface the structural inversion symmetry is broken, the environment of the magnetic atoms is non symmetric. The conduction electrons from the ferromagnet experience an electric field induced by the heavy metal atoms. In the electron frame this electric field is transformed into a magnetic induction $\overrightarrow{B} = -\frac{\overrightarrow{v} \times \overrightarrow{E}}{c^2}$ with $\overrightarrow{v}$ the velocity of the electrons, c the speed of light and $\overrightarrow{E}$ the electric field induced by the SOC. As electrons propagate and scatter off on heavy atoms, the spin-orbit interaction couples their motion to their spin, causing an indirect exchange between local magnetic moments $\overrightarrow{S}_i$ and $\overrightarrow{S}_j$. This gives rise to the interfacial Dzyaloshinskii-Moriya interaction (DMI), described by: $\mathcal{H}^{ij}_{DMI} = \overrightarrow{d}_{ij} \cdot (\overrightarrow{S}_i \times \overrightarrow{S}_j)$ [23]. The geometry of this model is schematized in the figure 1.11.

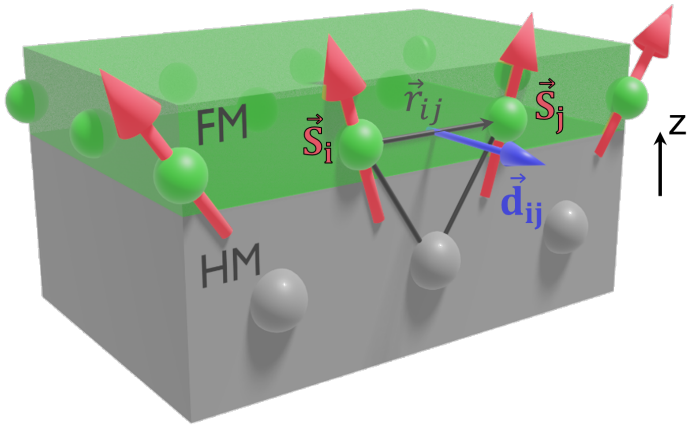

Figure 1.11: *(Figure taken from [5])*. Scheme of a HM/FM interface. The iDMI between two spins $\overrightarrow{S}_i$ and $\overrightarrow{S}_j$ is mediated by a third atom having a strong SOC. It results in the rotation of neighboring spin around the iDMI vector $\overrightarrow{d}_{ij}$ orthogonal to the plane created by the three-atom ($D < 0$ in this case).

- **Rashba DMI**

At the FM/MOx interface, the broken inversion symmetry combined with charge transfer between the ferromagnetic layer and the oxide leads to the formation of an electric field $\overrightarrow{E}_R$, oriented perpendicular to the plane of the films. As in the Fert-Levy model, this electric field is transformed, in the frame of the electrons, in the so-called Rashba magnetic field [26].

$$\overrightarrow{B}_{Rashba} = -\frac{\overrightarrow{v} \times \overrightarrow{E_R}}{c^2} \tag{1.24}$$

This field interacts with the spin of the electron via the magnetic moment creating an additional term in the Hamiltonian of the system [22]:

$$\mathcal{H}_R \propto \alpha_R(\overrightarrow{\sigma} \times \overrightarrow{k}) \cdot \hat{z} \tag{1.25}$$

With α_R the Rashba coefficient corresponding to the SOC strength, $\overrightarrow{\sigma}$ the Pauli matrices and $\overrightarrow{k}$ the wavevector. This Hamiltonian term favors spins perpendicular to both the electric field (in the z direction) and to the momentum of the electrons. As a result, the electronic bands are split, known as the Rashba effect. This leads to spin-momentum locking: electrons with different momenta carry spins with opposite orientations. Depending on the direction of their motion, the electrons experiences opposite field. As the electron moves between magnetic sites the local spin is transmitted to the local magnetic moment through s-d exchange coupling. It introduces a chiral interaction between neighboring spins and leads to a non collinear magnetization with a given sense of rotation which depends on the direction of motion of the electrons.

We just saw that the DMI originates from the SOC, however other material parameters could be interesting for their potential relationship with the electrostatic potential barrier at the interfaces of the ferromagnet. Specifically, the electro-negativity and the work function has been studied to understand their correlation with the DMI, [28]. A better relationship has been found

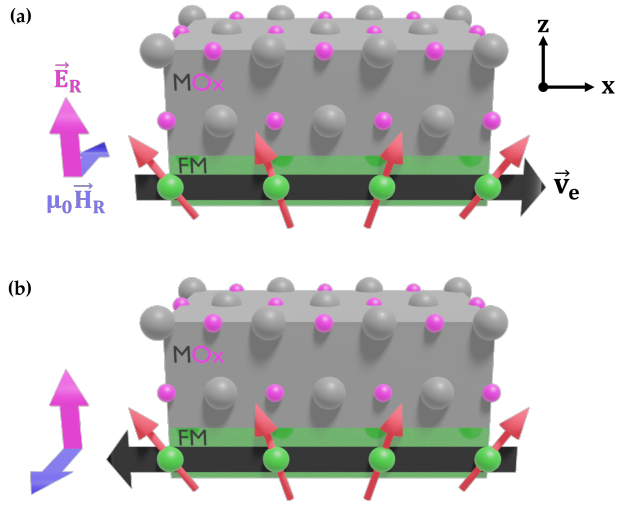

Figure 1.12: *(Figure taken from the PhD manuscript of Ch-E. Fillion [27]).* Scheme of a HM/FM interface. The electric field $\overrightarrow{E}_R$ (pink arrow) created by charge transfer leads to the Rashba magnetic filed $\mu_0\overrightarrow{H}_R$ (blue arrow) that depends on electron motion direction (black arrow). Electron's spins moving in the (a) $+\overrightarrow{x}$ and (b) $-\overrightarrow{x}$ direction experience opposite magnetic field around which their spin precess.

between the work function and the DMI. In [28], [29] a clear linear dependence of the effective DMI with the work function difference has been found in Pt/Co/Metal system.

1.2.2 The spin textures

The competition between all the energies described above stabilize different magnetic configurations. It is important to understand their origin and possible application. In the following we will go through a detailed explanation of the main magnetic configuration that can be stabilized in a tri-layer HM/FM/MOx system.

a. Domains and Domain Walls

A magnetic domain is a region, in a ferromagnetic material, where the magnetic moment are uniformly aligned. Firstly introduced by P. Weiss in 1907 to explain the spontaneous magnetization in ferromagnetic materials even without any external magnetic field. He developed later the *mean field theory*: in a ferromagnetic material, a magnetic moment experience a strong magnetic field coming from neighboring magnetic moment within a small region (domains). Later the origin of this mean field was explained by the exchange interaction, derived from quantum mechanics and detailed in the section 1.2.1.

Magnetic domains may form to minimize the total energy of the system. The exchange energy favors uniform magnetization, spins parallel, in a long range, promoting the apparition of large single domains. Meanwhile, the dipolar energy, because of the stray field, prefers neighboring spins having opposite direction and may lead to the formation of domains.

Magnetic domains are separated by magnetic domain walls (DWs). They are transition

regions where spins gradually rotate from one domain orientation to another over a finite width, called domain wall width δ_{DW}. This gradual rearrangement of spins costs in exchange and anisotropy energy since spins are not uniformly aligned and not along the easy axis. To minimize exchange energy, it requires a small angle between neighboring magnetic moments favoring a large domain wall width. Meanwhile to reduce anisotropy energy the magnetization tends to align along the easy-axis, which is the z direction in the case of a thin film laying in the (x,y) plane. This will thereby tend to stabilize thin domain wall. The domain wall width depends on the competition of these two energies and thus can be written as:

$$\delta_{DW} = \pi\sqrt{\frac{A_{ex}}{K_{eff}}} = \pi\Delta \tag{1.26}$$

A_{ex} is the exchange stiffness (J/m), K_{eff} the effective anisotropy constant (J/m^3). Δ is called the Bloch parameter.

Domain walls are usually categorized in two types: Bloch or Néel domain wall, schematized in the figure 1.13 for thin film with PMA, depending on the axis of rotation within the domain wall. For Bloch DWs the spins rotate around the normal to the domain wall. Meanwhile for Néel DWs the spins rotates around an axis tangent to the DW. A third type of domain wall can appear, the intermediate Domain Walls. This third category is characterized by the combination of both Bloch and Néel [30].

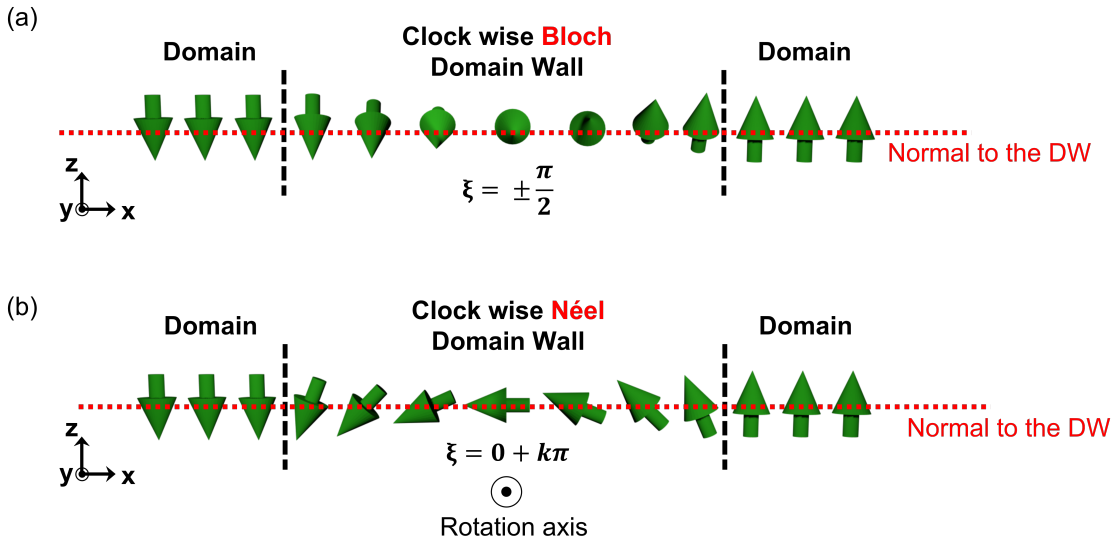

Figure 1.13: Scheme of a (a) clock wise Bloch domain wall and (b) clock wise Néel domain wall. The domain walls are delimited by the black vertical dotted line. The green arrows represent the spins and the red dotted line represents the normal to the domain wall.

Due to the induced canting of spin discussed in section 1.2.1, the DMI energy is a key parameter in the stabilization of a type of domain wall. In the case of no DMI, the dipolar energy favors Bloch type DWs to reduce surface and volume magnetic charges. Due to symmetry arguments DMI is known to favor Néel DWs in thin films with PMA [31],[5]. However if the DMI is not large enough the volume magnetic charges inside this type of DW will increase the dipoler

energy. Both energies compete, leading to intermediate DWs.

The creation of a domain wall results from the competition between various magnetic energy terms. This balance allows us to define the total surfacic energy in the case of a 1D domain wall:

$$E_{tot} = E_{ex} + E_{aniso} + E_{DMI} = A(\frac{\partial\theta}{\partial x})^2 + K_{eff}sin^2\theta + D\frac{\partial\theta}{\partial x} \tag{1.27}$$

With θ the angle between the magnetization and the easy axis, A the exchange stiffness, K_{eff} the effective anisotropy coefficient and D the DMI coefficient.
Minimizing this energy is equivalent to resolving the Euler-Lagrange equation :

$$\frac{\partial E_{tot}}{\partial\theta} - \frac{d}{dx}(\frac{\partial E_{tot}}{\partial\theta'}) = 0 \tag{1.28}$$

Where $\theta' = \frac{d\theta}{dx}$.

For a Bloch DW in bulk material neither the DMI or dipolar contribution has to be taken into account, therefore the equation 1.27 can be written :

$$E_{tot} = A(\frac{\partial\theta}{\partial x})^2 + K_u sin^2\theta \tag{1.29}$$

Here $K_u = \frac{K_s}{t_{FM}}$ the interfacial contribution to the magnetic anisotropy. Finally, we found the Bloch domain wall energy per unit area (the demonstration is detailed in the supplementary 9.3):

$$\sigma_{BlochDW} = 4\sqrt{AK_u} \tag{1.30}$$

By solving the equation 1.29 we can define a domain wall profile $\theta(x)$, which defines the spatial variation of the magnetization while crossing the DW along its normal.
The detailed demonstration is presented in the supplementary 9.3 2. We obtain for a Bloch domain wall:

$$\theta(x) = 2arctan(e^{\pm\frac{x-x_0}{\delta_{DW}}}) + k\pi, k\text{an integer} \tag{1.31}$$

Here x_0 represents the position at the center of the domain wall (where $\theta(x_0) = \pm\frac{\pi}{2}$) .

For Bloch domain walls in ultrathin film or Néel DWs, in addition to exchange and interfacial anisotropy energies, dipolar energy arises from magnetic charges. It is important to note here that we are neglecting these dipolar contribution for the moment to express the Néel DW energy, therefore we consider the domain wall profile of a Néel domain wall equivalent to the one of a Bloch domain wall. The DMI energy must also be considered. The equation 1.27 becomes :

$$E_{tot} = A(\frac{\partial\theta}{\partial x})^2 + K_{eff}sin^2(\theta) + D\frac{\partial\theta}{\partial x} \tag{1.32}$$

Here $K_{eff} = \frac{K_s}{t_{FM}} - K_d$ the effective anisotropy coefficient and D the DMI coefficient. The energy per unit surface of a Néel domain wall is (demonstration in supplementary 9.3) :

$$\varepsilon_{NeelDW} = 4\sqrt{AK_{eff}} \pm \pi D \tag{1.33}$$

As shown in the supplementary 9.3.3 the ± shows that the energy is decreased if the DMI coefficient D has the same sign as $\frac{\partial\theta}{\partial x}$. The derivative of the domain wall profile with respect to position x quantifies the local spin rotation across the wall. Therefore it shows that the DMI energy favors the stabilization of Néel domain wall with a specific sense of rotation, called chirality. This chirality depends on the sign of the DMI coefficient D. For a coefficient D negative $D < 0$ (resp. positive $D > 0$) the DMI favorises a clockwise (resp. counter clockwise) rotation.

The DMI energy stabilizes other magnetic chiral spin textures, including skyrmions, that are the central subject of many studies in the past decade.

b. Skyrmions

Skyrmions are chiral, swirling spin texture, that exhibit topologically non-trivial configurations. In 1962, Tony skyrme introduced a theoretical concept to describe baryons [32]. The first theoretical prediction of skyrmions in magnetic materials was then made in 1989 by Bogdanov et al[33]. However, it took two decades before their experimental observation: In 2009, S. Mühlbauer et al. reported the first experimental evidence of magnetic skyrmions in a bulk MnSi system [34]. This was followed in 2010 by X. Yu et al., who observed skyrmions in a FeCoSi thin film [35]. Skyrmions have many unique characteristics that make them promising candidates for next-generation spintronic devices. Their size can range from nanometers to micrometers, enabling high skyrmion densities [36]. Moreover, they can be stable at room temperature [37]. Skyrmions can be nucleated and annihilated using gate voltages [38] and they are efficiently manipulated by an electrical current [39]. These features allow for fast and low-energy control, with additional tunability provided by electrostatic gating. As a result, skyrmions are envisioned for many applications, including skyrmions racetrack memory [31], [40] or skyrmion based logic devices [40] but also neuromorphic computing [7].

Skyrmion are said to be "topologically protected". To understand this stability we can introduce the skyrmion number n [41],[42]:

$$n = \frac{1}{4\pi}\int \overrightarrow{m}\cdot(\frac{\partial\overrightarrow{m}}{\partial x}\times\frac{\partial\overrightarrow{m}}{\partial y})dxdy \tag{1.34}$$

To understand the meaning of this number one can pass through cylindrical coordinates (r, φ, z). The position vector in 2D space is given by $r = (rcos\varphi, rsin\varphi)$ with r the radial distance from the skyrmion center and φ azimuthal angle in the plane. The magnetization vector m is written $m = (cos\phi sin\theta, sin\phi sin\theta, cos\theta)$ with $\theta \in [0, \pi]$ the polar angle and $\phi \in [0, 2\pi]$ the azimuthal angle. All the spins are described in this cylindrical coordinates. Meanwhile its orientation is described in the spherical coordinates $(1, \theta, \phi)$. The geometry of the problem is defined and illustrated in the figure 1.14 (a) and (b).

In a skyrmion, the radial dependence of the magnetization is only in $\theta(r)$ (the vertical tilt), while the in-plane rotation ϕ depends only on the angle φ in real space. Then the skyrmion winding number reads :

$$n = \frac{1}{4\pi}\iint \frac{d\theta}{dr}\frac{d\phi}{d\varphi}sin\theta d\varphi dr \tag{1.35}$$

$$= \frac{1}{4\pi}\int_{r=0}^{r=\infty} sin\theta(r)\frac{d\theta}{dr}dr\int_{\varphi=0}^{\varphi=2\pi}\frac{d\phi}{d\varphi}d\varphi \tag{1.36}$$

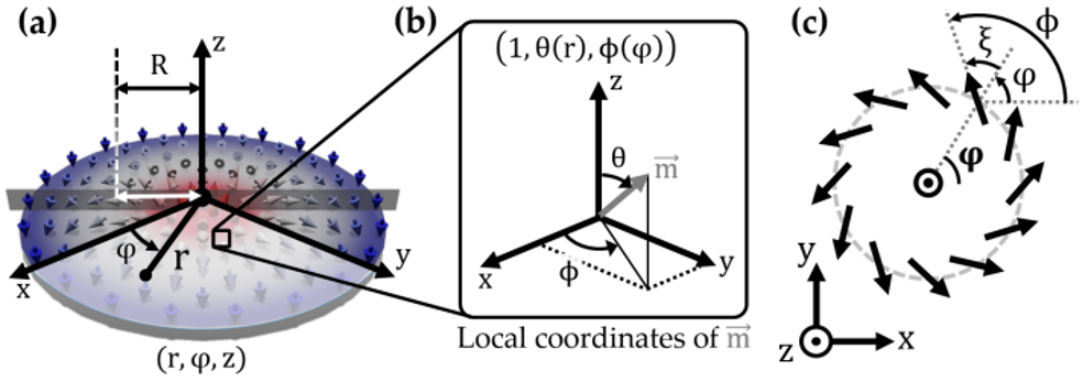

Figure 1.14: *(Figure taken from the PhD manuscript of Ch-E. Fillion).* Coordinate system used to define (a) the skyrmion and (b) the local magnetization vector. A given spin is locate in the skyrmion in (a) using the polar coordinate (r, φ, z) (here $z = 0$) while in (b) the orientation of each spin is defined locally using the spherical coordinates $(1, \theta(r), \phi(\varphi))$. (c) Scheme of the top view of a Dzyaloshinskii skyrmion where in addition to the previous angles discussed, we defined the helicity ξ.

$$= \frac{1}{4\pi}[cos(\theta(r)]_{r=\infty}^{r=0} \int_{\varphi=0}^{\varphi=2\pi} \frac{d\phi}{d\varphi} d\varphi \tag{1.37}$$

Initially, at the center of the skyrmion ($r = 0$) the magnetization is parallel or antiparallel to z, then $\theta(r = 0) = 0°or180°$ therefore $cos[\theta(r = 0)] = \pm 1 = p$. p being the polarity . On the other end in the ∞ limit the spin rotates to be opposite to the one in the center of the skyrmion meaning $\theta(r \to \infty) = 180°or0°$ leading to $cos[\theta(r \to \infty)] = \mp 1 = -p$. Here p is the skyrmion polarity, linked to the orientation of the spin in the center of the skyrmion. $p = +1$ when m parallel to z and $p = -1$ when $\overrightarrow{m}$ anti-parallel to +z. Therefore,

$$n = \frac{1}{4\pi}[p + p][\phi(\varphi)]_0^{2\pi} = p.W \tag{1.38}$$

p the polarity and W depends on the behavior of the magnetization along the perimeter of the skyrmion. One can define the azimuthal angle evolution as $\phi(\varphi) = \kappa\varphi + \xi$, κ being the vorticity (how many full rotations the in-plane magnetization makes as you go around the skyrmion) and ξ the helicity, as defined in the figure 1.14(c). Finally, we can write the winding number:

$$n = \frac{p}{2\pi}[2\pi\kappa + \xi - \xi] = p.\kappa \tag{1.39}$$

The winding number counts how many times the magnetization vector field $\overrightarrow{m}(r)$ wraps the unit sphere as you scan over the 2D plane of the magnetic material. It is a topological invariant, it means that two configurations with different winding number cannot be continuously deformed into one another without a discontinuity or singularity. Therefore, a skyrmion, having a winding number of ± 1, can't relax in a continuous magnetization, having a winding number of 0 (it cannot be wrapped around the unit sphere). The skyrmion is said topologically protected.

As for domains and domain walls, skyrmions results from the competition of the different energies. They are mainly stabilizes by the DMI which favors twisted configurations and determines the chirality and type of skyrmions. The exchange energy favors parallel alignment of neighboring spins which ensures a finite size for the skyrmion, resisting the sharp changes in spin direction that could be favored by DMI energy. The uniaxial anisotropy tends to favor spins aligned with the easy axis (perpendicular in the case of a thin film), and penalizes the radial rotation of magnetization in the skyrmion. The Zeeman energy from external fields can either stabilize or shrink the skyrmion depending on the direction of the field: a field aligned with the core lowers the energy and can help stabilize the skyrmion. In the case of Néel skyrmions the dipolar energy increases due to the volume magnetic charges. The skyrmion radius results from the competition between all these energies.
In [43] they developed an analytical topological soliton model in order to obtain a better physical insight of the differences between skyrmions and skyrmionic bubbles. Meanwhile skyrmions and skyrmionic bubbles are mainly distinguished by their size difference and the main stabilizing energy, they are topologically the same, therefore they are both referred in this paper as topological solitons. The energy of these solitons reads:

$$E_s[\theta(r)] = 2\pi t \int_0^\infty \left\{ A_{ex}[(\frac{d\theta}{dr})^2 + \frac{sin^2\theta}{r^2}] - K_u cos^2\theta - D[\frac{d\theta}{dr} + \frac{cos\theta sin\theta}{r}] - \mu_0 M_s H cos\theta + E_{demag} \right\} r dr \tag{1.40}$$

To avoid the difficulties to minimize E_s coming from the long range nature of the demagnetizing effects they restrict the problem to an ultra thin film to have a local approximation of the demagnetizing energy. In that case the volume contribution E_{demag}^{Vol} is negligible as compared as the surface one E_{demag}^{Surf}. In addition a short range uniform magnetization assumption is made. In that case the demagnetizing field can be written $H_{dz} = -M_z$. M_z being the magnetization pointing along the out-of -plane axis of the thin film, $\overrightarrow{z}$. We obtain $E_{demag}^{surf} = +\mu_0 \frac{M_s^2}{2} cos^2\theta$. This demagnetizing contribution to the total energy has the same dependency in θ than the anisotropy contribution thereby both of them will be combined into an effective anisotropy contribution.

Following the Euler equation in cylindrical coordinate:

$$A_{ex}[\frac{d^2\theta}{dr^2} + \frac{1}{r}\frac{d\theta}{dr} - \frac{sin(2\theta)}{2r^2}] + D\frac{sin^2\theta}{r} - K_{eff}\frac{sin2\theta}{2} - \mu_0 M_S H sin\theta = 0 \tag{1.41}$$

Where $K_{eff} = K_u - \mu_0 \frac{M_s^2}{2} = K_u - K_d$ the effective anisotropy constant. By solving this equation they access the evolution of each energy term with respect to the topological soliton radius, as represented in the figure 1.15(a).

They introduce an analytical model for each energy contribution and for the total energy of a topological soliton:

$$E_s = E_{exch} + E_{aniso} + E_{DMI} + E_{Zee} + E_{demag} \tag{1.42}$$

$$E_s = \frac{E_0}{\frac{2r}{\pi\Delta} + 1} + 4\sqrt{A_{ex}K_{eff}} \cdot 2\pi r t - \pi |D| \cdot 2\pi r t + 2\mu_0 M_S H \cdot \pi r^2 t - \mu_0 M_S^2 I(d) 2\pi r t^2 \tag{1.43}$$

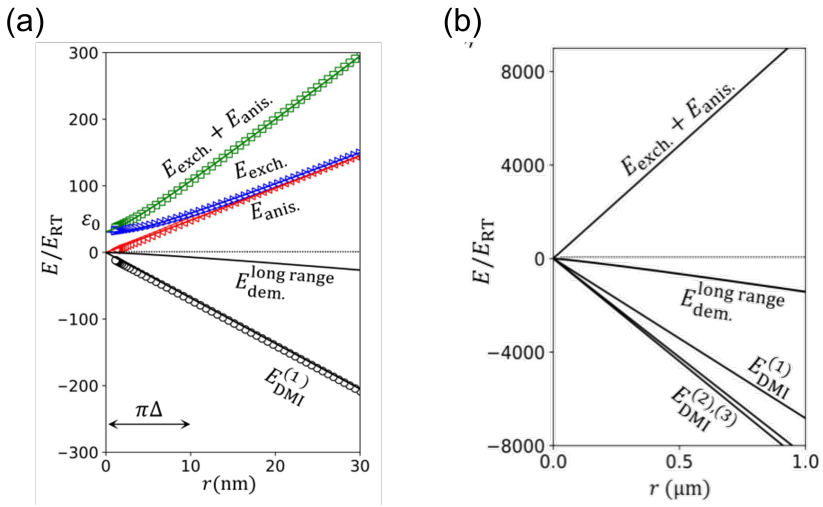

Figure 1.15: (*Extracted from [43]:*) (a) Exchange, Anisotropy, Demagnetizing and DMI energies normalised by the room temperature (RT) thermal energy with respect to the topological solitons radius coming from the topological soliton analytical model. (b) De-Zoom of the figure (a) for a radius between 0 and 1 μm. The DMI energy is plotted for $D^{(1)} = 2.8mJ/m^2$, $D^{(2)} = 3.46mJ/m^2$ and $D^{(3)} = 3.6mJ/m^2$.

$$E_s = \sigma_S \cdot 2\pi rt + 2\mu_0 M_S H \cdot \pi r^2 t - \mu_0 M_S^2 I(d) 2\pi r t^2 \tag{1.44}$$

Where σ_S is the topological soliton surfacic wall energy.

They defined the topological soliton solutions as the minima of E_s, thus use the derivative of the energy with respect of the radius $\frac{dE_S}{dr} = 0$ and $\frac{d^2E_s}{dr^2} > 0$. The figure 1.15 presents all the energies with respect to the radius derivated from their analytical model. Three different values of DMI are considerated as it is represented in the figure1.15(b) which is a de-zoom of the figure 1.15(a). As the energies nearly compensate each other, as we can see in the figure 1.16(a), a small variation on the DMI value modify the slope of E_S as it can be seen in the figure 1.16. Three types of topological soliton solutions are observed for the three different values of DMI. For smaller value of D ($E_s^{(1)}$) the solution is what is referred to as skyrmions: small radius ($\sim 1 - 10nm$), that increases with D, exists without applied field (figure 1.16(b) left). For a larger DMI ($E_s^{(2)}$), in presence of magnetic field (figure 1.16(b) middle) two minima are found leading to the coexistence of skyrmions and skyrmionic bubbles. Finally over a critical DMI value ($E_s^{(3)}$), the total energy presents a negative slope over all values of radius in absence of external field, figure 1.16(a). In presence of magnetic field, figure 1.16(b) right, a minimum in the energy is restored due to the Zeeman interaction , which dominates the evolution of the total energy at large values of r. This minimum enables the formation of skyrmionic bubbles. The evolution of the types of topological soliton solutions with the value of the DMI shows that skyrmions are stabilized by the iDMI, whereas skyrmionic bubbles are mostly stabilized by the dipolar and Zeeman interactions.

In conclusion, the stabilization of skyrmions, skyrmionic bubbles or both at the same time depends on the DMI value and on the presence of an external field or not. Based on this they

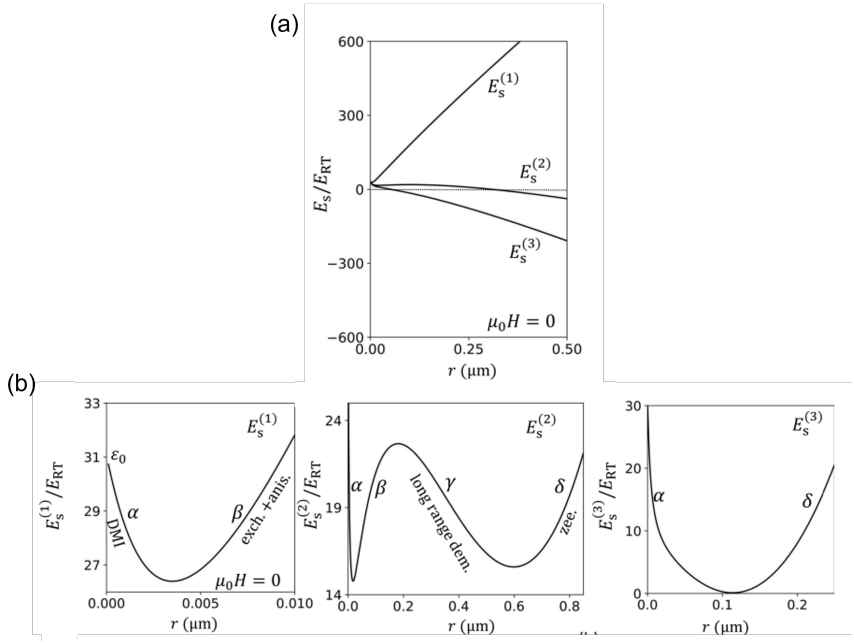

Figure 1.16: (*Extracted from [43]:*) (a) Topological soliton energy E_s normalized by the RT thermal energy plotted for the three different DMI values detailed in 1.15 (b) De-zoom on the soliton energy for each value of D $D^{(1)} = 2.8mJ/m^2$, $D^{(2)} = 3.46mJ/m^2$ and $D^{(3)} = 3.6mJ/m^2$ (left to right) corresponding to an external magnetic field of respectively $\mu_0 H = 0$, $\mu_0 H = 0.28mT$ and $\mu_0 H = 2mT$.

present a topological solitons phase diagram show in figure1.17. Skyrmions appears in zone 1, this topological solitons solution persist down to $H = 0$ and disappear along the blue line, called the skyrmion bursting line. This line ends at the critical point (D_{cs}, H_{cs}) for which no local maxima is found for E_s. Skyrmions can also be stabilized in zone 2, above the critical point, thanks to the Zeeman energy that restores a local minima.
Magnetic bubbles solution appears in zone 4 (see figure 1.17 (b)), superposed with the zone 1, delimited by the $H = 0$ line, the skyrmion bursting line and the bubbles collapsing red line. Skyrmions and skyrmionic bubbles coexist in this region. The skyrmion bursting line and the bubbles collapsing one meet at the critical point (D_{cs}, H_{cs}). When decreasing D the collapse field decrease until the zone 4 vanishes, the wall energy becomes too large to be compensated by the demagnetizing energy.
Finally, in zone 0 and 3 no topological solitons solution is found.

Finally, skyrmionic bubbles and skyrmions can be distinguished based on two main criteria. First, while skyrmions are mainly stabilized by the iDMI, skyrmionic bubbles are mostly stabilized by dipolar interactions.
Second, skyrmions typically exhibit a compact, nanometer-scale core, whereas skyrmionic bubbles consist of a larger circular domain surrounded by a homochiral domain wall.

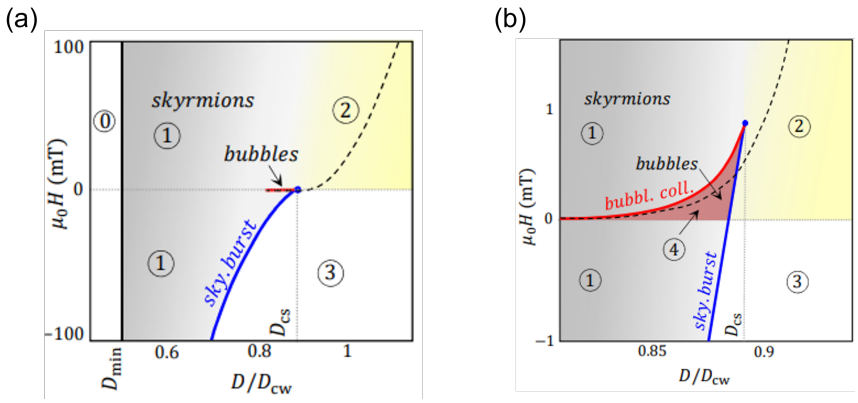

Figure 1.17: (*Extracted from [43]:*) Topological soliton phase diagram. The blue line represents the skyrmion bursting line and the red line corresponds to the bubbles collapsing line. The dashed line is the line at which E_s becomes negative Above this line the low energy cost of topological solitons and DWs favours the formation of a topological soliton lattice or a stripe/helical phase [44]. 5 regions are represented: 0 and 3 - no topological soliton solution. 1 - stabilization skyrmion region, 2- Skyrmionic bubbles stabilized thanks to the Zeeman energy and 4 - Skyrmionic bubble stabilization region.

1.3 Conclusion

In this chapter, I introduced the fundamental concepts of magnetism, with a particular focus on ferromagnetic thin films in tri-layer systems. I detailed the different energy contributions, namely, the Zeeman, dipolar, exchange, anisotropy, and Dzyaloshinskii-Moriya (DMI) energies. I then examined how the competition between these energies leads to the formation and stabilization of different spin textures, such as magnetic domains and skyrmions.

Skyrmions have attracted interest in recent years due to their promising potential in various spintronic applications. Understanding their creation, stability, and dynamics, as well as developing methods to control them, is therefore essential. This is the background to the research I carried out during this thesis.

Chapter 2

Control of the magnetic properties in a tri-layer system

2.1 Material dependence 54
2.1.1 Influcence of the oxidation state 54
2.1.2 Influence of the ferromagnetic thickness 57
2.2 Gate voltage control of magnetic energies 60
2.2.1 Voltage control of magnetic anisotropy (VCMA) 60
2.2.2 Voltage control of Dzyaloshinskii-Moriya interaction (VCDMI) 63
2.3 Dynamic of spin textures 67
2.3.1 Motion under an external magnetic field 69
2.3.2 Motion under an electrical current 73
2.3.3 Motion of magnetic skyrmions - Thiele equation 77
2.4 Conclusion 81

The control of magnetic spin textures, and specifically skyrmions, is essential for their potential use in memory and device applications. In this section, we review the literature on the different approaches that have been developed to control skyrmions and their properties. We first summarize how material parameters influence the key energy terms and magnetization properties, and then discuss dynamic control techniques, with a particular focus on skyrmion dynamics in tri-layer systems.

2.1 Material dependence

In a tri-layer system such as Heavy Metal/Ferromagnet/Metal Oxide (HM/FM/MOx), both thicknesses of the ferromagnetic layer and top heavy metal layer are known to modify energies, as seen in the previous chapter. Thereby, they are playing a key role in the stabilization of spin textures and particularly of skyrmions. A fine tuning of the material properties is needed in order to stabilize skyrmions.

2.1.1 Influcence of the oxidation state

It is well known that the oxidation of the ferromagnetic layer and specifically at the interface with the metal layer (FM/M) influences magnetic properties and spin properties [45]. It has been clearly shown that the perpendicular magnetic anisotropy (PMA) is linked to the spin-orbit coupling. Indeed in [46] they show an enhancement of the anisotropy in a Pd/Co multilayer system due to the hybridization between the Pd d and Co d states. Later it has been shown that a control of the oxidation at the top interface in Pt/CoFe/AlOx used in magnetic tunnel junction can be achieved by tuning the thickness of the Al layer leading to a rotation from in plane anisotropy to PMA and inversely [47]. The bonding at the FM/oxide interface enhances orbital hybridization and thereby increases interface anisotropy [45],[47]. However, over-oxidation can consume the ferromagnet or change the FM/MOx interface, reducing PMA. In 2007, Manchon et al [48] perfomed X-ray analysis in Pt/Co/AlOx trilayers showing that high temperature annealing enhances PMA.

Other studies show a dependence of the DMI strength with respect to the oxidation state at the interface. In [49] they used a method based on the measurement of the saturation velocity v_{sat} of field driven chiral Néel domain walls to study the DMI in Pt/Co/MOx trilayer:

$$v_{sat} = \frac{\pi}{2}\gamma\frac{D}{M_s} \tag{2.1}$$

Where D is the DMI strength, M_s is the spontaneous magnetization and γ is the gyromagnetic ratio.

As this saturation velocity is independent of the DMI sign they also use a technique based on the measurement of the propagation of Néel domain walls by an out-of-plane magnetic field with a constant in plane magnetic field applied H_x. The speed of the DW reaches a minimum when H_x compensates the H_{DMI} field, an effective field related to the DMI. Then, they deduce the average DMI energy using:

$$H_{DMI} = \frac{D}{\mu_0 M_S \Delta} \tag{2.2}$$

Where $\Delta = \sqrt{A/K_{eff}}$, A being the exchange stiffness and K_{eff} the effective anisotropy constant.

The figure 2.1(a) represents the velocity of the domain walls motion with respect to the magnetic field applied in plane B_x. The minimum of velocity is reached when the B_x compensate an effective H_{DMI} field coming from the DMI interaction that pins the DWs in a Néel configuration. In the figure 2.1(b) the oxidation at the top interface is schematized and the DMI coefficient value is shown for different positions along the wedge of the top Metal layer and for two different metals: AlOx (left) and GdOx (right). They highlight the variation of the effective DMI strength with the oxidation of the Co/MOx interface: an optimal oxidation leads to the maximum strength of DMI.

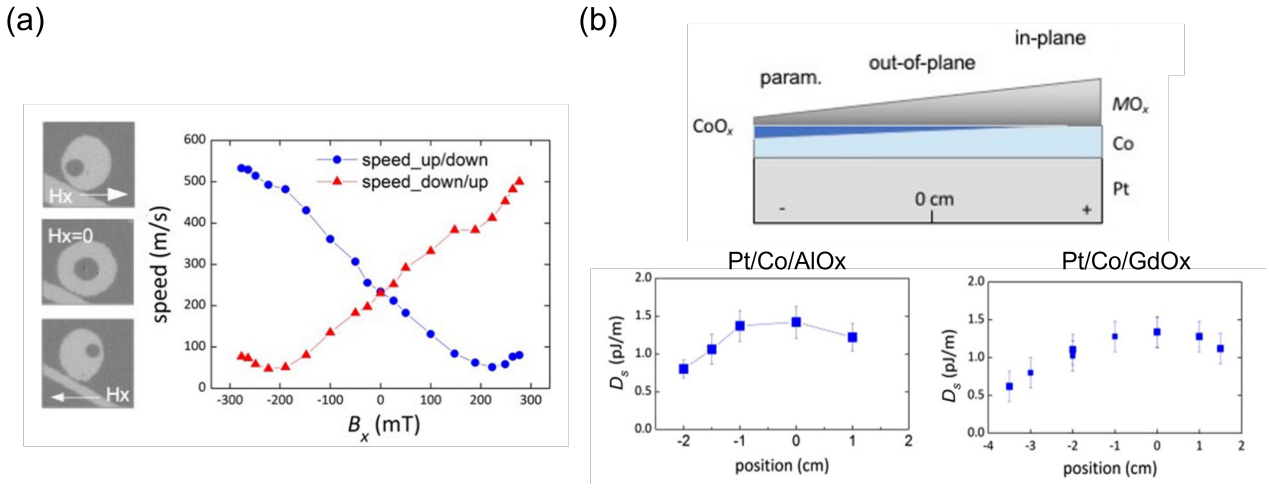

Figure 2.1: *(extracted from [49])* (a) Velocity of the domain wall motion (in m/s) under an external perpendicular magnetic field with respect to the constant in plane field B_x applied in (mT). (b) The top is the scheme of a cut along the top HM wedge of the Pt/Co/MOx tri-layer system. The anisotropy is switching from In-plane for the thicker region of the top metal layer to out-of plane then paramagnetic when decreasing the thickness, when the oxidation reach the ferromagnet. In the bottom the DMI coefficient D_S is measured for different position along the wedge for two different tri-layers Pt/Co/AlOx and Pt/Co/GdOx.

In another study [50] in addition to showing a dependence of the DMI amplitude with the oxidation state, they also reveal a change in sign of the DMI coefficient for different oxidation states of a CoFe/TaOx interface and thus on the chirality of the interaction. This result is presented in the figure 2.2 where a change of the DMI coefficient sign is shown both when (1) the ferromagnet is oxidized and the oxidation start to appear in the top Ta layer: (CoFe/-CoFeOx/Ta) ⇒ (CoFe/CoFeOx/TaOx/Ta) and (2) the oxidation moves away from the interface : (CoFe/CoFeOx/TaOx/Ta) ⇒ ((CoFe/Ta/TaOx/Ta)

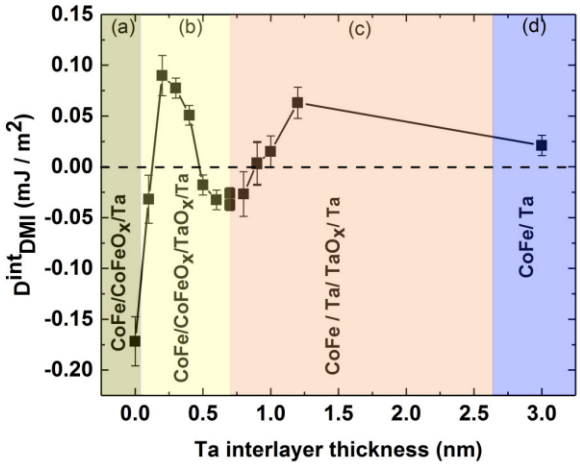

Figure 2.2: *(Extracted from [50])* DMI coefficient in mJ/m^2 with respect to the thickness of the Ta interlayer thickness. A change in sign of the DMI coefficient is noticeable for the different oxidation state at the interface CoFe/TaOx.

A more recent study conducted in the team by R.Kumar et al,.[51] demonstrated a sign inversion of the DMI as a function of the oxidation state at the top interface in the Ta/FeCoB/TaOx tri-layer, which are the basis of the samples used in this thesis. In this study the two top layers of this tri-layer structure are deposited as a wedge, one perpendicular to the other, allowing the access to different thickness combinations (t_{FeCoB};t_{Ta}). This geometry allows to investigate the evolution of the magnetic parameters independently with both the oxidation at the top interface FeCoB/TaOX and ferromagnetic layer thickness.

Using Brillouin light scattering (BLS) measurements on three different samples with different oxidation state of the top FeCoB/TaOx interface, the authors determined the sign of the DMI coefficient. The results, presented in the figure 2.3, show a change in the chirality of the DMI: for an under-oxidized state (Ta/FeCoB/Ta/TaOx) the DMI is negative whereas for an overoxidized state (Ta/FeCoB/FeCoBOx/TaOx), a positive DMI is observed. It is important to note that the convention generally used for the sign of the DMI using BLS measurements are the opposite of the one we used and explained in the section 1.2.1. This observation directly demonstrates that the effective DMI sign can be controlled by tuning the oxidation state at the top interface. Additionally, in this study, the authors subtracted the DMI contribution coming from the bottom interface (green line in the figure 2.3) from the total effective DMI, showing a sign inversion of FeCoB/TaOx interface contribution with the oxidation state. This highlights the important role of the top interface oxidation state in the DMI sign change mechanism.

To experimentally stabilize skyrmions, the ferromagnet and the top heavy metal layer are deposited in a wedge, one perpendicular to the other allowing a continuous variations and combinations of thicknesses (t_{FM} ; t_{HM}). As just discussed, the oxidation state strongly influences both the anisotropy and the DMI. However, the ferromagnetic thickness, as well, will influence these parameters.

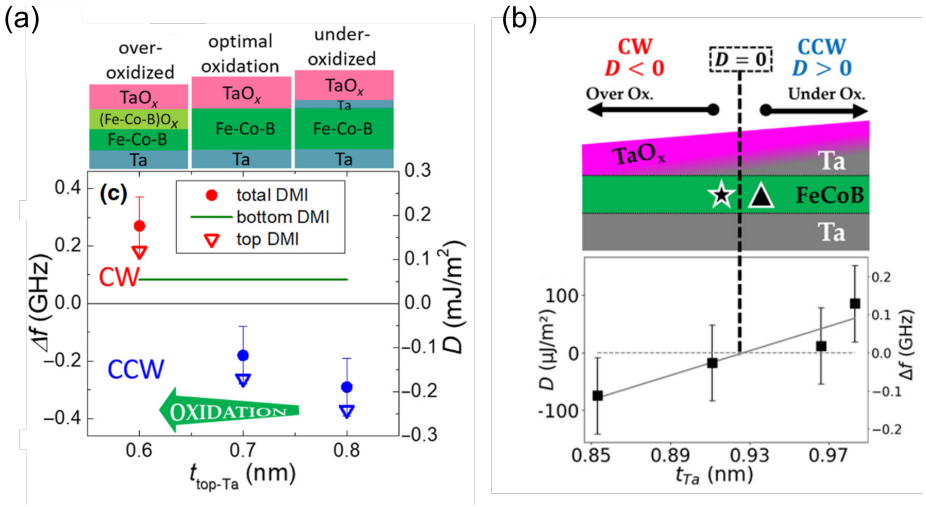

Figure 2.3: *(Extracted from [51])*: (a)**Left axis** Frequency shift Δf extracted from BLS measurements. **Right axis** the corresponding DMI value. The green line represented the contribution of the bottom interface to the total DMI, taken from the literature. A schematic cross section of the tri-layer is represented on top for the different oxidation state at the interface FeCoB/TaOx. These measures has been done in three different samples, each deposited on-axis. (b) However, a bit later, similar measurements, using BLS, on a similar tri-layer system but using a top Ta gradient in order to change to oxidation state at the top interface has been performed also in the team [52] that shows similar results for the sign inversion fo the DMI coefficient with respect to the oxidation state. It is important to note that in between the two studies the convention concerning the sign of the DMI coefficient and the chirality is note the same. The explanation of both convention are detailed in section 1.2.1

2.1.2 Influence of the ferromagnetic thickness

As seen in the section 1.2.1 variations in ferromagnetic layer thickness affect several energies and interactions. The main consequences are seen on the magnetic anisotropy and the DMI, two key interactions involved in the stabilization of spin textures. One of the first experimental observation of what is now known as perpendicular magnetic anisotropy (PMA) was reported by Gradmann and Müller in 1968 [9], in ultrathin NiFe (111) films. Although the term "PMA" was not used at the time, they clearly demonstrated a transition to out-of-plane magnetization in films just a few atomic layers thick. This behavior was interpreted as a Néel-type surface anisotropy which, at the time, had been theorized [53] but not experimentally demonstrated. This surface-induced anisotropy and its dependence on thickness were further studied in later works. For instance, in 1986 Draaisma et al [54] investigated Pd/Co multilayers and showed that, as the Co layer thickness decreases below 7 Å, the interfacial anisotropy overcomes the shape and magnetocrystalline anisotropies, leading to a switch from in-plane to perpendicular magnetization. This transition provides direct evidence for the dominance of interfacial contributions at low thickness. Three years later, in 1989, Zeper et al [55] shows also this transition in anisotropy in Pt/Co thickness. Particularly they experimentally measured PMA for Co thickness below 12 Å. The decrease in anisotropy induced by the Curie temperature has also been reported for Co layer thinner than 7 Å, when it becomes paramagnetic at measuring temperature. The

evolution of the anisotropy they measured with respect to the Co thickness is represented in the figure 2.4.

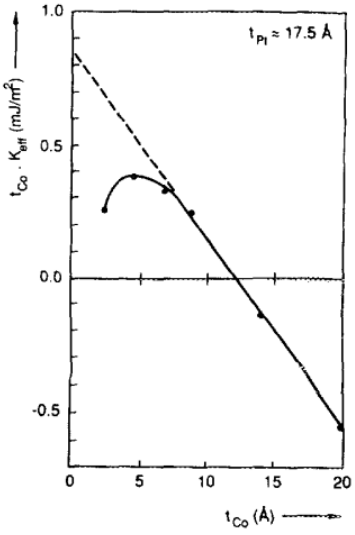

Figure 2.4: *(Extracted from [55])* Evolution of the effective anisotropy coefficient K_{eff} multiplied by the thickness of the ferromagnet t_{Co} (in mJ/m^2) with respect to the thickness of the ferromagnetic layer t_{Co} (in Å).

More recent works have investigated the evolution of the DMI amplitude with respect to the thickness of the ferromagnet. In 2015, Cho et al[56] used Brillouin light scattering (BLS) to measure the DMI in Pt/Co/AlOx and Pt/CoFeB/AlOx samples. Their results, shown in 2.5(a), quantitatively establish that the DMI energy density scales inversely with the ferromagnetic thickness, confirming its interfacial origin. This monotonous behavior was later confirmed by Lo Conte et al. [57], who used the current induced DW motion (CIDWM) technique, this technique is described in more details in the section 2.3.2. While these studies reproduced the $1/t_{FM}$ dependence, they also report quantitative differences in the measured DMI strength compared to BLS. In addition, Mokhtari et al. [58] supported their experimental findings with simulations, showing consistent DMI behavior with respect to FM thickness, as shown in the figure 2.5(b). They also demonstrated a reduction in DMI in ultrathin regions, attributed, like PMA, to thermal effects near the Curie temperature, which, as seen in the section 1.2.1, can significantly affect the magnetic properties at low thickness, leading to a paramagnetic region.

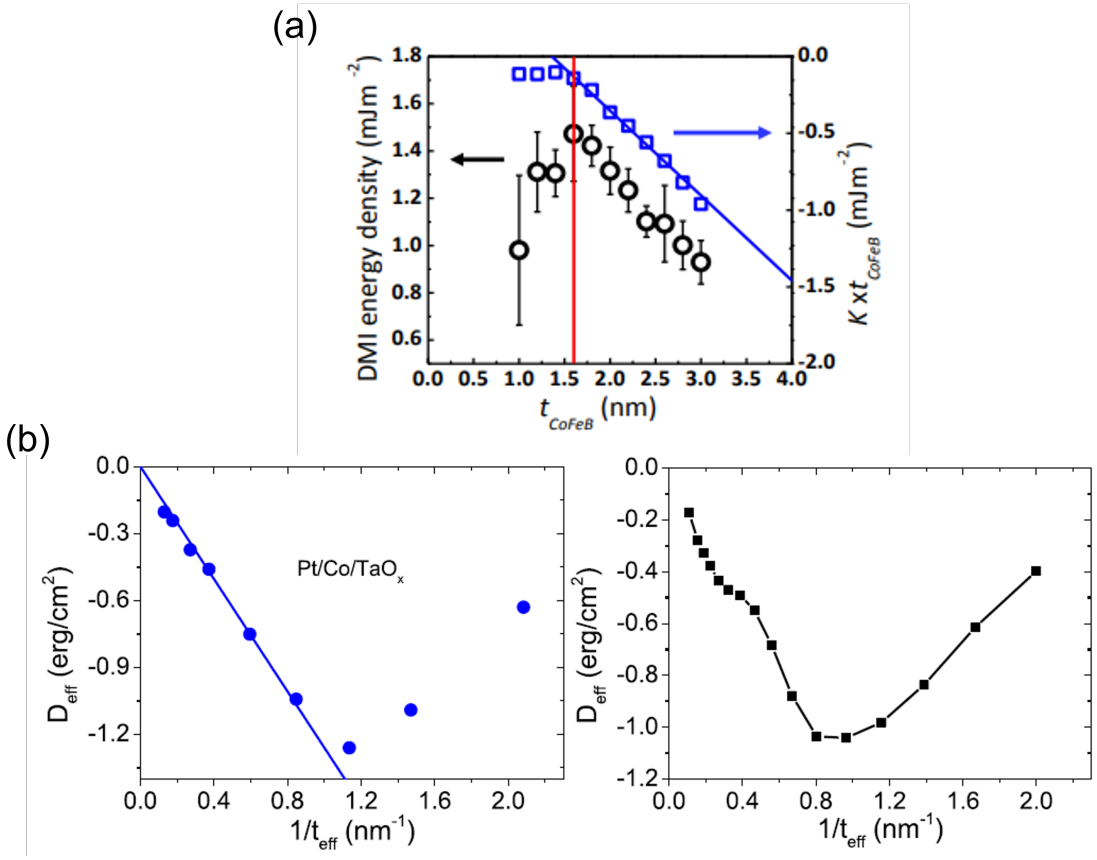

Figure 2.5: (a) *(Extracted from[56])* Evolution of the DMI energy density (black circles) and the effective anisotropy coefficient multiply by the thickness of the ferromagnet (blue squares and curve) both in mJ/m^2 with respect to the thickness of the ferromagnet in the tri-layer system Pt/CoFeB/AlOx (b) *(Extracted from [58])* Evolution of the DMI coefficient D_{eff} in erg/cm^2 with respect to the inverse to the thickness of the ferromagnet. The blue curve on the left correspond to experimental measurements in a Pt/Co/TaOx tri-layer system meanwhile the black curve on the right correspond to simulated values.

In the team, R.Kumar et al. also demonstrated the dependence of the DMI sign with respect to both the oxidation and the ferromagnetic layer thickness in the skyrmion region [51]. The figure 2.6(a) shows the anisotropy map of the sample, for which the measurement method and interpretation are detailed in Chapter 3 section 3.2.2. Two transitions in DMI sign are observed: one with respect to the oxidation state, discussed in the previous section 2.1.1, appears in the region between points 6 and 7, which corresponds to the transition from perpendicular magnetic anisotropy (PMA) to in-plane anisotropy (IPA), and one appear for the FeCoB thickness variation, in the region between point 2 and 4 in the figure 2.6(a), at the PMA to PM region.

To probe the DMI in the PMA-IPA transition region, the authors employed the current-induced motion (CIM) technique, described in Section 2.3.2. This method uses the fact that the direction of skyrmion motion under current, linked with spin-orbit torques (discussed in the section 2.3.2, depends on their chirality and on the sign of the spin hall effect in the HM: for Ta underlayer clockwise (CW) skyrmions move along the current direction, while counterclockwise

(CCW) ones move against it [59]. By looking at the motion of skyrmions in regions with nearly constant oxidation, the authors observed a reversal in chirality, and thus in the sign of the DMI, between positions 1 and 5, as shown in Figure 2.6(b) where the sense of motion is inverted. This confirms that, beyond oxidation, the ferromagnetic layer thickness also plays a crucial role in determining the DMI sign.

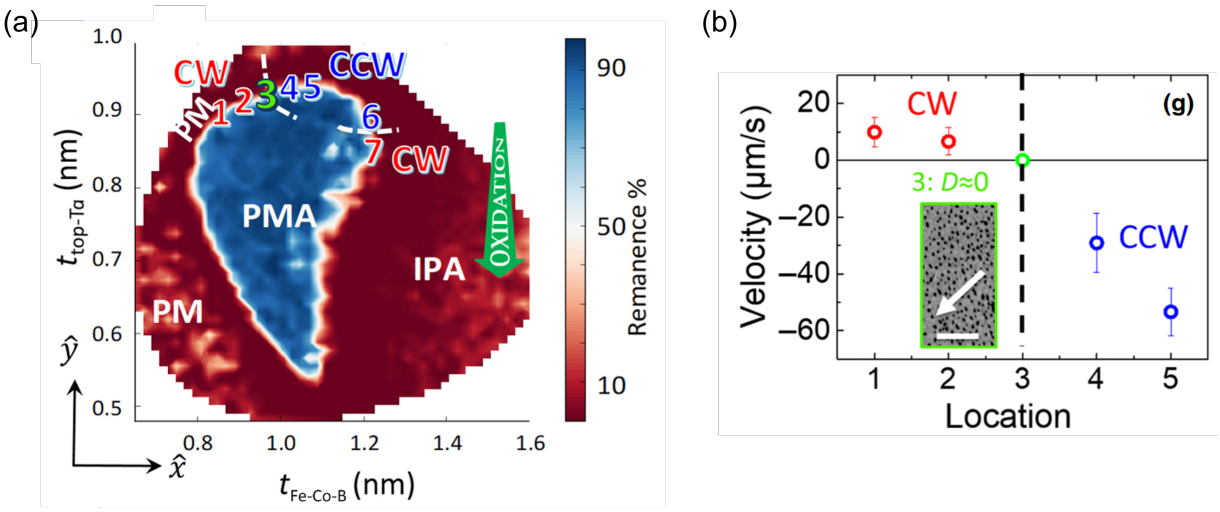

Figure 2.6: *(Extracted from [51])* (a) Remanence map of the sample. The blue region corresponds to the perpendicular magnetic anisotropy (PMA). The red region corresponds to in-plane anisotropy (IPA) and paramagnetic state (PM). Numbers indicate the localisation where the skyrmion motion is studied. The red (resp.blue) numbers corresponds to a clockwise (resp. counter clockwise) chirality. (b) Velocity of the spin textures in each location represented by the numbers At position 3, nearly no motion is visible.

2.2 Gate voltage control of magnetic energies

Many studies focus on the manipulation of the oxidation state at the interface with the objective of tuning dynamically both the anisotropy and the DMI energies, impacting the spin textures. A well-known technique is the gate voltage, a dynamic, local and low power technique, that can influence both the anisotropy, in which case we refer to voltage control of magnetic anisotropy (VCMA), or the DMI, called voltage control of the DMI (VCDMI).

2.2.1 Voltage control of magnetic anisotropy (VCMA)

The VCMA refers to the ability to tune the magnetic anisotropy energy through the application of a gate voltage. First demonstrates in 2007 by Weisheit et al. [60] where they demonstrates a reversible modification of the anisotropy in FePt and FePd by applying an electric field.

Three mechanisms can be at the origin of this effect. First, the electrostatic effect, where the gate voltage induces charge accumulation or depletion at the FM/Ox interface. This alters

the local charge density and energy levels, modifying the orbital hybridization and thus the spin-orbit coupling, which contributes to anisotropy [61],[62],[63]. Second, the ionic mechanism, in which the applied voltage leads to ion migration at the FM/MOx interface. Different ions are actually used to modify the anisotropy. For example in [64] they experimentally demonstrated a control of the anisotropy by playing on the accumulation and removal of hydrogen ions H^+ at Co/GdOx interface using a gate voltage. In [65], Q. Zhang et al. demonstrates the magnetization control via the discharge/charge cycling of a lithium-ion battery (LIB). They have been able to reversibly manipulate magnetism by voltage-tunning of the lithium quantity of a nanoscale $\alpha - Fe_2O_3$-based electrode. It can also be oxygen ions migration that modifies the oxidation state, again affecting orbital hybridization and anisotropy [66], [67],[68]. And finally, strain effect, in which they use piezoelectric substrates. By applying a voltage into this substrate the crystal lattice will be deformed, mostly elongated (resp.contracted) along one direction and contracted (resp.elongated) in the two orthogonal directions. In [69] they show that this deformation of the substrate induces an inversion of magnetic anisotropy in a ferromagnetic thin film. They show, using ferromagnetic resonance measurements, that the in-plane anisotropy can be inverted if the polarity of the voltage applied is changed. Using SQUID magnetometry they also show the possibility to irreversibly or reversibly rotate M by only changing the voltage applied.

VCMA represents a promising approach for low-power magnetization switching in spintronic devices[60], [70], [71]. Specifically it is now of particular interest for MRAM [72] or also in magnetic tunnel junction (MTJ): first electric field induced switching of MTJ devices was reported by Wang et al.[73] and Shiota et al.[74]. More recently Urrestarazu et al. [75] use the VCMA effect to nucleate/annihilate at low power skyrmions in MTJs.

The strength of the VCMA effect is characterized by the coefficient β_{Ks} defined as the change in anisotropy energy per unit electric field ($fJ/(V \cdot m)$), with values range typically from $\sim 50fJ/(V \cdot m)$ to over $10^4 fJ/(V \cdot m)$. The figure 2.7, extracted from the review [16], presents a summary of the efficiencies of the VCMA effect obtained in both FM/MOx interfaces and magnetic tunnel junction (MTJ). They highlight the importance of the PMA in nowadays applications as magnetic random access memory (MRAM) or MTJs while also describing its microscopic origin. As shown in the figure 2.7 the strongest VCMA effects are associated with ionic migration and strain effect, highlighting the crucial role of interface oxidation and interatomic distance.

This oxygen ion migration has been experimentally observed by U.Bauer et al. [71]. They used transmission electron microscope (TEM) and electron energy loss spectroscopy (EELS) analysis to directly detect the oxygen front inside the Ta/Pt/Co/GdOx system. The TEM picture of the sample is displayed in the figure 2.8(a). In (b) we see the EELS analysis at the pristine state $V_g = 0V$ with the red points corresponding to the amount of Oxygen ions and the blue dot the Cobalt one. The measurements are done along the green line starting at the Pt/Co interface. It means that in the figure 2.8(b) the position 0 corresponds to the Pt/Co interface. The voltage is applied in-situ thanks to a tip, as we can see in the figure 2.8(a) in the top right corner. In (c) the authors show that the application of a negative gate is pushing the oxygen ions **towards** the position 0, so towards the Pt/Co interface meanwhile in (d) we see that the application of a positive gate is pushing the oxygen ions **away** from this interface.

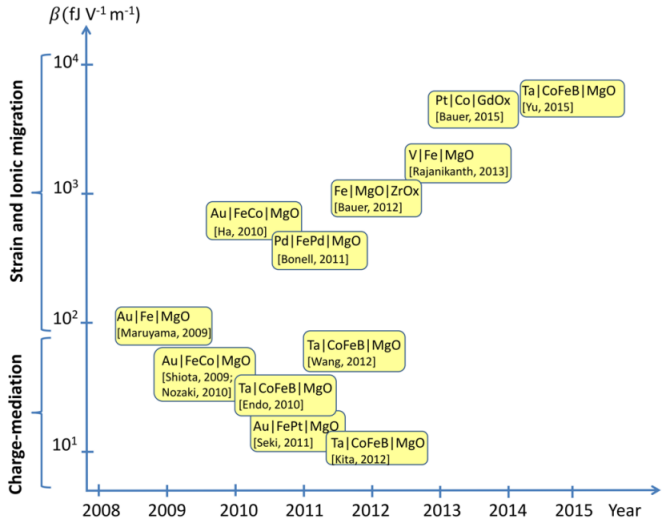

Figure 2.7: *(Extracted from [16])* Summary of the VCMA efficiencies both at FM/MOx interfaces and in magnetic tunnel junction (MTJ). Two mechanisms can be differentiated: the strain and ionic migration, that give higher efficiencies than the charge-mediated effect.

The measurement of VCMA can be achieved using different techniques. One of the most widely used is the ferromagnetic resonance (FMR), which probes the magnetization dynamics in a ferromagnet. The magnetization is in resonance thanks to the application of a RF magnetic field to compensate for the losses. Finally, the analysis of the resonance peak gives access to key paramaters such as the anisotropy [76],[69]. In [77], Yu et al. experimentally demonstrated strain induced modulation of PMA in (001)-PMN-PT/Ta/CoFeB/MgO/Ta structures using ferromagnetic resonance measurements. They measured a very large efficiency value of $\beta_{Ks} = 7000 fJ/(V \cdot m)$.

VCMA can also be characterized using magnetometry, such as Magneto-optical kerr effect (MOKE). When a material is magnetized, the polarization of the reflected light changes slightly. Since this rotation is sensitive to the magnetization direction, MOKE can be used to measure magnetic hysteresis loops and detect changes in anisotropy under applied gate voltages [78], the MOKE technique is detailed in the section 3.2.1. In 2020, A.Fassatoui et al. [68] studied the VCMA in Pt/Co/MOx tri-layer system. In addition to reporting a large VCMA efficiency $\beta > 1200 fJ/V \cdot m$ measured in Pt/Co/AlOx samples, they also demonstrates the reversibility of the VCMA effect in both Pt/Co/AlOx and Pt/Co/TbOx. they attributed this VCMA to ionic effect. In contrast the effect was found to be irreversible in Pt/Co/MgOx structures, linked in that cease to the Mg^{2+} cation motion. Other magnetometry methods can be used to explore VCMA effect as VSM-SQUID or with MR [70],[72].

Finally, a more recent method uses harmonic hall measurement to detect VCMA. [79]. By applying an AC voltage across an Hall bar simultaneously with a gate voltage both first and second harmonic Hall voltages can be detected. This approach enables the separation of fast electrostatic effects from slower ionic contributions to VCMA by using high modulation frequencies.

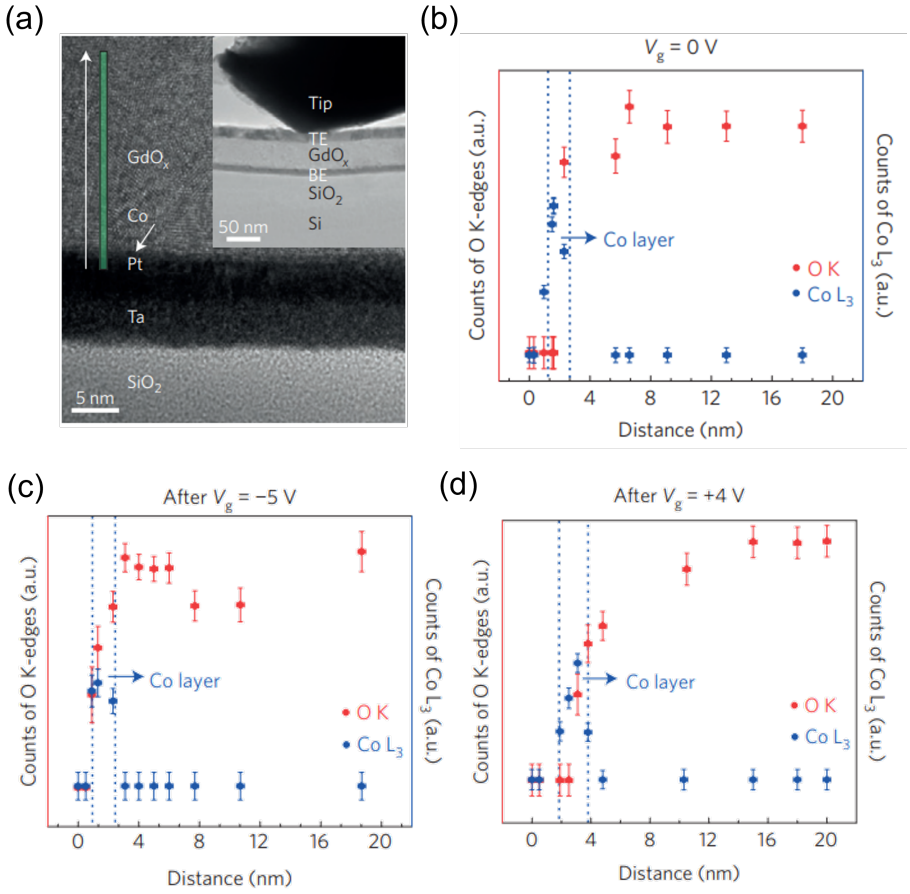

Figure 2.8: *(Extracted from [71])* (a) TEM cross section of the Ta/Pt/Co/GdOx sample. (b), (c) and (d) EELS analysis for the application of a gate of respectively 0V, - 5V and +4V. The x-axis represents the distance from the Pt/Co interface. The **left y-axis** correspond to the count of oxygen O K edges in red and **right y-axis** the count of cobalt Co L edges in blue.

2.2.2 Voltage control of Dzyaloshinskii-Moriya interaction (VCDMI)

VCDMI refers to the modulation of the DMI strength through the application of a gate voltage or an external electric field. Similarly to VCMA, different mechanisms can contribute to VCDMI.

First, as in the case of VCMA, the gate voltage applied to an oxide layer can induce charge accumulation or depletion at the interface. This leads to a modification of the electronic band structure, including shifts in the Fermi level and changes in the occupation of electronic states. This influences the interfacial spinorbit coupling, which is a key parameter in the apparition and magnitude of the DMI.

Second, the application of a gate voltage at a FM/MOx interface can induce oxygen ion migration, which leads to a change in the local oxidation state. This migration alters the orbital hybridization between the FM 3d and O 2p orbitals, thereby modifying the spin-orbit coupling and impacting the DMI strength [49]. In a study by L.Herrera Diez et al.[80] BLS measurements

were used to study the evolution of the DMI strength under ionic-liquid gating in a $Pt/Co/HfO_2$ ultrathin film. Following the application of a $-3V$ gate voltage, a decrease in the DMI strength was observed. Moreover, the DMI strength was found to stabilize after approximately two minutes of voltage application, and the change was irreversible.

As for VCMA, we can quantify the VCDMI in term of efficiency $\beta_{DMI} = \frac{\Delta D}{\Delta E}$ in $fJ/(V \cdot m)$, meaning how much the DMI strength changes for a specific electric field application. In one of the first demonstrations of VCDMI, Nawaoka et al. [81] observed a change in the DMI constant of $\Delta D = 40nJ/m^2$ under a 1 V gate voltage in an Au/Fe/MgO multilayer. Despite this, the estimated efficiency , $\beta_{DMI} = 3fJ/(V \cdot m)$, remained low, partly because the Fe layer was 20 nm thick, larger than the charge screening length, limiting the influence of the electric field to the interface FM/HM. At this time it was the one considered as responsible of the origin of the DMI through the Fert-Levy model, not expected to be very sensitive to gate voltage.

Later, Srivastava et al. demonstrated a much larger effect (130%) in ultrathin Ta (3)/FeCoB(0.9)/TaOx(1) tri-layer system, with the thicknesses expressed in nm. Using BLS and p-MOKE measurements they explored both long (few hours) and short (few minutes) time scale effect of the electric field on DMI strength. The figure 2.9 extracted from [82] presents DMI change for both cases. We can see that for short time scale the efficiency is order of magnitude smaller $\beta^S_{DMI} = 150fJ/Vm$ as for long time scale where $\beta^L_{DMI} = 600fJ/Vm$. For short time measurements they suggest that the negative (resp.positive) electric field created by the gate adds (resp. compensate) with the Rashba field at the HM/MOx interface reinforcing the idea that the large sensitivity of the DMI to the gate voltage can be explained by the Rashba field at the FeCoB/TaOx interface. Meanwhile, for long time measurement they attribute the DMI modulation to oxygen migration. The sample is initially slightly under-oxidized, a negative gate will push the oxygen ions towards the ferromagnet resulting in a more optimally oxidized state increasing the Rashba field. However, as for VCMA, this phenomenon is not symmetric, a positive gate de-oxidizes the interface by attracting the ions back into the top Ta layer changing the crystalline and orbital structure. The origin of the DMI is then expected to change to a Fert-Levy DMI. This mechanism is schematized in the figure 2.9(c).

Schott et al. investigated the voltage control of DMI by analyzing the variation of the equilibrium stripe domain width in a Pt/Co/AlOx trilayer system. Under an constant electric field the sample is saturated using an out-of-plane external magnetic field. The magnetic field is then turned off and the characteristic domain wall width L_{eq} is then estimated using a 2D Fourier transform of the image recorded few seconds after. From the characteristic domain wall width they deduced the domain wall energy σ_w following :

$$L_{eq} = C \cdot texp(\frac{\pi\sigma_w}{2K_d t}) \tag{2.3}$$

Where t is the Co thickness (0.49nm), K_d the dipolar constant and C is a model-dependent constant.
As seen in the section 1.2.2 the domain wall energy σ_w can be written as :

$$\sigma_w = 4\sqrt{A_{ex}K_{eff}} - \pi\,|D| \tag{2.4}$$

From these measurements, they extracted a remarkably high VCDMI efficiency, with a coefficient $\beta_{DMI} = 1100 \pm 700fJ/(V \cdot m)$ to $\beta_{DMI} = 2000 \pm 700fJ/(V \cdot m)$ [83]. To obtain a more

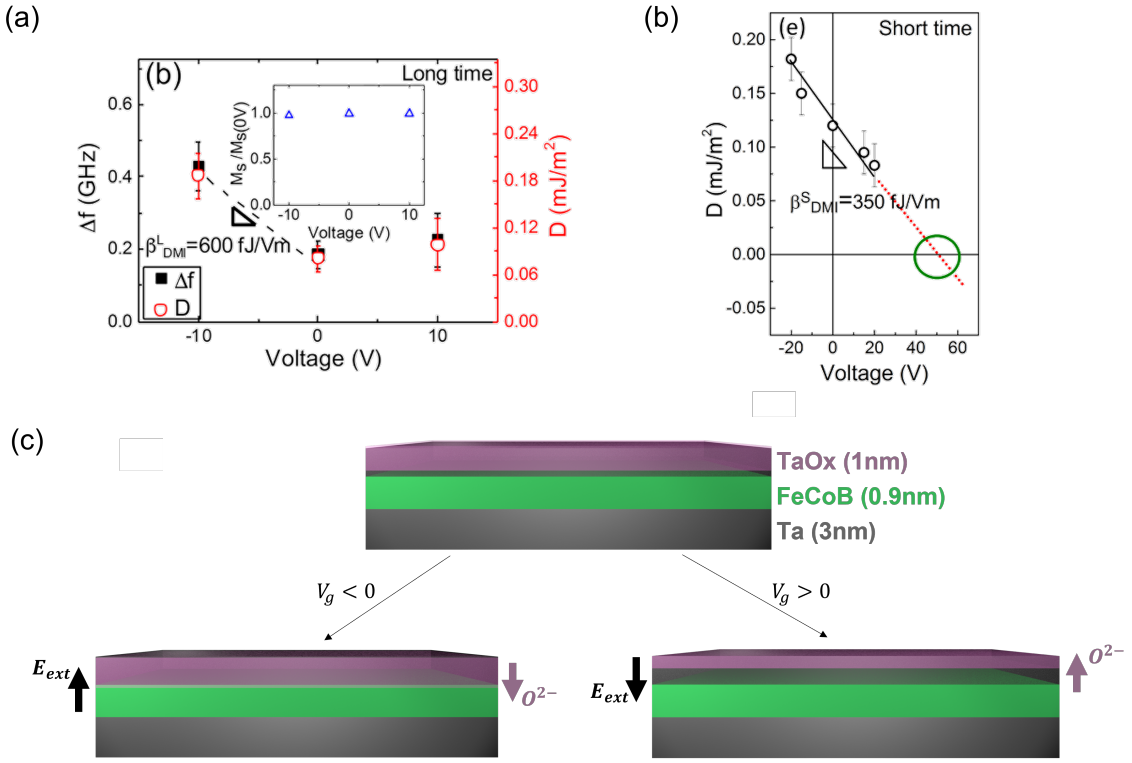

Figure 2.9: *(Extracted from [82])* (a) Evolution of both the frequency difference between stokes and anti-stokes peaks Δf (in GHZ) measured by BLS and the DMI coefficient D deduced (in mJ/m^2) with respect to the applied voltage (in V) for long time application. A VCDMI efficiency of $\beta^L_{DMI} = 600 fJ/(V \cdot m)$ is found. (b) Evolution of the DMI coefficient D (in mJ/m^2) with respect to the applied voltage for short time application. It is important to note an error in the calculation of the VCDMI efficiency. In the paper they show $\beta^S_{DMI} = 350 fJ/(V \cdot m)$ when in reality it is $\beta^S_{DMI} = 150 fJ/(V \cdot m)$. This error mainly comes from a factor 2 in the voltage taken into account for the calculation. The convention used for the sign of the DMI is opposite to the one we use, see the section 1.2.1. (c) Schematic representation of the effect of the application of a gate in the tri-layer system Ta/FeCoB/TaOx. Initially the top Ta is slightly under-oxidized. The application of a negative (resp.positive) gate voltage V_g induce an external electric field E_{ext} pushing towards (resp away) to the ferromagnetic layer.

consistent comparison with results from different studies and device architectures, they introduced a normalized coefficient, η_{DMI} which takes into account the interfacial origin of DMI. It is defined as:

$$\eta_{DMI} = \frac{\Delta D_s}{\varepsilon_e \Delta E} \tag{2.5}$$

Where D_S is the surface DMI coefficient, $\varepsilon_e = \varepsilon_0 \varepsilon_r$ the effective permittivity of the oxide and ΔE is the applied electric field. This approach accounts for the surface charge induced at the interface rather than the electric field alone. In VCDMI studies the use of materials with higher permittivity can induce larger effects for the same applied voltage. Consequently, the η_{DMI} coefficient provides a more meaningful comparison in term of the underlying physical mechanism. The figure 2.10 recapitulates the already measured VCDMI coefficients. We see that the β_{DMI}

coefficient values varied up to 3 orders of magnitude between different studies meanwhile the η_{DMI} coefficient values show only one order of difference for the same mechanism. This small variation of the η_{DMI} factor despite the change in materials and techniques of measurements could suggest that the underlying physical phenomenon is the same or very similar for all the samples measured.

Seed nm	FM nm	MOx nm	β_{DMI} fJ/(V·m)	η_{DMI} 10^{-12}J·m/C
Pt (3)	Co (0.49)	AlO_x(6)/HfO_x(53)	1100–2000 ± 700	3.9–7.2
Ta(3)	FeCoB(0.65)	TaO_x(1)/AlO_x(10)/HfO_x(50)	600	3.2
Ta(3)	FeCoB(0.65)	TaO_x(1)/AlO_x(10)/HfO_x(50)	158	0.61
Au(50)	Fe(20)	MgO(10)/SiO_2(270)	3.2	1.72
Pt(4)	Fe(2)	MgO(367)	75	2.65
Ta(2.6)/Pt(2.4)	Co(0.78)/Pd(0.4)	MgO(2)/HfO_x(50)	67	0.38
V(20)/Fe(20)	Co(0.14)	MgO(5)/SiO_2(50)	100	5.5
V(20)/Fe(20)	Co(0.26)	MgO(5)/SiO_2(50)	65	14.5
Pt	Co(0.6)	MgO	26	0.6–1.76

Figure 2.10: *(Extracted from [83])* Table summarizing VCDMI efficiencies coming from different studies and calculating the equivalent normalized coefficient η_{DMI}. It shows a smaller difference in between all the VCDMI efficiencies.

In the Ta/FeCoB/TaOx tri-layer with a double wedge system similar to the one used in [51] and described in the section 3.1.1, Ch-E.Fillion et al. observed a persistent and reversible chirality switch of the DMI controlled by a gate voltage [52]. BLS measurements shows a DMI sign change along the top Ta gradient consistent with what has been shown in [51]. By applying a gate voltage near the DMI sign transition region, the authors have been able to reverse the chirality of the spin textures (skyrmions and DW) and of the DMI. Moreover, by changing the polarity of the gate they are able to reversibly and reproducibly control the sign of the DMI as illustrated in the figure 2.11(a)-(f). The persistance of the inversion after the gate voltage is back to 0V makes the authors attribute this phenomenon to oxygen ion migration based on the time dependence of chirality switching process.

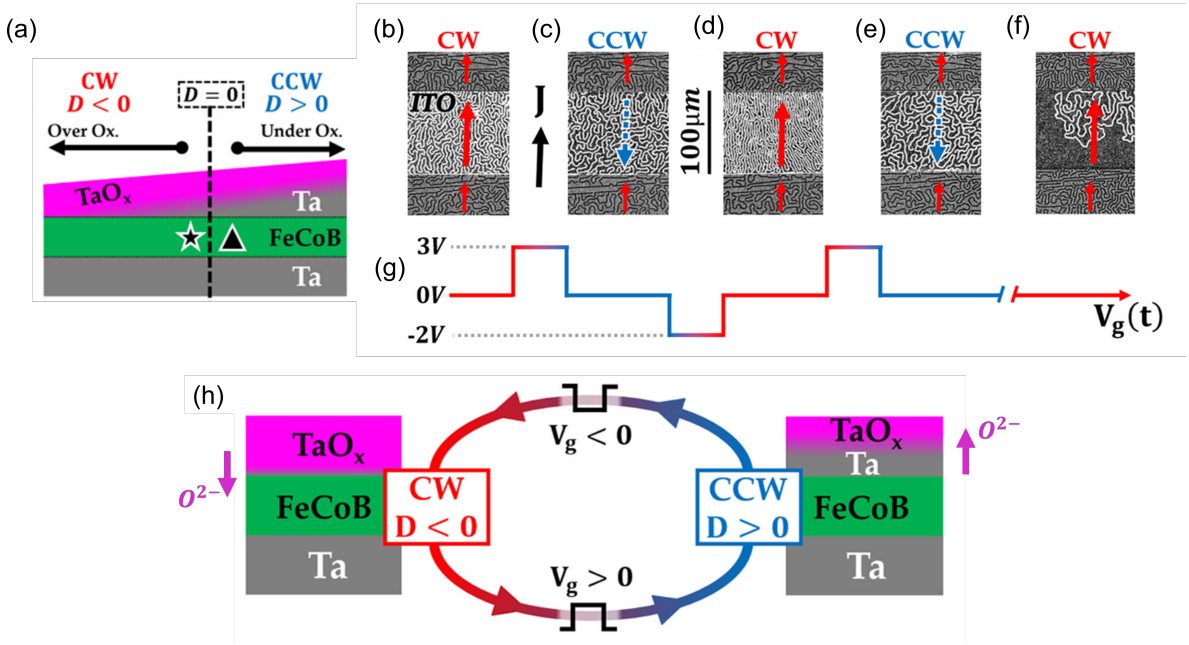

Figure 2.11: *(Extracted from[52])* (a) Scheme of an horizontal cut along the ferromagnet gradient of the tri-layer Ta/FeCoB/TaOx. The black star and triangle represent the region close to D=0 where the gate is applied. (b)-(f) MOKE observation of the DW motion under current for an external applied field $\mu_0 H \simeq 30\mu T$. (g) Schematic representation of the gate voltage applied to reverse the chirality. The gate is applied during 90s and then back to 0V for the current injection. (b) Initially the DW are clockwise (CW). After the application of a +3V gate pulse the chirality is reversed, (c) DW are counter Clockwise (CCW). Next, a negative gate voltage pulse of -2V is applied, chirality changes once again (d) the DW are back to CW. (e) After a positive gate pulse the chirality is set to CCW. (f) After $\sim$ 2h the chirality switches without gate. (h) Schematic summary of the chirality reversal using a gate voltage in the Ta/FeCoB/TaOX tri-layer system. A positive (resp. negative) gate switches a CW (resp.CCW) chirality to a CCW (resp.CW) one due to the oxygen ion migration at the top interface represented by pink arrows.

2.3 Dynamic of spin textures

The competition between all the energies contribute to the stabilization of spin textures and set a magnetic state. All these interactions contribute to the effective magnetic field H_{eff} that will act on the magnetization :

$$\overrightarrow{H}_{eff} = \overrightarrow{H}_{exch} + \overrightarrow{H}_{dip} + \overrightarrow{H}_{zee} + \overrightarrow{H}_{aniso} + \overrightarrow{H}_{DMI} \tag{2.6}$$

The magnetic field created by each energy is defined via the functional derivative of the magnetic energy with respect to the magnetization : $\overrightarrow{H}_i = -\frac{1}{\mu_0 M_S}\frac{\partial E_i}{\partial \overrightarrow{m}}$. With E_i the energy and $\overrightarrow{m}$ the normalized magnetization.
The response of the magnetic moments to this effective fields is characterized by the Landau-Lifshitz-Gilbert (LLG) equation [84],[85]:

$$\frac{d\overrightarrow{m}}{dt} = -\gamma_0 \overrightarrow{m} \times \overrightarrow{H}_{eff} + \alpha \overrightarrow{m} \times \frac{d\overrightarrow{m}}{dt} = \overrightarrow{\tau}_F + \overrightarrow{\tau}_D \tag{2.7}$$

Where $\gamma_0 = \mu_0 |\gamma|$ with γ the gyromagnetic ratio in $rad/(s.T)$ and $\frac{\gamma}{2\pi}$ in GHz/T) , $\overrightarrow{m}$ the normalized magnetization, H_{eff} the effective field and α the Gilbert damping parameter. This equation describes the evolution of the magnetization vector at each point in space and time. The first term in the LLG equation describes the precession of an isolated magnetic moment under the effective field. In this case, the magnetization experiences a torque $\overrightarrow{\tau}_F$ from the effective field (first term in eq.2.7), causing it to precess around the field direction (see Figure 2.12). This term is conservative and thus, in the absence of other effects, the precession would continue indefinitely. However, in real materials, the magnetization is coupled to its environment, including neighboring magnetic moments, conduction electrons, and the lattice. These couplings enable the exchange of angular momentum and energy, resulting in damping. This is represented by the second term in the LLG equation. It leads to the gradual alignment of the magnetization with the effective field over time [86]. This damping term introduces a second torque, $\overrightarrow{\tau}_D$, which acts perpendicular to the precessional torque and serves to reduce the angle between the magnetization and the effective field (second term in eq.2.7), see figure 2.12. The dynamics of the magnetization depends thereby on the balance between these torques and the stabilized state is reached when the total torque exerted on the magnetization is zero, in that case $\frac{d\overrightarrow{m}}{dt} = 0$.

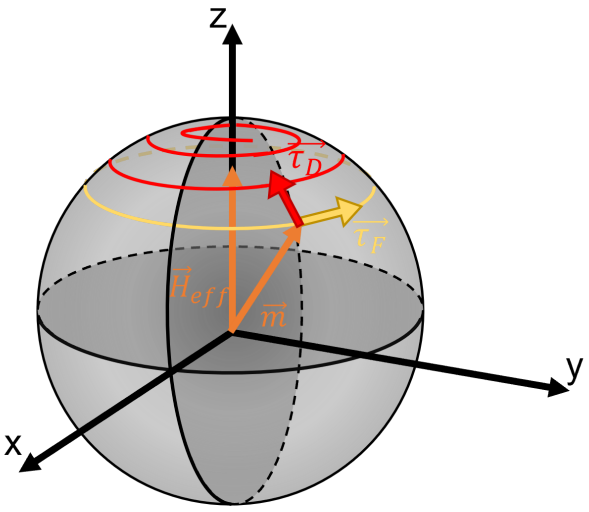

Figure 2.12: Scheme of the precession of the magnetization $\overrightarrow{m}$ in a constant effective field $\overrightarrow{H_{eff}}$. Two torques act on the magnetization, $\overrightarrow{\tau}_F$ induced by the effective field which gives the precession and $\overrightarrow{\tau}_D$ which corresponds to the damping and tends to align the magnetization with $\overrightarrow{H_{eff}}$.

One key achievement to be able to use spin textures and skyrmions in different applications is to move and control them. Different techniques exists such as spin waves [87],[88], stress and strain [89], [90], [91], [92], light or thermal gradient [93], [94],[95]. Here we described in more details two techniques using: 1- an external magnetic field and 2- an electrical current.

2.3.1 Motion under an external magnetic field

To understand better how an external magnetic field $\overrightarrow{H}_{eff}$ is affecting the magnetization we re-write the equation 2.7 in the initial Landau-Lifshitz form, using the fact that the damping α is small:

$$\frac{\partial \overrightarrow{m}}{\partial t} = -\frac{\gamma_0}{1+\alpha^2}(\overrightarrow{m} \times \overrightarrow{H}_{eff}) - \frac{\alpha\gamma_0}{1+\alpha^2}\overrightarrow{m} \times (\overrightarrow{m} \times \overrightarrow{H}_{eff}) = \overrightarrow{\tau}_{FL} + \overrightarrow{\tau}_{DL} \tag{2.8}$$

An external magnetic field interacts with the magnetization via the Zeeman interaction. To minimize the total energy, the spins tend to align with the direction of the effective field. In systems with magnetic domains separated by a domain wall, this interaction favors the expansion of the domain aligned with the applied field and the shrinking of the opposite domain. This results in a net force on the domain wall, causing it to move.

The figure 2.13 schematize the example of two magnetic domains separated by a Bloch domain wall (DW) with an external magnetic field $\mu_0 \overrightarrow{H}_{ext}$ applied along the $+\overrightarrow{z}$ direction. The corresponding torque $\overrightarrow{\tau}_{ext} \propto -\overrightarrow{m} \times \overrightarrow{H}_{ext}$ exert a force only into the spins inside the DW. The spin on the edge, constituting the domain, are collinear to the external field resulting in a zero torque. In the figure 2.13 we consider a Bloch DW along the x-axis with the magnetization along the y-axis. Looking at the spin in the middle of the DW (n°4) we see that the external field creates a torque $\overrightarrow{\tau}_{ext} \propto -\overrightarrow{x}$, step (a) in the figure 2.13. The rotation of each spin inside the DW due to this torque induces volume charges. Indeed volumes magnetic charges are expressed as :

$$\rho_m = -\overrightarrow{\nabla}.\overrightarrow{M} = -\left(\frac{\partial M_x}{\partial x} + \frac{\partial M_y}{\partial y} + \frac{\partial M_z}{\partial z}\right) \tag{2.9}$$

It is easy to see that a Bloch DW at rest does not have volume magnetic charges as there is no magnetization along the $\overrightarrow{x}$ axis (the axis of the DW) and $\overrightarrow{M}$ only varies along the x-axis. However, under the influence of the torque the rotation of the spin creates a magnetization x-component M_x and therefore volume magnetic charges. These charges create a demagnetizing field $\overrightarrow{H}_d \propto \overrightarrow{x}$, step(b) figure 2.13, which in his turn applies a torque on the already tilted magnetization $\overrightarrow{\tau}_d \propto -(\overrightarrow{y} - \varepsilon\overrightarrow{x}) \times \overrightarrow{H}_d \propto -(\overrightarrow{y} - \varepsilon\overrightarrow{x}) \times \overrightarrow{x} \propto \overrightarrow{z}$, step (c). This torque lifts the magnetization inside the DW towards the direction of the external magnetic field. Finally, as explained above, in the LLG equation the damping will exert a torque on the tilted magnetization $\overrightarrow{\tau}_\alpha \propto -\overrightarrow{m} \times (\overrightarrow{m} \times \overrightarrow{H}_{eff}) \propto \overrightarrow{m} \times (\overrightarrow{\tau}_{ext} + \overrightarrow{\tau}_d) \propto \overrightarrow{x} + \overrightarrow{z}$, step (d). Magnetization inside the domain wall will then rotate of a constant angle ϕ. We see also that the damping term participates, with the demagnetizing field, to lift the the spin towards the external magnetic field axis, in the $\overrightarrow{z}$ direction.

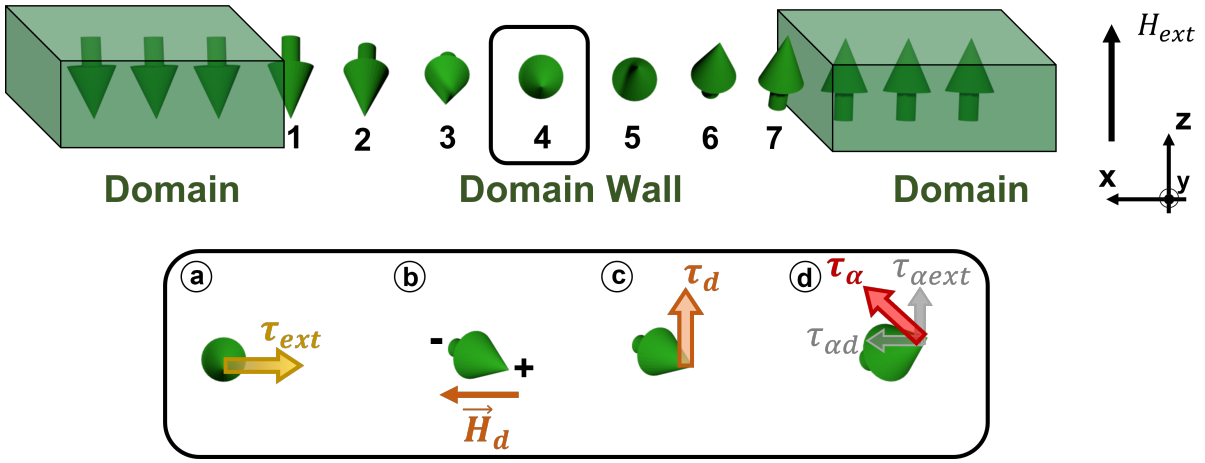

Figure 2.13: Scheme of the effect of the application of an external magnetic field H_{ext} along the $+\vec{z}$ direction, on a Bloch domain wall. The corresponding torque is written τ_{ext} (a), the rotation of each spins will induces magnetic charges and therefore a dipolar field $\vec{H}_d$ (b). The corresponding torque is displays as τ_d (c), it lifts the magnetization towards the direction of the external magnetic field. (d) represents the effect of the torque coming from the damping in competition with the both the external and dipolar field.

In the case of a Néel DW the effect stays the same. Initially with a magnetization in the center of the DW pointing in the $+\vec{x}$ direction, the applied external field will creates a torques that will rotate the spin in the $+\vec{y}$ direction. This have two consequences, the reduction of the dipolar field but this dipolar field, as for a Bloch DW, will lift the magnetization of the domain wall towards the direction of the external field, in the $+\vec{z}$ direction. In this case as well the damping torque compete with the two torques, creating in turn a torques, resulting in a rotation of the magnetization inside the DW. For Néel DWs an additional torque is coming from the effective DMI field.

However, real materials are not perfect, they contain defects, grain boundaries, inhomogeneities, etc. that can pin the DWs. In the case of a low applied magnetic field, the DWs sticks to these pinning sites, occasionally jumping from one site to another due to thermal activation. This is what is called the creep regime, for which the velocity of DWs is low (generally < 10 m/s) and follow the creep law [96]. Above a certain external field, the pinning sites can be neglected and the velocity of the DW start to be linear with the external field value, this is the linear/flow regime. This regime, first proposed by Walker in 1974 [97] in the bulk, is characterized by a high domain wall mobility, as we can see in the figure 2.14. Above a critical value of the applied external field, $\vec{H}_W$, the damping cannot compensate anymore the torque created by the external field, this is the Walker breakdown. As a consequence, the magnetization inside the DW starts to precess around the external field during the propagation, this is the precession regime or the so-called Walker regime [97]. As seen in the figure 2.14 the velocity decreases sharply as well as the domain wall mobility.

The DMI implication into the DW motion and velocity has been studied numerically and analytically by Thiaville et al. in PMA samples [30]. In a Pt/Co(0.6 nm)/AlOx system, the authors extract a progressive transition from a Bloch DW, with no DMI, into a Néel DW, when

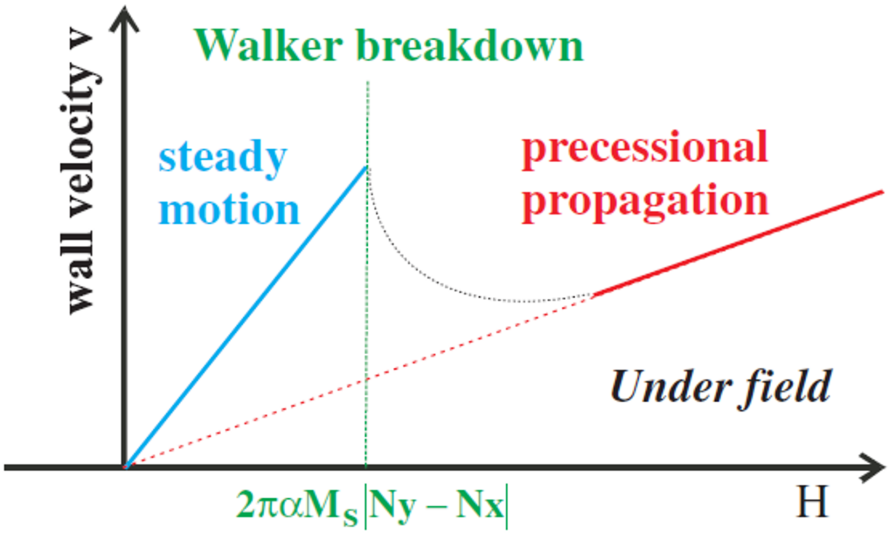

Figure 2.14: *(Extracted from [98]):* Domain wall velocity with respect to the external magnetic field H. For small external magnetic field the velocity of domain wall increase linearly with the applied field. This regime is called the steady regime. Above a critical value of H, called the Walker breakdown field expressed as $H_{WB} = 2\pi\alpha M_S|N_y - N_x|$ (expressed in cgs unit) the regime start to be precessional, the velocity decreases.

the DMI coefficient reaches a critical value $D > D_C \sim 0.13 mJ/m^2$. Then, they developed a model to study the velocity of these intermediate structures, called the Dzyaloshinskii domain walls, under an external out-of-plane field. The figure 2.15 shows that the DMI increases the steady state regime, increasing the value of the Walker breakdown field, with no change in the mobility. The presence of DMI strongly increases the velocity of the DWs. This is due to the blocking of the DWs, by the DMI, into a Néel orientation that suppresses the precession of the magnetization inside the DWs. Experimentally Thiaville et al. measured the velocity of DWs inside Pt/Co (0.6)/AlOx. They compared their results with the study of Metaxas et al. on the creep and flow regimes of magnetic domain-wall motion Pt/Co(t)/Pt with t = 0.5 - 0.8 nm[99], where the authors concluded that the motion is in the precessional regime with a damping of $\alpha = 0.3$, the linear regime being "hidden" by the pinning.
With Pt/Co/AlOx, [30] the authors obtained a velocity in the flow regime at least 5 times larger with a high mobility, suggesting a motion in the linear regime. However the applied external field is higher than the supposed Walker breakdown field for this system, implying a motion in the precessional regime with a lower mobility. To explain this high velocity and mobility while being above the usual Walker field, the authors show that a DMI strength $D \sim 1 mJ/m^2$ or more can prevent precession even above the classical Walker field. In that case the modified Walker field varies proportionally to the DMI field and therefore to the DMI coefficient D. The DMI has for consequence to increase the Walker breakdown threshold.

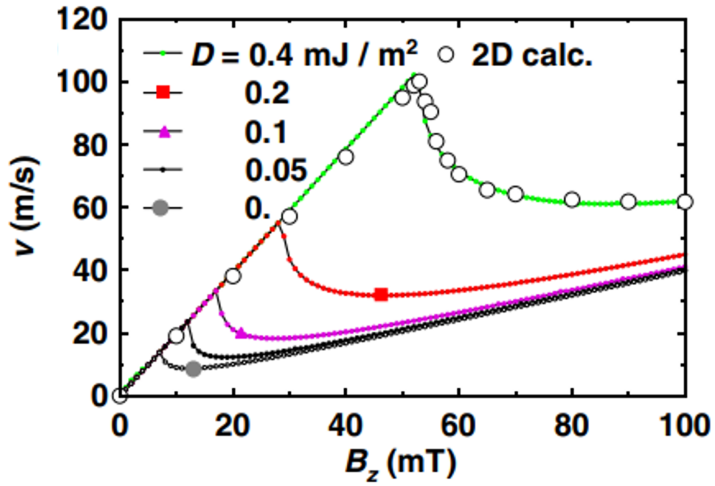

Figure 2.15: *(Extracted from [30]):* Evolution of the domain wall velocity with respect to the external magnetic field B_z for different value of DMI coefficient D = [0; 0.05; 0.1; 0.2; 0.4] mJ/m^2.

In [100], Pham et al. compared the Pt/Co/Pt and Pt/Co/AlOx case, presented in the figure 2.16. The DMI allows to reach higher value of DW velocity, up to hundred of m/s. The authors shows that in Pt/Co/Pt systems the Walker breakdown field is expected to be low, as a consequence the motion is precessional. By contrast, in antisymmetric system, as Pt/Co/AlOx, the DMI increases the Walker field and stabilizes a steady state regime up to larger external field value.

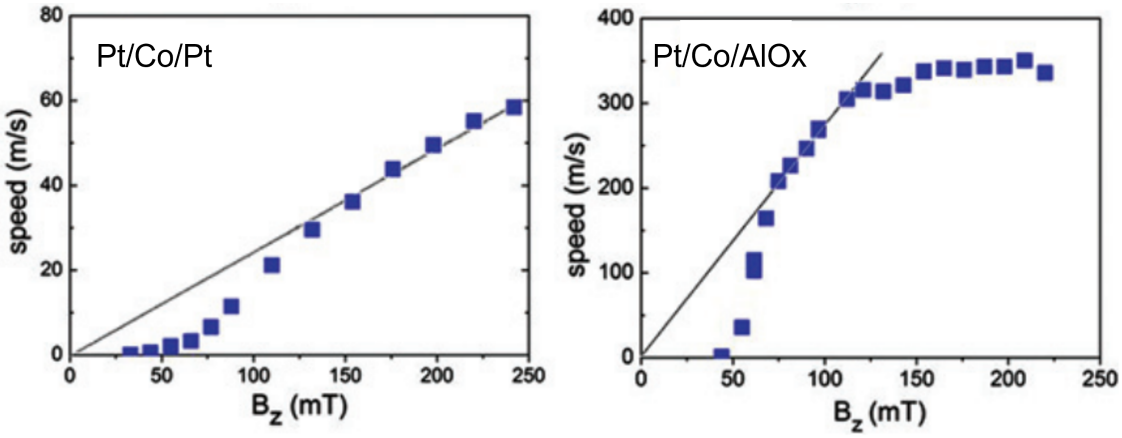

Figure 2.16: *(Extracted from [100])* Comparison of the domain wall velocity with respect to the external magnetic field B_z between two different systems: (Left) Pt/Co/Pt and (Right) Pt/Co/AlOx.

2.3.2 Motion under an electrical current

The idea by using electrical current is to control the magnetization using the spin momentum of the conducting electrons that transfer it to the local magnetization. There are two main mechanisms that have been intensively studied: the spin-transfer torque (STT) and the spin-orbit torque (SOT).

Spin-transfer torque (STT):

The spin transfer torque mechanism was first introduced theoretically in 1996 by Slonczewski [101] and Berger [102]. As explained above, STT arises when spin-polarized conduction electrons transfer their angular momentum to a local magnetization. Devices can be categorized in two different types: pillars, for which composed of two ferromagnetic layers separated by a non-magnetic one (FM1/NM/FM2). In these devices, a current flows through a ferromagnetic material (FM1), called the fixed layer, the spins of the electrons tend to align with the local magnetization resulting in an outgoing current electron $\overrightarrow{J}_e$ which is spin-polarized. It will then interact with the magnetization inside a second layer of ferromagnetic material (FM2), called free layer. The two ferromagnetic layers are separated by a non-magnetic one, called a spacer. The nature of the spacer is what differentiate a magnetic tunnel junction (MTJ) from a spin valve. The former one uses an insulator to separate both FM layers while the second uses a metal.
The second type of devices are the domain walls, as the spin-polarized electrons pass through a non-uniform magnetization region like a DW, they exert a torque on the local magnetic moments. Which induces an alignment with the incoming spin orientation. The angular momentum is transferred from the electrons to the magnetic texture.

The effect of spin-polarized current on the magnetization in a non uniform case is described by two additional torques in the LLG equation, [103]:

$$\frac{d\overrightarrow{m}}{dt} = -\gamma_0 \overrightarrow{m} \times \overrightarrow{H}_{eff} + \alpha \overrightarrow{m} \times \frac{d\overrightarrow{m}}{dt} + \overrightarrow{\tau}_{ad} + \overrightarrow{\tau}_{non-ad} \tag{2.10}$$

The first torque occurs by assuming the adiabacity of the current polarization (it assumes the electron spin follows the local magnetization perfectly), and full transfer of angular momentum to the local magnetization applies:

$$\overrightarrow{\tau}_{ad} = -(\overrightarrow{u} \cdot \overrightarrow{\nabla})\overrightarrow{m} \tag{2.11}$$

$\overrightarrow{u}$ is the spin drift velocity, directed along the direction of the electron motion. Its amplitude is $\|\overrightarrow{u}\| = \frac{JPg\mu_B}{2eM_s}$ where J is the current density, P its spin polarization rate, g the Landé factor, μ_B the Bohr magneton, e the charge of the electron and M_s the saturation magnetization. The factor $\frac{g\mu_B}{2eM_s}$ quantifies the domain wall motion per unit of spin-polarized current density. This adiabatic torque pushes the spin textures (e.g DW) along the electron direction.

In the adiabatic limit, at low current the spin-transfer torque is fully compensate by an internal restoring torque. As a consequence, the DW magnetization precess but the DW doesn't move. Above threshold, the internal torque is not sufficient and DW motion occurs, together

with a continuous precession of the DW magnetization. However, a discrepancy has been found between the theoretical and experimental values of this threshold. Experimentally a steady motion of the DW is reached at lower current than predicted by the simulation. This indicates that corrections must be added to the assumption of perfect adiabaticity of the polarization and the full transfer of angular momentum to resolve this, Zhang et al. [104] and Thiaville et al. [105] introduced a second torque, non-adiabatic, arising from the misalignment between the electron spins and the local magnetization:

$$\overrightarrow{\tau}_{non-ad} = \beta \overrightarrow{m} \times ((\overrightarrow{u} \cdot \overrightarrow{\nabla}) \overrightarrow{m}) \tag{2.12}$$

Where β is a dimensionless coefficient that quantifies the strength of the non-adiabatic torque. In the ideal adiabatic limit, electron spin always stays aligned with the local magnetization as it moves through the DW. In reality, spin relaxation prevent this alignment, creating this additional torque, which directly competes with the damping term. The inclusion of this torque breaks the symmetry between the adiabatic torque and the internal restoring torque that would otherwise only distort the DW, thereby enabling steady DW motion at experimentally relevant currents.

One turning point in the motion of spin textures is demonstration that Spin Orbit Torque (SOT) can efficiently drive chiral spin textures in 2011 by Miron et al. [106]. The authors measured, in Pt/Co/AlOx, a current-induced DW velocity up to $400 m/s$, which is order of magnitudes higher than what has been measured previously.

Spin-orbit torque (SOT):

The second well-known mechanism is spin-orbit torque (SOT) [107]. SOT arises from spin-orbit coupling (SOC) in systems where an electric current is applied in a heavy metal (HM) layer adjacent to a ferromagnet. The SOC links the spin and momentum of conduction electrons in the HM, giving rise to spin currents and spin accumulation, typically via the spin Hall effect or Rashba effect. These spin currents diffuse into the ferromagnet and exert torques on its magnetization.

The SOT can be decomposed in two contributions called field-like $\overrightarrow{\tau}^{FL}_{SOT}$ and damping-like $\overrightarrow{\tau}^{DL}_{SOT}$ torque, perpendicular from each other. They are expressed as:

$$\overrightarrow{\tau}^{FL}_{SOT} = -\gamma_0 \overrightarrow{m} \times \overrightarrow{H}_{FL} = -\gamma_0 c_{FL} \overrightarrow{m} \times (\overrightarrow{j} \times \overrightarrow{z}) \tag{2.13}$$

$$\overrightarrow{\tau}^{DL}_{SOT} = \gamma_0 \overrightarrow{m} \times \overrightarrow{H}_{DL} = \gamma_0 c_{DL} \overrightarrow{m} \times [\overrightarrow{m} \times (\overrightarrow{j} \times \overrightarrow{z})] \tag{2.14}$$

Where $\gamma_0 = \mu_0 |\gamma|$, γ being the gyromagnetic ratio. $c_{DL/FL}$ the effective fields per unit current density, $\overrightarrow{j}$ the current density and $\overrightarrow{z}$ the direction along which the symmetry is broken.

Let's now explore the two mechanism at the origin of the spin currents and spin accumulations: the spin Hall effect (SHE) and the Rashba Edelstein effect:

1 - Spin Hall Effect (SHE):

The spin hall effect is a transport phenomenon first introduced in 1971 by Dyakonov and Perel [108]. A charge current is converted into a transverse spin current via spin-orbit coupling: When applying a current $\overrightarrow{J}_c$ into a heavy metal layer, due to a strong spin-orbit interaction the electrons having opposite spins are deflected in opposite transverse directions, creating a spin current $\overrightarrow{J}_s$ perpendicular to the charge current $\overrightarrow{J}_c$, with the spin polarization perpendicular to both currents. This is schematized in figure 2.17. As a result there is a spin accumulation at the interface with the ferromagnetic layer [108], that will interact, by exerting a torque (SOT), with the spin textures inside the ferromagnet. The efficiency of the charge-to-spin conversion is characterized by the spin Hall angle (SHA) [109] $\theta_{SHE} = J_s/J_c$ which is material dependent. For atoms this efficiency scales as $\propto Z^4$[110], Z being the atomic number. The SHE is more efficient using heavy metal as Pt [59],[111],[112] , Pd, W [113], Ta [59],[114]. Also, the spin Hall angle can be either positive or negative depending on the material, which leads to opposite spin polarization at the edges of the HM layer and thus opposite direction of motion of spin textures in the adjacent FM layer [59]. In the figure 2.17 the SHA is considered negative. Two torques, generated by the spin current, act on the magnetization: a field-like torque $\overrightarrow{\tau}^{FL}_{SHE}$ and a damping-like torque $\overrightarrow{\tau}^{DL}_{SHE}$. We can expressed them as:

$$\overrightarrow{\tau}^{FL}_{SHE} = -\left|\gamma\right| \mu_0 H_{FL}(\overrightarrow{m} \times \overrightarrow{\sigma}) \tag{2.15}$$

$$\overrightarrow{\tau}^{DL}_{SHE} = \left|\gamma\right| \mu_0 H_{DL}(\overrightarrow{m} \times (\overrightarrow{m} \times \overrightarrow{\sigma})) \tag{2.16}$$

Where $\overrightarrow{\sigma}$ is the spin accumulation vector. It arises from the spin current: $\overrightarrow{j_s} \propto \overrightarrow{j_c} \times \overrightarrow{\sigma}$, $\overrightarrow{m}$ the magnetization and $\mu_0 H_{DL/FL} \propto \theta_{SHE}$ proportional to the spin hall angle, represents the efficiency of the respective torques. In the figure 2.17 a simplified clock-wise Néel DW is represented inside the ferromagnet. Both torques are represented for the central grey spin of the Néel DW.

Both components of this torque depends on both the direction of magnetization within the DW and the spin accumulation. This implies that, in HM/FM system, the motion will be in opposite directions depending on the chirality of the magnetic texture: Clockwise (CW) (resp. Counter Clock-Wise (CCW)) DW moves along (resp. against) the current when using an HM with a negative spin Hall angle like Ta [59]. As a consequence, studying the motion of spin textures under an electrical current allows to have access to their chirality, and as we have seen in the section 1.2.1 this chirality is linked to the sign of the DMI coefficient D. The current-induced motion (CIM) is therefore a useful technique to study the DMI.

2 - The Rashba-Edelstein effect:

Predicted in 1990 by V.M.Edelstein [115] the Rashba-Edelstein effect (REE) is as well a charge-to-spin conversion mechanism in which a two-dimensional in-plane charge current generates a surface spin accumulation. In 2013, Rojas Sanchez et al.[116] demonstrates that the Rashba effect at interfaces can be used for efficient charge-to-spin conversion in spintronics.

The broken symmetry in a HM/FM interface creates an interfacial electric field $\overrightarrow{E}_R$ parallel to the axis along which the symmetry is broken, here the $\overrightarrow{z}$ axis. This electric field interacts

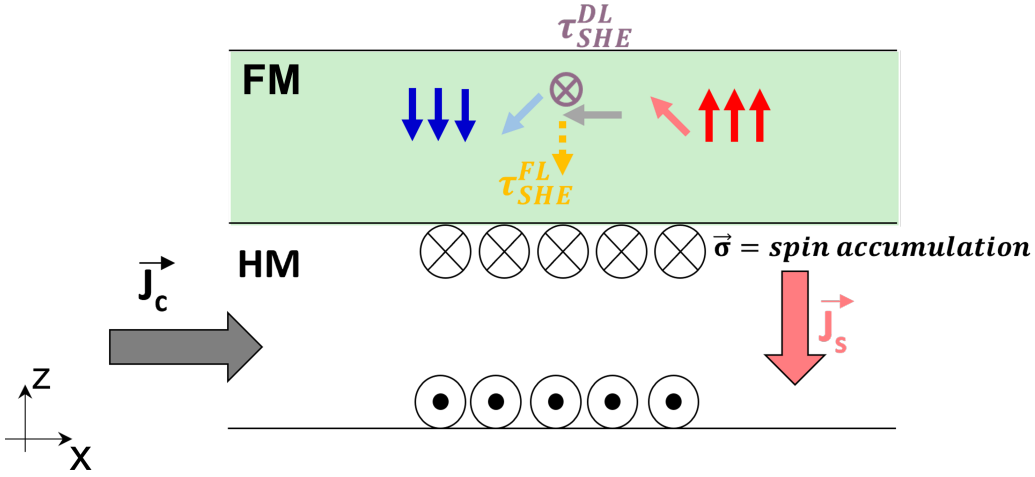

Figure 2.17: Scheme of the spin Hall effect (SHE): An charge current $\overrightarrow{J}_c$ is applied along the x direction in an heavy metal material. Due to the spin-orbit interaction a spin current $\overrightarrow{J}_s$ is created as well as a spin accumulation $\overrightarrow{\sigma}$ at the edges of the heavy metal and particularly at the interface with a the ferromagnetic layer. the spin textures inside the ferromagnet (represented by colored arrows) rotates under the influences of two torques: the field-like torque τ_{SHE}^{FL} and the damping-like torque τ_{SHE}^{DL}.

with the spin through the spin orbit coupling (SOC), as explained in the section 1.2.1. This interaction can be described by the Hamiltonian :

$$H_{Rashba} = \alpha_R(\overrightarrow{\sigma} \times \overrightarrow{k}) \cdot \hat{z} \tag{2.17}$$

Where α_R is the Rashba coefficient, $\overrightarrow{\sigma}$ the Pauli matrices vector and $\overrightarrow{k}$ is the momentum of the electrons.
This leads to the so-called spin-momentum locking: electrons having a momentum $\overrightarrow{k}$ have spins preferentially perpendicular to $\overrightarrow{k}$ and the electric field $\overrightarrow{E}_R$. Then, applying a charge current in the $+\overrightarrow{x}$ direction induce a shift in the electron distribution in the $\overrightarrow{k}$-space, more electrons are moving along the $+\overrightarrow{x}$ direction. Due to spin-momentum locking these electrons are carrying spin polarized in the $-\overrightarrow{y}$ direction. This creates an accumulation of spin $\overrightarrow{S}$ polarized in the $-\overrightarrow{y}$ direction at the interface.
The REE effect have then a similar effect on the magnetization than the SHE: two torques are acting on the magnetization in the ferromagnet, a field-like torque $\overrightarrow{\tau}_{Rashba}^{FL}$ and a damping-like one $\overrightarrow{\tau}_{Rashba}^{DL}$, that read:

$$\overrightarrow{\tau}_{Rashba}^{FL} = -\gamma\mu_0 H_R^{FL}(\overrightarrow{m} \times \overrightarrow{S}) \tag{2.18}$$

$$\overrightarrow{\tau}_{Rashba}^{DL} = -\gamma\mu_0 H_R^{FL}[\overrightarrow{m} \times (\overrightarrow{m} \times \overrightarrow{S})] \tag{2.19}$$

Finally, in our tri-layer system HM/FM/MOx, both SHE and REE can be responsible of the motion under an electrical current. However discussions and studies on the effect of each

torques has been done on the relative importance of each one [117]. First, in metallic system such as HM/FM/MOx, it has been shown that the effect of SHE can be reduced to the effect of the damping-like torque: $H_{SHE}^{FL} << H_{SHE}^{DL}$ [118]. For the REE one generally considers only the effect due the field-like torque τ_R^{FL} [118], [119]. Thus, in our HM/FM/MOx systems, it can be considered that the damping-like torque originates from the SHE and the field-like torque originates from the Rashba effect. Finally, by considering the geometry of our system (HM/FM system in a parallel geometry), it has been shown that the steady state dynamic is due to the damping-like term of the SHE τ_{SHE}^{DL}. While the field-like term only induces a small initial drift and vanishes in the steady state [109].
However, it is important to note that recent studies show that interface engineering as light-metal insertion, control of the ferromagnetic thickness or the choice of the heavy element can enhance the REE field-like component in some stacks. In [120] the authors report an enhancement of the SOT efficiency in Pt/Co/Al/Pt. For thin layer of Co ($t_{Co} = 0.5 - 1.2nm$) the authors found a ratio $\frac{H_{FL}}{H_{DL}} > 1$, even reaching 2.5 for $t_{Co} = 0.55nm$. They attribute this enhancement to the increase of the interfacial Rashba contribution in the case of Al insertion. The authors conclude that the Rashba contribution is dominating in this system, being impossible to reach such ratio value considering only SHE. In this study the authors also point out the recent theory that put in evidence the generation of orbital torques coming from the additional orbital currents in light elements generated from orbital Hall effect and/or orbital Rashba effects.

For our studies, chapter7 in HM/FM/MOx tri-layer systems, we only consider the SHE damping-like torque $\overrightarrow{\tau}_{SHE}^{DL}$, responsible of the steady motion. The LLG equation can then be written:

$$\frac{d\overrightarrow{m}}{dt} = -|\gamma_0| \overrightarrow{m} \times \overrightarrow{H}_{eff} + \alpha \overrightarrow{m} \times \frac{d\overrightarrow{m}}{dt} - \gamma \mu_0 H_{DL} (\overrightarrow{m} \times (\overrightarrow{m} \times \overrightarrow{\sigma})) \tag{2.20}$$

With all the terms described in details previously.

2.3.3 Motion of magnetic skyrmions - Thiele equation

The application of an external magnetic field constitute one way to move skyrmions, more precisely a gradient of magnetic field [121], [122], or an oscillating external magnetic field [123] can be applied. However, in the context of this thesis we will focus in this section on the motion of skyrmions using an electrical current.

We consider a skyrmion with a stable, circular geometry, i.e., without deformation during its motion. This assumption holds at low current densities and once the skyrmion motion has reached a steady regime. In this case, the current-induced dynamics can be described by the Thiele equation [124]:

$$\overrightarrow{G} \times \overrightarrow{v} - \alpha \bar{\bar{D}} \cdot \overrightarrow{v} + \overrightarrow{F}_{ext} = 0 \tag{2.21}$$

Where G is the gyrocoupling vector, $\overrightarrow{v}$ is the velocity of the skyrmions, $\bar{\bar{D}}$ is the dissipative tensor, related to the damping of the system and $\overrightarrow{F}_{ext}$ the external forces applied on the skyrmion. In the case of an electrical current applied in (x,y) plane of an HM/FM/MOx tri-layer system,

with the inversion symmetry along the $\overrightarrow{z}$ axis the external force is $\overrightarrow{F}_{ext} = \overrightarrow{F}_{DL}$, the force coming from the damping-like torque of the SHE. We can express each terms as :

$$\overrightarrow{F}_{DL} = \begin{pmatrix} \overrightarrow{F}_{DL,x} \\ \overrightarrow{F}_{DL,y} \\ 0 \end{pmatrix} ; \overrightarrow{F}_{DL,i} = \mu_0 M_s t_{FM} H_{DL} \int\int (m_x \frac{\partial m_z}{\partial i} - m_z \frac{\partial m_x}{\partial i}) dxdy \tag{2.22}$$

$$\overrightarrow{G} = \begin{pmatrix} 0 \\ 0 \\ G \end{pmatrix} ; \overrightarrow{G} = -\frac{M_s t_{FM}}{\gamma} \int\int \overrightarrow{m} \cdot (\frac{\partial \overrightarrow{m}}{\partial x} \times \frac{\partial \overrightarrow{m}}{\partial y}) dxdy \tag{2.23}$$

$$\bar{\bar{D}} = \begin{pmatrix} D_{xx} & D_{xy} \\ D_{yx} & D_{yy} \end{pmatrix} ; D_{ij} = \frac{M_s t_{FM}}{\gamma} \int\int (\frac{\partial \overrightarrow{m}}{\partial i} \cdot \frac{\partial \overrightarrow{m}}{\partial j}) dxdy \tag{2.24}$$

With M_s being the saturation magnetization, t_{FM} the thickness of the ferromagnet and γ the gyromagnetic ratio.

In the Thiele equation, $\overrightarrow{F}_{DL}$ is the force coming from the torques in the case of the spin Hall effect and inducing the motion of skyrmion. The second term, $-\bar{\bar{D}} \cdot \overrightarrow{v}$ is a dissipative force, proportional to the damping and oriented opposite to the velocity of the skyrmion. This is equivalent to a viscous force. Finally, $\overrightarrow{G} \times \overrightarrow{v}$ is the gyrotropic force (an equivalent of hydrodynamic Magnus force). This term arises from the topology of the spin texture. For a skyrmion, $\overrightarrow{G} = -4\pi n \frac{M_s t_{FM}}{\gamma} \hat{z}$ where n is the skyrmion number (± 1). It acts perpendicular to the skyrmion velocity and is responsible of the skyrmion Hall effect, i.e the transverse deflection of the skyrmion trajectory under current, that will be explain in more details later.

By assuming a motion in (x,y) plane we can write: $\overrightarrow{v} = (v_x, v_x, 0)$ and $G = (0, 0, G_z)$ also by considering rotational symmetry in the (x,y) plane the terms outside the diagonal in D are orthogonal and they cancel out: $(\partial \overrightarrow{m}/\partial x) \cdot (\partial \overrightarrow{m}/\partial y) = (\partial \overrightarrow{m}/\partial y) \cdot (\partial \overrightarrow{m}/\partial x) = 0$ and the terms in the diagonal are equal and named D. The Thiele equation is then written :

$$\begin{pmatrix} -Gv_y \\ Gv_x \\ 0 \end{pmatrix} - \begin{pmatrix} \alpha D v_x \\ \alpha D v_y \\ 0 \end{pmatrix} + \begin{pmatrix} F_{DL,x} \\ F_{DL,y} \\ 0 \end{pmatrix} = 0 \tag{2.25}$$

By resolving this (calculation detailed in the supplementary 9.4 we obtain:

$$\begin{cases} v_x = \frac{\alpha D F_{DL,x} - G_z F_{DL,y}}{G_z^2 + \alpha^2 D^2} \\ v_y = \frac{G_z F_{DL,x} + \alpha D F_{DL,y}}{G_z^2 + \alpha^2 D^2} \end{cases} \tag{2.26}$$

As a result the skyrmion is deflected from the direction of the driving force by an angle $\varphi_{SkHE} = arctan(\frac{v_y}{v_x}) = \frac{G}{\alpha D}$, called the skyrmion hall angle [125], [126],[127].

The first experimental observation of the motion of skyrmions under an electrical field has been realized by Jonietz et al.[128] in 2011 where they observed a rotation of the diffraction pattern in a skyrmion lattice of manganese silicon. Later in 2013, Iwasaki et al. [129] show a linear relationship between the current injected and the velocity of the skyrmions in confined

structures, as shown in the figure 2.18. They also control the creation and annihilation of skyrmions in this confined structure using an electrical current and an external magnetic field. In 2012, Yu et al. [130] imaged using in-situ Lorentz transmission electron microscopy the current-induced motion of skyrmions.

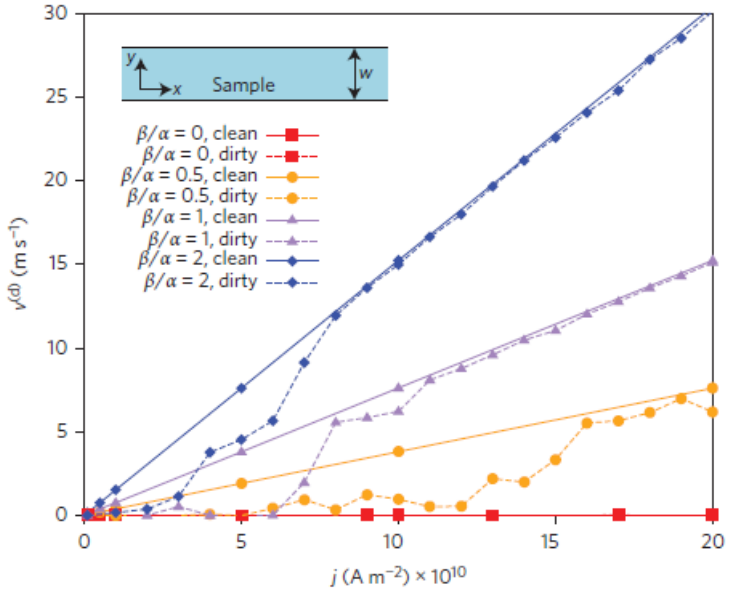

Figure 2.18: *Figure taken from[129]* Drift velocity $V^{(d)}$ of the skyrmion as a function of the current density j for different value of the ration β/α, extracted from micromagnetic simulations. β being the non-adiabatic effect coefficient and α the Gilbert damping coefficient. Clean (resp. dirty) sample corresponds to an impurity concentration of n = 0 (resp. n= 0.1 %).

This motion of skyrmion under current opens new possibility for spintronics devices as memory or logic devices, in 2013, Fert et al.[5] proposed the generation and motion of skyrmions in tracks as shown in the figure 2.19.

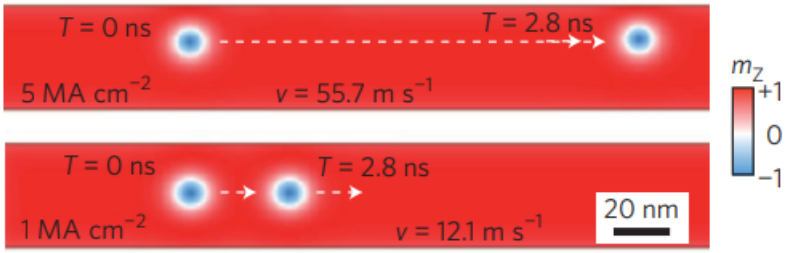

Figure 2.19: *Figure taken from [5]* Modelisation of the motion of skyrmions (in blue) inside a magnetic track (red) under an injected current with SOT.

As explained before, under an electrical current the gyrotropic force induces a deflection of the direction of motion of the skyrmions, the skyrmion Hall angle. In 2017, Jiang et al. [126] presents the first direct observation of this skyrmion Hall angle, in an Hall bar prepared from

the Ta/FeCoB/TaOx system. They show that the skyrmions escape the creep regime for a current density $J_e > 1.5 \times 10^6 A.cm^{-2}$. Above this threshold, they studied the skyrmion angle and developed a phase diagram, presented in figure 2.20. The authors show an increase of the deflection with the current density. Also, for current density larger than $|J_e| > 8 \times 10^6 A.cm^{-2}$ a saturation of the skyrmion Hall angle is observed, indicating that the system has entered the flow regime and that the motion is no longer governed by pinning. They also show that by reversing the the perpendicular magnetic field, the topological charge (Q in this paper) of the skyrmion is also reversed. This sign reversal leads to the opposite direction of the gyrotropic force $\overrightarrow{G} \times \overrightarrow{v}$ (called topological Magnus force in this paper) resulting in the opposite skyrmion Hall angle

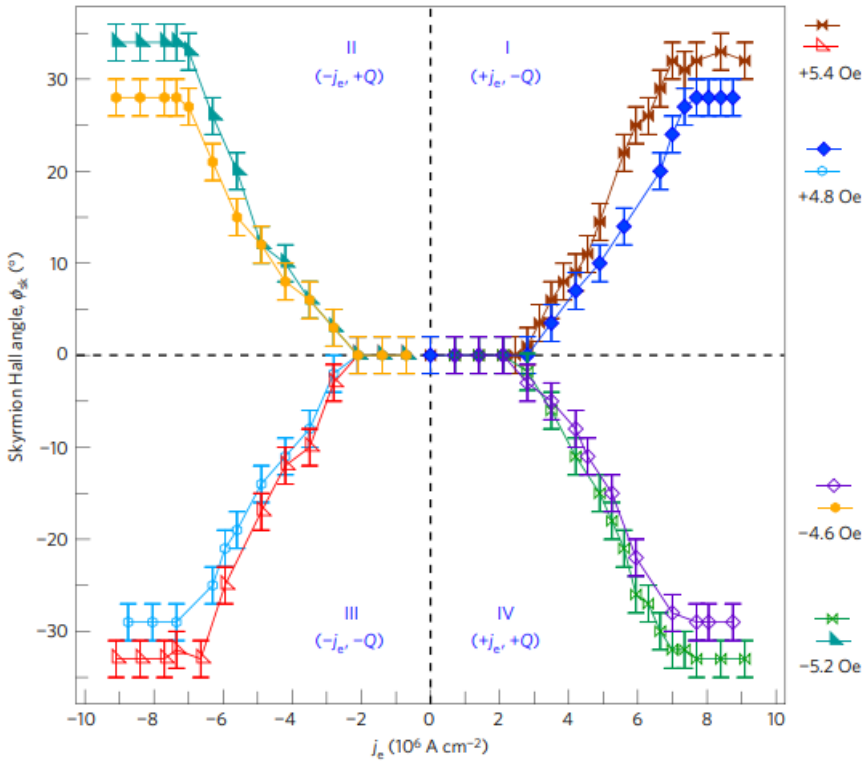

Figure 2.20: *Figure taken from [126]* Phase diagram of the skyrmion Hall angle ϕ_{sk} with respect to the current density j_e applied for different polarity of the current, different skyrmion number (Q in this article) and different external field applied.

The current-induced skyrmion motion is a central part in this thesis. In the chapter 4, I used the current induced motion technique to study the DMI sign in the Ta/FeCoB/TaOX tri-layer system. Also, in the chapter 6, I studied the control of the DMI chirality using a gate voltage in which the skyrmion moves, in a track, by the application of an external electrical current. Finally, I focused on the study of the motion of skyrmions under an electrical current in the chapter 7, using micromagnetic simulations. In that part of the manuscript, I studied skyrmion motion under current of $10^{10} A/m^2$ and $10^{11} A/m^2$, with a particular interest on the skyrmion hall angle.

2.4 Conclusion

The objective of this thesis is to advance in the control of a single skyrmion using a gate voltage. The broken inversion symmetry, combined with the strong spin-orbit coupling of the tantalum, makes the tri-layer Ta/FeCoB/TaOx an attractive system to study the skyrmions. Many studies have already explored the control and understanding of magnetic spin textures behavior in this system or in similar ones.
In this chapter, I first investigated the material dependence of the magnetic properties in our system. I then reviewed previous work on gate-voltage control of key magnetic energies and parameters. In particular, I focused on the modulation of magnetic anisotropy and the Dzyaloshinskii-Moriya interaction (DMI), two central points in the stabilization and manipulation of magnetic spin textures. Finally, I discussed the mechanisms governing their motion with a focus on the current-induced dynamics and an overview of the work already achieved on this subject.

Part II

Process and Characterization techniques

Chapter 3

Experimental techniques

3.1 Sample fabrication 86
3.1.1 Tri-layer deposition 86
3.1.2 Patterning process for gate voltage control 90
3.2 Characterization Techniques 92
3.2.1 Magneto-Optical Kerr Effect 92
3.2.2 MOKE magnetometer 93
3.2.3 MOKE microscope 94
3.2.4 HAXPES measurements 96

The objective of this thesis is to investigate the behavior of skyrmions. This includes a two-fold aim: to better understand their properties and to develop methods for controlling them. In particular, the work focuses on the electrical control of individual skyrmions via the application of a gate voltage. Achieving this requires a comprehensive understanding of both the material properties and skyrmion dynamics. Additionally, the sample geometry must be specifically designed and processed to enable a gate application.

This chapter presents the experimental techniques employed in the fabrication of the samples, as well as the characterization instruments used to investigate their properties.

The chapter is separated in two main parts: The first one describes the sample process. Starting from the description of the deposition technique of the Ta/FeCoB/TaOx tri-layer. The fabrication process for preparing samples suitable for gate voltage application will also be described.
The second part focuses on the different characterization techniques and instruments used to study the sample and image the skyrmions.

3.1 Sample fabrication

3.1.1 Tri-layer deposition

The tri-layer system is grown using on- and off-axis magnetron sputtering on a Si/SiO_2, 100 mm-diameter substrate.
Magnetron sputtering is a physical vapor deposition (PVD) technique used to grow thin films. The material to be deposited, referred to as a target, is fixed to a cathode within a chamber. A negative high DC voltage is applied between the cathode and the anode in the chamber filled with Argon gas, creating a plasma state. The high-energy ions composing this plasma are propelled toward the cathode, they will then reach the target and transfer their energy to the target's atoms. These atoms are then ejected, travel in the vacuum environment of the chamber and finally are deposited on the substrate.
Two geometries can be considered inside the chamber depending on the desired form of deposition. The first one, called the on-axis sputtering technique, is used to achieve uniform deposition, specifically for the bottom Ta layer in our sample. The figure 3.1 illustrates the On-axis geometry deposition of the magnetron sputtering technique. In this case, the target and the substrate are aligned to their center. A variation of 2 to 5% thickness can be observed on the edge of the sample with a diameter of 100 mm.

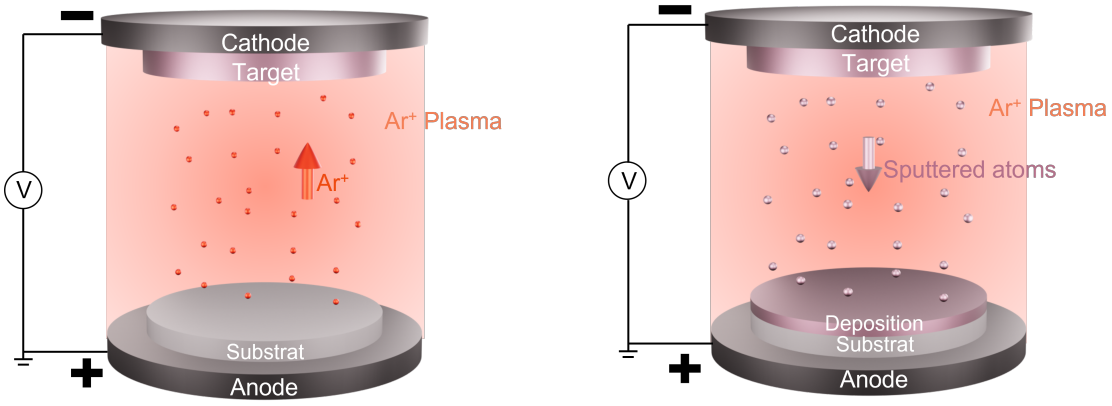

Figure 3.1: *On-axis magnetron sputtering technique:* (a) In the chamber the substrate (in light gray) is aligned with the target (in pink). A high DC voltage is applied in between the anode and the cathode creating an Ar^+ plasma (in light orange). High energy Ar^+ ions move toward the target. (b) It results in the expulsion of target's atoms that are deposited on the substrate uniformly.

The second geometry, namely the Off-axis deposition technique, consists of intentionally misaligning the sample with respect to the target, resulting in non-uniform thickness along one axis of the sample. This geometry is schematized in the figure 3.2.

We used this technique to obtain thickness gradient in our samples. When the target is bombarded by plasma ions, its atoms are ejected in different directions, forming a cone-shaped deposition zone. By adjusting the position of the sample to be deposited with respect to the

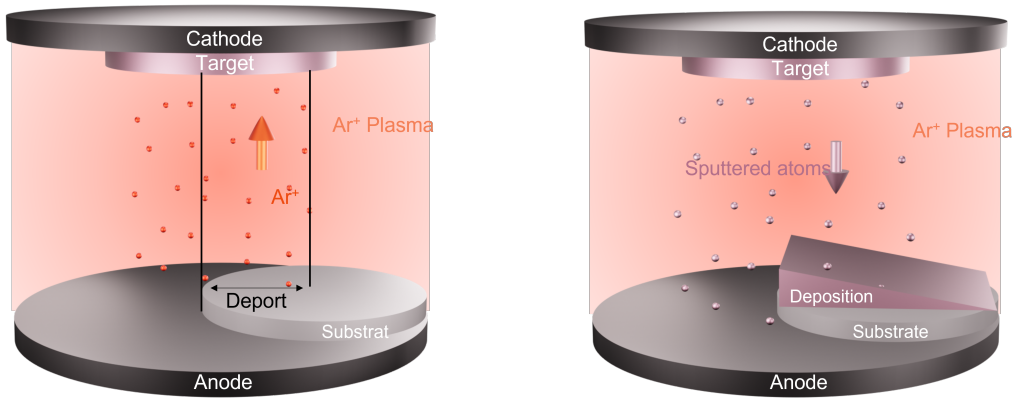

(a) (b)

Figure 3.2: *Off-axis magnetron sputerring technique:* (a) In the chamber the substrate (in light gray) is mis-aligned with respect to the target (in pink) of a distance called deport. A high DC voltage is applied in between the anode and the cathode creating an Ar^+ plasma (in light orange). High energy ions Ar^+ moved toward the target. (b) it results in the expulsion of target's atoms that are deposited on the substrate following a cone-shape deposition zone, leading to gradient deposition on the substrate.

center of this deposition zone we can play on the gradient of the wedge. As shown in the figure 3.3 within this cone, the thickness of the deposited layer follows the path of the thick pink line: it remains constant near the center and linearly decreases as the deport increases.

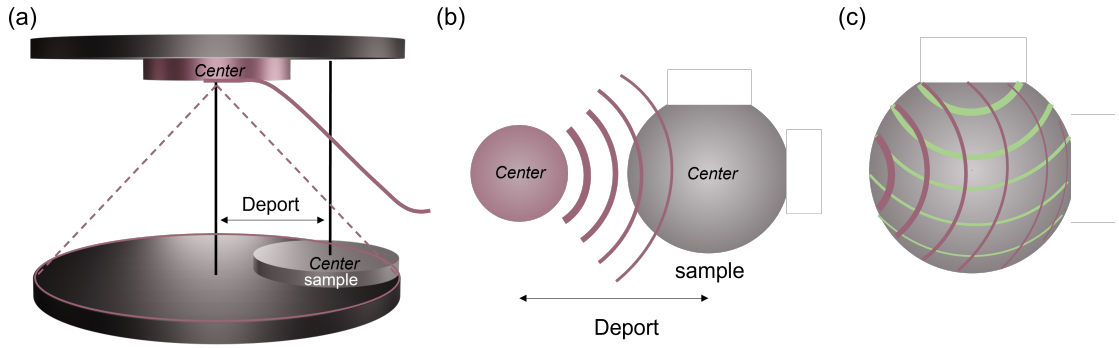

Figure 3.3: (a) 3D Scheme of Off-axis deposition technique. The sample is misaligned with respect to the target by a value "deport". The dotted line represents the conical deposition distribution and the thick pink line represents the thickness of the deposited layer with respect to deport (b) Top view of the off-axis deposition, pink lines represents the iso-thickness lines and (c) Is the resulting deposition for both wedge in the x and y direction. Colored lines represent the iso-thicknesses of both material on the sample.

Due to the cone-shaped deposition profile, the thickness remains constant along circular paths centered on the deposition axis. The green curve in figure 3.4 shows the distribution of the deposition. The red curve represent the linear approximation used to estimate the thicknesses of the materials on the wafer. The figure 3.5 shows the normalized difference between the

approximation and the deposition. The error in the thickness value is estimated to 5% in the edge of the sample and decreases to 1% at 1.5cm of the edge.

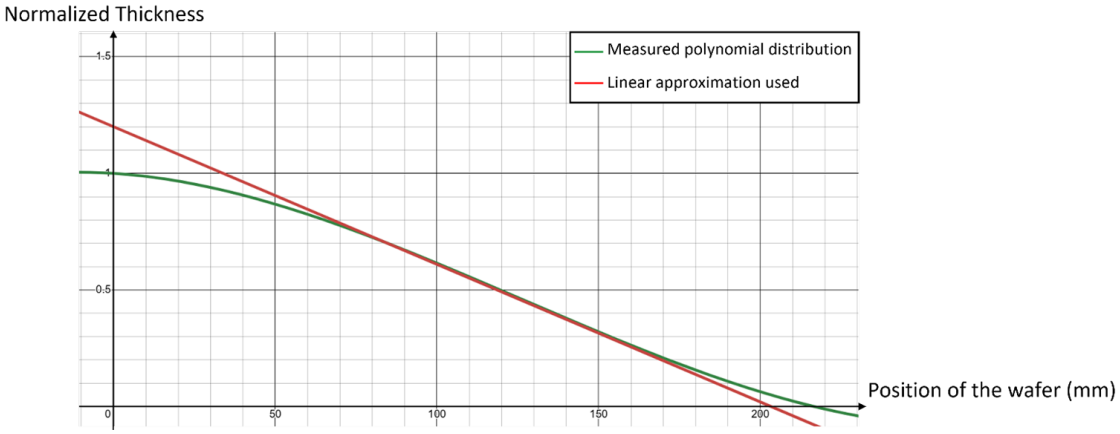

Figure 3.4: Variation of thickness deposited on an off-centered wafer. Position 0 corresponds to the center. Red line is the fit used for reconstructing remanence maps while green curve is the XRR characterized variation.

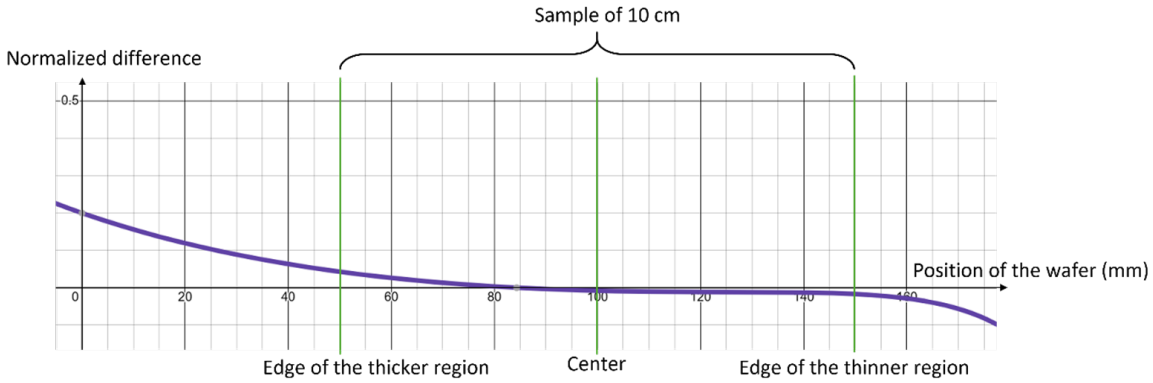

Figure 3.5: Normalized difference between the linear approximation and the measured deposition distribution. The wafer, of 10 cm width, is center at 100 mm in the x axis.

In our sample, we applied this principle to deposit gradient of thickness on two layers. The sample is turned by 90° in between the deposition of each layer in order to have one gradient perpendicular to the other. We take the convention that the FeCoB thickness varies along the x-axis meanwhile the top Ta thickness is along the y-axis as shown in the figure 3.6(b) and (c). The FeCoB target composition is $Fe_{72}Co_8B_{20}$. Finally, the top Ta layer is oxidized by exposition to oxygen in a treatment chamber, at a pressure of 150 mbar during 10 seconds, represented by the pink layer in the figure 3.6(d). This step is performed to break the symmetry of the two interfaces Ta/FeCoB and FeCoB/TaOx and therefore to cancel the annulation of the two opposite DMI contributions, as we have seen in the section 1.2.1. Indeed, the oxidation of the top layer associated with the geometry of the deposition in a wedge leads to three different oxidation states at the top interface named under-oxidized (FeCoB/Ta/TaOx),

optimally oxidized (FeCoB/TaOx), and over-oxidized (FeCoB/FeCoBOx/TaOx), as illustrated in the figure 3.7.

To prevent oxidation of the samples a capping layer of 0.5 nm of aluminum *Al* is deposited, at the end, using the on-axis sputtering technique and subsequently oxidized at air.
An annealing step is then performed under secondary vacuum at 225°C for 30 min to increases the interface quality and thereby trigger PMA, as it has been shown in [45], [131].

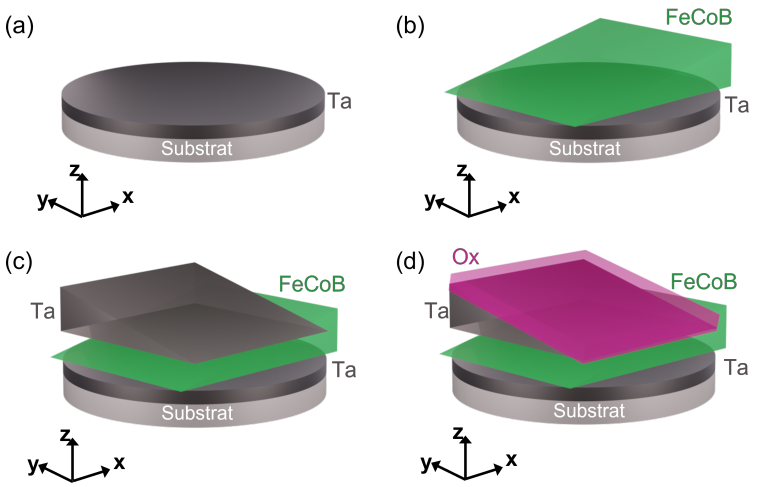

Figure 3.6: *Scheme of the deposition of the tri-layer system step-by-step:* (a) Uniform deposition of the bottom Ta layer using On-axis sputtering. (b) First gradient, of FeCoB (in green), along the x-axis using the Off-axis geometry. (c) Second gradient, of the top Ta layer, in the y direction. (d) and finally the uniform oxidation step of the top Ta layer.

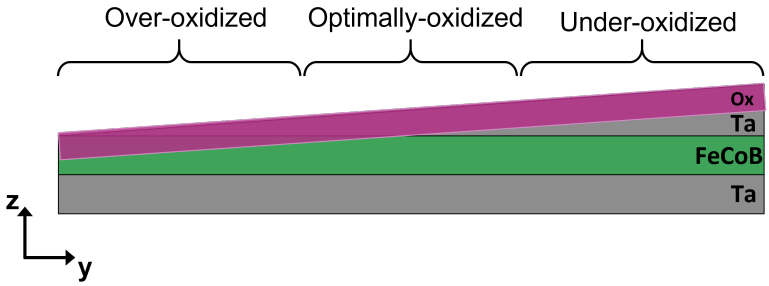

Figure 3.7: (*Figure adapted from the PhD manuscript of Ch-E. Fillion*) Schematic cross-section of the tri-layer system along the y-axis for a given FeCoB thickness. Following the oxidation step, the wedge-shaped deposition of the top Ta layer results in three distinct oxidation states: over-oxidized (where the FeCoB layer is also oxidized), optimally oxidized (corresponding to the Ta/FeCoB/TaOx tri-layer), and under-oxidized (where the top Ta remains non-oxidized at the FeCoB interface).

3.1.2 Patterning process for gate voltage control

All the depositions of the tri-layer has been performed by S.Auffret and J.Faure-Vincent. The ALD deposition step has been performed in collaboration with S.Pizzini in Institut Néel. The deposition of the dielectric layer has been performed in the BCAi clean room by V.Bolcato.

To study the effect of voltage gating on skyrmion, the sample must be modified through several processing steps. The goal is to fabricate capacitor-like devices that allow the application of an electric field in the out-of-plane (z) direction across the tri-layer system previously described in 3.1.1. This process has been developed in Néel Institute by Anne Bernand Mantel and has been used by three former PhD students in the team, Marine Schott, Titiksha Srivastava [132] and Charles-Elie Fillion [27]. In addition to their work and with the aim to be able to detect and control a single skyrmion we developed a new geometry of deposition of our tri-layer and of the gate pads. The complete fabrication process is described below and schematized entirely in the figure 3.8. It consists of three main steps: 1- micropatterning of the tri-layer system in tracks, 2- Atomic Layer Deposition (ALD) of an insulating layer, 3- micropatterning of the pads used to applied the gate voltage.

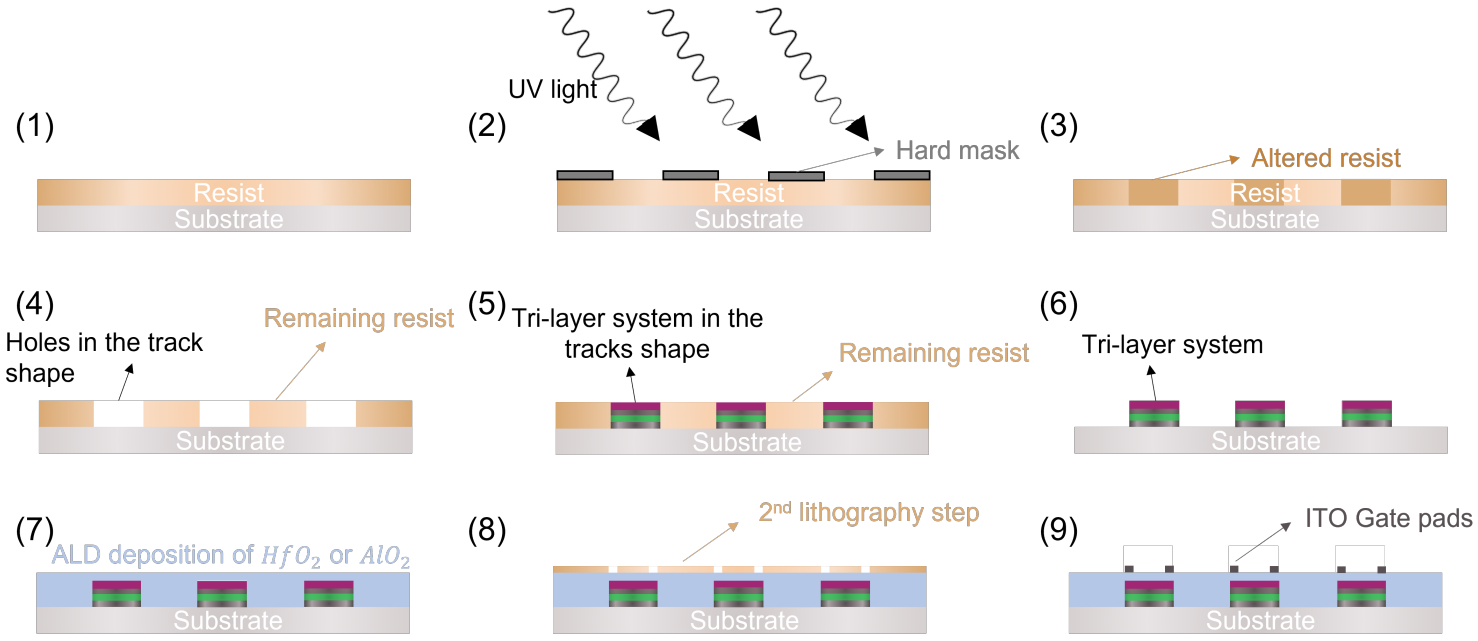

Figure 3.8: *Scheme of the process of the sample describe step-by-step:* (1) Deposition of the resist, (2) Illumination fo the sample through a hard mask, (3) The resist is altered, (4) Development, the altered resist disappear, (5) deposition fo the tri-layer system in the shape of the crosses, (6) Lift-Off, the remaining resist is removed, (7) ALD deposition of $Hf0_2$ or ZrO_2, (8) 2nd lithography with the shape of the gate electrodes and (9) Deposition of ITO and lift-off.

Micropatterning of the tri-layer system

The first processing step is to deposit the trilayer system in a specific geometry made specifically for the control of a single skyrmion. The diameter of the skyrmions studied are $\sim 2-3\mu m$, therefore, we designed a track of $5\mu m$ width in order to stabilize a single skyrmions inside and to avoid as much as possible the edge effects. To do so we use a standard UV-lithography process. The whole principle of laser lithography is schematize in the figure 3.8 from steps (1) to (4). A layer of photoresist is first deposited using a spin-coating technique. We deposit few drops of the product on the sample that then starts to rotate at 4000 rpm (rotation per minute) assuring a uniform deposition of the photoresist over the whole sample with a thickness of $\simeq 1.2\mu m$ as shown in the figure3.8 (1). The sample is then placed on a hot plate at 100°C during 60s to dry the photoresist. The next step is to illuminate the sample through a chromium mask, step(2) in the figure 3.8.

This mask is there to illuminated the sample in precise location of the sample in order to "draw" the needed geometry, shown in the figure 3.9. This represents the design of one cross where the tri-layer system will be deposited, thousands of it are actually designed in the mask. By illuminating the photoresist the light is modifying its molecular structure (step (3) of the figure 3.8).
In the next step, which is the development step, we immerse the sample into a developer. If the resist used is positive (resp.negative) the illuminated parts are dissolved (resp. remains). In our fabrication process we used a positive resist, called AZ 5214E that we invert to become a negative one by illuminating a second time the sample without mask. Holes in the form of the wanted tracks are then patterned, the result is shematized in the figure 3.8 (4).
The tri-layer system described in the previous part is then deposited inside the patterned tracks step (5) in the figure 3.8. The next step is the lift-off, the sample is immersed inside a solution that is dissolving the remaining resist on the sample. Only the tri-layer system patterned in tracks shape remains on our sample. This is illustrated in the figure 3.8 step (6).

Atomic Layer Deposition (ALD) of an insulating layer

The second step of the process is the deposition of an electric insulator/ ionic conductor, a critical step to apply the gate voltage. This step is performed using Atomic Layer Deposition (ALD) technique. ALD deposition is used to grow ultrathin-film thanks to the very good precision on the layer thickness, in the order of the Å or the monolayer scale depending on the material deposited. For this technique the sample is placed in a chamber under vacuum. As an insulating layer we used HfO_2 or ZrO_2, a metal precursor containing hafnium (Hf) or zirconium (Zr) is then introduced into the reaction chamber. The precursor molecules chemically adsorb onto the substrate surface forming a monolayer. The excess precursor is then removed by purging with an inert gas (Argon). A reactant (oxidant) is introduced to convert the metal precursor into metal oxide (HfO_2 or ZrO_2), we used water vapor (H_2O). This cycle is then repeated the number of times needed to obtain the wanted thickness of material, which, in our case, is 20 nm. The result is schematized in the figure 3.8 (7).

Micropatterning of the Indium Tin Oxide (ITO) pads to apply the gate

The final step of our process is the patterning of the ITO transparent gate electrodes used to apply the gate while observing the change in skyrmion behavior. The design is represent in the figure 3.9 by the purple region.
This step is exactly the same than for the tri-layer system, holes in the shape of the electrodes are patterned using the UV lithography technique, with the same resist and same process. The figure 3.8 steps (8) and (9) are showing the completed process of a sample.

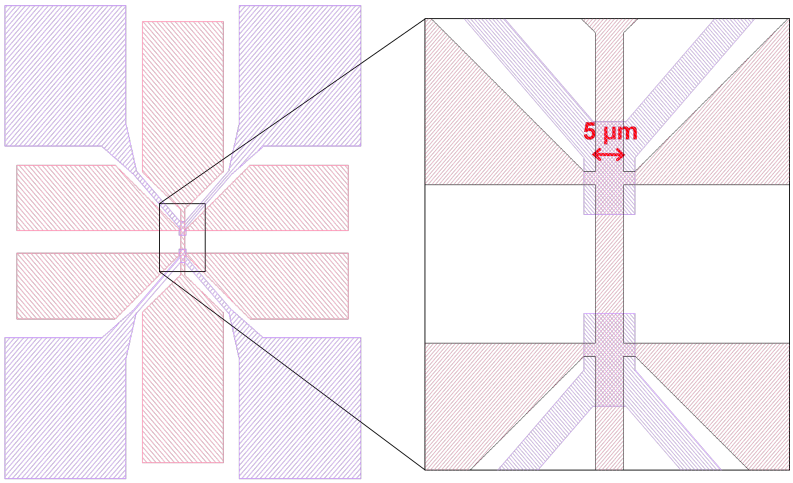

Figure 3.9: Full layout of one Hall cross device. The tri-layer Ta/FeCoB/TaOX is deposited following the pink geometry. The Indium Tin Oxide gate pads are deposited in the geometry of the purple regions.

3.2 Characterization Techniques

Once the magnetic samples are fabricated, different techniques can be used to study and characterize their magnetic properties. More specifically, we measure the magnetic response of the sample and we optically observe the magnetic textures and their behaviors under current. These studies and measurements are possible thanks to the Magneto-Optic Kerr Effect (MOKE).

3.2.1 Magneto-Optical Kerr Effect

The Magneto-optical Kerr Effect (MOKE) is based on the interaction between light and the magnetization. This effect is the change of either the polarization, ellipticity and/or intensity of light when it is reflected from the surface of a magnetic material. The measurements consist in sending a linearly polarized laser beam onto the magnetic sample with a certain angle α with respect to the normal direction to the sample. The reflected light is then analyzed to determine the change in polarization produced by the interaction between the laser and the local magnetization.
There are different configurations of the MOKE depending on the direction of the magnetization of the sample with respect to the incident laser. They are illustrated in figure 3.10:

1 - Polar : Corresponding to the figure 3.10(a). In this case the magnetization M is perpendicular to the sample surface but parallel to the plane of incidence. The reflected light undergoes rotation (Kerr rotation) and ellipticity (Kerr ellipticity) due to the interaction with the out-of-plane magnetization.
2 - Longitudinal : The case figure 3.10(b). Here M is parallel to the sample surface and parallel to the plane of incidence. It causes both Kerr rotation and ellipticity, but the magnitude of the effect is usually smaller compared to polar MOKE.
3 - Transversal : Illustration figure 3.10(c). The magnetization is parallel to the sample surface and perpendicular to the plane of incidence. The relectivity is modified, unlike polar and longitudinal MOKE, transverse MOKE does not induce Kerr rotation. Instead, it modifies the intensity of the reflected light due to changes in reflectivity.

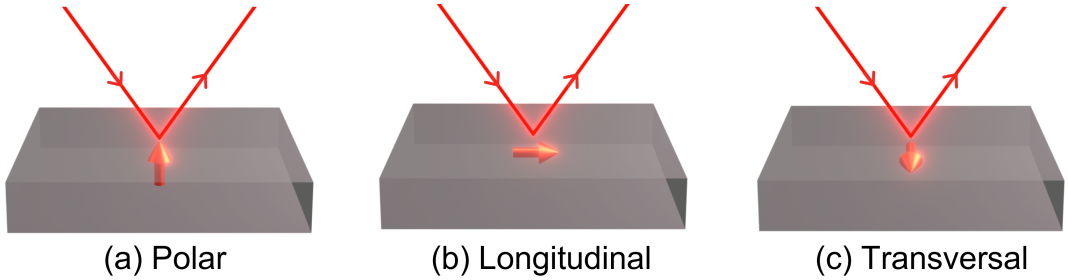

Figure 3.10: Scheme of the different configurations for the Magneto-Optic Kerr Effect. Thick red arrow represent the magnetization of the sample. Thin red lines show the laser path

3.2.2 MOKE magnetometer

The MOKE magnetometer is a powerful tool for studying the magnetic properties of materials, operating based on the Magneto-Optical Kerr Effect. We use the NanoMOKE3 by Durham Magneto Optics Ltd, that provides automatic mapping. A laser beam passes through a polarizer before being directed onto a magnetized sample subjected to an external magnetic field. After reflection, the beam passes through an analyzer that detects changes in polarization induced by the sample's magnetization. Finally, the laser reaches the photo detector, which measures the Kerr rotation and ellipticity With an incident angle of 45°, the setup is sensitive to the three Kerr effects (polar, longitudinal, and transverse) depending on the magnetization orientation.

Based on the Kerr rotation measurement, the MOKE magnetometer automatically records hysteresis loops, M(H), for a perpendicular external magnetic field. The figure 3.11 presents the three types of hysteresis curves that we can obtain by MOKE measurements. In (a) we see a noisy signal with negligible magnetization and no saturation. This characterized the paramagnetic state for which no magnetic signal is detected. Meanwhile, the hysteresis curve (b) displays a typical square hysteresis loop characteristic of the perpendicular magnetic anisotropy region, with a well-defined square shape, clear magnetization saturation, a large coercive field H_c and normalized remanence close to 1. Finally, the hysteresis curve (c) exhibits a S-shaped hysteresis loop with a smooth progression toward the saturation associated with a small coercive field H_c characterizing an in-plane anisotropy. A high magnetic field is required to reach the saturation

due to the strong demagnetizing field opposing the perpendicular alignment, and the in-plane anisotropy resisting the out-of-plane orientation. A low remanence is also a notable feature, indeed after removing the field, the magnetization tends to align in the plane.

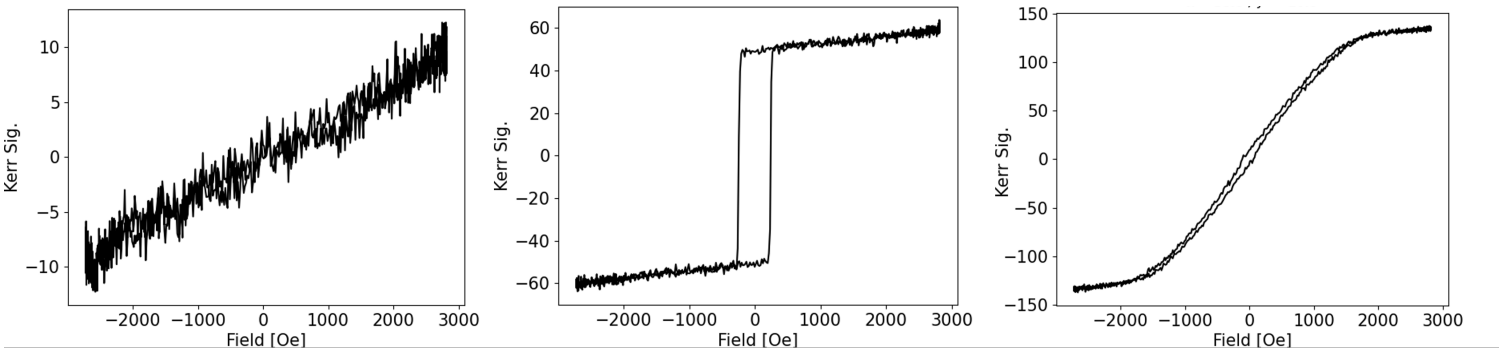

(a) Paramagnetic (b) Perpendicular Magnetic Anisotropy (c) In PlaneAnisotropy

Figure 3.11: Example of hysteresis curves obtained with the MOKE magnetometer for (a) a paramagnetic state, (b) the region with perpendicular magnetic anisotropy and (c) the in-plane anisotropy region. A correction factor of 1.727 maybe needed to apply on the measured coercive field, due to the small parasitic in-plane component of the external field coming from the coil.

Hysteresis curve are recorded on a grid with a spacing of $2mm$ in our cases, enabling the reconstruction of a spatial map for the measured magnetic properties such as the coercive field, saturation magnetization, and remanence. These spatial maps are then converted into thicknesses map. Indeed, due to the geometry of the deposition the iso-thickness lines follow a circle. The figure 3.3 illustrates this phenomenon. In the off-axis geometry, the sample is deliberately misaligned with respect to the target by a certain distance, referred to here as the "deport." As a result, the deposition follows a conical distribution, illustrated by the pink dotted line in the figure. As discussed in the section 3.1.1, it is necessary to convert (x,y) coordinates into a couple of thicknesses (t_{FeCoB}; t_{Ta}). The calculations necessary to achieve it are detailed in the supplementary 9.1. This will leads to a deformation of the (x,y) map as illustrated in the figure 3.12.

3.2.3 MOKE microscope

A second tool based on the magneto optical Kerr effect is the polar MOKE microscope. Based on the same physics, the MOKE microscope allows, in addition of recording hysteresis curve, the optical imaging of the magnetic textures such as domains or skyrmions.

The source of light is a red LED, with a wavelength of $\sim 630nm$. The light first passes through a polarizer to ensure it is strictly linearly polarized. Diaphragms and optics are put on the way to control the the amount of light and orientate it into the objectives lens that is used to focus the beam onto a small spot on the sample, allowing high-resolution imaging. The sample is lying on a motorized stage on top of a coil to apply a controlled perpendicular magnetic field to the sample during observation. After reflection on the sample, the light passes through another polarizer (thus used as an analyzer), with a polarization axis almost perpendicular to

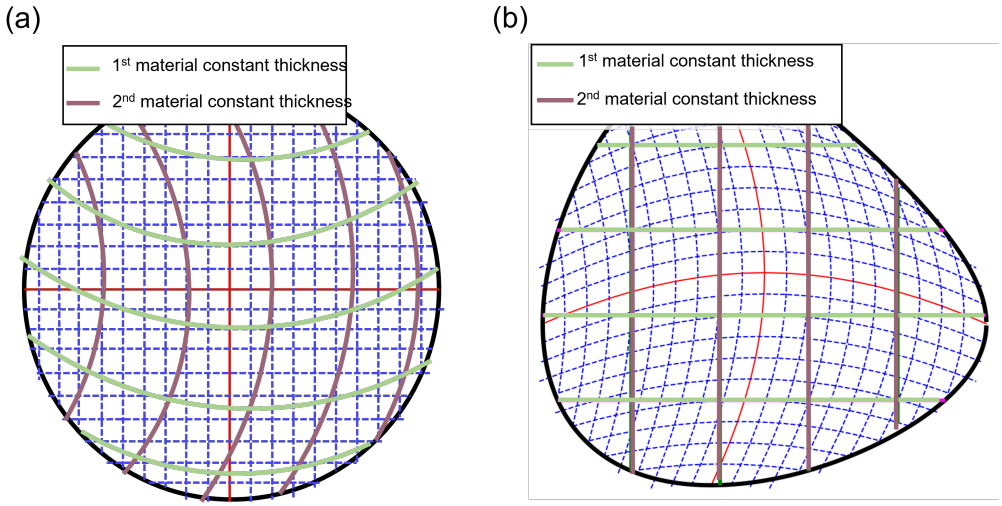

Figure 3.12: *Figure based on the PhD manuscript of Ch-E. Fillion:* Schematic representation of the sample showing iso-thickness lines for the two deposited materials, highlighted in pink and green. In (a), the lines are shown in the (x, y) spatial plane, where they appear circular due to the deposition geometry. In (b), the same lines are represented in the (t_{FeCoB} ; t_{Ta}) thickness space, where they appear linear, although the sample geometry is distorted.

the first polarization axis in order to convert small Kerr rotations into intensity variations. A CCD camera captures the image formed by the reflected and analyzed light. The operation is schematized in the figure 3.13(a).

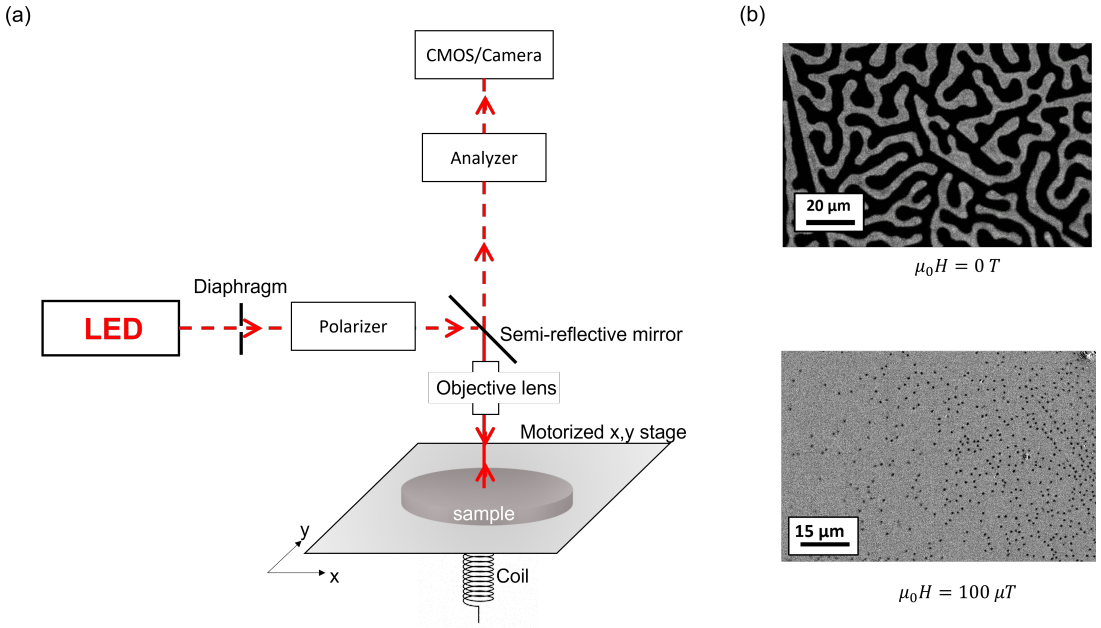

Figure 3.13: (a) Scheme of the operation of the MOKE microscope. The red line represents the path of the light.(b) Example of a MOKE differential image of domain walls (top) and skyrmions (bottom).

For the measurements, depending on the local magnetization, the reflected light experiences a slight rotation. The analyzer translates these small changes into changes in light intensity. The camera records the resulting image: areas with different magnetization directions appear as different brightness levels (contrast). By sweeping an external magnetic field, one can also record hysteresis loops locally or image dynamic domains or skyrmions motion by differential images. For such images, first the magnetization is saturated and a reference image is acquired. As the external magnetic field is varied, changes in the magnetization direction occur. By subtracting the reference image from subsequent images, magnetic contrast is generated. The figure 3.13(b) presents an example of the optical image of domains (top) and skyrmions (bottom) obtained using MOKE.

During our studies on domain walls and skyrmions we also used current and voltage sources in order to inject current and apply a gate. The sample is glued on a sample holder. This latter is then connected to the Keithleys where we control the injection of current and voltage. Typically we inject a current of $\sim$ hundreds of μA that corresponds to a current density in the order of the GA/m^2 and a gate of $\sim$ few V. Microbonding technique is used to connect the sample to the sample holder

3.2.4 HAXPES measurements

During my thesis I participated to a synchrotron run in Synchrotron SOLEIL - CNRS - CEA Paris-Saclay. The project was led by S. Pizzini from Institut Néel. We performed hard x-ray photoelectron spectroscopy (HAXPES) measurements supervised by the beamline manager J-P.Rueff and the beamline scientist D.Ceolin.

X-Ray Photeoelectron Spectroscopy (XPS) is a powerful technique used to analyze the chemical composition or the electronic structure of the surface of a large variety of materials. The physics is based on the photoelectric effect. The sample is irradiated with X-Rays, these photons will then eject core-level electrons from the atoms of the material. The kinetic energy of the emitted photoelectrons is measured and finally the binding energy is calculated. An XPS spectrum typically shows peaks corresponding to core-level electrons. The analysis of the energy, shape, and area under each peak gives information on the element via the binding energy, the oxidation state if small shifts in the energy is observed or if the shape of the peak is changed and finally it can also give information on the concentration of chemical species.
The information depth of XPS is determined by the inelastic mean free path (IMFP) of the photo-excited electrons in the material. Typically the minimum of IMFP corresponds to kinetic electron energies between 40 and 100 eV. This kinetic electron energy is defined in XPS measurements by the photon energy, generally of the order of $10^2 - 10^3$ eV, which gives rise to an information depth in the order of a few tens of Å. XPS is then mostly used to study surfaces.

To have information on bulk or interfaces the energy of the used photons has to increase in order to have a higher kinetic electron energy. Based on the exact same principle as XPS, HArd X-Ray PhotoElectron Spectroscopy (HAXPES) measurements use higher photon energy values. Generally of synchrotron radiation sources, this allows the ejection of core-level electron

coming from the bulk or interfaces situated below a layer or more of material. The IMFP of these electrons is also increased, allowing them to be fully ejected of the sample and reach the detection sensor. Figure 3.14(a) illustrates the principle of X-Ray spectroscopy and Figure 3.14 shows an example of spectrum that we can obtain. We can see in this example the $2p_{1/2}$ and $2p_{3/2}$ peaks of Co and CoO measured with X-Rays with $h\nu = 9keV$ at SOLEIL.

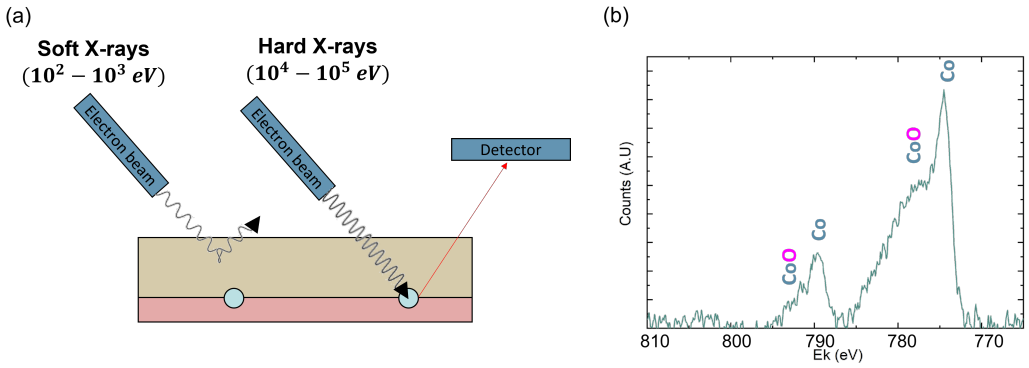

Figure 3.14: (a) Sketch representing the X-Ray Photoelectron Spectroscopy comparing low ($10^2 - 10^3$ eV) kinetic energies of the emitted photo-electron and high ($10^4 - 10^5$ eV) values corresponding respectively to the XPS and HAXPES type of measurement. The light blue dot represent the atoms and the red arrows are the ejected core-level electrons. (b) Example of a resulting Co 2p spectrum from a HAXPES measurement with 9 keV x-rays at GALAXIES beamline in SOLEIL synchrotron, the background has been substracted. The measurement is made on a CO layer burried below 5nm of HfO_2.

We performed measurements using HAXPES technique to measure the oxidation state of gated Co/AlOx interfaces, that are buried below 5nm of HfO_2 and 3 nm of Pt, study detailed in the section 5.

Part III

Results

Chapter 4

Material dependence of the DMI sign

4.1 Introduction 101
4.2 Experimental Observation 101
4.3 *Ab initio* study 107
4.4 Conclusion 114

4.1 Introduction

To fully harness the potential of skyrmions, precise control and a comprehensive understanding of their behavior are essential. We are studying a weak-DMI system where skyrmions are stabilized by dipolar energy and have a characteristic size in the micrometer range. Due to the low DMI amplitude, even a slight change in the materials can reverse the DMI sign, thereby controlling skyrmion chirality. That is why a deep understanding of the DMI mechanism and its characteristics in our sample is crucial.

This chapter presents a complete study of the DMI in the tri-layer system Ta/FeCoB/TaOx presented in detail in 3.1.1. In the first section, we will explore the measurement of the DMI sign and the corresponding DMI sign map. The second section will cover the *ab initio* calculations of the DMI, together with a comparison with the experimental results. Lastly, we will go into the phenomena responsible for the observed reversal of the DMI sign.

4.2 Experimental Observation

Previous studies [51] on this system found a reversal of the chirality of skyrmions in two distinct regions, as discussed in the section 2.1.2. Figure 4.1 presents the remanence map of the system. In the previous section, we described the deposition of the Ta/FeCoB/TaOx tri-layer system using a double wedge configuration, with the two wedges deposited perpendicular to each other. This arrangement results in variations of the magnetic properties along the directions of both wedges. The nanoMOKE measurements are useful to study this change in magnetic properties. The figure 4.1(a) presents an example of a remanence map obtained for the tri-layer. The hysteresis curves in the figure 4.1(b) are plotted for a constant value of the top heavy metal

layer thickness to study the ferromagnetic wegde effect. Below a critical thickness t_{DL} the Curie temperature is below the room temperature due to size effect leading to a paramagnetic state. It is important to specify here that the paramagnetic state is also coming from the oxidation of the ferromagnetic layer which leads as well to a magnetic dead layer. With the increase of the ferromagnetic layer the Curie temperature increases and the ferromagnet is not fully oxidized, leading to the appearance of perpendicular magnetic moment and thereby out-of-plane anisotropy (PMA). The coercive field increases as well and a clear saturation state can be reached with a clear remanent magnetization. When the ferromagnet reaches the critical thickness t_c the dipolar term K_d of the effective anisotropy coefficient K_{eff} becomes greater than the surfacic term K_s leading to a transition from out-of-plane to in-plane magnetization. The hysteresis curve of the in-plane state is characterized by the S-shape curve, a lower remanence and a high field is needed to reach the saturation state.

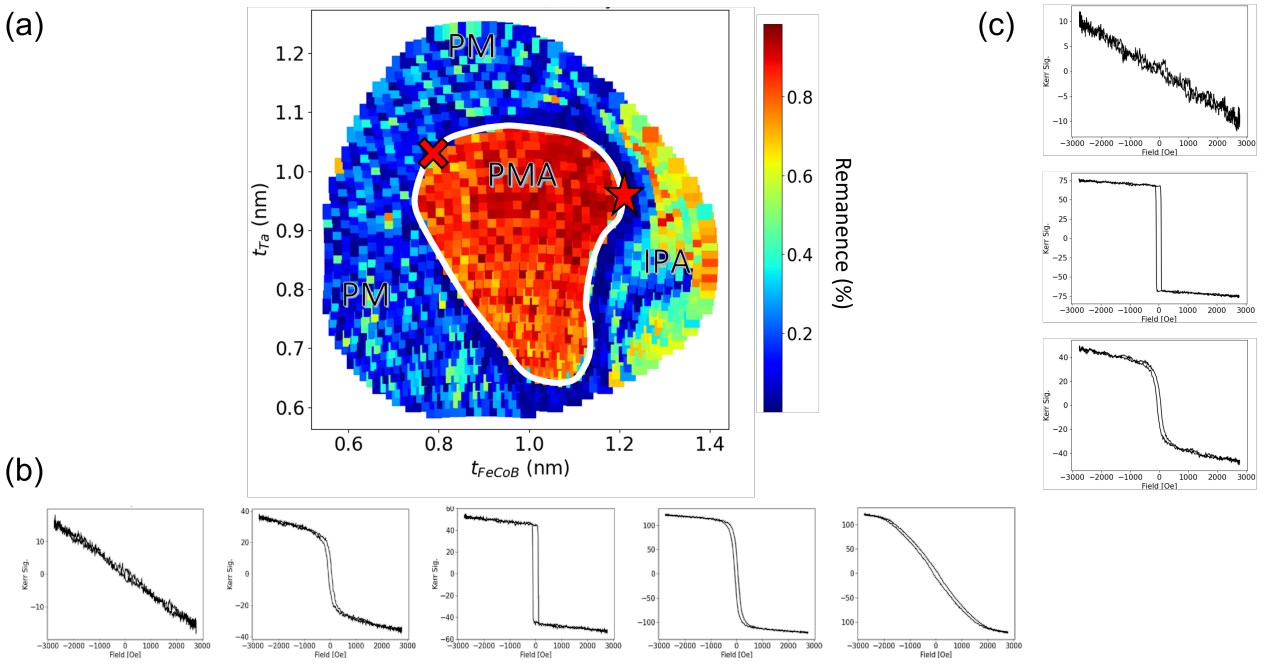

Figure 4.1: (a)Remanence map of tri-layer system Ta/FeCoB/TaOx measured by MOKE magnetometry. The perpendicular magnetic anisotropy region is displayed in orange (large remanence) meanwhile the Paramagnetic (PM) region in blue (low remanence). The transition region between PMA and PM or In-Plane Anisotropy (IPA) is represented by the white line. The chirality inversion found in [51] is depicted by the red star and cross. (b)

In the figure 4.1(c) the effect of the wedge of the top heavy metal layer, and therefore of the oxidation at the interface, is clear. Indeed, for the thicker region of the layer we clearly see that we are in a paramagnetic state, with a weak Kerr signal amplitude and no hysteresis loop. This paramagnetic state is coming from the dead layer, indeed it has been shown experimentally that the presence of Ta atoms at the interface with FeCoB leads to a decrease of the magnetic moments for Fe atoms next to Ta, leading to a magnetically dead layer, which is supported by ab-initio calculations [133], [134] and can be seen in figure 4.12. Then, by decreasing progressively the thickness of the top Ta layer an hysteresis loop starts to appear with a clear saturated

magnetization value, a coercive field and a normalized remanence value close to 1. This justifies the use of the remanence map to identify the interesting region in our sample. Indeed, we have seen in the section 1.2.2 that stabilized skyrmions appear when the anisotropy switches from Out-of-plane to In-plane or to a paramagnetic state. Finally, when the top Ta thickness becomes too thin the FeCoB layer start to be oxidized, leading again to a paramagnetic state.

The white line represents the region where skyrmions are stabilized, with the two chirality inversion points identified experimentally in [51], explained in the section 2.1.1, marked by a red star and cross. At the specific ferromagnet thickness corresponding to the inversion points, moving vertically along this map (i.e., along the top Ta gradient and thus modifying the oxidation state at the interface) leads to an inversion of the DMI sign. This suggests that the chirality, and consequently the sign of the Dzyaloshinskii-Moriya Interaction (DMI), depends on the oxidation state of the top interface. This has been confirmed by Brillouin Light Scattering (BLS) measurements in [52] but also theoretically predicted [135] and experimentally observed on a similar system (Cu/CoFeB/Ta/Ox) [50]. Secondly, the thickness of the top Ta layer differs at the two inversion points. This implies that, for a specific intermediate thickness of the Ta layer, moving horizontally along the ferromagnet gradient also leads to an inversion of the DMI sign. This suggests that the ferromagnet thickness also influences the DMI sign. This dependence has not yet been studied in detail and this phenomenon was not expected. Indeed the DMI has an interfacial origin, the thickness of the ferromagnet should, in principle, affect only its magnitude but not its sign. However, these observations suggest otherwise, indicating a potential additional contribution that requires further investigation.

To obtain a complete and comprehensive understanding of our sample, particularly the DMI sign within our system, we propose to investigate the DMI sign across the entire PMA region, beyond the two previously identified points.
To study the DMI sign within the PMA region, we employed the current induced method (CIM), as detailed in section 2.3.2. While this method does not yield a quantitative value for the DMI, it offers a significant advantage in terms of speed over techniques like Brillouin Light Scattering (BLS). In addition, BLS measurements do not have enough resolution in weak-DMI systems like this one. In this study, the exact value of the DMI is not the primary objective, rather, we focus on determining the sign of the interaction and its variation as a function of the thicknesses of the two top layers, Fe and Ta. The CIM method requires the injection of current, which necessitates the preparation of the sample. Specifically, the sample is cleaved around the region of interest, identified through a MOKE (Magneto-Optical Kerr Effect) map of the entire sample, as shown in Figure 4.2 (a). This map is constructed by assembling individual MOKE microscope images (each grey square in the figure represents a single image), which are then stitched together. The MOKE map enables us to accurately locate the region relevant to our study. This region of the sample is then cleaved and glued on a sample holder made of copper, as we can see on the figure 4.2 (b). It is therefore possible to connect the sample and the sample holder using a wire bonding machine. Sample holder being itself connected to a current generator through the connectors. The current sent is in the order of magnitude of few mA to tens of mA creating a density of current in the order of $[GA/m^2]$ in the middle of two contacts.

The direction of motion was analyzed for all white points indicated in Figure 4.2 (b). The (x, y) coordinates of each point on the sample were determined by defining the center of the

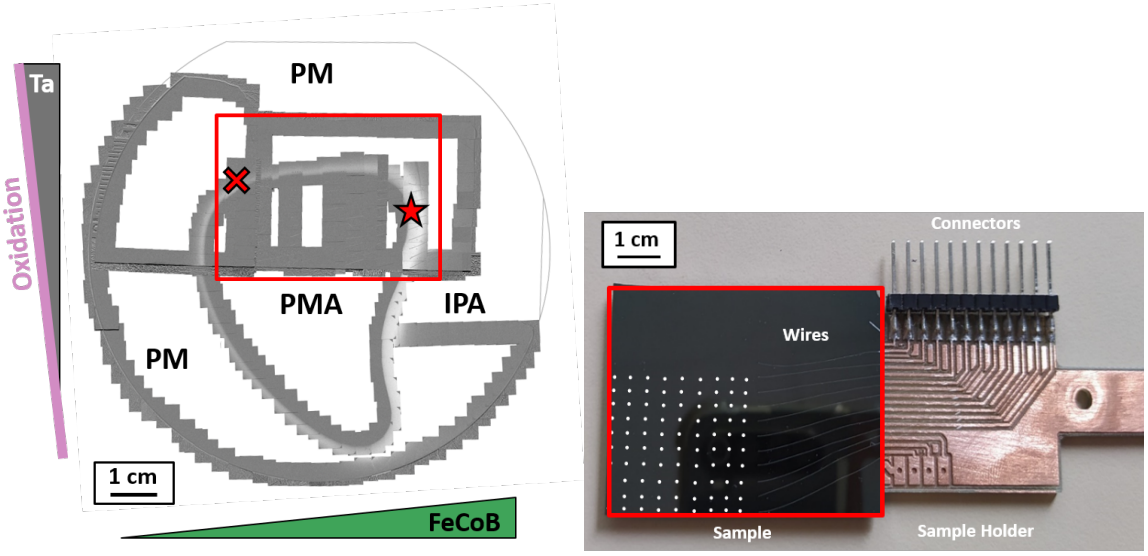

(a) (b)

Figure 4.2: (a) Assembly of MOKE microscopy images taken all around the sample and the transition region (white contrast). This type of image is taken by saturating the magnetization by applying an external perpendicular magnetic field. This saturated state is used as a background reference. The magnetic field is then progressively decreased, revealing the transition region as a contrast with the background. The red star and cross correspond to the two inversions in sign of the DMI previously found in [51]. The red rectangle represent the region of interest of our study. Region that has been cleaved and can be seen in (b) on the sample holder made of copper. In this picture, we also see the connectors allowing the connection with the current generator. The white dots on the sample represents all the points where we send current to study the motion o the domain walls.

sample as the origin, (0,0). This allowed us to generate a DMI sign map as a function of the spatial coordinates across the sample. To construct this map based on the thicknesses of both the ferromagnetic (FeCoB) layer and the top Ta layer, we converted the (x, y) coordinates into their corresponding thickness values. Since the two wedges were deposited using the off-axis technique (detailed in Section 3.1.1), a set of calculations is required to derive the thicknesses from the spatial coordinates. They are detailed in section 9.1.

The resulting map of the DMI sign as a function of both the ferromagnetic and heavy metal layer thicknesses is shown in Figure 4.3. Each square on the map corresponds to a point where current was injected to observe the motion of domain walls (DWs). On the right side of the figure, MOKE images display the DWs and their movement in response to the applied current. In the map, clockwise (CW) domain walls (DWs), moving along the current, are indicated by purple full squares, while counterclockwise (CCW) DWs, moving against the current, are represented by orange empty squares.

The intersections between the anisotropy transition (from dark grey to light grey) and the DMI sign transition (red dashed line) correspond to the thickness pairs around (t_{FeCoB}= 1.16

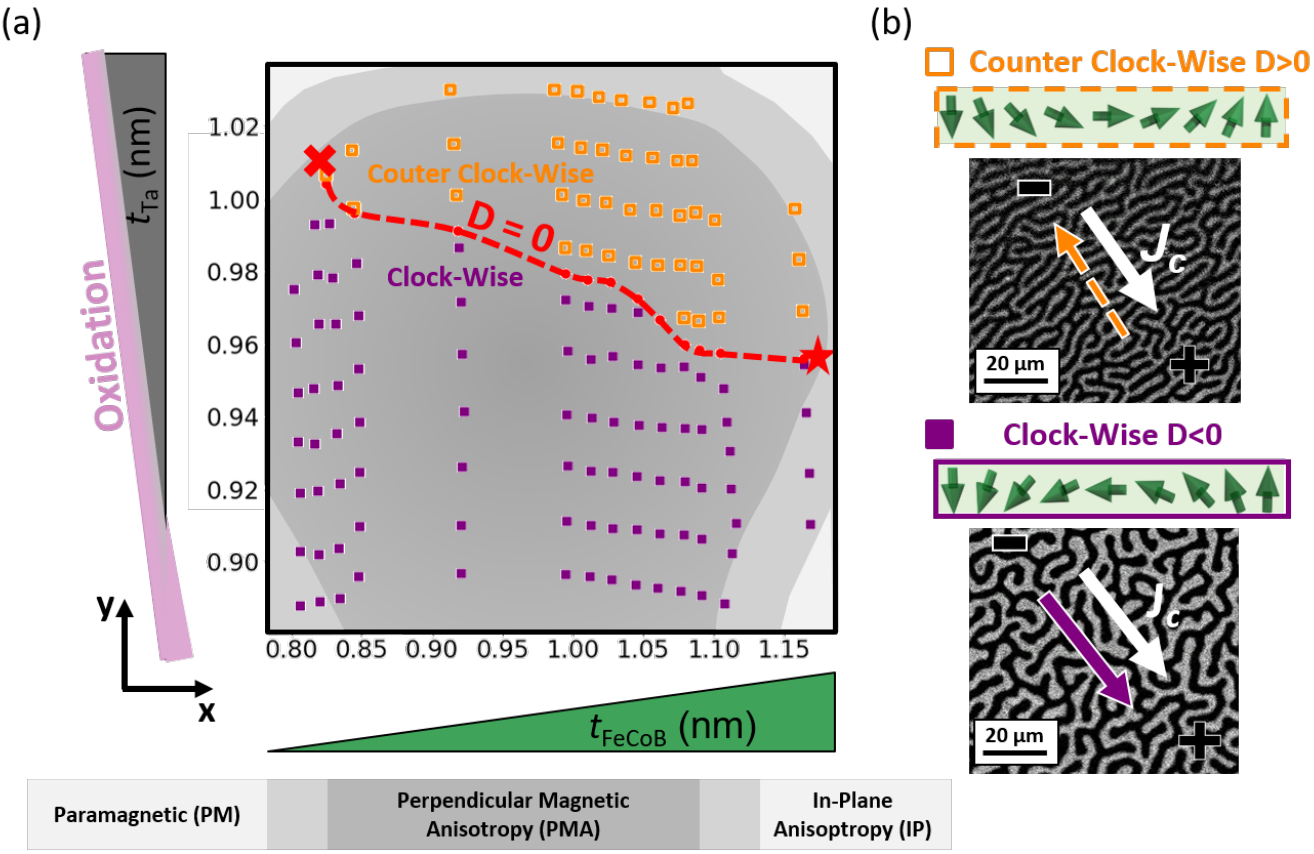

Figure 4.3: ***Left***: Map of the DMI sign overlaid on a simplified version of an anisotropy map. The dark grey region represents the area with perpendicular magnetic anisotropy (PMA). Orange squares correspond to counterclockwise (CCW) domain walls, while purple squares indicate clockwise (CW) domain walls. The red star and cross mark the previously identified DMI sign inversion points ([51]). The red dashed line connecting these points represents the DMI sign transition, where the DMI is zero. ***Right***: MOKE images showing CCW (top) and CW (bottom) domain wall motion. The blue arrows indicate the direction of the applied current, while the orange and purple arrows show the respective direction of domain wall motion.

nm; t_{Ta} = 0.96 nm) and (t_{FeCoB}=0.82 nm; t_{Ta}=1.01 nm), respectively. Previous studies, such as [51], reported variations in the thickness of FeCoB of 0.15 nm between the two intersections, and 0.05 nm for Tantalum. In contrast, our study finds a larger variation of 0.34 nm for the ferromagnetic material and the same 0.05 nm for Tantalum. The consistent variation in Ta thickness across both samples suggests stability in this parameter. However, the larger variation in ferromagnet thickness in our study may be attributed to the fact that the transition zone in our sample was centered on the wafer, while in the previous sample, it was located near the wafers edge. This difference in positioning likely introduced edge effects, altering the ferromagnetic thickness values for which the transition is happening. Also it is noteworthy that the deposition technique does not allow a perfectly reproducible system.
If we are now interested in the evolution of the DMI sign transition, depicted by the red dotted line, we can note a stair-like evolution. This may suggest that the DMI stays constant until

a certain amount of material changes. Adding or removing some atomic layers of ferromagnet seems to have an impact on the DMI characteristics even if, as said before, the DMI is of an interfacial origin.

In order to understand the phenomena leading to this DMI sign coefficient dependence with the ferromagnet thickness, we ask the Theory and Modeling group of Spintec to conduct an *ab initio* study. The figure 4.4 is presenting schematically the toy model, a similar but simplified interface, used in the *ab initio* calculation, Fe_n/Ta_m where n and m denote the number of layers for each material. To represents the change in oxidation at the interface two scenarios can be modeled. They are represented in figure 4.4(a) and (b). (a) represents the change in oxidation state while moving along the Ta gradient by changing the number of oxygen ions in the calculation. While (b) represents the change in oxidation at the interface by changing the distance of the oxygen ions from the interface. The figure 4.4(c) represents the gradient of ferromagnet by changing the number of Fe monolayers.

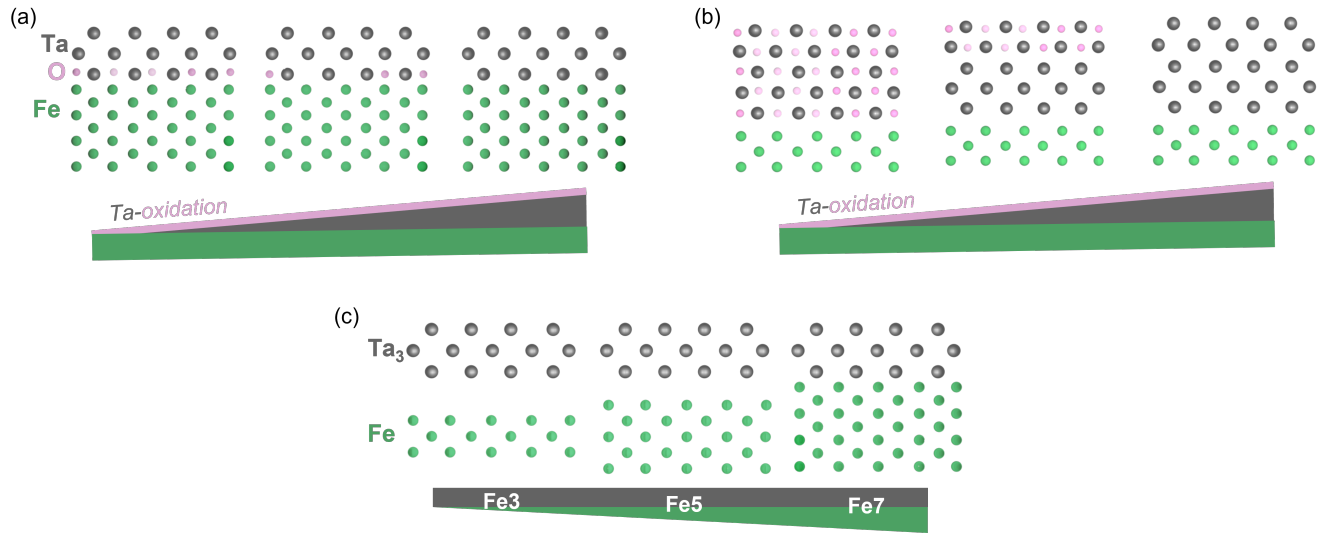

Figure 4.4: (a) The Fe_m/Ta_3 system used in the *ab initio* calculations with a decreasing number of the Oxygen atoms (pink balls) following the top Ta wedge. Ta and Fe are represented respectively by gray and green balls. (b) The Fe_m/Ta_5 system used in the *ab initio* calculations with a change in the oxygen position from the interface (c) The Fe_m/Ta_3 system for m = 3, 5 and 7, following the FeCoB experimental wedge. All figures are schematic representations; interatomic distances are not to scale and are exaggerated to better highlight the differences between the cases shown.

4.3 *Ab initio* study

All the *ab initio* calculations has been performed by Fatima Ibrahim, Libor Vojacek and Mairbek Chshiev in Spintec.

For the *ab initio* calculations the main problem is the size of the studied system. The closer from reality the better it is, but the biggest and complex the system is modeled the more time it will take to compute the calculation that is why some approximations and hypothesis have to be done. First, we can make the hypothesis, as in [51], that the DMI contribution from the bottom interface remains constant across the entire wafer, regardless of the wedge position. Since the bottom interface is the same on the wafer, it is reasonable to consider the top interface contribution as the origin of the DMI sign change. That is why in the calculation we will only compute this top interface.

As discussed in the section 3.1.1, in the experimental study the ferromagnetic layer is composed of 72% of Iron, 8% of Cobalt and 20% of Boron: $Fe_{72}Co_8B_{20}$.
It is noteworthy to say that most of the boron migrates away from the interface during the annealing step of the sample preparation. In addition, given the higher proportion of Fe relative to Co, the use of pure Fe for the *ab initio* calculation is thereby relevant.

Experimentally the oxidation rate at the interface is tuned by the wedge deposition of the top Ta layer. Meanwhile, in the calculation, TaOx is modeled by adding oxygen atoms at the interface. The wedge effect is then obtained by tuning the ratio between Ta and O atoms at the interface, as it can be seen in the figure 4.4(a) where we can see the decrease of the number of oxygen atoms (pink atoms) at the interface.

Finally, for the *ab initio* calculation, the model Fe_n/Ta_m, with n and m the number of layers for each material respectively, is chosen to represent the top interface of the experimental tri-layer system.

The number of Ta modeled monolayers is also interesting to note. As we can see in the figure 4.5, where the DMI has been calculated for two systems Fe_7Ta_3 and Fe_7Ta_5, the number of Ta mono layers does not impact the overall behavior of the DMI coefficient sign. The study has then been done with 3 monolayers of Ta when the oxidation change is modeled by a change in the number of oxygen atoms at the interface and on 5 monolayers when the calculations are done while changing the distance from the interface of the oxygen atoms.

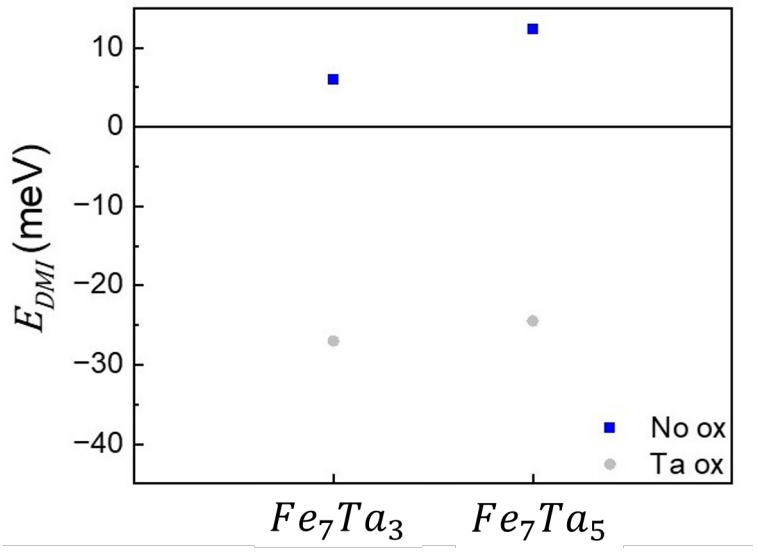

Figure 4.5: DMI energy of both system Fe_7Ta_3 and Fe_7Ta_5 for both oxidized (gray points) and non oxidized (blue points) Tantalum.

In this study, the Dzyaloshinskii-Moriya interaction (DMI) energy was calculated using constrained spin-spiral supercell method [136], [137], [138] of the Vienna Ab initio Simulation Package (VASP) [139]. The Fe/Ta interface is modeled by a supercell of three monolayers Ta on top of Fe with varied thickness from three to nine monolayers followed by a sufficient vacuum layer of 20 Å. The atomic coordinates are relaxed in the out-of-plane direction, with the in-plane parameter fixed to the bulk Fe, until the forces became smaller than 1 meV/Å. Then, the system is forced first into a CW and then in a CCW configuration. This process provided the respective energies for both chiralities. The DMI energy was then obtained by calculating the difference between the two energies, as described by the following expression:

$$E_{DMI} = E_{CW} - E_{CCW} \tag{4.1}$$

With,

$$d_{tot} \propto E_{DMI} \tag{4.2}$$

Let's study both scenarios to change the oxidation state at the interface:

1- Number or oxygen atoms in the interfacial Ta monolayer:

A preliminary investigation into the influence of both bulk and interfacial Ta oxidation on the DMI sign reveals that oxidizing only the interfacial Ta layer (Ta_1) is sufficient to affect the DMI. As shown in figure 4.6, the gray star indicating the case where only the first Ta layer at the interface is oxidized, the resulting DMI energy is very similar to the case where all the Ta layers are oxidized (left case in 4.6 represented by an empty triangle). Notably, the most significant change in DMI energy occurs when oxygen atoms are introduced in the third Ta monolayer from the interface, at which point the sign of the DMI energy changes. Beyond this, the DMI energy converges to a value comparable to that of the non-oxidized case. This observation indicates that the primary contribution to the DMI originates from the first 2 Ta or TaOx layers at the interface. Additionally, it highlights the relatively minor influence of Ta thickness and the oxidation of Ta layers beyond three monolayers from the interface.

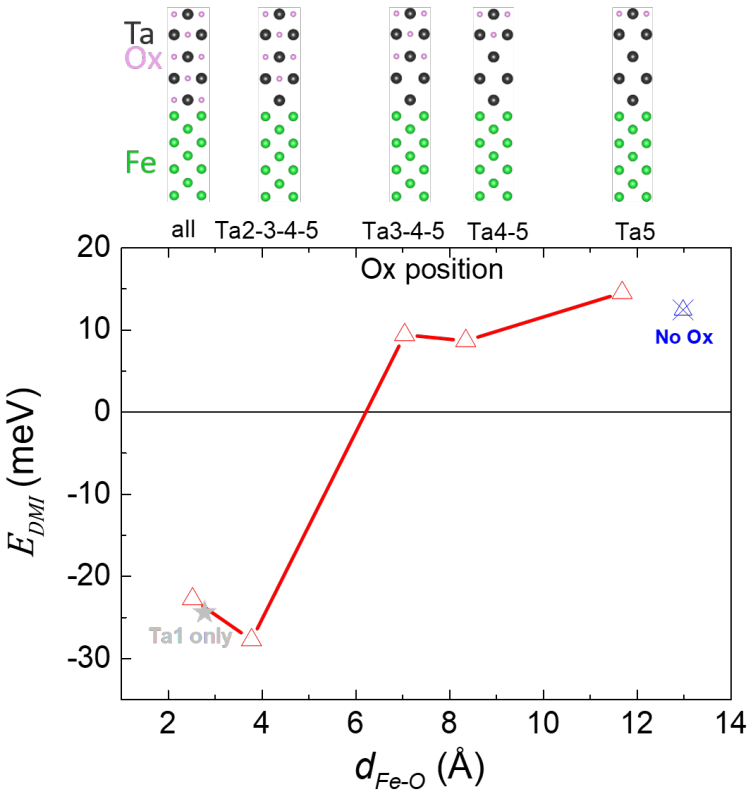

Figure 4.6: Energy of the DMI with varying distance between the first layer of Fe at the interface and the oxygen atoms. The different systems are represented on top of the curve. The energy of the DMI in case of the oxidation of the first layer of Tantalum (Ta_1) is represented by the gray star meanwhile the case of no oxidation by the blue crossed triangle.

The figure 4.7 presents the E_{DMI} values with respect to the number of Fe monolayers and for different oxidation percentages at the interface. We see an agreement in term of the sign of the DMI energy with respect to the experimental map. Indeed, for large thickness of the top Ta layer and the higher thickness of ferromagnet the DMI energy is positive, then this energy becomes negative when we moved along the two gradients.

Consistently with our experiments, we see a change in sign for the DMI energy with respect to the oxidation. More precisely for 5 to 9 monolayers of Fe the sign change happens for low oxidation percentage (between 0% and 25%). This result is consistent with the experimental results depicted in 4.3. If we look for a constants thicknesses of ferromagnet the change in DMI sign happens experimentally for high thicknesses of the top Ta layer, meaning for low oxidation at the interface.

The second remarkable change in sign in the *ab initio* DMI map is the change between 3 and 5 monolayers of Fe for 0% of oxidation. Here again it is qualitatively consistent with the experiment where a change in sign is observable with respect to the ferromagnetic layer for thick value of the top Ta layer (around 0.98 nm of Ta).

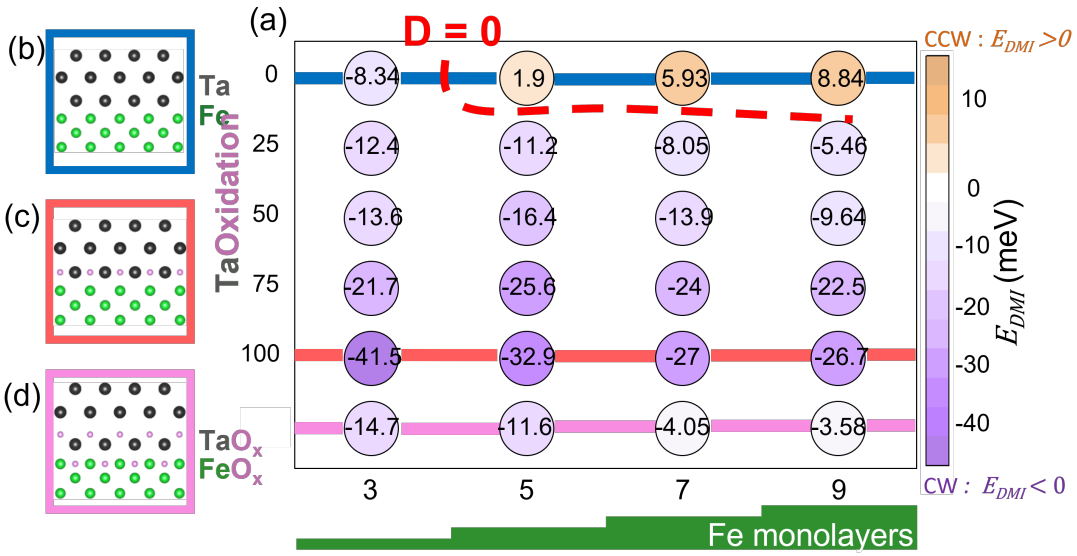

Figure 4.7: *ab initio* DMI map. (a) DMI energy (E_{DMI}) calculated from first principles for varied Ta interfacial oxidation state (in percentage) and Fe thickness (in monolayers) in Fe/Ta interface. The crystallographic structures used are shown for (b) non-oxidized Ta, (c) fully oxidized Ta, and (d) simultaneously oxidized Ta and Fe interface. The red dashed line designates the DMI sign inversion.

For higher value of oxidation at the interface no DMI sign change is found by calculation which is once again confirmed with the experimental map shown in the figure 4.3. Higher value of oxidation corresponds experimentally to smaller value of Ta thickness. In this case, looking to 0.95 nm and below, we see no sign change as well.

Finally, when oxidation reaches the Fe layer the DMI value starts to decrease leading to values close to 0 for greater Fe thickness. Experimentally it corresponds to thinner Ta region, which we have not yet studied. However, future investigations could verify the agreement between *ab initio* calculations and experimental results in this region. Additionally, the DMI value approaching zero for a high number of Fe monolayers could suggest an inversion of the DMI sign in this thin Ta region.

2- Change of the oxygen distance from the Ta/Fe interface:

For this study 5 monolayers of Ta were used to have more data points on the distance of the oxygen atoms to the interface. The figure 4.8 represents the calculated E_{DMI} values as a function of Fe thickness for different oxygen distances from the Fe interface ranging from non-oxidized (b) to fully oxidized Ta layers (e). We observe that the DMI sign change as a function of the Fe thickness is now present for several oxygen positions.

In the case of non-oxidized Ta the DMI sign change is, as in the previous study, located in between 3 and 5 monolayers of Fe. Which is also the case when oxygen atoms are located in the 5th Ta monolayer (the farther from the interface). For the case where the oxygen atoms are located in the three farther monolayers (3rd, 4th and 5th), green line and box in the figure 4.8 (a) and (d), the DMI sign change occurs in between 5 and 7 monolayers of Fe. For the

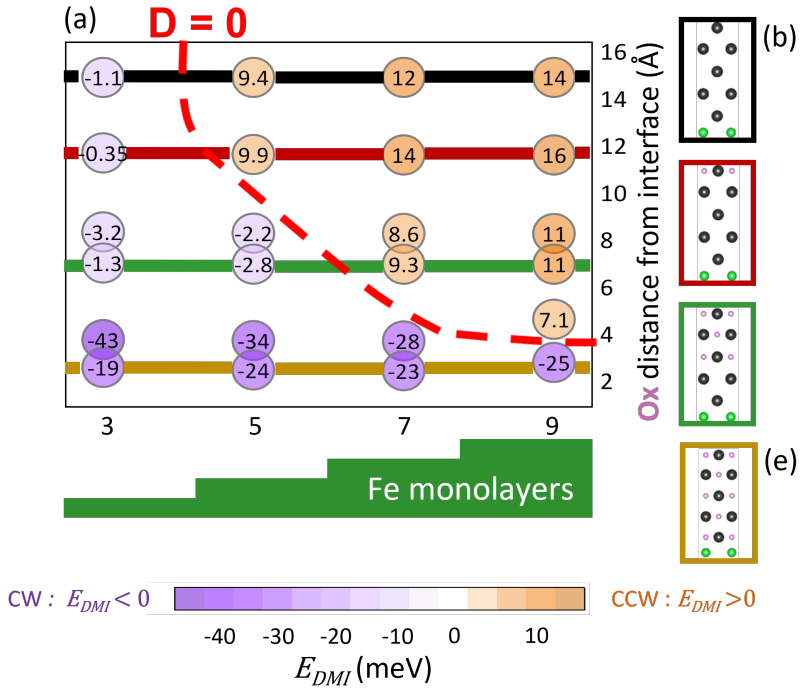

Figure 4.8: *ab initio* DMI map. (a) DMI energy (E_{DMI}) calculated from first principles for varied distance of the oxygen atoms from the Ta/Fe interface with respect to the Fe thickness (in monolayers). The crystallographic structures used are shown in (b) - (e) from (b) non-oxidized Ta to (d) fully oxidized Ta. The red dashed line designates the DMI sign inversion.

case where only the interfacial Ta monolayer is non-oxidized, the DMI sign shift between 7 and 9 monolayers of Fe. Finally, for the fully oxidized case, yellow line, we see that no DMI sign change occurs.

A quantitative comparison between both DMI sign maps results an experimental values remains difficult due to contribution of the bottom Ta/FeCoB interface contribution in the experimental DMI behavior. However, *ab initio* calculation support the experimental finding of a DMI sign change with the thickness of the ferromagnetic layer.

Also, an explanation on the physical phenomena at the origin of this sign change is still missing. As the oxidation effect has already been studied experimentally [49],[50],[140] and theoretically [135], [141]. In these works, they show that the charge transfer between the Co and O atoms modifies the Co 3d - HM 5d hybridization, thereby altering the 3d density of states at the Fermi level and consequently the DMI. We therefore concentrate here on the mechanism governing the DMI sign change with respect to the ferromagnet thickness.

Indeed, as explained before, the DMI involved in our system is of interfacial nature, it is then unexpected that the number of Fe mono layers has an impact on the DMI coefficient sign. To have a deeper understanding we look first at the layer-resolved difference in the chirality-dependent spin-orbit coupling energy written as:

$$\Delta E^k_{SOC} = E^k_{CW} - E^k_{CCW} \tag{4.3}$$

From the figure 4.9(a), representing this layer-resolved SOC energy, we see that the main contribution to the SOC energy is coming from this interfacial layer of Ta, as expected from the Fert-Levy DMI mechanism [139]. This further supports previous findings regarding the main role of interfacial Ta atoms in influencing DMI behavior. Also, we see the change in sign in the first layer of Ta at the interface between 3 monolayers of Fe (red curve) and 5 monolayers (black curve)

It should be noted that the Fe/Vacuum interface contributes significantly to the SOC energy. As shown in Figure 4.9 (a), for the three systems Fe_5Ta_3, Fe_7Ta_3, and Fe_9Ta_3, the SOC energy contributions from the three Fe atoms closest to the vacuum converge, indicating a saturation point. However, in the case of the Fe_3Ta_3 system, this convergence is not achieved, suggesting that the vacuum's influence on SOC energy cannot be easily corrected in that case. Then, it has been chosen to keep the vacuum contribution in the calculations.
Then, it is interesting to compare the $5d$ orbital-resolved SOC energy in this interfacial layer. The figure 4.9 (b) depicts it for both cases of 3 and 5 monolayers of Fe, where the DMI sign reversal occurs. We see that the difference is mainly due to the hybridization between d_{z^2} and d_{xz}, which is negative for Fe_3Ta_3 and becomes positive for Fe_5Ta_3.

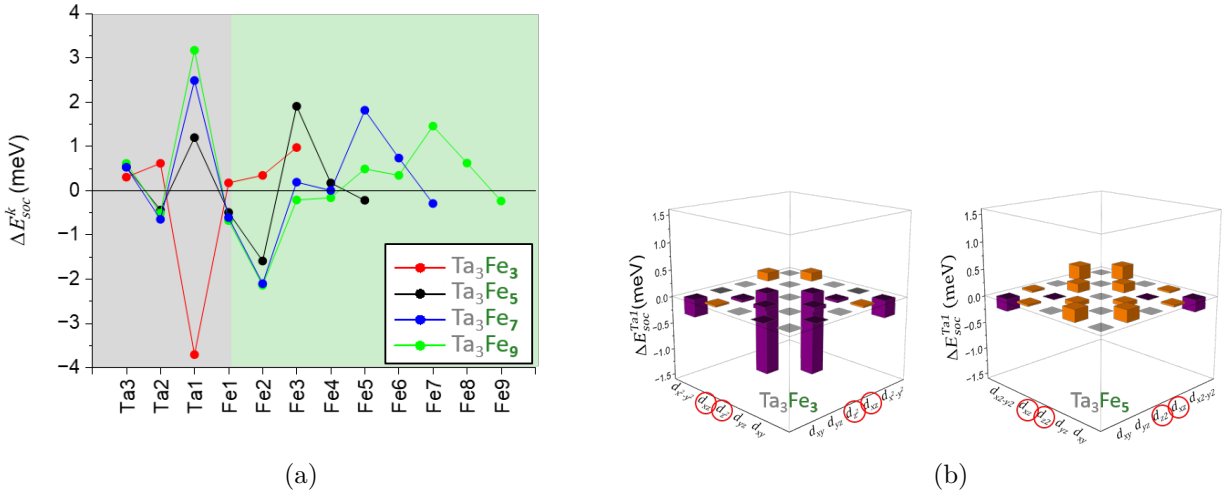

(a) (b)

Figure 4.9: (a) Layer resolved spin-orbit coupling (SOC) energy for the system Fe_m/Ta_3 with m = 3, 5, 7 and 9, the number of monolayers of Fe. The gray and green background represent respectively the Ta and Fe monolayers. (b) $5d$ orbital resolved SOC energy $\Delta E^{Ta_1}_{SOC}$ of the interfacial Ta_1 layer for ***(left)*** Fe_3Ta_3 and ***(right)*** Fe_5Ta_3 systems. Purple (resp.orange) rectangles represent negative (resp.positive) value.

Using first-order perturbation theory, we can further investigate the impact of d-orbital hybridization on the DMI.
The first order perturbation theory is a method in quantum mechanics used to approximate the properties, such as energy, of a system that is only slightly different from a system that

can be solved exactly. Mainly it consist to add a small perturbation in the Hamiltonian so that we can write $H_{tot} = H_0 + H'$ with H_0 the unperturbed Hamiltonian of the system and H' the Hamiltonian perturbation, small compared to H_0 in order to neglect higher-order corrections.

In our study the principal contribution to the DMI is, as we mentioned before, the $5d$ orbital states of the interfacial Ta_1 layer. Therefore, the perturbation induced by the DMI on the total energy can be written as:

$$\left\langle \Psi_{lm,s} \left| \widehat{H_{SOC}} \right| \Psi_{lm,s} \right\rangle \tag{4.4}$$

Where $|\Psi_{lm,s}>$ represents the spin-dependent occupied states of Ta_1. From this method we deduce that the highest contribution to the DMI for fully occupied orbitals is given by :

$$\left\langle d^{\uparrow}_{z^2} + d^{\downarrow}_{xz} \left| \sigma_y L_y \right| d^{\uparrow}_{z^2} + d^{\downarrow}_{xz} \right\rangle = -\sqrt{6} \tag{4.5}$$

$$\left\langle d^{\downarrow}_{z^2} + d^{\uparrow}_{xz} \left| \sigma_y L_y \right| d^{\downarrow}_{z^2} + d^{\uparrow}_{xz} \right\rangle = +\sqrt{6} \tag{4.6}$$

It is consistent with what we deduce from the orbital resolved SOC energies: the transition between d_{z^2} and d_{xz} is the main contribution. However, these two matrix elements correspond to fully occupied d-orbitals. We then need to compare the occupation of the d-orbitals of the first layer of Ta at the interface in Fe_3Ta_3 and Fe_5Ta_3 in order to understand the mechanism behind the change in sign.

Indeed, as depicted by the graph in the figure 4.10 when going from 3 to 5 monolayers of Fe we see that both $d^{\uparrow}_{z^2}$ and $d^{\downarrow}_{xz}$ occupation level is decreasing. Meanwhile, at contrary, both $d^{\downarrow}_{z^2}$ and $d^{\uparrow}_{xz}$ occupation is increasing. This means that the matrix element giving a negative contribution to the Spin Orbit Coupling (SOC) energy of the interfacial Ta_1 (eq.4.5) decreases while the one giving positive contribution (eq.4.6) increases, making switch the sign of the DMI. In the supplementary 9.2 a more detailed calculation of the intra and interlayer contribution to the DMI is displayed.

In fact, the change in the d-orbital occupation is triggered by the structural relaxation induced by the increase in the FM thickness. Indeed, the unit cell is fixed on the Fe/Ta value of unit cell, the system then relaxes in the z direction. In the figure 4.11(a) we see the variation of the interfacial distance z between Ta_1-Fe_1 for the different calculated structures. As the Fe thickness increases, z decreases which triggers the change in the occupation of the overlapping d-orbitals, mainly the out-of-plane ones d_{z^2} and d_{xz} represented in the figure 4.11(b).

The decrease of the interatomic distance z, generated by the increase of the number of Fe monolayers m, has a direct impact on the magnetic properties. The figure 4.12 is showing the magnetic moment per atoms for different thicknesses of Fe. As highlighted in the figure, we see that the magnetic moment of the Fe atom at the interface Fe_1 is decreasing as m is increasing (green arrow). Meanwhile the magnetic moment of the interfacial Ta_1 atoms is increasing negatively (gray arrow) with the number of Fe monolayer. Both of this is caused by the change in occupation of the orbitals induced by the structural relaxation change with z.

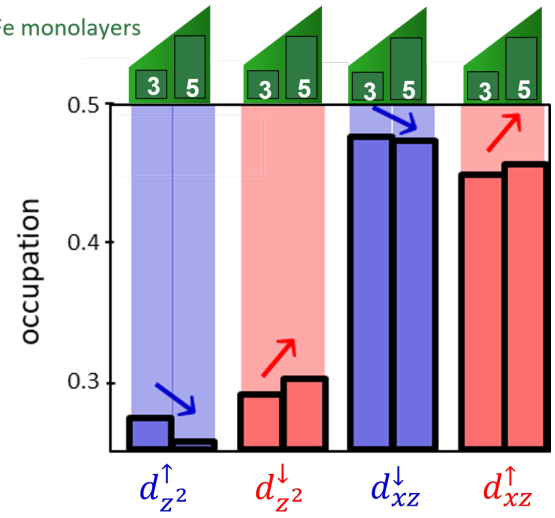

Figure 4.10: The spin dependent d-orbital occupations (precisely d_{z^2} and d_{xz}) of Ta_1 in Fe_3Ta_3 and Fe_5Ta_3, referred to as 3 and 5. Blue and red color refer respectively to eq. 4.5 and eq. 4.6

.

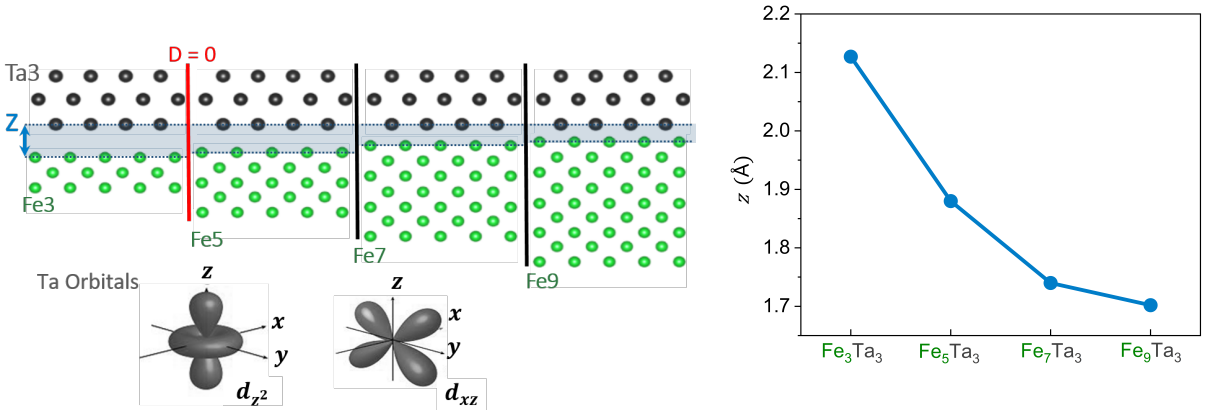

(a) (b)

Figure 4.11: (a) Fe_mTa_3 structure with m = 3,5,7 and 9, the change in sign of DMI is indicated between the case m = 3 and m= 5 with the red line. In blue, the interatomic distance at the interface between Ta and Fe is represented and noted z. We see that this distance is decreasing as the m is increasing. Below, a Schematic representation of d_{z^2} and d_{xz} Ta orbitals. (b) Value of the interatomic distance z for each number of monolayer of Fe.

4.4 Conclusion

In this chapter we have been able to understand a new mechanism governing the Dzyaloshinskii-Moriya interaction chirality. By conducting a combined experimental and *ab initio* study we highlight the dependence of the DMI sign both with the oxidation state at the top interface and the thickness of the ferromagnet. *Ab initio* calculations reproduced well the experimental results and enabled the deep understanding of these phenomena. Particularly we reveal the

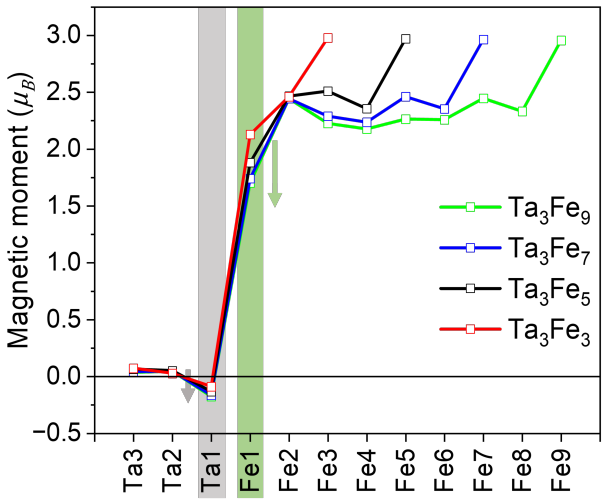

Figure 4.12: Magnetic moment μ_B par atom for the four system Fe_mTa_3 with m = 3,5,7 and 9 respectively in red, black, blue and green.

implication of the occupation of the orbitals leading to a decrease in the interatomic distance at the interface between the Ta and Fe layers as shown in the figure 4.13 (a) on the right projection.

This connection between the interatomic distance z and the inversion of the DMI sign offers exciting perspectives for controlling chiral domain walls and skyrmions through strain. In this context, a growing research field explores the potential of nucleating and propagating skyrmions using transient strain induced by surface acoustic waves [142], [143], [90].

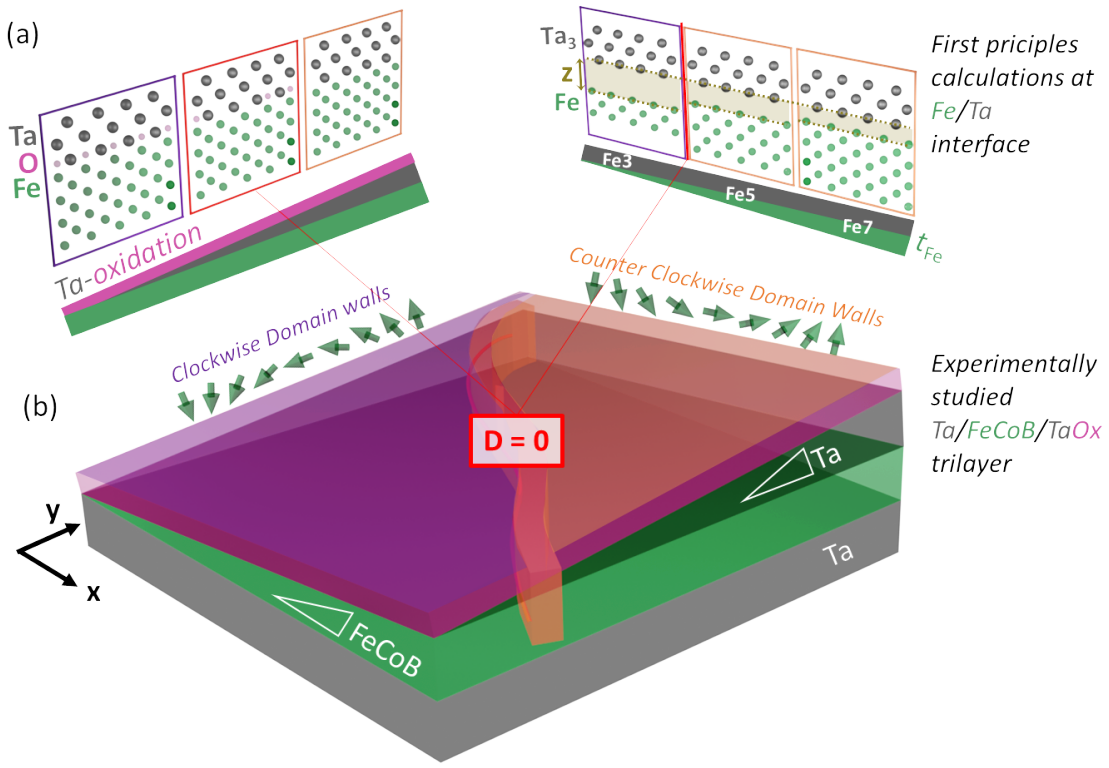

Figure 4.13: Schematic summary of the joint experimental and *ab initio* study.(a) Projection of the modeled top interface Fe_n/Ta_m with ***Left:*** the Fe_7/Ta_3Ox system with a decreasing number of the Oxygen atoms (pink balls) following the top Ta wedge in (b). Ta and Fe are represented respectively by gray and green balls. And ***Right:*** the Fe_m/Ta_3 system for m = 3, 5 and 7. The interatomic distance z is also represented and decrease with the increase of m. For both projection the change in DMI coefficient sign is display in red. Both projection is the *ab initio* system corresponding to (b) 3D Schematic representation of the experimental tri-layer Ta/FeCoB/TaOx. Both wedge are represented. The CW and CCW regions found in the experimental study are displayed one top of the tri-layer by respectively the purple and the orange regions. The red band represents the transition fo the DMI coefficient sign zone., where D = 0.

Chapter 5

Hard X-ray photoelectron spectroscopy measurements on gated Pt/Co/AlOx trilayers

5.1 Introduction 117
5.2 Magnetic properties 118
5.3 The HAXPES measurements 124
5.4 Conclusion 128

5.1 Introduction

The results presented in this chapter have been published in Physical Review Applied in which I am one of the author [144].
The project was led by S. Pizzini and C. Balan. I participated to the process of the samples and I assisted to the synchrotron measurements.

Magnetic textures, such as skyrmions and chiral domain walls, are formed thanks to the Dzyaloshinskii-Moriya interaction (DMI) and are stabilized by the interplay of various energy contributions, such as exchange, Zeeman, dipolar, and anisotropy energies. Anisotropy energy plays a critical role in stabilizing these spin textures. Thereby, understanding and controlling the anisotropy in our samples constitutes a new interesting approach to manipulating spin textures like skyrmions.

While the previous chapter focused on the evolution of DMI sign as a function of the oxidation state at the ferromagnet/heavy metal (FM/HM) interface and the thickness of the ferromagnetic layer, this chapter will explore the manipulation of interfacial magnetic anisotropy.

Various approaches have been established to modulate anisotropy in ferromagnets, including chemical substitution, epitaxial strain, and the application of an electric field, commonly referred

to as Voltage Control of Magnetic Anisotropy (VCMA), which will be the focus of this chapter.

Recently, VCMA has emerged as a promising technique for enhancing the efficiency of spintronic devices [72], [145]. Notably, studies have demonstrated that anisotropy manipulation in ultra-thin ferromagnetic films via an electric field can be attributed either to strain effects [16], electronic effects [146], [70] or magnetoionic effects [71],[147]. In the electronic case, as an answer to the applied electric field, the number of electrons in d orbitals at the interface is modified, leading to a change in the different magnetic characteristics of the material. Meanwhile, in the case of magnetoionic phenomena, the gate voltage-induced electric field drives ions towards or away from the ferromagnetic interface, as discussed in the section 2.2.1. This process directly impacts interfacial magnetic properties, including anisotropy and DMI.

Thereby, different physical mechanisms have been explored, including magnetoelastic coupling through piezoelectric substrates, electrostatic charge accumulation and, as discussed in this chapter, magnetoionic effects. Indeed, many studies make the hypothesis of an ion-migration origin to explain the strong and non-volatile variation of anisotropy when using a gate voltage [71], [147], [148] and it has been shown using TEM measurement [71]. However, a direct experimental verification within an actual device is still missing to confirm this hypothesis.

This chapter demonstrates experimentally, the magnetoionic origin of the non-volatile strong anisotropy variation using gate voltage in a Pt/Co/AlO_x/HfO_2 system, similar to the Ta/FeCoB/TaOx system but with larger DMI and anisotropy.
In a first part we will compare the magnetic properties of reference samples with those of gated samples, to show the evolution of the oxidation rate at the Co/oxide interface. This study will then be supported by Hard X-ray Photoelectron Spectroscopy (HAXPES) measurements detailed in the second part of the chapter.

5.2 Magnetic properties

The study has been made on a tri-layer system composed of Pt(3)/Co (0.46-0.87)/Al(0.9-2.56) (thicknesses in nm), in which the two top layers are deposited in a wedge, one perpendicular to each other. The sample is then oxidized by oxygen plasma (as explained in the section 3.1.1). In the same spirit as the system studied in the previous chapter, the wedge of aluminium allows a progressive oxidation of the Co/Al interface along the sample, as it can be seen on the figure 5.1. For a defined thickness of cobalt, three different oxidation states are then observed along the wedge of aluminium: underoxidized (Co/Al/AlOx) is found for the thicker value of Al; by decreasing the Al layer we then reach the optimally oxidized state (Co/AlOx), associated to maximum of perpendicular magnetic anisotropy (PMA) and finally for the thinner Al values the cobalt layer starts to be oxidized, which we refer to as the over oxidized case (Co/CoOx/AlOx).

As in the previous chapter, both Co and Al wedges will have an impact on the magnetic properties of our sample. More precisely it will impact the magnetic anisotropy coefficient that

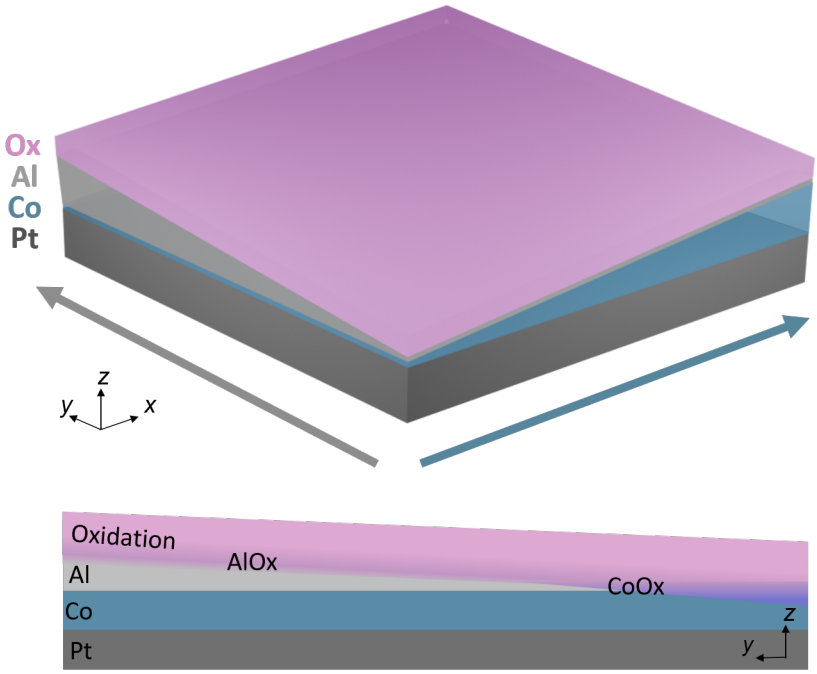

Figure 5.1: (top) 3D representation of the tri-layer system Platinium/Cobalt/Aluminium-Oxide system with the two top layers, Co and Al, deposited in a wedge respectively in the x and y direction. (bottom) (adapted from [144]) Lateral view for a cut in a specific thickness of Co. It shows the evolution of the oxidation state at the Co/Al interface. Three main oxidation states can be seen : underoxidized (Co/Al/AlOx), optimally oxidized (Co/AlOx) and overoxidized (Co/CoOx/AlOx).

can be written:

$$K_{eff} = \frac{K_S}{t} - K_d \tag{5.1}$$

With K_s the surface anisotropy constant, t the thickness of the ferromagnet and K_d the dipolar anisotropy term expressed as $K_d = \frac{1}{2}\mu_0 M_s^2$, μ_0 being the vacuum permeability and M_s the sponteneous magnetization value. The wedge of cobalt will, by definition, change the thickness t and therefore tune the anisotropy coefficient. Simultaneously, the aluminum wedge on the top layer modulates the oxidation state at the interface, which directly influences the surface properties of the system. In particular, the oxidation state affects the surface anisotropy coefficient K_s leading to a change in the effective anisotropy coefficient K_{eff}.
This double wedge system leads to the apparition of different regions of anisotropy. Figure 5.2 presents the remanence map of this sample measured using a polar magneto-optical Kerr effect (MOKE) magnetometer. The In-Plane (IP) anisotropy and the ParaMagnetic (PM) states are displayed in blue while the Perpendicular Magnetic Anisotropy (PMA) region is in orange, corresponding to the optimum of oxidation.

To analyze the magnetic properties with respect to the oxidation state, we selected five reference samples (Ref1 - Ref5) with a fixed Co thickness of 0.75 nm and different thicknesses of the top Al layer (Ref1: 2.6nm, Ref2: 1.9nm, Ref3: 1.75nm, Ref4: 1.6nm, Ref5: 1.1nm) meaning an increase of the oxidation rate at the interface Co/AlOx from Ref1 to Ref5.

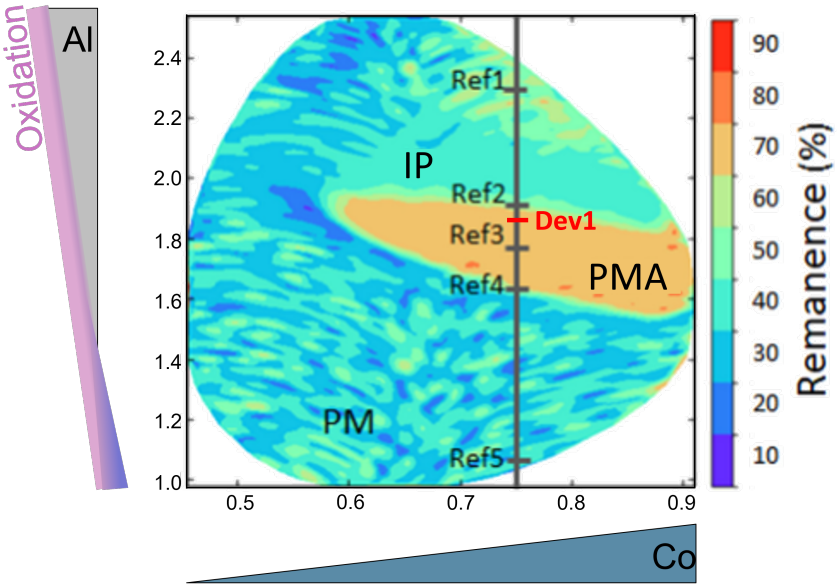

Figure 5.2: (adapted from [144]) Remanence map of tri-layer system Pt/Co/AlOx. The perpendicular magnetic anisotropy (PMA) region is displayed in orange meanwhile the Paramagnetic (PM) and In-plane (IP) anisotropy regions are in blue. The position of reference samples are indicated by RefX = Pt/Co/AlOx reference samples with a fixed Co thickness of 0.75 nm and different Al thicknesses with increasing oxidation of the Co layer. The position of the device 1 is also indicated by Dev1

The hysteresis loop measurements, carried out with a MOKE microscope, are displayed in Figure 5.3. The signals of Ref1 and Ref5 are characterized by a linear behavior, negligible magnetization, and no saturation. Meanwhile, Ref3 displays a typical square hysteresis loop characteristic of the PMA region, with a well-defined square shape, a clear magnetization saturation and a large coercive field. In contrast, Ref 2 and Ref 4 exhibit S-shaped hysteresis loops, indicative of the transition between PMA and the IP and PM regions, respectively. Notably, these loops feature small coercive fields and a smooth progression toward saturation.

In order to compare the magnetic properties before and after the application of a gate voltage and to provide insights into the oxidation process, we developed the capacitor-like device illustrated in the figure 5.4. Starting with a sample with the composition and magnetic properties close to the one of Ref2, a 5nm layer thickness of HfO_2 is deposited by ALD (technique detailed in the section 3.1.2 on top of our network of Pt/Co/Al strips processed UV lithography and lift-off. This layer plays the role of an electronic insulator with ionic conductor characteristics. $50 \times 50 - \mu m^2$ 3-nm-thick Pt electrodes were then patterned on top of the magnetic structures, allowing the application of a gate voltage on the devices.

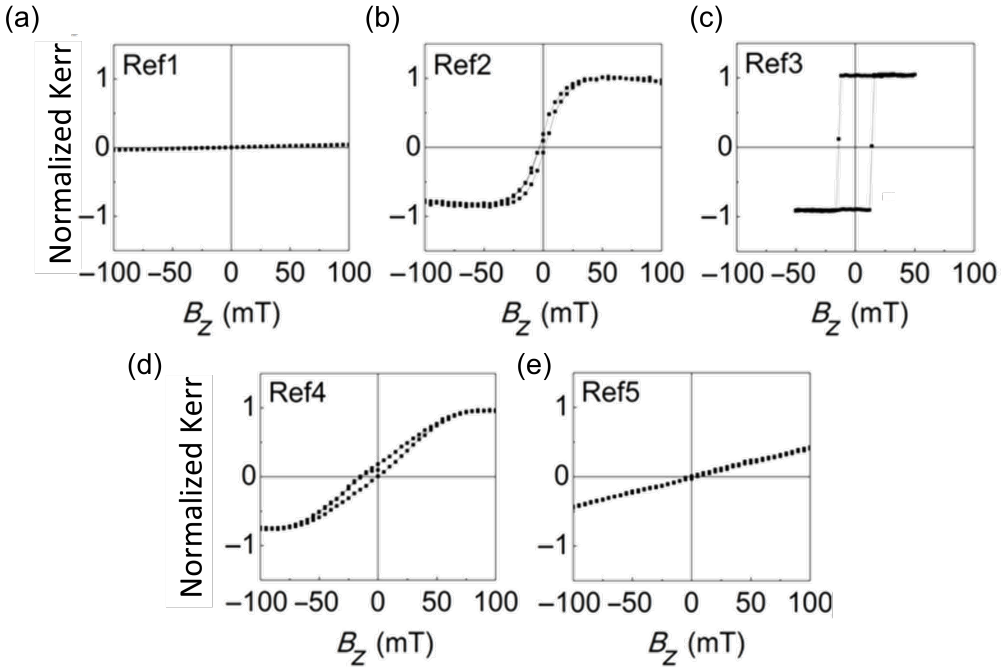

Figure 5.3: (adapted from [144])(a,e) Hysteresis curves of the reference samples (Ref1-5) measured by polar MOKE. The normalized Kerr signal is displayed with respect to the external magnetic field B_Z expressed in mT, applied perpendicularly to the sample surface.

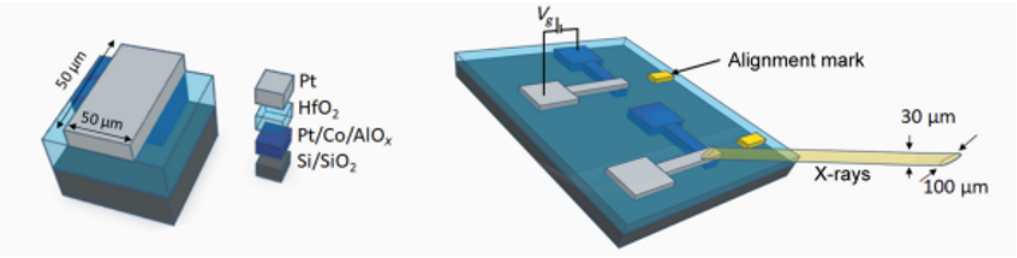

Figure 5.4: (From [144]) Scheme of the capacitor-like devices together with the geometry of the HAXPES measurements. The tri-layer Pt/Co/AlOx is represented in dark blue, the HfO_2 layer in light blue and the Pt electrode in grey.

The hysteresis curves of five devices subjected to various gate voltage values and/or different application durations are shown in Figure 5.5. A detailed summary of the devices' history is provided in Table 5.1.

Five devices (DEV1 to DEV5) were prepared in different magnetic states for their study by HAXPES. Dev1 was left in the pristine state where no voltage was applied. Dev1 device is close to the reference sample Ref2

Before the application of the gate, each of the five capacitors has the same initial state with an S-shape hysteresis curve with zero remanence, also observed for the Ref2 sample. Thus, initial oxidation state for all the devices is the same as the one of Ref2, i.e close to the PMA-IP transition.

A gate voltage was then applied on Dev2-5. The hysteresis curves of Dev2 and Dev3, corre-

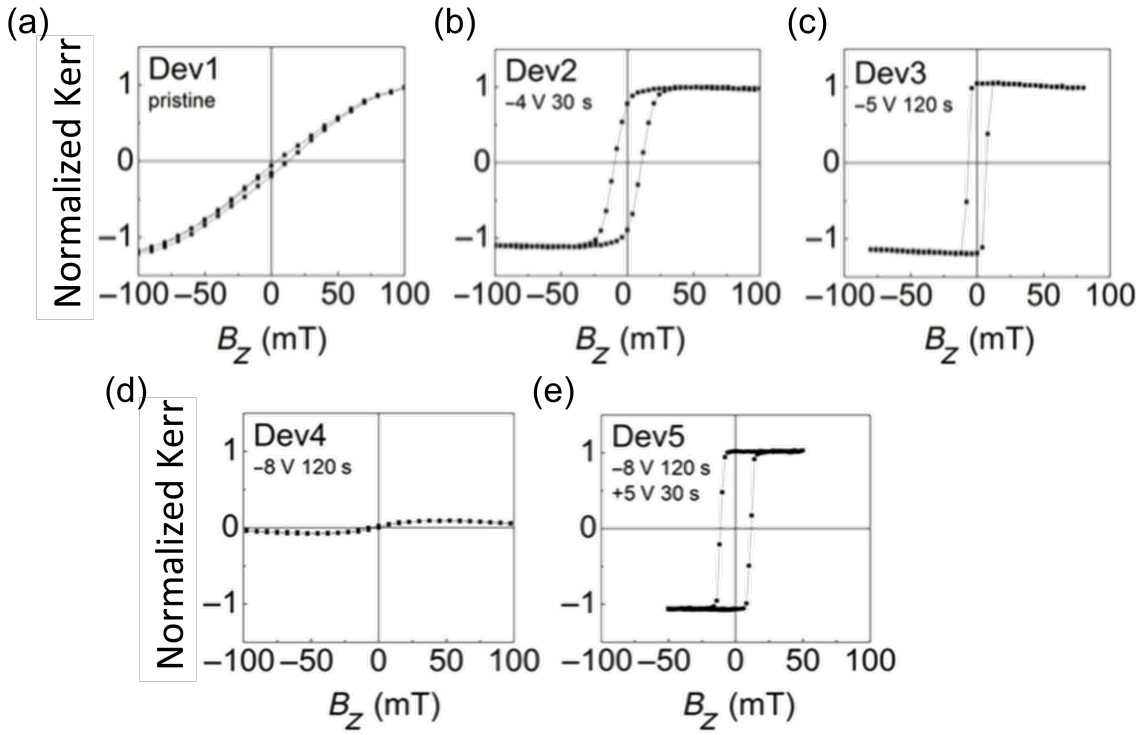

Figure 5.5: (From [144])(a,e) Hysteresis curves of the capacitor-like device samples (Dev1-5) measured by polar MOKE measured in the pristine state (Dev1), and after the application of the gate voltage of a given value and duration. (Dev2-Dev5) The normalized Kerr signal is displayed with respect to the external magnetic field B_Z expressed in mT, applied perpendicularly to the sample surface.

sponding to the application of -4V for 30 seconds and -5V for 120 seconds, respectively, exhibit open square loops, indicating a modification of the anisotropy caused by gating. When compared to the reference sample's hysteresis curve, a similar shape is observed in the Ref3 sample. The coercive field (H_c) is increased, and saturation is reached abruptly around H_c. Notably, the difference between Dev2 and Dev3 lies in the switching behavior, which becomes more abrupt at a higher gate voltage (Dev3). Dev2 is in an intermediate state between the Ref2 and Ref3 hysteresis curve, meanwhile Dev3 corresponds more to Ref3. This suggests that a higher gate voltage increases the PMA and thereby advances the oxidation state of the interface.

A gate voltage of -8V for 120 seconds was applied to the Dev4. The hysteresis curve presents the feature of a paramagnetic state, with no remanence nor saturation magnetization. The anisotropy decreases and the loop closes, meaning a decreases of the PMA linked with a switch to the PM state and therefore, by comparison with the reference samples, an increase of the oxidation at the interface. With these results, we highlight that the consequences of a gate voltage application on the anisotropy is equivalent to a change in the oxidation state at the Co/Al interface.

After studying the persistent changes in anisotropy, an interesting point to study is the re-

Devices	Gate voltage applied (V)	Duration (s)	Anisotropy region	Ref sample associated
Dev1	0		transition IP-PMA	Ref2
Dev2	-4	30	OOP	Ref3
Dev3	-5	120	OOP	Ref3
Dev4	-8	120	PM	Ref5
Dev5	-8 / +5	120 / 30	PM / OOP	Ref5/Ref3

Table 5.1: Summary of the gate voltage applied to all the device samples, the time of application, the anisotropy region measured by the hysteresis curves and the reference samples situated in the same anisotropy region.

versibility of the phenomenon. To do this, we applied on Dev5, first, a gate of -8V for 120s, reaching the same paramagnetic state as Dev4, then +5V for 30s. By doing this, we see in Figure 5.5(e) that we recover the PMA characteristics in the hysteresis curve with an open square loop, showing that the effect of the gate is reversible.

In summary, increasing the magnitude of the negative gate voltage induces progressive changes in anisotropy, transitioning from an in-plane anisotropy state to a paramagnetic state, passing through a state with perpendicular magnetic anisotropy. Furthermore, the application of a positive gate voltage allows the system to revert to its previous anisotropy state. This phenomenon is the voltage control of the magnetic anisotropy, detailed in the section 2.2.1 and it is schematized for our study in the figure 5.6.

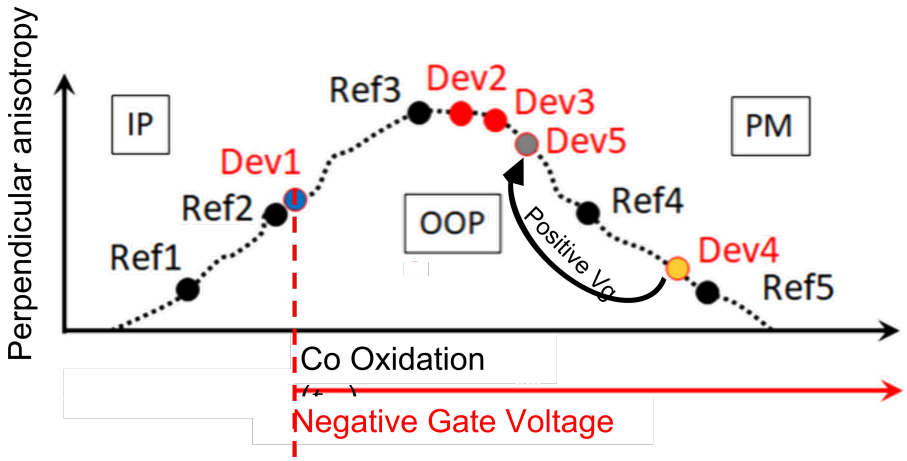

Figure 5.6: (Adapted from [144]) Schematic representation of the perpendicular magnetic anisotropy with respect to the oxidation state of the Co layer (or in other term with respect to the thickness of the top Al layer). IP, OOP and PM region are displayed. The black dots represent the different Reference samples (RefX) position meanwhile the colored dots represent the devices samples DevX that have undergone the gate voltage.

It is noteworthy to say that the change of anisotropy coming from the application of the gate is nonvolatile as the magnetic state stays for weeks after the application. This constitutes a good argument to state the magnetoionic origin of the phenomenon and exclude an electronic

effect as the driving mechanism, which would result in a return to the initial state.
This suggests a gate-controlled motion of oxygen ions at the interface in our system. To confirm this statement, complete the experimental proof of the magnetoionic origin of the PMA evolution, its correlation with the oxidation state at the interface and identify the type of migration ion, we performed Hard X-ray Spectroscopy (HAXPES) measurements.

5.3 The HAXPES measurements

The HAXPES measurements were performed at the GALAXIES beamline of the synchrotron SOLEIL in Saint-Aubin. A detailed explanation of this type of measurement is reported in the section 3.2.4. This technique allows us to have access to the chemical composition of our sample. The high energy of the x-rays employed in this technique enables to focus on the composition of the Cobalt layer buried below other layers (5nm of HfO_2 + 3nm of Pt). More precisely we look here at the Co 2p binding energy to study the oxidation state of the ferromagnet. Indeed, the binding energy of the core-level electron is the energy needed to eject this electron from its orbital, overcoming the attractive force of the nucleus and the surrounding electronic environment. The 2p peak provides then more detailed information about the chemical composition of the Cobalt as it is more sensitive to chemical changes. In addition, the Co 2p core levels typically generate stronger and more distinct signals associated with a distinct spin-orbit splitting ($2p_{1/2}$ and $2p_{3/2}$) permitting the acquisition of additional information about the electronic structure and bonding.

The raw spectra of the reference samples (Ref1 - Ref5) are shown in figure 5.7(a). The spectra are shifted along the y axis to enable the comparison between each other.

Going from Ref1 spectra to Ref5 spectra we clearly see the correlation between the thickness of the Al layer with the oxidation of the Co layer. The first reference sample Ref1 corresponds to a pure Co state (highest thickness of Al layer) with the peaks of Co $2p_{1/2}$ at 792 eV and Co $2p_{3/2}$ at 778 eV. For Ref 5, which has the thinner Al layer we see two CoO peaks at respectively 796 eV and 782 eV. This sample corresponds to the pure CoO case [149], [150]. Two additional satellite peaks can be distinguished easily in this spectrum, noted 's' in the figure 5.8, at 803 and 786 eV. These satellite peaks are coming from the charge transfer between the orbital *2p* of the oxygen and the orbital *3d* of the Cobalt. Indeed, after the *2p* electron is removed, the system is left in an ionized state, which could be influenced by charge transfer. The charge transfer mechanism modifies the electronic environment. It impacts the binding energy by influencing: the degree of hybridization between Co *3d* and O *2p* orbitals and the effective Coulomb repulsion between the core hole ($2p5$) and the 3d-electron system. The main peaks are typically associated with the ground-state configuration of the system, while satellite peaks correspond to higher-energy configurations resulting from charge transfer:

$$2p^6d^7 \rightarrow 2p^53d^7 + e^- \text{ (satellite peaks)}$$
$$2p^6d^8L \rightarrow 2p^53d^8L + e^- \text{ (main peaks) where L stands for the hole in the oxygen ligand}$$

The transfer of electrons from cobalt to oxygen leads then to a shift in the binding energy between the CoO peaks and the Co ones.

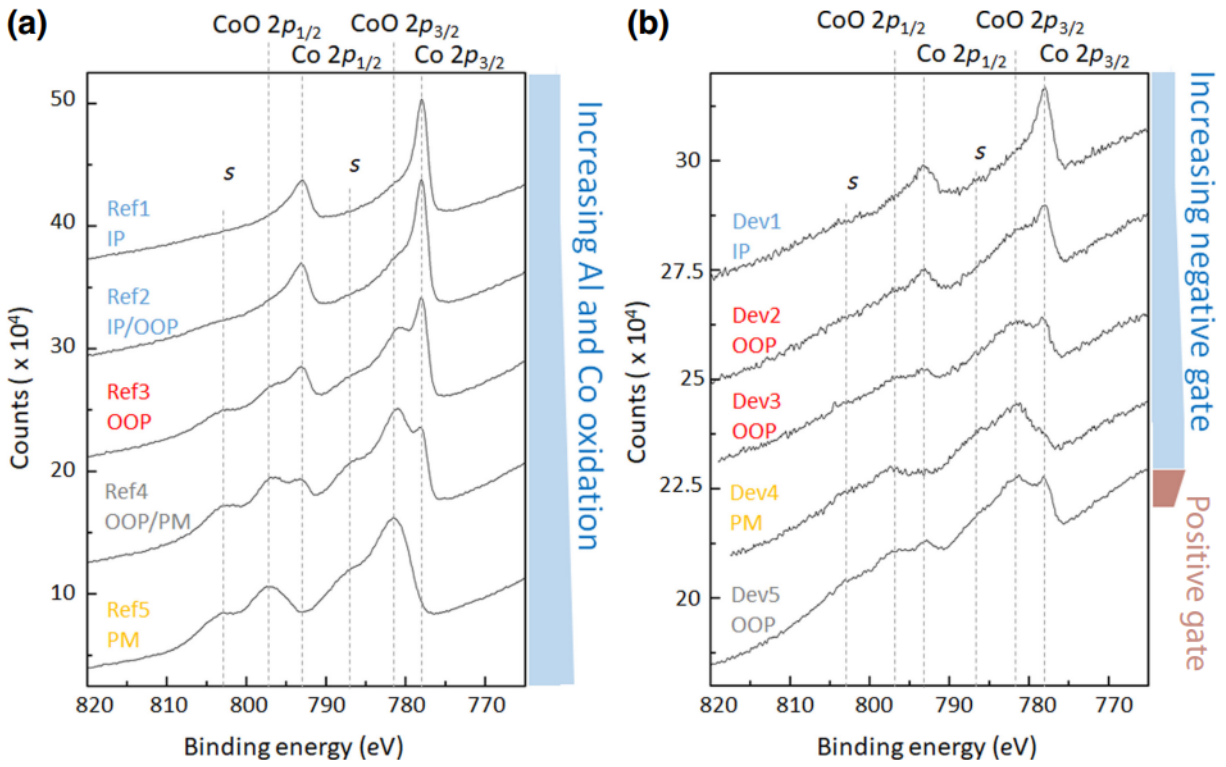

Figure 5.7: (From [144]) Co *2p* HAXPES spectra for (a) the reference samples and (b) the gated devices. It displays the counts (proportional to the number of electrons that reach the sample) with respect to the energy of the electrons. To enable a clear comparison, the curves have been shifted on the y axis.

In the spectra shown for Ref2 and Ref3, the Co peaks prevail, although the emergence of CoO peaks is also evident. In the Ref4 curve, corresponding to the transition region of anisotropy from out-of-plane to paramagnetic, we see that the tendency is invert, the Co peak is smaller than the CoO one, the sample is more oxidized.
As expected, with this first comparison, we see the progressive oxidation level of the cobalt due to the gradient of Al thickness, in the different reference samples.

We then conducted the same measurements on the gated devices (Dev1-Dev5). By comparison with the reference HAXPES curve, we are consequently able to state about the oxidation of the cobalt layer after the application of a gate voltage. In figure 5.7(b) the raw Co *2p* data are displayed. We notice more noise in the measurement coming from the additional HfO_2 layer deposited on top of the device samples. Also, the peaks are less visible. To obtain a clearer vision on the evolution of the CoO and Co peaks we substracted the background of the measurements and fitted the spectra using Gaussian fonctions. The best fits are shown in figure 5.8. It is important to note here that, in order to reduce the measuring time (which was more than 10 hours per measurement) we removed the Pt electrode after having apply certain value of gate voltage during a certain amount of time (detailed in the table 5.1). This reduced the measurement time to $\sim 1.5h$ per spectrum.

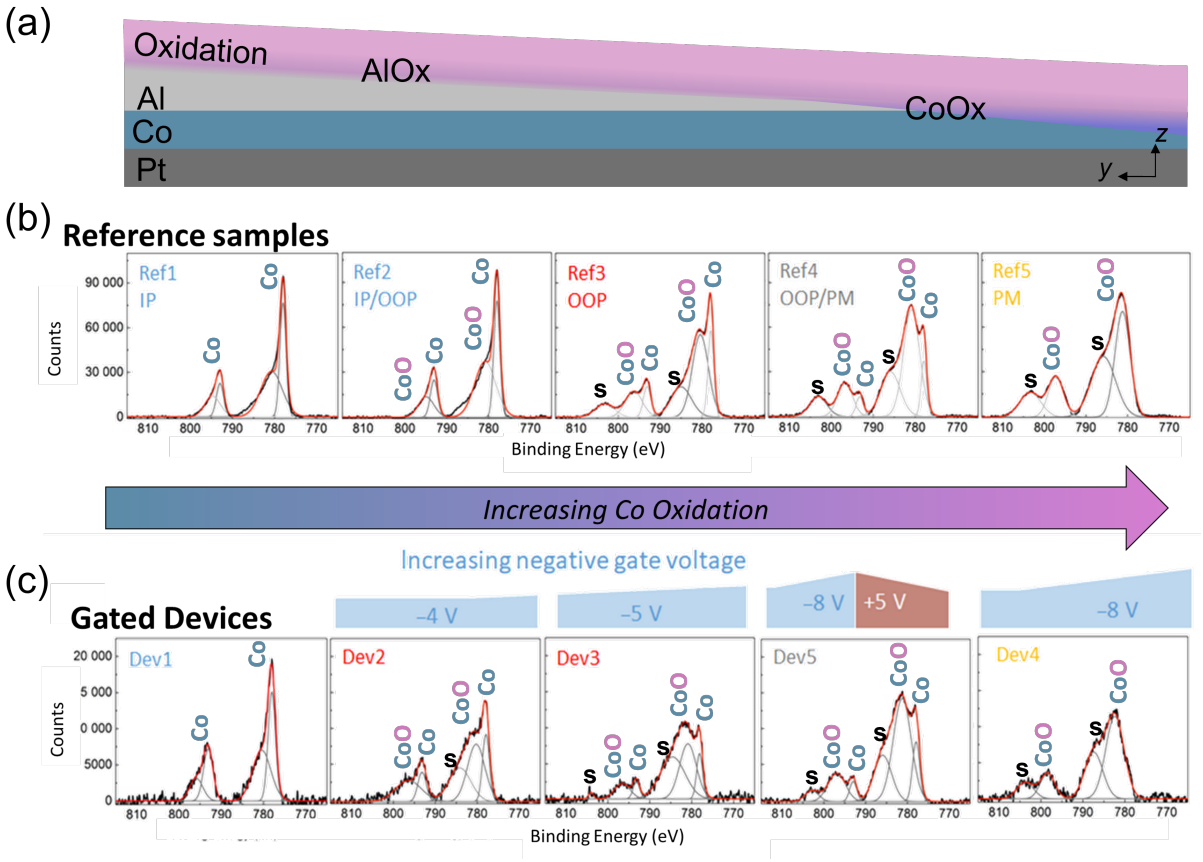

Figure 5.8: (Adapted from [144]) (a) Lateral cut for a specific thickness of Cobalt is displayed allowing the comparison between the HAXPES spectrum and the respective oxidation state for a decreasing Al thickness. (b)-(c) Background substracted HAXPES spectra of the reference samples (b) and gated devices (c). They are displayed from left to right following the increase of the Co oxidation.

The first device Dev1 represents the initial state, no gate has been applied. This initial state corresponds well to the Ref2 curve. The Dev2 and Dev3 curve shows the progressive increase of the CoO levels with the gate voltage. Dev2 and Dev3 have undergone respectively -4V during 30 seconds and -5V during 120 sec. In both of these curves, we see the Co peak decreasing meanwhile the CoO one increases. By applying -5V we reach the point where the Co and CoO peaks, both $2p_{1/2}$ and $2p_{3/2}$, are on the same level. The HAXPES curve for Dev4, for which we applied -8V during 1min 30sec, displays the same configuration as the Ref5 sample, with the Co peaks disappearing and only oxidized cobalt peaks present. This first investigation proves the influence of the gate voltage on the oxidation state of the ferromagnetic layer. More precisely this study brings the missing experimental proof of the magnetoionic origin, with O^- ions, of the strong anisotropy variation associated with the application of a gate. In addition, we show the reversible character of this phenomenon by applying a +5V gate to a device that has undergone previously a -8V gate voltage. The curve of Dev5 shows the re-apparition of the two peaks of Co in the spectrum. The magnetoionic effect promotes nonvolatile vanishes of PMA and is reversible.

The combined analysis of anisotropy measurements and HAXPES spectra reveals an increase in oxidation associated with the applied negative gate voltage. To further illustrate the correlation between these parameters, Figure 5.9 presents the percentage of oxidized cobalt as a function of the thickness of Al, extracted from the area of the corresponding peaks in the HAXPES spectra. This percentage corresponds to the relative CoO content in the sample and was calculated using the ratio CoO/(CoO + Co). The Al thickness is plotted from the highest value to the smallest one to match the sample number (Ref1 → Ref5 / Dev1 → Dev5). The PMA anisotropy region is highlighted in grey. The displayed error bars are estimated at 15%. This comes from the limited escape depth of the photoelectrons that influences the contribution of different layers to the spectral weight which decreases with the distance from the surface. Therefore, the HAXPES technique is more sensitive to the cobalt layer closer to the top surface.
In Figure 5.9(a), that represents the CoO percentage in the reference samples, we clearly see

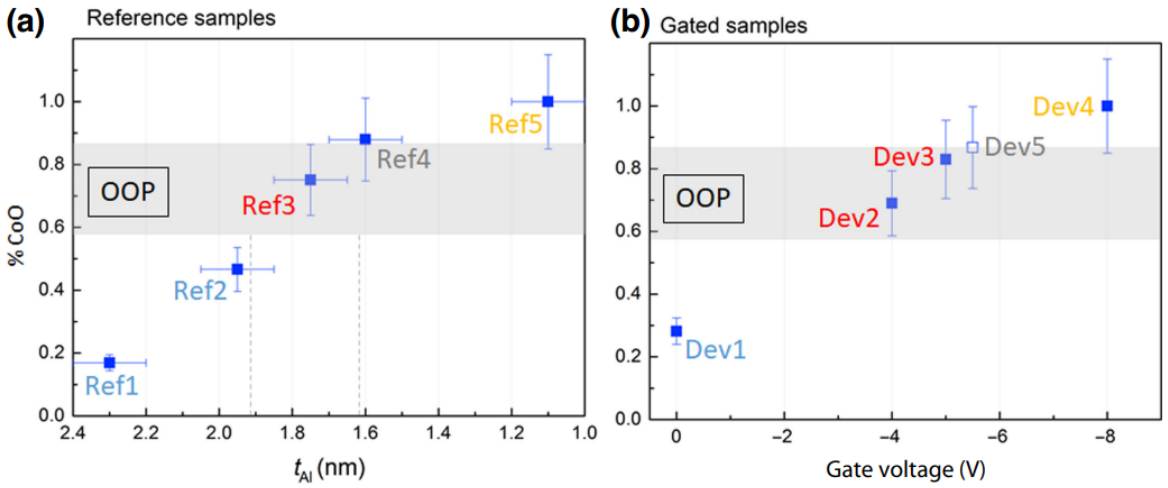

Figure 5.9: (From [144]) Oxidation percentage of the Cobalt layer, calculated using the ratio $\frac{CoO}{CoO+Co}$, with respect to (a) the thickness of the top Aluminum layer expressed in nm, it displays the values of the reference sample (b) the gate voltage applied, to shows the value of the gated devices. The Out-of-plane anisotropy region is highlight by the gray strip.

the increasing oxidation level in each sample, as expected for a decrease of the top Al thickness. Similarly, in Figure 5.9(b), this evolution is also visible for the devices samples, and the decrease between the Dev4 and Dev5 samples highlight once more the reversibility of the phenomenon. The Out-Of-Plane magnetization region is estimated to correspond to an oxidation between 60% and 88% (gray region in figure 5.9). For Ref3 sample, corresponding to the maximum remanence zone in the tri-layer system, it reaches 75% of CoO content.

5.4 Conclusion

This study constitutes a direct experimental evidence of the oxygen ion-migration under a gate voltage and therefore of the magnetoionic origin of the oxidation of Cobalt layer in Pt/Co/AlOx samples. High-energy photoemission spectroscopy (HAXPES) measurements, combined with anisotropy studies performed on both reference and gated samples clearly confirmed the modification of the oxidation state induced by the gate voltage. These findings establish that the well-known gate voltage-driven changes in perpendicular magnetic anisotropy (PMA) can be attributed to oxygen migration at the interface.
Furthermore, the analysis of the CoO percentage in the samples defines a specific oxidation range within which the magnetization is out-of-plane. Since this range is consistent for both reference and gated devices, it reinforces the conclusion that gate-controlled manipulation of magnetic anisotropy in the Pt/Co/AlOx system originates from interfacial oxygen migration.
The gate voltage control of magnetic anisotropy and the understanding of the underlying oxygen migration mechanism opens the way of the development of many applications, such as low-power logic and neuromorphic spintronic devices.

Chapter 6

Chirality reversal by gate voltage

6.1 Introduction 129
6.2 The sample: choice of the optimal parameters 130
6.3 Gate voltage application on domain walls in track 133
6.4 Gate voltage application on skyrmions in track 138
6.4.1 Optimization of the process 138
6.4.2 Attempt to reverse the chirality of a single skyrmions and problems encounter 141
6.5 Conclusion 146

6.1 Introduction

Magnetic skyrmions are currently of considerable interest both for the underlying physics and their potential applications, as they are small quasiparticles that can be moved by an electric current. In a previous work, Kumar et al [51] also reported the existence of two chirality reversal points in this tri-layer system within the region where skyrmions are energetically favorable. In the chapter 4 we mapped the chirality of the spin textures, and thus the sign of the DMI, in between these two points in the perpendicular magnetic anisotropy region. Improving our understanding of the DMI evolution in our sample. As discussed in the chapter 5 the application of a gate voltage locally changes the oxidation state at the ferromagnet/oxide interface. Also, Fillion et al. [52] showed the ability to adjust the interface magnetic properties, fundamental to the stability of skyrmions, by a gate voltage. In a nm-thick tri-layer system consisting of Heavy Metal (HM) / Ferromagnet(FM) / Metal Oxide (MOx), specifically Ta/FeCoB/TaOx, they proved that a gate voltage can not only create and erase skyrmions [132], but also modify the amplitude of the Dzyaloshinskii-Moriya interaction (DMI) [82] and its sign [52]. Such method is interesting for spintronics application since it allows a control of devices with low power consumption and provides an additional versatile, local and dynamic degree of freedom. Based on these results, this chapter investigates the gate-voltage control of the DMI sign, and consequently, the control of spin-texture motion inside μm-tracks.

First, I present the choice of the material parameters that seems more suitable for this

experiments. Then I describe the reversal of domain wall chirality inside a track. Finally I will discuss the attempts to control the chirality of a single skyrmion in a track using a gate voltage, the experimental challenges encountered, and the conclusions drawn.

6.2 The sample: choice of the optimal parameters

The tri-layer system used for this study is the same as presented before in the chapter 4 and studied in the team [27], [51],[132] : Ta/FeCoB/TaOx, with the top two layers deposited in a wedge allowing the stabilization of skyrmions, as seen in the section 3.1.1. We have seen that both wedges act on the anisotropy: by changing the ferromagnetic layer thickness we play on the effective anisotropy coefficient K_{eff}, and more particularly on the relative contribution of the dipolar and surface anisotropy. As discussed in the section 2.1.2. The second wedge, of the top heavy metal layer (tantalum) induces a change in the oxidation state at the interface with the ferromagnet. As seen in the section 2.1.1, a change in the oxidation at the interface influences the hybridization of the orbitals, playing on the anisotropy. Using the MOKE magnetometer (described in the section 3.2.2) we are able to obtain the map of the remanence of our sample. The remanence is the value of the magnetization that remains in a magnetic material after the external magnetic field has been reduced to zero, and after saturation. By analyzing the remanence map we can distinguish between perpendicular magnetic anistropy (PMA), in-plane anisotropy (IPA) and paramagnetic (PM) regions. The figure 6.1 shows the remanence map of our sample. The detail of all the different regions and their characteristics is written in the chapter 4 as the system is the same.

Skyrmions are stabilized at the transition region between perpendicular magnetic anisotropy (PMA) and in-plan anisotropy (IPA) or paramagnetic (PM) region. R.Kumar et al. [51] showed experimentally the existence of two chirality inversions in the region of the skyrmions. Using Brillouin light scattering (BLS) measurement the authors show the inversion in the DMI sign and revealed the presence of two regions where the DMI is zero. These two regions are represented by the red cross and star in the figure 6.1.

In the context of controlling a single skyrmion using a gate voltage, both regions may be relevant. They not only offer the possibility of skyrmion stabilization but also allow operation near the zero-DMI region, where relatively small gate voltages can significantly influence interfacial properties. A key phenomenon to consider in this context is the voltage-controlled magnetic anisotropy (VCMA), as discussed in Section 2.2.1. It is well established that the application of a gate voltage can modulate the magnetic anisotropy [70], [16],[151]. In our study, where the objective is to reverse the sign of the DMI and thereby switch the chirality of skyrmions via gate voltage, it is essential to take into account the variations in anisotropy induced by the applied voltage that could compete with the change in DMI. VCMA may as well influence the stability and size of the skyrmions and should ideally be reduced at the maximum.

In Chapter 4, I presented a detailed investigation of the DMI sign within the perpendicular magnetic anisotropy (PMA) regime of the tri layer system Ta/FeCoB/TaOx. Specifically, we examined how the sign of the DMI evolves as a function of both the ferromagnetic layer thickness and the oxidation state at the interface. This analysis enabled us to construct a DMI sign map

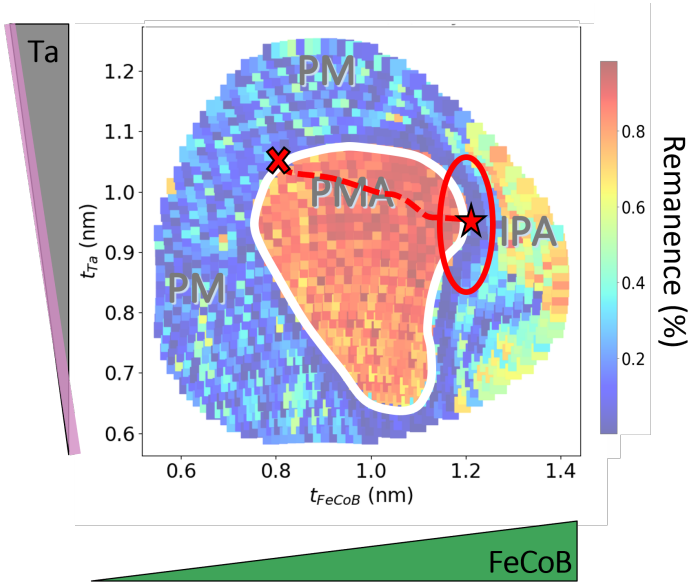

Figure 6.1: Remanence map of tri-layer system Ta/FeCoB/TaOx measured by MOKE magnetometry. The perpendicular magnetic anisotropy region is displayed in orange (large remanence) meanwhile the Paramagnetic (PM) region in blue (low remanence). The transition region between PMA and PM or In-Plane Anisotropy (IPA) is represented by the white line. The chirality inversion found in [51] is depicted by the red star and cross. The $D = 0$ line presented in chapter 4 is show by the red dashed line. The red ellispe corresponds to the interesting region for the study of the chirality reversal.

for the PMA region, in between the two regions previously studied in [51]. The resulting DMI sign map is shown in Figure 4.3.

Using current-induced domain wall motion measurements, we were able to determine the chirality of the domain walls and thereby the sign of the DMI, including the region where DMI ~ 0, represented by the red dotted line in Figure 4.3(a). A comprehensive discussion of our method and conclusions regarding the evolution of the DMI sign is provided in Chapter 4.

A particularly relevant feature for chirality control is the shape of the DMI = 0 (red dotted line) near the two skyrmion regions: the transition between PMA and the paramagnetic state (marked by a red cross) and the transition between PMA and in-plane anisotropy (red star). Near the paramagnetic boundary, the zero-DMI line is nearly vertical, implying that changes in oxidation primarily preserve the DMI sign. In contrast, near the PMA to in-plane anisotropy transition, the zero-DMI line is almost horizontal, indicating that small variations in oxidation can induce a sign reversal in the DMI.

We also note that the transition between the PMA and IPA regions (red star) is essentially vertical, whereas the transition between the PMA and PM regions (red cross) is horizontal. This indicates that variations in the interfacial oxidation state have a weaker effect on the anisotropy at the red-star location.

These differences are important for the gate-voltage control of skyrmion chirality. As demonstrated by the HAXPES measurements presented in chapter 5, applying a gate voltage modifies the oxidation state at a similar FM/Ox interface. In the region near the PMA to IPA transition (red star), this modulation can cross the DMI = 0 line while remaining along the skyrmion region, potentially enabling chirality reversal with relatively small gate voltages. Thus, this region, highlighted by the red ellipse in figure 6.1, is particularly promising for achieving efficient voltage control of single skyrmions.

Based on these conclusions, a first experimental demonstration of chirality switching using a gate voltage was carried out by Ch.-E. Fillion [52] in full sheet films. The initial step to apply a gate voltage consists of depositing a $10-20nm$ ZrO_2 or HfO_2 layer, which serves as both an electrical insulator and an ionic conductor. Both dielectric materials show similar results, the choice was made on the availability of the material and the previous deposition done using the ALD setup. In this configuration, the flow of electrons is blocked, while the application of a gate voltage induces the migration of oxygen ions.

The gate voltage is applied via an indium tin oxide (ITO) metallic pad, which offers the advantage of optical transparency, thereby enabling the in-situ observation of spin texture dynamics using a magneto-optical Kerr effect (MOKE) microscope. The specific deposition techniques for both the dielectric and ITO layers are detailed in Section 3.1.1, while the MOKE imaging method is described in Section 3.2.1. A schematic representation of the complete layer stack used in the experiment is provided in Figure 6.2.

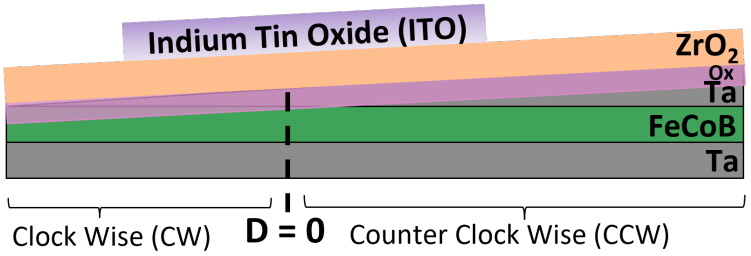

Figure 6.2: 2D cut of the full system along the top Ta wedge. With the ZrO_2 layer and the Indium Tin Oxide pads on top of the tri-layer system.

To summarize the work presented in [52] (and detailed in Section 2.2.2), the authors demonstrated that, by applying a gate voltage in the region near the red star (as defined in Figure 4.3), it is possible to reversibly and persistently switch the chirality of spin textures, skyrmions and domain walls (DWs), in full films. The objective of our study is to extend this approach to individual spin textures, specifically focusing on the control of single domain walls and skyrmions confined in tracks. On the contrary, this previous work focused on full film samples, where skyrmions were annihilated and then new skyrmions were stabilized with a new chirality following the application of a gate. This process resulted in a loss of information. The next objective is to change the chirality of a single skyrmion without this information loss, thereby preserving the same skyrmions throughout the process.

6.3 Gate voltage application on domain walls in track

The first step is the design of the tracks. I developed a Hall cross geometry, presented in the figure 6.3(a). This geometry has been thought to develop in the future electrical measurement of the Hall resistance, enabling the electrical detection of magnetic textures and particularly of skyrmions. The pink part corresponds to the magnetic tri-layer region. The purple part is the ITO electrodes used to apply the gate. In between them, a layer ($\sim 18nm$ thick) of ZrO_2 or HfO_2 is deposited. By applying a current I in the vertical magnetic track, spin textures are moving. The two purple ITO electrodes along this tracks are the region where the gate will be applied and therefore where the change of chirality may happen. In the figure 6.3(b) a MOKE image of a device is shown.

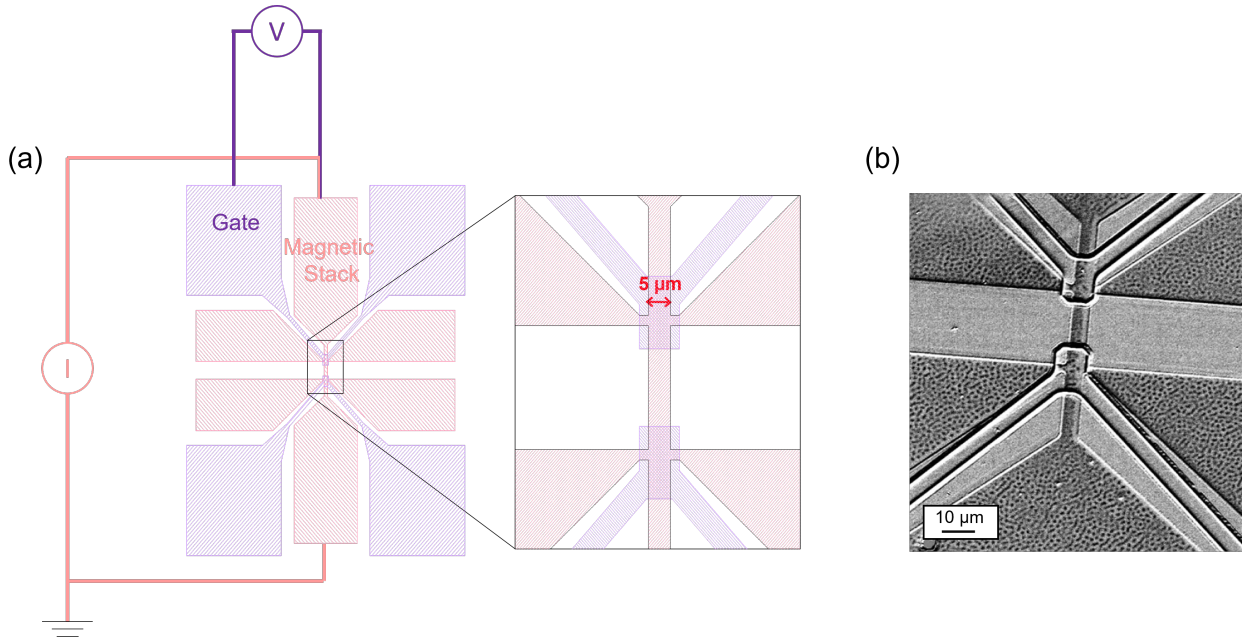

Figure 6.3: (a) Full layout of one Hall cross device. The tri-layer Ta/FeCoB/TaOx is deposited following the pink geometry. The Indium Tin Oxide gate pads are deposited in the geometry of the purple regions. A current I is applied along the long track and the gate voltage is applied in between the tri-layer system and the ITO pad passing through the dielectric layer(not indicated in the figure). (b) P-MOKE differential imaging of one Hall cross devices.

While the determination of the current density required to move spin textures is straightforward, typically on the order of $\sim 5GA/m^2$, the gate voltage necessary to reverse the chirality is more complex to assess. In the work of Fillion et al. [52], a gate voltage of approximately 3-4 V was sufficient to induce a chirality switch in full films. However, it remains uncertain whether this voltage range is directly applicable to confined geometries as tracks.

Additionally, the quality of the dielectric layer, ZrO_2 or HfO_2, plays a crucial role in defining the maximum applicable gate voltage. Beyond a critical value, known as the threshold voltage, the insulating properties degrade, leading to current leakage through the dielectric. To determine this threshold, I-V (current-voltage) measurements are systematically performed before

any gating experiments, in region of the sample with paramagnetic behaviour in order not to damage the interesting devices.

Figure 6.4(a) shows an IV curve characteristic of a good insulating device: the current remains negligible until a threshold voltage(9V here), is reached. Beyond, a measurable leakage current (on the order of tens of nA) appears, indicating the onset of dielectric breakdown. In contrast, Figure 6.4(b) illustrates a different behavior: no clear threshold is observed, and the current reaches the compliance limit (of $1\mu A$) even at low voltages. This suggests poor dielectric quality, where the current flows through the ITO layer and the oxide into the magnetic stack, preventing effective gating. In such cases, the gate voltage is not properly applied to the magnetic sample and current is rather injected in pinhole sites. Different reasons can be at the origin of this current injection: the thickness of the effective dielectric layer or the quality of the deposition are the ones relevant for us.

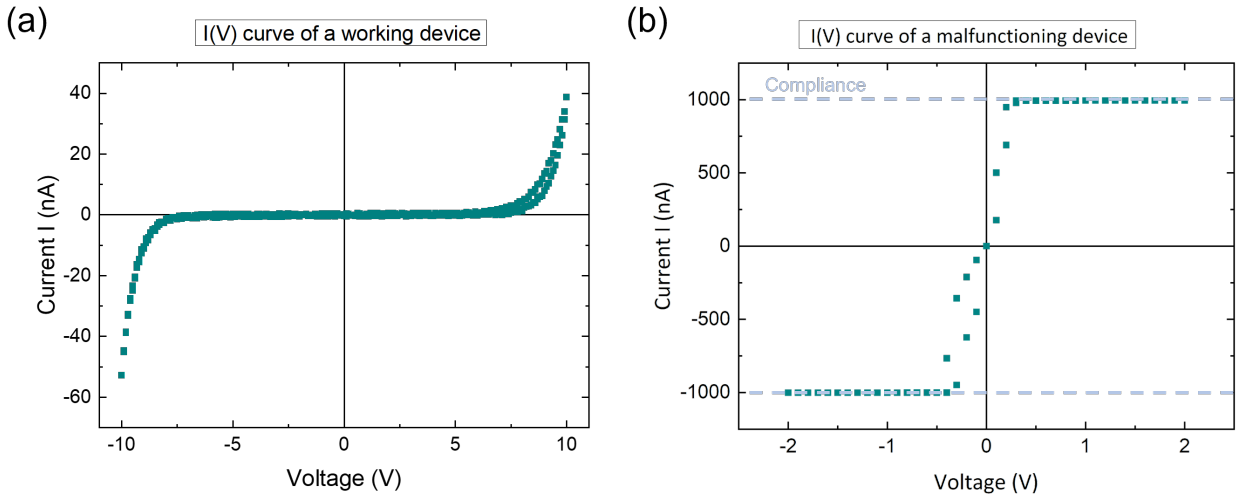

Figure 6.4: Current measured through the HfO_2 layer with respect to the gate voltage applied for a (a) working layer acting like an electronic insulator and (b) malfunctioning sample allowing electrical current to flow through the layer.

Once the threshold voltage is determined we need to locate on the sample the interesting region (close to the red star in the anisotropy map presented in the figure 6.1). To do so, contrary to full sheet sample, we cannot perform MOKE magnetometer mapping to access quickly magnetic properties. Instead, we use the MOKE imaging method to find the skyrmion region, as explained in the section 3.2.3. The figure 6.5 shows the reconstituted map of the magnetization of our sample. Each square is a differential image taken under the MOKE microscope that has been then superposed with the neighboring images using defects, edges of the sample, and patterned crosses to superpose as precisely as possible one image after the other. It is now easy to identify the interesting region for our study, as the contrast is different in the devices delimiting the PMA region. The interesting region is represented in the figure 6.5 by the region free of hatched and more specifically in the red circle. We note here that the I-V measurements has been performed in the hatched purple region.

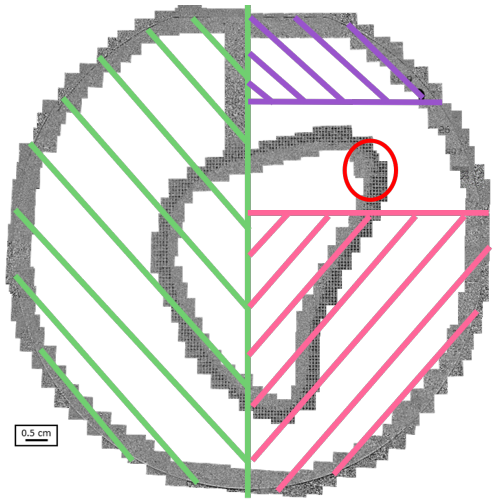

Figure 6.5: P-MOKE map of the sample. Each 0.5 cm size square is an image taken from the MOKE microscope then superimposed to each other to form the whole map. The transition of anisotropy is where the black and white contrast change. The hatched purple region is where the I-V curves has been measured. The red circle in the region free of hatches is where the gating experiments are performed.

Now that both the region of interest and the threshold voltage have been identified, the gating experiments can be carried out. Figure 6.6 shows the experimental setup. The sample is first mounted onto a sample holder and electrically connected using micro-bonding technique. The holder is then placed under the MOKE microscope and connected to two sourcemeters: one to inject the current and the other to apply the gate voltage.

Different phenomena have been observed while applying a gate voltage on DWs. First we are able to invert the chirality of the domain walls inside the track by applying a gate. The figure 6.7 summarize the principle: starting by an initial state of a counter clockwise chirality of the domain walls by applying a negative gate of $-2V$ during 1 min 30s the chirality is inverted, the domain walls becomes clockwise. This is consistent with the results of Ch-E. Fillion et al. [52]. In addition, we wanted to test the reversibility of this process. We therefore applied a positive gate successively after the first inversion of chirality. A second inversion of chirality is obtained by applying a positive gate of $+2V$ during 2 min. It is worth noting that this second reversal is not stable over time: after a few seconds, the chirality relaxes back to the intermediate state. To initially switch the chirality from CCW to CW, a negative gate voltage is applied in order to drive oxide ions toward the ferromagnet. Since oxidation of the sample is more favorable than reduction, this explains why the reversal towards CCW is not persistent whereas towards CW it is.

)m!p

During the gating experiments to reverse the chirality we also noticed different behaviors: First, the application of a gate voltage, with the appropriate polarity, reduces the velocity of the domain walls, making their motion more difficult to observe. Consequently, a higher applied current was required to induce DW motion. This effect can be explained by the fact that gating modifies the value of the Dzyaloshinskii-Moriya interaction (DMI) coefficient. As reported in [30], the velocity of spin textures is strongly linked to the DMI strength. This change in the

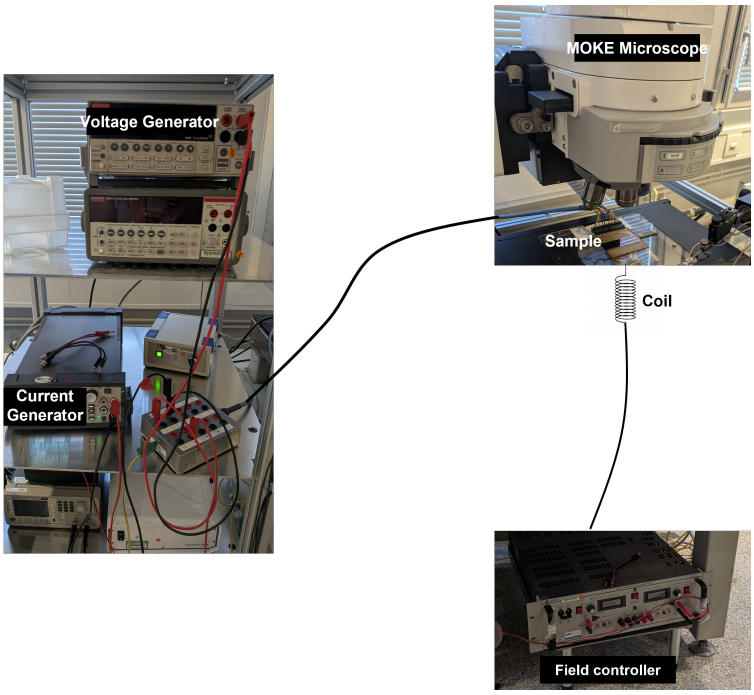

Figure 6.6: Picture of the MOKE microscope setup: The sample and sample holder are placed on a motorized stage above a coil controlled by a KEPCO in order to applied an external magnetic field (picture below) on the sample and below the microscope. The current and the gate are injected into the sample thanks to two Keithley 4550 (left picture).

velocity with the DMI comes from the the fact that small DMI value leads to the stabilization of intermediate or Bloch spin textures. In these intermediate or Bloch-type spin textures the efficiency of spin-orbit torque (SOT) is lower due to the spin orientation within the texture. Since SOT is the main driving mechanism for current-induced motion in our system, this reduction in efficiency directly leads to a lower DW velocity.

We also noticed that once chirality inversion occurred, a competition arise between the domain walls located at the edge of the ITO pad (region indicated by the red circle in Fig. 6.8(a)). In the example shown in the figure, the domain walls were initially clockwise (purple arrow outside the ITO pad). After applying a gate voltage of +2 V for 2 minutes, the chirality beneath the ITO pad was reversed, and the domain walls in this region became counterclockwise. At the pad edge, domain walls of opposite chirality met and annihilated. One possible explanation is that the interaction between domain walls of opposite chirality leads to their mutual annihilation. Alternatively, a sudden change in chirality could destabilize the spin textures, causing their disappearance. In either case, a clockwise (resp. counterclockwise) domain wall located outside the gate pad is not energetically favored upon entering a counterclockwise (resp. clockwise) region, due to the inversion of the DMI coefficient sign, as explained in the section 1.2.1.

Finally, we noticed in some cases that, after bonding the Hall cross and before applying any gate voltage, a change in the anisotropy under the ITO pads occurred, as shown in Fig. 6.8(b). This is visible by the change in the external field necessary to stabilize skyrmion. A first hypothesis was that this change originated from the deposition of the ITO pads. However, this

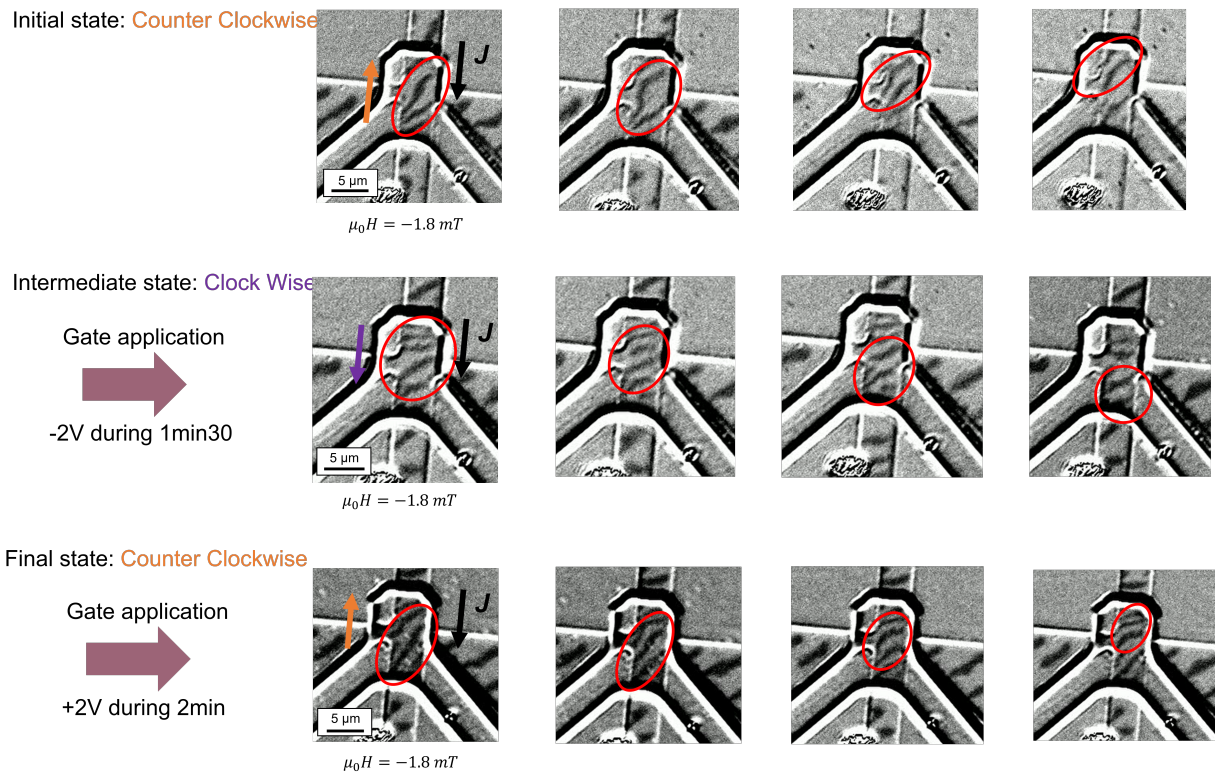

Figure 6.7: MOKE imaging of a Hall cross under an external field of $\mu_0 H = -1.8mT$. A current density of $\sim 5GA/m^2$ is injected in the vertical track. Initially the domain walls are counterclockwise, moving against the current density J. After the application of a negative gate of -2V during 1min30s the chirality is reversed, the DWs became clockwise, moving along the current J. Finally after the application of a positive gate of +2V during 2 min the initial chirality is found back.

was refuted by observations of the Hall cross prior to wire bonding, since the size of domain walls was identical inside and outside the ITO pads. We then suppose that this change in anisotropy is caused by the wire bonding step. The use of ultrasonic vibrations might create small electrical potentials and affect the anisotropy, particularly in the very sensitive transition region where the experiments are performed. This change in anisotropy prior to any gate voltage application was observed in different Hall crosses across multiple samples. However, this is not systematic: some crosses and samples did not exhibit it.

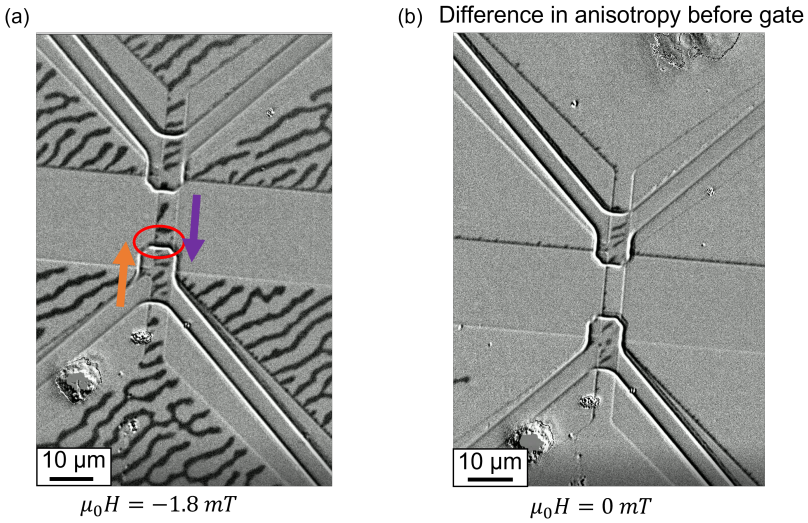

Figure 6.8: (a) MOKE imaging of a Hall cross under an external field of $\mu_0 H = -1.8mT$. The orange (resp.purple) arrow represents the direction of motion of the counterclockwise (resp.clockwise) domain walls located below (resp. outside) the gate pads. The red circle corresponds to the region where DWs with each chirality meet. (b) MOKE imaging of a Hall cross under an external field of $\mu_0 H = 0mT$. The anisotropy below and outside the gate pads is different.

6.4 Gate voltage application on skyrmions in track

The second step in this study is to reverse the chirality of a single skyrmion in a track. First, few problems need to be addressed: skyrmions are located in the left edge of the track, making their motion more difficult. Also, there are only a limited number of interesting devices for this study on the full sample. We will see in a first part the optimization of the process performed to address these problems. Then in a second time we will presents the experimental try on the reversal of chirality of the skyrmions and the problems encounter in the application of the gate.

6.4.1 Optimization of the process

1- As we can see on the figure 6.9(a) skyrmion are close to the left edge of the vertical track making their motion difficult due to edge effect.

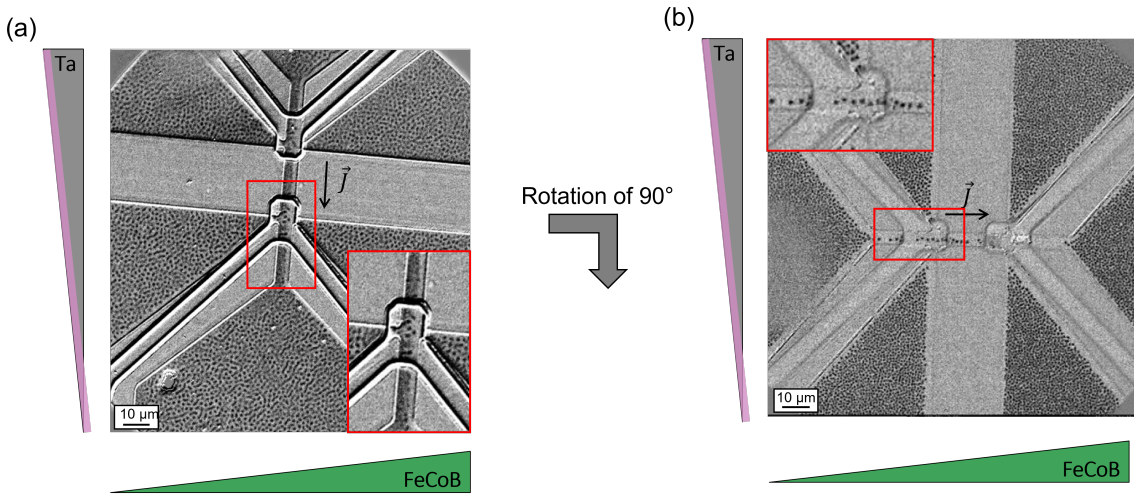

Figure 6.9: P-MOKE differential images of one device (Hall cross) with different orientations of the long track, along which the current is applied and the skyrmions are moving: (a) parallel to the top Ta wedge and (b) parallel to the FeCoB wedge. The 90° rotation is made during the first lithography step, described in the section 3.6.

While Jiang et al. [126] attribute the accumulation of skyrmions at the device edges to the skyrmion Hall effect (see Section 2.3.3), we argue that this accumulation instead arises from a shadowing effect occurring during the deposition of the ferromagnetic layer. Indeed, if the accumulation were due to the skyrmion Hall effect, reversing the applied current would cause the skyrmions to accumulate on the opposite edge of the track, which is not observed in our experiments. Moreover, the accumulation of skyrmions is already present before to the application of any current.

Figure 6.10(a) recalls the wedge deposition technique used for our thin films. Figure 6.10(b) shows a schematic side view of a patterned Hall cross. During deposition, the resist used to define the Hall cross geometry partially blocks the incoming tilted flux near its edges, thereby reducing the deposited thickness in the regions shown with gray and red hatching. We refer to this as the shadow effect. As a result, skyrmions tend to be trapped at the opposite edge of the device. To avoid this effect we decided to turn by 90° the devices with respect to the deposition direction in order to align the long track with the target of the material to be deposited; in this case the ferromagnetic layer FeCoB. The figure 6.11(a) represents the previous deposition position, the Hall cross is represented in green in the scheme (we voluntarily omit to represent the gate pad for a better understanding). The long track is perpendicular to the direction of the wedge leading to the shadow effect. By turning by 90°, figure 6.11(b), the long track is aligned with the deposition direction, reducing the shadow effect.

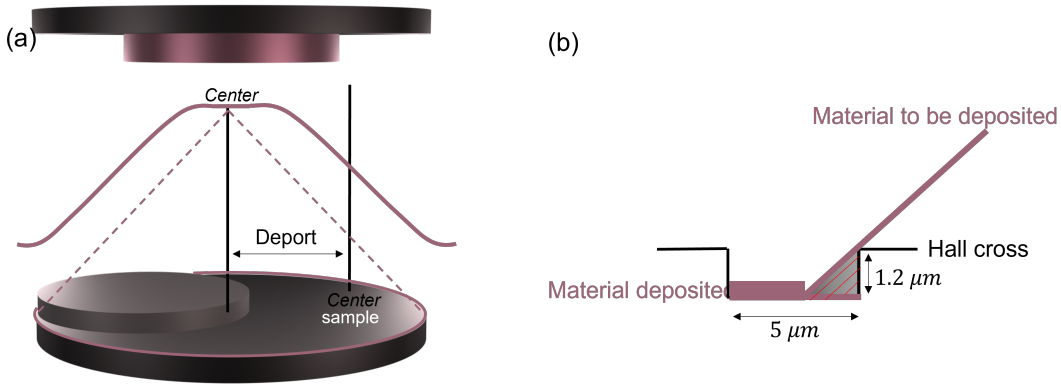

Figure 6.10: (a) 3D Scheme of Off-axis deposition technique. The sample is misaligned with respect to the target by a value "deport". The dotted line represents the conical deposition distribution and the thick pink line represents the thickness of the deposited layer with respect to deport. (b) Side view scheme of the the long track in one of the Hall cross device. In pink the material to be deposited, in our case the ferromagnet. The track being perpendicular to the wedge the deposition technique results in a "shadow" effect, represented by the gray and red hatched area.

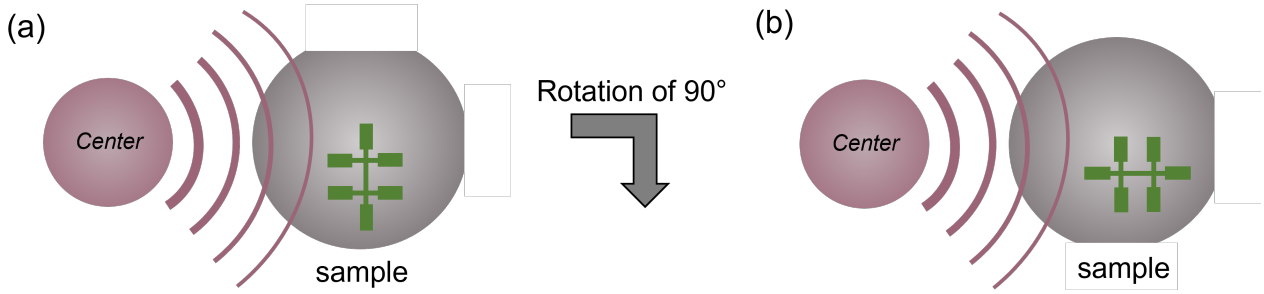

Figure 6.11: Top view of the off-axis deposition, pink lines represents the iso-thickness lines. A zoomed Hall crossed is represented in green for the different orientations of the long track: (a) perpendicular to the direction of deposition and (b) parallel to the direction of deposition.

The figure 6.9(b) shows the result, skyrmions are aligned and in the center of the track enabling a good motion under current with less pinning on the track edges.

2 - The second challenge concerns the number of Hall crosses on a 4-inch wafer that meet the conditions required for our gating experiments. Only a few devices are located in the anisotropy transition region needed to stabilize skyrmions and are simultaneously close to the DMI ~ 0 zone. To increase the number of potentially usable devices, we focused our fabrication on the relevant region by reducing the wedge gradient by reducing the slope value during the deposition, as explained in section 3.1.1. this leads to a broadening of the overlap between the anisotropy transition and the DMI ~ 0 zones. The figure 6.12(a) is the previous anisotropy map of our sample. In the figure 6.12(b) we show the zoom on the interesting region, represented by a red circle, at the transition between perpendicular magnetic anisotropy (PMA) and the in-plane

anisotropy (IPA).

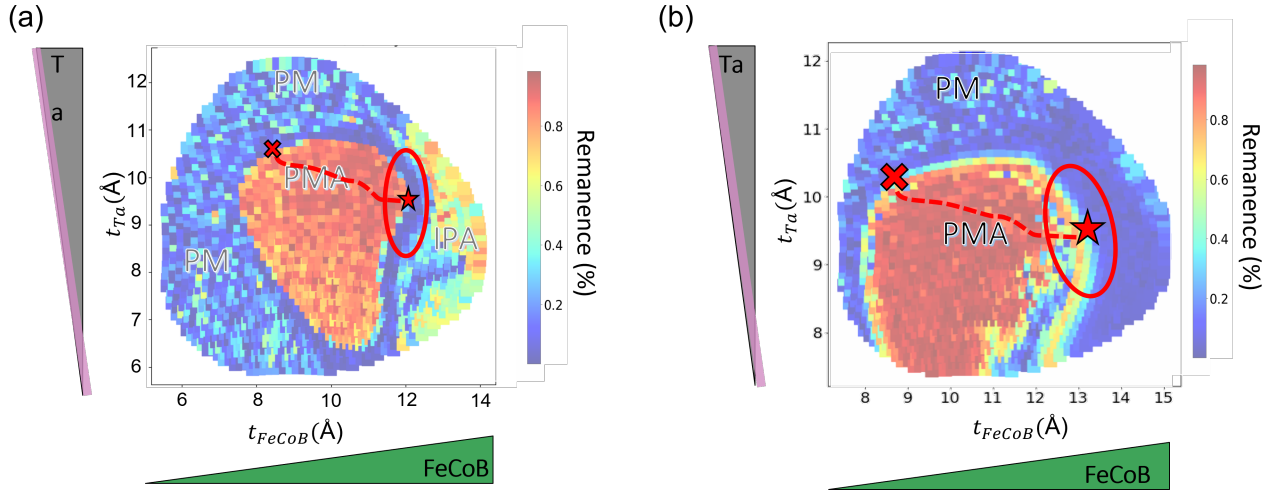

Figure 6.12: Remanence map of tri-layer system Ta/FeCoB/TaOx measured by MOKE magnetometry. The perpendicular magnetic anisotropy region is displayed in orange (large remanence) meanwhile the Paramagnetic (PM) region in blue (low remanence). The transition region between PMA and PM or In-Plane Anisotropy (IPA) is represented by the white line. The chirality inversion found in [51] is depicted by the red star and cross: (a) For the wedges used in the previous studies and (b) with reduced gradients to zoom on the interesting region. The red ellipses are the region of interest for the chirality inversion measurement.

6.4.2 Attempt to reverse the chirality of a single skyrmions and problems encounter

Despite optimization of both the samples and the devices, the application of a gate voltage was not successful in reversing the chirality of a single skyrmion. During our trials, we encountered several issues that could explain this inability to reverse chirality in our samples. In the following, we describe each of these problems and discuss the conclusions that can be drawn from them.

First, in many of our samples, we encountered a problem during the ALD deposition step: the process occasionally stopped midway due to a connection failure between the control computer and the ALD system. At this point, we could either proceed with gating experiments on the partially deposited sample, or attempt to resume the deposition. In most cases, the dielectric layer exhibited defects that rendered gating impossible, as its insulating properties were lost. Indeed, IV measurements performed on these samples showed a conductive behavior, as illustrated in Fig. 6.4(b). We also tried to resume deposition after an interruption; however, the IV characteristics remained characteristics of conductive behavior. We attribute this to the fact that, when the disconnection occurred, the deposition chamber returned to atmospheric pressure, which likely altered the surface and prevented the resumed process from reproducing the quality of a continuous deposition. In addition, a visible color gradient was sometimes observed on the wafers after interrupted ALD deposition of the dielectric layer (Fig. 6.13(a)), which we

attribute to non-uniform film thickness. It is worth noting that this color gradient was not always present, but in all cases of interrupted deposition, the IV measurements indicated a low quality conductive dielectric layer.

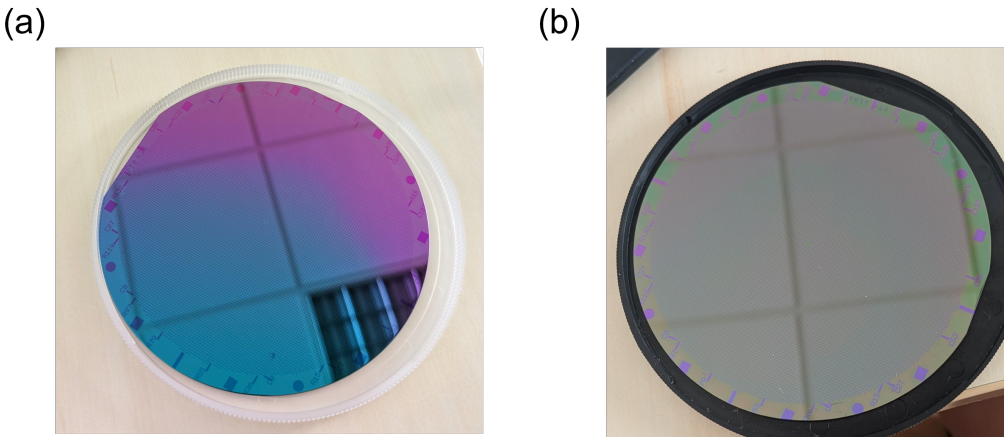

Figure 6.13: Picture of the sample after ALD deposition of the dielectric layer (a) the deposition has been interrupted, a gradient of color can be seen over the sample and (b) the deposition finished properly, the color of the sample is uniform.

For the sample for which the ALD deposition worked, the IV measurements shows that the insulating characteristics of the dielectric layer was "unbreakable". We apply until $\pm 20V$, no threshold voltage is found. However to apply the gate the threshold voltage and the breaking is not relevant, even more to avoid. Therefore the minimum limit of $20V$ is more than enough for our gating experiment that require generally few volts. But this could indicate a problem with the dielectric layer, either in term or deposition parameters or quality.

The dielectric deposition was primarily performed using the ALD system at Institut Néel. We also attempted depositions with another ALD machine at BCAi. However, the first deposition obtained there was fully conductive, and the second did not yield better results than those from the Institut Néel. Consequently, we decided to continue using the first machine, which provided the depositions enabling the reversal of domain wall chirality, presented before.

The samples for which we conduct gating experiments didn't show a reversal in the chirality of skyrmions. However some phenomenon has to be noted. First, as talked for the chirality reversal of the domain walls inside the tracks, a change in the anisotropy is seen as well. This is the VCMA, explained in the section 2.2.1. The figure 6.14 shows that the application of a negative gate voltage changes the size and the density of skyrmions. The initial chirality of these skyrmions was counterclockwise, thus the application of a negative gate is needed to reverse the chirality. However before it is possible to see a change in the direction of motion of the skyrmions, proof of the reversal of chirality, the skyrmions under the gate appear smaller than before, the density of skyrmion increases as well, figure 6.14(b). While the reduced size of skyrmions makes them difficult to see using the MOKE microscope, the increased density favored the interaction in between skyrmions which, once again, makes the motion of skyrmions more difficult.

The videos and images are acquired using the MOKE microscope with differential imaging

method. First, the sample is saturated magnetically, and a background image is taken in this state. Then, the external magnetic field is reduced, allowing spin textures to appear in the differential image obtained by subtraction from the background. This technique is highly sensitive to any motion of the sample, the microscope, or other optical components. As a result, the background must be updated regularly. A new background is done, figure 6.14(c), showing that under the gate no skyrmions can be stabilized anymore, the magnetization of the whole track under the gate pads have a different polarity, which is not reversible, even by the application of an external field.

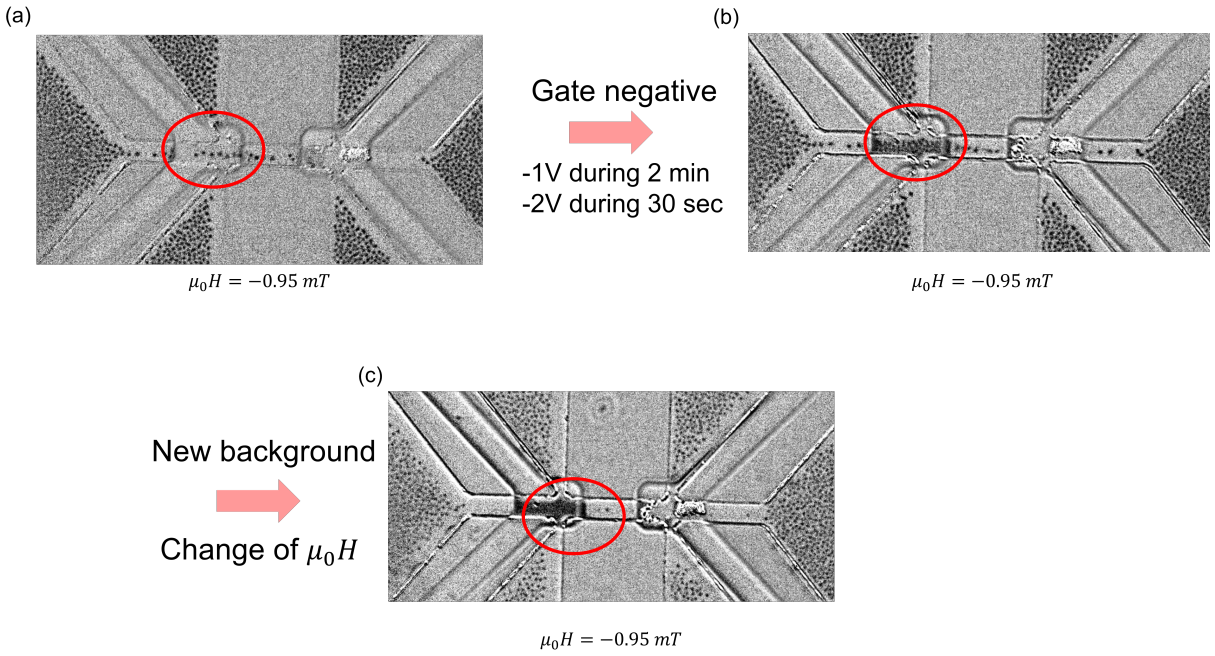

Figure 6.14: P-MOKE differential imaging of one Hall cross device at (a) pristine state, with a line of skyrmion stabilize in the track (b) after the application of a gate voltage -1V during 2min and -2V during 30sec, the size of the skyrmions under the gate reduces and the density increases (c) a new background image is taken, no possibility to stabilize skyrmions anymore.

In the figure 6.15 we see that the application of a positive gate can also change the spin textures. Initially skyrmions were stabilized, figure 6.15(a). After the application of a positive gate the skyrmions disappear, figure 6.15(b). A new background image is done and under the same conditions only domains are stabilized under the gate, figure 6.15(c).

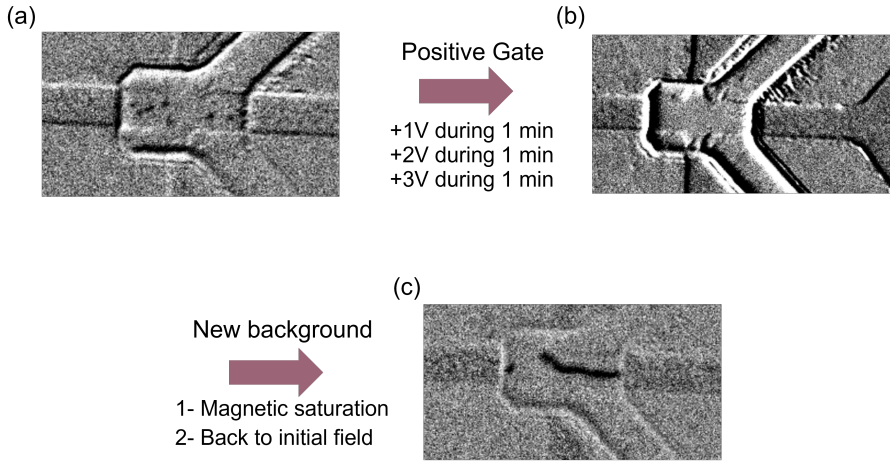

Figure 6.15: P-MOKE differential imaging of one Hall cross device at (a) pristine state, skyrmions are stabilized under the gate. (b) after the application of a gate voltage of +1V, +2V, +3V (all during 1 min), skyrmions under the gate disappeared (c) a new background image is take, only domains can be stabilized under the gate.

To reverse this effect we try to apply a gate of opposite polarity. As shown in the figure 6.16(a)-(b), the first application of a negative gate increased the density of skyrmions under the gate and reduced their size. Then, after the application of a positive gate we see the stabilization of bigger skyrmions, as in the initial state, figure 6.16(c).

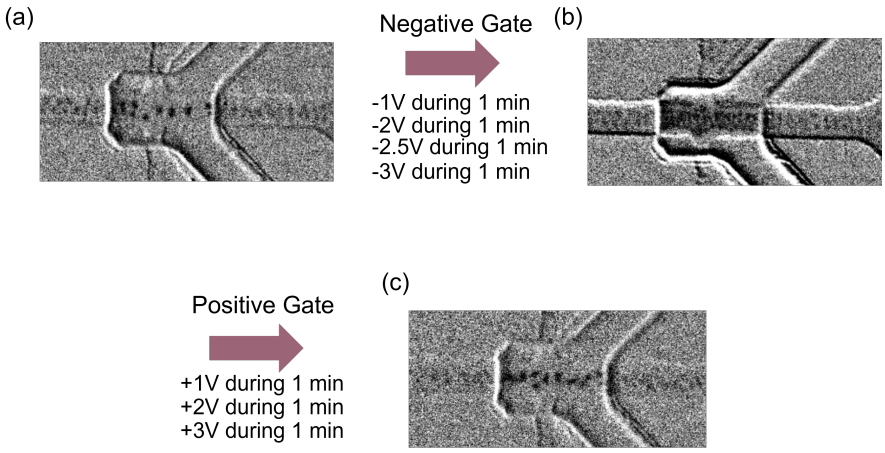

Figure 6.16: P-MOKE differential imaging of one Hall cross device at (a) pristine state, line of skyrmion is stabilize under the gate. (b) After the application of a gate of -1V, -2V, -2.5V during 1min each and -3V during 30 sec, the size of skyrmions under the gate is reduced and the density is increased (c) positive gate voltages of +1V, +2V, +3V during 1min each is now applied, the initial state of anisotropy is found back.

This change in anisotropy under the application of a gate voltage is actually expected, as it is a well-known effect called the voltage control of magnetic anisotropy (VCMA), detailed in the section 2.2.1. In our case, the study is at the transition region between the perpendicular

magnetic anisotropy (PMA) and the in-plane anisotropy. As discussed before, applying a gate modifies the oxidation state at the interface between the ferromagnet and the heavy-metal oxide layer. As discussed in section 1.2.1, the stabilization of skyrmions requires specific material parameters, which is why we use a double-wedge system. It is therefore not surprising that the application of a gate can shift the anisotropy away from the optimal conditions for skyrmion stability. A deeper and more systematic study on the anisotropy change in our sample would be necessary to progress towards the control of a single skyrmion in a track, which was not possible during my PhD due to the many problems I had with the ALD deposition.

It is noteworthy to say that other different behaviors that can corrupt the possibility to reverse the chirality of skyrmions has been observed:

• The use of one of the gate pad can have consequences on the other one even if the second one is not connected. Either the gate "breaks" (seen optically under the MOKE microscope) either the anisotropy change. This could suggest the presence of defects in the dielectric layer but it can also been explain by an in-plane gradient of potential created by the current application as Ch-E. Fillion detailed it in his manuscript [27]. The figure 6.17 (a)-(c) schematizes the application of a gate without current applied, leading to a homogeneous gate voltage application. Meanwhile, if a current is applied, figure 6.17(d)-(f) the gate application becomes inhomogeneous due to the additional potential coming from the current source. This could be at the origin of the change observed under a non-connected gate.

• A difference in the chirality below the ITO pads and in the tracks outside the pads has also been observed in non-gated devices few times, as it has already been observed on domain walls. We suspect is this case as well the wire bonding step, used to connect the sample to the sample holder, to be at the origin of this. Indeed ultrasonic vibrations are used in the micro bonding technique that can create a small potential that could be seen as a gate voltage application.

However these phenomena were not consistently observed in every sample or in every device, making it difficult to conclude on their role in the non-reversibility of the chirality.

Finally, for the moment, the reversal of chirality and therefore the control of a single skyrmions in a track could not be achieved. Even if a decrease of the velocity may be seen after the application of a gate, an indication of a DMI closer to 0 and so an approach to the change of chirality. It is complicated to quantify the velocity of a skyrmion in a track due to the stability of the focus over the time in the setup. Therefore we choose to not discuss about this change of velocity as a result. Even if it is important to note that the reduction of the velocity that we observed could be a proof that we are close to reverse the chirality. However we also notice an anisotropy change, happening before the reversal of the chirality.

However, it is still important to note that there is a change, either in terms of anisotropy or velocity of the skyrmions. This confirms the application of a gate. Some other studies are needed to understand the different difficulties encountered, their consistence over different devices and/or samples and what can be done to overcome them and successfully reverse the chirality of a single skyrmion in a track.

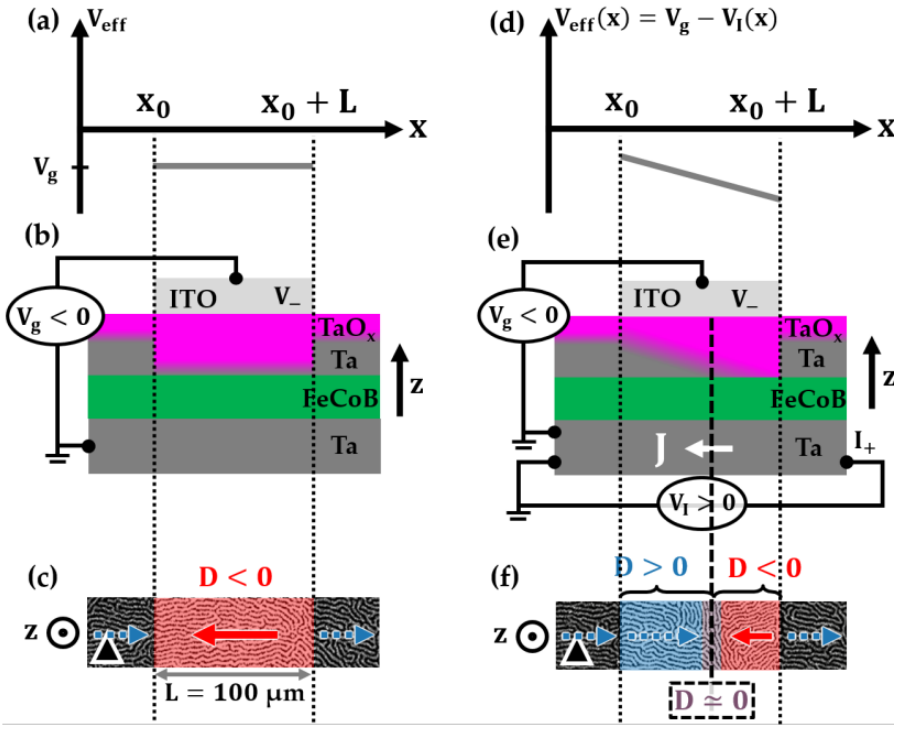

Figure 6.17: *Figure taken from the PhD manuscript of Ch-E. Fillion [27]*: Scheme of the gate voltage application on the Ta/FeCoB/TaOx tri-layer system(ac) Without current: (a) the gate voltage is applied uniformly, (b) the oxidation state change at the interface is uniform, and (c) a homogeneous change in the DMI sign is obtained. (d)-(f) with current: (d) an additional gradual potential $V_I(x)$ is created (e) the oxidation change becomes non-uniform under the gate, and (f) this induces a non-uniform change in the DMI sign beneath the gate pad.

6.5 Conclusion

In this chapter, I investigated the possibility of reversing the chirality of spin textures in a magnetic track. We demonstrated that it is possible to control the direction of motion of domain walls, and therefore their chirality, via gating. However, the control of a single skyrmion in a track was not achieved. Two main limitations prevented this: 1- Issues during the ALD deposition of the dielectric layer, which compromised the electrical insulation required for reliable gate voltage application, and 2- Changes in magnetic anisotropy under gating that obscured the detection of chirality reversal.
These effects made it difficult to confirm whether chirality reversal could occur under these conditions.

To progress towards this goal, several studies could be envisioned. First, a detailed investigation of the dielectric layer as its deposition parameters and/or uniformity could ensure robust gating conditions. Second, a systematic study of gate-voltage control of magnetic anisotropy in our samples will help clarify the observed behavior and identify the conditions for chirality reversal.

Finally, if skyrmion chirality reversal is achieved, it will be important to examine the behavior of skyrmions as they exit the gated region. As observed for domain walls, abrupt changes in chirality at the gate pad edges can lead to the disappearance of spin textures, possibly due to competing DWs with opposite chirality or the sudden change in chirality imposed by the oxidation state at the interface. Understanding these transitions will be crucial for future device integration.

Chapter 7

Micromagnetic analysis of skyrmion trajectories in systems with weak Dzyaloshinskii-Moriya interaction

7.1 Introduction 149
7.2 Micromagnetic simulation parameters and initial state 150
7.3 Motion of skyrmions under small current 157
7.3.1 Trajectories 157
7.3.2 Large Skyrmion Approximation 163
7.3.3 Effect of the damping on the trajectories 166
7.4 Motion of skyrmions under high current 169
7.5 Conclusion 176

7.1 Introduction

We have seen in the previous section an experimental study of a static and dynamic control of the skyrmion chirality. We particularly highlighted the link between the Dzyaloshinskii-Moriya interaction sign with the chirality that associated with a chiral dependent motion of the spin textures allowed us to map the DMI sign in our tri-layer system. Then, we detailed a dynamic way to control the chirality using a gate voltage. The combination of these two studies should allow the control of the motion of the skyrmions. But in order to fully understand their motion, in particular in weak DMI regime as in the experimental samples, we performed micromagnetic simulation

In a first part we describe the parameters used for the simulation to stabilize skyrmions associated with a study of the skyrmion characteristics, such as the radius, the domain wall width and the helicity with respect to the DMI value. Then, in a second part, we study the motion of skyrmions under a small current density ($J = 10^{10} A/m^2$). Particularly we focus on the trajectories of the skyrmions to validate a model describing the trajectory of the skyrmion only with measurable parameters, such as the radius, the domain wall width, the helicity and

the polarity. In the same time we also study the effect of damping on skyrmion trajectories. Finally, we increased the current density to $J = 10^{11} A/m^2$ to see the effect on the skyrmion dynamics.

The simulations presented in this chapter build upon the previous work of Ch-E. Fillion, as reported in his PhD manuscript [27]. In the present work, I have reproduced all of his simulations and further extended the study, especially with varying damping and the study of high current regime.

7.2 Micromagnetic simulation parameters and initial state

For this study we performed micromagnetic simulation using Mumax^3 software package [152],[153]. First we performed a static study of the skyrmions. Simulation parameters are described in the table 7.1. Experimentally the ferromagnet is iron rich, however using Fe based parameters leads to the stabilization of skyrmionic bubbles, too large to be efficiently studied due to simulation size and thus time problem. Therefore the parameters in the table 7.1 correspond to Cobalt based parameters, adjusted from [125], allowing the stabilization of nanometer size skyrmions, more convenient to study them in simulations. Parameters has been optimized to allow the stabilization of Bloch skyrmions even at $D = 0$.

Number of cells	(N_x, N_y, N_z)	(512, 512, 1)
Size	(L_x, L_y, L_z)	(512, 512, 1) nm
Periodic Boundary Conditions	PBC	(10,10, 0)
Magnetic damping	α	0.05; 0.5; 1
External magnetic field (for dynamic study)	$\mu_0 H_{ext}$	-6 mT
Magnetization	M_s	1.42×10^6 A/m
Exchange Stiffness	A_{ex}	1.6×10^{11} J/m
Uniaxial anisotropy	K_u	1.27×10^6 J/m^3
Interfacial DMI	D	[-0.5; +0.5] mJ/m^2

Table 7.1: Simulations parameters

The goal of this study is to study the motion of the skyrmions under low and high current, Periodic Boundary Conditions (PBC) are therefore set to approximate a large (infinite) system while applying a current. However to ensure the stabilization of a single skyrmion and remove any neighbor effects we first apply the demagnetizing field of an infinite saturated thin film all around the simulated cell to stabilize first single skyrmions. To do so we calculate the field of an infinite thin film to which we remove the one of the simulated 'box'. Finally, we obtained the demagnetizing field necessary to simulate an infinite thin film in the surrounding of the simulation cell. The figure 7.1 summarizes this process.

Using this method we stabilize a single skyrmion for a set of DMI value $\in [-0.5; +0.5]$ mJ/m^2. A first parameter intrinsic to the skyrmion is its helicity. As defined in the figure 7.2(a) the helicity is the angle in between the spin in the middle of the domain wall of the skyrmion and the

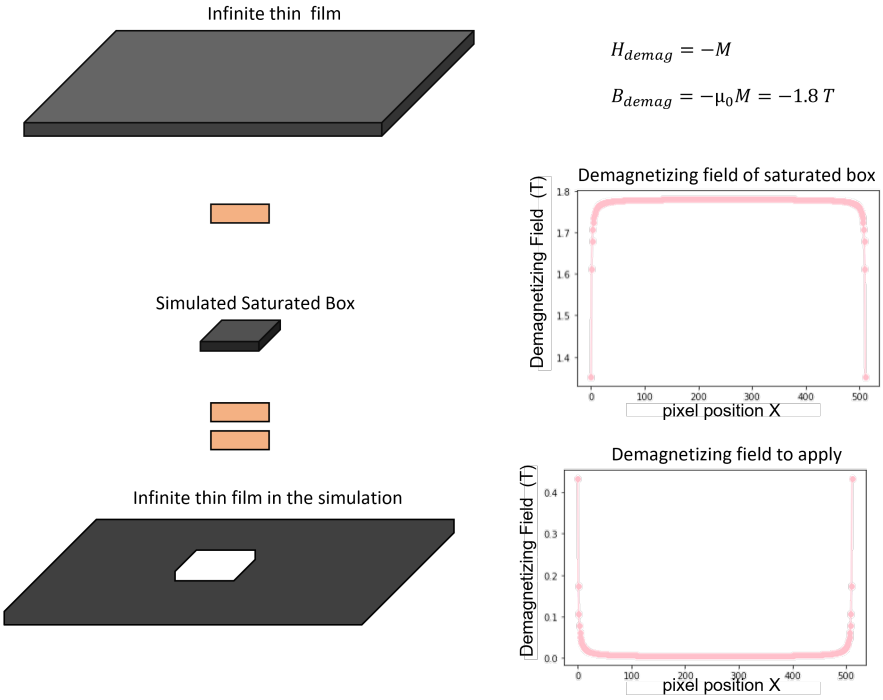

Figure 7.1: Demagnetizing field applied to simulate a single skyrmion in an infinite thin film.

radial unit vector coming from the center of the skyrmion. This value, while stabilizing statically a skyrmion, is constant all around the domain wall but is evolving with the DMI as shown in the figure 7.2(b). A large DMI stabilizes pure Néel skyrmion of both chirality depending on the sign of the DMI coefficient D: in our case a positive DMI stabilizes a counter clockwise skyrmion with an helicity of $\xi = \pm\pi$ meanwhile a negative DMI stabilizes a clockwise pure Néel skyrmion with an helicity of $\xi = 0$. These pure Néel skyrmions are observed for values of DMI larger than a critical values $|D| = \left|D_C^N\right| = 0.4mJ/m^2$, we call this regime the large DMI regime.
When the DMI coefficient reaches $D = 0$ a Bloch skyrmion is stabilized, with an helicity of $\xi = \pm\pi/2$. For a DMI value $|D| < \left|D_C^N\right|$, in the low DMI regime, we see a gradual evolution of the helicity, skyrmions helicity have both a Néel and Bloch component, we called them intermediate skyrmions. While the Néel component direction is set by the DMI sign, the Bloch component can be of both chirality nothing favoring one with respect to the other. Therefore the continuous transformation from a CW Néel skyrmions to a CCW one can follow two different channels, energetically degenerated, depending on the chirality of the Bloch component, as shown in the figure 7.3. The two chiralities for a same value of DMI are then obtained by starting from a counterclockwise Néel skyrmion, decreasing the DMI until obtaining a clock-wise Néel and increasing again the DMI until $+0.5\ mJ/m^2$ (following the black arrow in figure 7.3).

Measurement method of the skyrmion helicity using python.

To measure the helicity of the skyrmion we use the in-plane magnetization component m_x and m_y at the center of the domain wall width (position of the measured radius). We calculate the angle ξ between the magnetization and the radial direction.

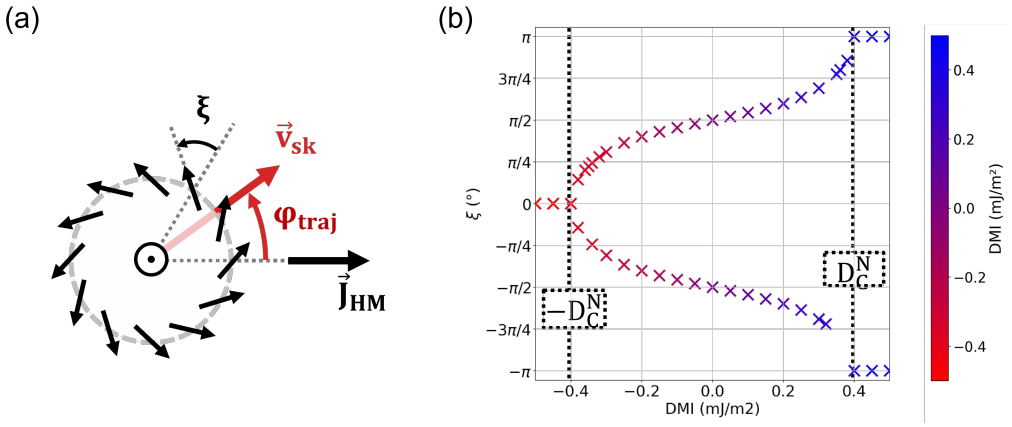

Figure 7.2: (a) Definition of the important quantities of the study: the applied electrical current $\overrightarrow{J}_{HM}$, the helicity of the skyrmion ξ, the direction of motion of the skyrmion $\overrightarrow{v}_{sk}$ and the trajectory angle linked φ_{traj}. (b) Evolution of the helicity with respect to the DMI coefficient value for both chiralities, extracted from the simulations. The critical values of DMI $\pm D_C^N$ for which we consider a pure Néel skyrmion are represented by the black dotted lines.

We also observe a significant change in the skyrmions size. The figure 7.4(a) shows the evolution of the skyrmions radius with respect to the DMI value. Larger skyrmions are obtained for the largest DMI value (close to $D = \pm 0.5 mJ/m^2$). The radius value decreases as the DMI is getting closer to 0. As explained in the section 1.2.2 the domain wall energy can be written :

$$\sigma = 4\sqrt{AK_{eff}} - |\pi D cos(\xi)| \tag{7.1}$$

Here we add a $cos(\xi)$ term to take into account the variation of the helicity in the simulated skyrmion, particularly for the intermediate skyrmions. Both the dipolar and DMI energies tend to stabilize skyrmion. The dipolar interactions, to reduce the stray field coming from the magnetic charges, tend to enlarge the skyrmion. But this increases cost in term of DW energy. However, this energy is reduced by the DMI in the case of Néel type skyrmion. Therefore larger Néel skyrmions can be stabilized compared to Bloch ones. A difference is also noticeable when looking at the domain wall width evolution with respect to the DMI value, plotted in the figure 7.4. The variation of domain wall width is linked with the variation of the volume magnetic charges when the helicity change. We measure a difference of $\Delta\delta_{DW} \simeq 24nm$ between a pure Néel skyrmion and a Bloch one. Close to the critical values of DMI, D_C^N, the evolution of the domain wall width slows down and reaches a plateau.

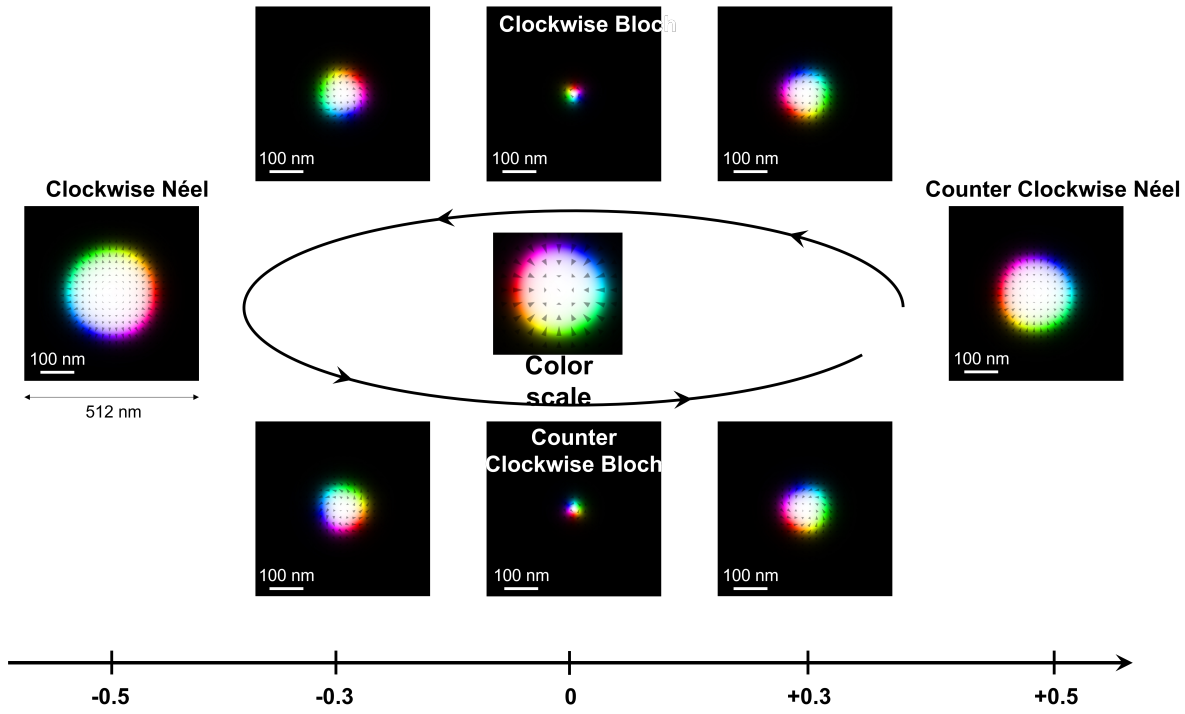

Figure 7.3: Evolution of the simulated skyrmions for a DMI coefficient D between -0.5 and +0.5 mJ/m^2. The two energetically degenerated channels are shown, representing the two chiralities: clockwise (top) and counter clockwise (bottom). The different colors represents the in-plane orientation of the magnetization. The color scale is plotted in the middle with grey arrow to represents the direction associated with each color.

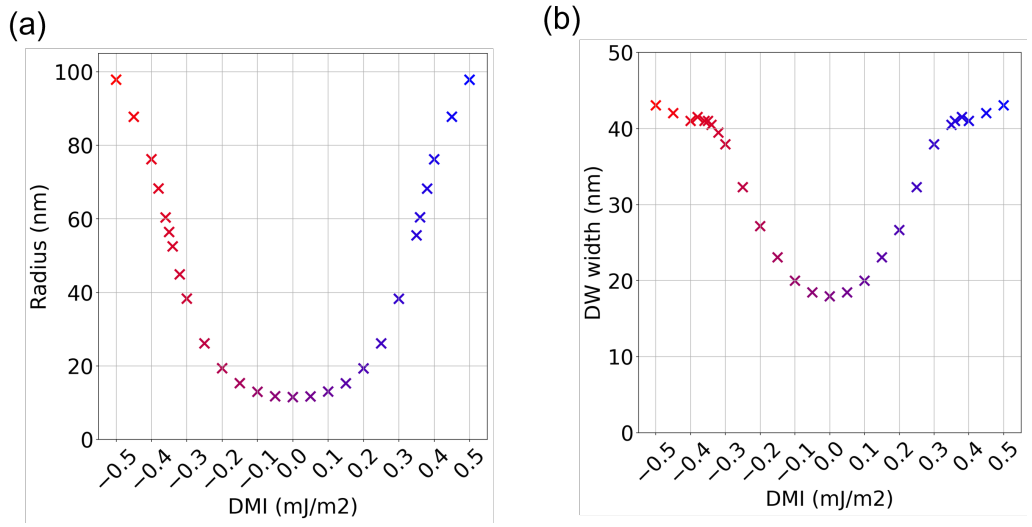

Figure 7.4: (a) Evolution of the radius (in nm) of the skyrmion as a function of the DMI coefficient value (in mJ/m^2). (b) Evolution of the domain wall width (in nm) of the skyrmion as a function of the DMI coefficient value (in mJ/m^2).

Measurement method of the radius and the domain wall width using python.

To measure both the radius and the domain wall width, we work using the spatial distribution of the z component of the magnetization $m_z(\overrightarrow{r})$, $\overrightarrow{r}$ representing the position, on the (x,y) grid, of the spin we are looking at.

To measure the skyrmion radius, we start from its center and scan m_z component of the magnetization along the a given direction. The radius is defined as the distance from the center to the point where m_z changes sign, corresponding to the skyrmion boundary.

To estimate the domain wall width, we fit the m_z profile in the transition region (around the skyrmion radius) using a linear fit. This fit is extrapolated to determine the points where $m_z = +1$ and $m_z = -1$, and the domain wall width is defined as the distance between these points or equivalently from the slope of the fit at $m_z = 0$. An example for both a Bloch and Néel skyrmion is shown in figure 7.5

Both the radius and domain wall width measurement are limited by the resolution of the simulation, the pixel size. Therefore, $\Delta R = 1nm$ and $\Delta\delta_{DW} = 1nm$.

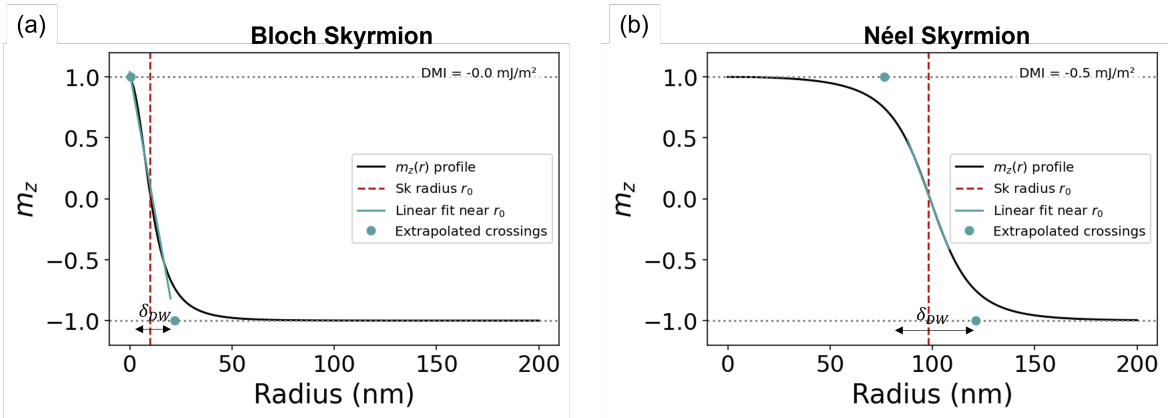

Figure 7.5: Profile of the z-component of the magnetization m_z for (a) a Bloch skyrmion and (b) a Néel skyrmion. The average radius measured is represented by the red line and the fit around the average radius, used to measured the domain width, is represented by the blue line. Blue points represent the points where $m_z = +1$ and $m_z = -1$, find by extrapolation of the fit.

To understand more the role of the DMI in the stabilization of skyrmions Ch-E. Fillion, in his thesis developed an analytical model describing the underlying mechanism. We will describe this model in the following, more details can be found in his manuscript [27].

As we have seen in the section 1.2.2 the DW surface energy in the absence of DMI is:

$$\sigma_{DW}^{B} = 4\sqrt{A_{ex}K_{eff}} \tag{7.2}$$

Where A_{ex} is the exchange stiffness and $K_{eff} = K_u - K_d$, K_u being the uniaxial anisotropy coefficient and $K_d = \frac{1}{2}\mu_0 M_s^2$ the dipolar contribution. It corresponds to the DW energy of a

Bloch DW in the limit of ultrathin films.

By adding DMI in the system two additional competing terms in the surface energy density appear: 1- the DMI favors non collinear spin orientation with a Néel rotation and thus change the DW energy $\sigma_{DW}^{N} = 4\sqrt{A_{ex}K_0} - |\pi D|$. However, if we only consider the DMI contribution the minimization of the surface energy of the DW σ_{DW} always leads to the stabilization of a pure Néel type DW whatever the amplitude of the DMI coefficient. This is not true in the case of low DMI system, as shown in the figure 7.2. Indeed, in weak DMI system, it is not possible anymore to neglect 2- the creation of volume magnetic charges due to the Néel component of the DW. These charges act like an additional anisotropy term that favors Bloch DW.

Taking into account these two terms the intermediate DW surface energy is written:

$$\sigma_{DW} = 4\sqrt{A_{ex}(K_0 + K_d^V cos^2\xi)} - |\pi D cos(\xi)| \tag{7.3}$$

With $K_d^V = \frac{1}{2}\mu_0 N_{xx} M_s^2$. N_{xx} being the demagnetizing factor of a DW perpendicular to the x direction, approximated by $\sim \frac{tln2}{\delta_{DW}}$ in thin film [154], δ_{DW} the domain wall width and t the ferromagnetic film thickness.

Now by minimizing this expression with respect to ξ we obtain the expression of the equilibrium helicity with respect to the DMI value (detailed calculation are shown in the supplementary 9.5):

$$\xi(D) = \pm cos^{-1}\left(-\pi D\sqrt{\frac{K_0}{K_d^V(16A_{ex}K_d^V - \pi^2 D^2)}}\right) \tag{7.4}$$

The two degenerated Bloch components highlighted in the figure 7.3 come from the $\pm$ sign in eq. 7.4. The evolution of the helicity with the DMI, extracted from the model of the equation 7.3, is represented in the figure 7.6(a). By integrating the domain wall energy density σ_{DW} over the surface of the skyrmion, Ch-E.Fillion showed, in the figure 7.6(b), the comparison between the energy of the DW to the thermal energy $\frac{\sigma}{k_B T}$ as a function of the helicity. This comparison provides insight into the stability of the skyrmion and identifies the energetically favored configuration in different DMI regimes with respect to a critical DMI value D_C^N.

This comparison as a function of helicity provides insight into the stability of the skyrmion and identifies the energetically favored configuration in different DMI regimes.

Indeed, two regimes can be distinguished: for $|D| \geq \left|D_C^N\right|$ the DMI contribution overcomes the volume magnetic charges. In this case, only one minimum is found (red and blue curves in the figure 7.6(b)), corresponding to the unique Néel chirality imposed by the sign of the DMI. Then, for $|D| < \left|D_C^N\right|$ the DMI no longer compensates anymore the volume magnetic charges, a Bloch component starts to appear and thus two energetically degenerated minima can be found.

Because of its interfacial nature the DMI favors Néel type DW, with the sign of the DMI setting the chirality. However, nothing favors one Bloch component to the other, leading to these two degenerated states. Each minimum is surrounded by two maxima, therefore conserving the Néel component favored by the DMI sign. By increasing the DMI value, the energy barrier decreases and vanishes for the critical value of DMI D_C^N. This critical value can be extracted

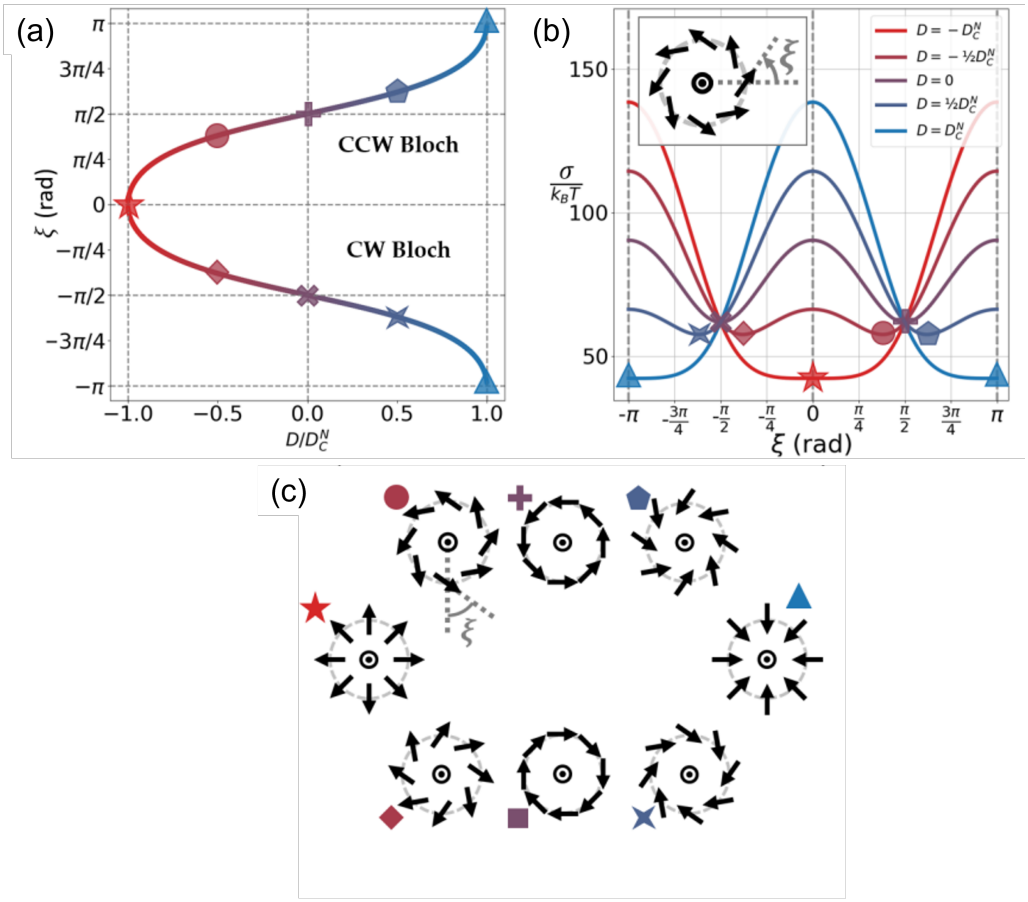

Figure 7.6: *(Extracted from [27]):* (a) helicity evolution as a function of the DMI value for both chiralities, extracted from the model. (b) Comparison of the domain wall energy with the thermal energy as a function of the helicity of the skyrmion for specific value of DMI. (c) Scheme of the skyrmion stabilize at specific points of the graph in (b).

from the equation 7.4 (detailed calculation can be found in the supplementary 9.5):

$$\left|D_C^N\right| = \frac{4}{\pi}\sqrt{\frac{A_{ex}K_d^V}{K_0/K_d^V + 1}} \tag{7.5}$$

Finally, Ch-E.Fillion compared this model to the simulated value that we both obtained, that I represented in the figure 7.4. As it can be seen in the figure 7.7(a) a mismatch in between the simulations (colored crosses) and the model (green dotted line) is observed due to difference in the critical DMI coefficient. The model predicts $D_{C,m}^N \simeq 0.21 mJ/m^2$ while the one extracted from the simulations is $D_{C,s}^N \simeq 0.41 mJ/m^2$. This is likely due to an underestimation of the volume magnetic charges in the model coming from the approximation of the dipolar energy in the DW. However, as shown in the figure 7.7(b) by normalizing the DMI value by the respective critical DMI coefficient, the model follows the simulated with accuracy. We conclude then that the simulations can provide a more accurate value of the magnetic volume charges and the model can predict the equilibrium helicity for a given DMI coefficient after normalizing with the critical

DMI.

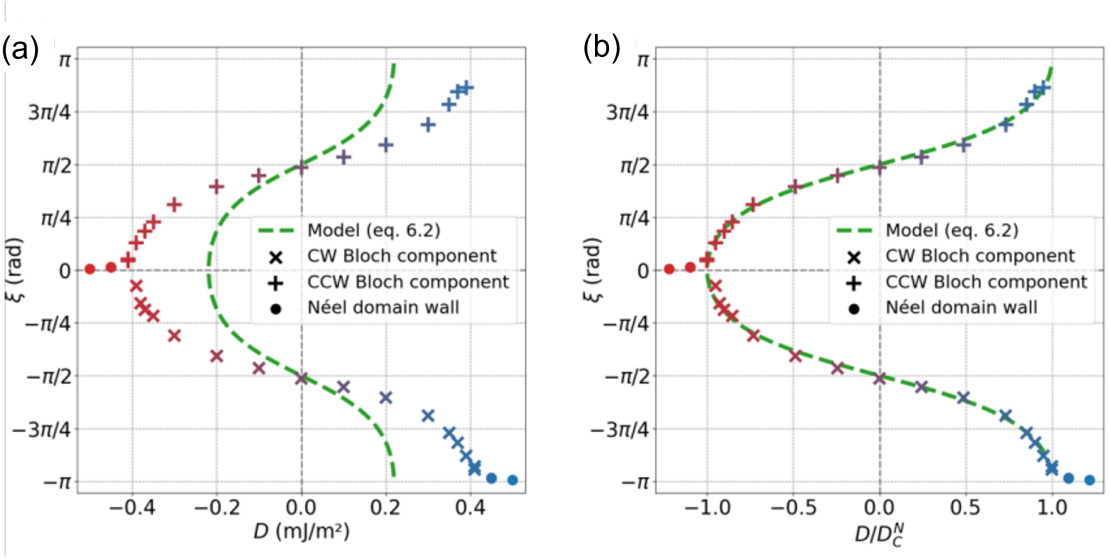

Figure 7.7: *(Extracted from [27]:* (a) Comparison of the helicity as a function of the DMI calculated using the analytical model (green dotted line) and extracted from the simulations (colored crosses). (b) The DMI is normalized by the critical DMI value.

7.3 Motion of skyrmions under small current

7.3.1 Trajectories

Now that we studied the static skyrmion characteristics under the simulations parameters we can focus on their motion under an electrical current.
As discussed in the section 2.3.2, while applying a current inside a heavy metal layer the spin Hall or Rashba Edelstein effects leads to an accumulations of spins at the interface with the ferromagnet. These spins are injected in the ferromagnet and then applied a spin transfer torque. As discussed in the section 2.3.3 the motion of skyrmions is mainly due to the damping like torque:

$$\overrightarrow{\tau_{DL}} = |\gamma|\,\mu_0 H_{DL}(\overrightarrow{m} \times (\overrightarrow{m} \times \overrightarrow{\sigma})) \tag{7.6}$$

Where γ is the gyromagnetic ratio, μ_0 the permeability of the vacuum and $\overrightarrow{\sigma}$ is the spin accumulation vector (the direction of the injected spins).

In the micromagnetic simulation software used here (Mumax3.10 [155]), spin orbit torque are not directly coded. This situation is instead modeled with the spin transfer torques, coded as a current density J injected in the $\overrightarrow{z}$ direction with a spin polarization $P = 0.1$ in the $\overrightarrow{y}$ direction. In this section, the current density is set to $J = 10^{10} A/m^2$, this value has been chosen to induce a measurable motion of the slowest skyrmions while avoiding any deformations that

can occur at higher current densities. The polarity in Mumax3.10 corresponds to the experimental spin Hall angle θ_{SH}, which in corresponds to same order of magnitude than the spin Hall angle of Ta. This choice keeps the simulations close to experimental parameters and enables to study the motion of a single skyrmion in a ideal case with no deformations. The material and simulations parameters are the same as in the previous section, except for the external magnetic field that is now constant at $-6mT$, see Table 7.1. To avoid any edge effects, Periodic Boundary Conditions (PBC) are set.

A current is injected for all the skyrmions stabilized in the previous section with a DMI value varying in $[-0.5; +0.5]$ during $120ns$. To study the trajectory of the skyrmions we are tracking the center of the skyrmions. To do so the resulting images obtained after the simulations are converted into black and white, then they are binarized depending on the orientation of the magnetization, black part are attributed to 1 while white one (the skyrmion) corresponds to 0. Then, to locate the center of the skyrmion, we look at the column and the row having the highest number of 0 inside, resulting in one set of coordinates (x_c,y_c) for the center. This process is done for all the images obtained. We plot in the figure 7.8 all the trajectories obtained.

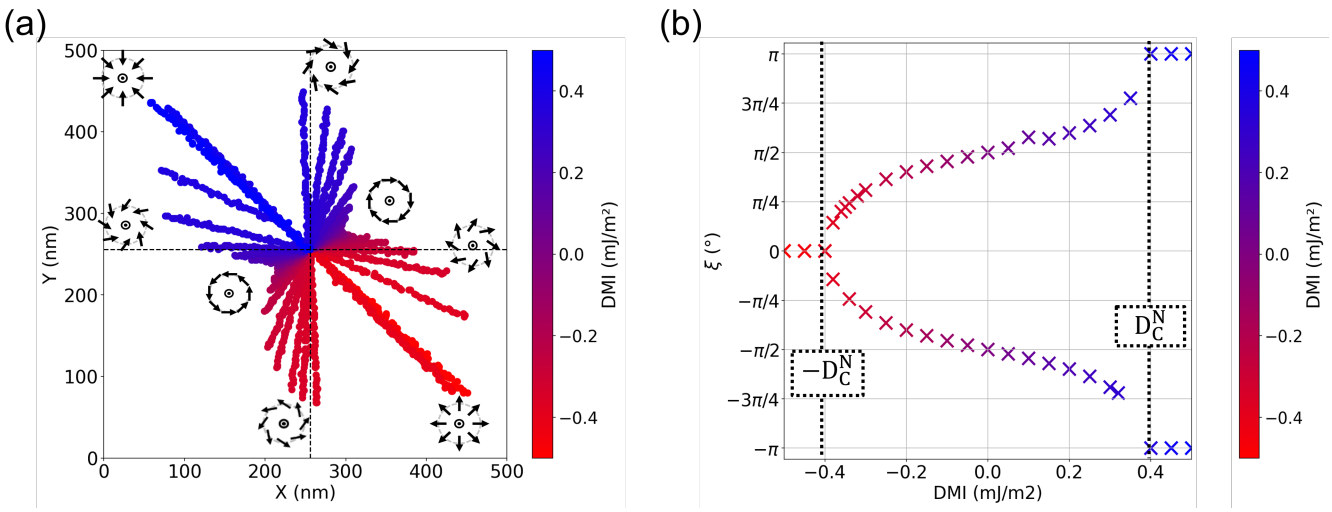

Figure 7.8: (a) Trajectories of skyrmions driven by an electrical current density $J = 10^{10}\mathrm{A/m}^2$, for different values of the DMI ranging from -0.5 to $+0.5\mathrm{mJ/m}^2$. The color of each curve corresponds to a specific DMI value, and schematic skyrmions are shown close to their own trajectory to illustrate specific DMI values.(b) Evolution of the helicity angle as a function of the DMI value, measured $2ns$ after the application of the current. The color code is the same as in (a). Two critical DMI values are highlighted, D_C^N and $-D_C^N$, which mark the onset of pure Néel skyrmions with helicities $\xi = \pm\pi$ and $\xi = 0$, respectively.

We see that skyrmions with different values of DMI have different directions of motion. This is linked with the evolution of the helicity with the DMI value, as discussed in the previous section. A good control on the DMI will therefore allow the tuning of the helicity and finally give a precise control on the direction of motion of the skyrmion. In addition we can also see that skyrmion velocity is different depending on the DMI value, all the simulations were done for a time of $120ns$, we clearly see that skyrmion having a DMI value close to $\pm 0.5mJ/m^2$

(Néel skyrmions) went farther, so have a higher velocity, than the skyrmions close to a DMI $= 0mJ/m^2$ (Bloch skyrmions).

A useful equation while talking about skyrmion motion and direction is the Thiele equation, described in the section 2.3.3. Taking as an assumption a skyrmion with a stable, circular geometry, i.e., without deformation during its motion. :

$$\overrightarrow{G} \times \overrightarrow{v} - \alpha \bar{\bar{D}} \cdot \overrightarrow{v} + \overrightarrow{F}_{ext} = 0 \tag{7.7}$$

Where G is the gyrocoupling vector, $\overrightarrow{v}$ is the velocity of the skyrmions, $\bar{\bar{D}}$ is the dissipative tensor, related to the damping α of the system and $\overrightarrow{F}_{ext}$ the external forces applied on the skyrmion. Here $\overrightarrow{F}_{ext} = \overrightarrow{F}_{DL}$, the force coming from the damping-like torque of the SHE.

The geometry of our system is shown in the figure 7.9(a) and (b). The position of each spin inside the skyrmions can be described by the coordinates (r, φ, z) and the orientation of each spin itself can be express using local coordinates (1, θ_0, ϕ_0).

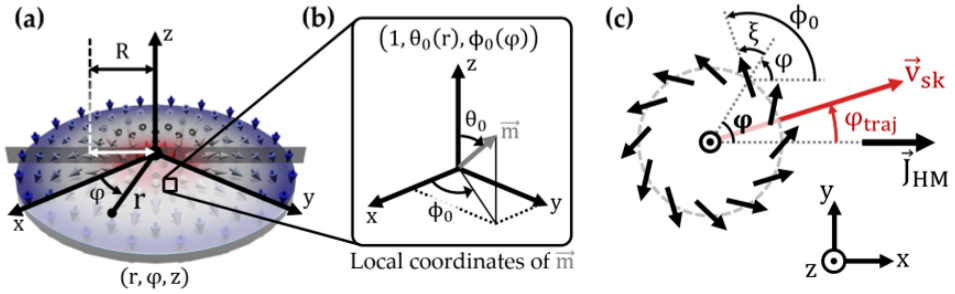

Figure 7.9: *Figure taken from the PhD manuscript of Ch-E. Fillion [27]*: Coordinate system used to define (a) the skyrmion and (b) the local magnetization vector. A given spin is locate in the skyrmion in (a) using the polar coordinate (r, φ, z) (here $z = 0$) while in (b) the orientation of each spin is defined locally using the spherical coordinates $(1, \theta(r), \phi(\varphi))$. (c) Scheme of the top view of a Dzyaloshinskii skyrmion where in addition to the previous angles discussed, we defined the helicity ξ.

We can then express each term of the Thiele equation 7.7 in this coordinate system as:

- The Gyrotropic vector $\overrightarrow{G}$:

$$\overrightarrow{G} = \begin{pmatrix} 0 \\ 0 \\ G \end{pmatrix}, G = \frac{M_s t_{FM}}{\gamma} \int_S sin(\theta)(\overrightarrow{\nabla}\theta \times \overrightarrow{\nabla}\phi) r dr d\phi = -4\pi n \frac{M_S t_{FM}}{\gamma} \tag{7.8}$$

With M_S the saturated magnetization, t_{FM} the thickness of the ferromagnet, γ the gyromagnetic ratio and n the skyrmion winding number $n = p \cdot W$, where p is the polarization $p = \pm 1$ and W describes the evolution of the magnetization along the skyrmions perimeter: $W = \frac{[\phi(\varphi)]_0^{2\pi}}{2\pi}$. As we can see in the figure 7.9 $\phi(\varphi) = \varphi + \xi$ therefore W = 1 and n = p. Finally,

$$G = -4\pi p \frac{M_S t_{FM}}{\gamma} \tag{7.9}$$

• The dissipative tensor $\bar{\bar{D}}$:

$$\bar{\bar{D}} = \begin{pmatrix} D_1 & 0 \\ 0 & D_1 \end{pmatrix}, D_1 = \frac{M_s t_{FM}}{\gamma} \int_S \left((\overrightarrow{\nabla}\theta)^2 + sin^2(\theta)(\overrightarrow{\nabla}\phi)^2 \right) r dr d\phi \tag{7.10}$$

$$D_1 = \frac{M_s t_{FM}}{\gamma} \pi \int_{r=0}^{+\infty} \left[r(\frac{\partial\theta}{\partial r})^2 + \frac{sin^2(\theta)}{r} \right] dr = \frac{M_s t_{FM}}{\gamma} \beta_0 \tag{7.11}$$

With β_0 a dimensionless parameter coefficient expressed as:

$$\beta_0 = \pi \int_{r=0}^{+\infty} \left[r(\frac{\partial\theta}{\partial r})^2 + \frac{sin^2(\theta)}{r} \right] dr \tag{7.12}$$

This parameter corresponds to the adimensional exchange integral. The first term in eq. 7.12 corresponds to the usual exchange term while the second term is a curvature exchange term which therefore increases when the skyrmion radius decreases.

• The external force $\overrightarrow{F}_{ext}$:

As explained in the section 2.3.3, the motion of skyrmions is mainly due to the damping-like spin orbit torque, therefore:

$$\overrightarrow{F}_{ext} = \overrightarrow{F}_{DL} = \mu_0 M_S t_{FM} H_{DL} (\beta_1 + \beta_2) \begin{pmatrix} cos(\xi) \\ -sin(\xi) \\ 0 \end{pmatrix} \tag{7.13}$$

Where β_1 and β_2 are dimensionless coefficient that reads:

$$\beta_1 = \pi \int_{r=0}^{+\infty} r(\frac{\partial\theta}{\partial r}) dr \tag{7.14}$$

$$\beta_2 = \pi \int_{r=0}^{+\infty} sin[\theta(r)] cos[\theta(r)] dr \tag{7.15}$$

From the Thiele equation we can extract the expression of the velocity coordinates, the derivation is detailed in the supplementary 9.4:

$$\begin{cases} v_x = \frac{\alpha D_1 F_{DL,x} - G_z F_{DL,y}}{G_z^2 + \alpha^2 D_1^2} \\ v_y = \frac{G_z F_{DL,x} + \alpha D_1 F_{DL,y}}{G_z^2 + \alpha^2 D_1^2} \end{cases} \tag{7.16}$$

With α the damping parameter, D_1 the dissipative coefficient, $F_{DL,x/y}$ the projection along x/y of the damping-like torque force on the magnetization and G_z the gyrotropic coefficient. From this we can extract the trajectory angle $\varphi_{traj}(\xi)$ of the skyrmion:

$$\varphi_{traj}(\xi) = arctan \left(\frac{v_y(\xi)}{v_x(\xi)} \right) \tag{7.17}$$

Both velocity components depend on the helicity through the damping-like spin orbit torque force $\overrightarrow{F}_{DL}$. The efficiency of this torque on the magnetization within the ferromagnet, which drives the motion of spin textures, depends on the local spin orientation, and thus on the helicity.

$$\begin{aligned}\frac{v_y}{v_x} &= \frac{G_z F_{DL,x}+\alpha D_1 F_{DL,y}}{\alpha D_1 F_{DL,x}-G_z F_{DL,y}} \\ &= \frac{\frac{G_z}{\alpha D_1}F_{DL,x}+F_{DL,y}}{F_{DL,x}-\frac{G_z}{\alpha D_1}F_{DL,y}} \\ &= \frac{\frac{G_z}{\alpha D_1}cos(\xi)-sin(\xi)}{cos(\xi)+\frac{G_z}{\alpha D_1}sin(\xi)} \\ &= \frac{\frac{G_z}{\alpha D_1}-tan(\xi)}{1+\frac{G_z}{\alpha D_1}tan(\xi)} \end{aligned} \tag{7.18}$$

With $\frac{G_z}{\alpha D_1} = \frac{-4\pi p}{\alpha\beta_0}$, then:

$$\frac{V_y}{V_x} = \frac{\frac{-4\pi p}{\alpha\beta_0}-tan(\xi)}{1+\frac{-4\pi p}{\alpha\beta_0}tan(\xi)} \tag{7.19}$$

We can write $A = \frac{-4\pi p}{\alpha\beta_0}$ and $B = -tan(\xi)$:

$$\frac{v_y}{v_x} = \frac{A+B}{1-AB} \tag{7.20}$$

We recall the trigonometry formula:

$$arctan\left(\frac{A+B}{1-AB}\right) = arctan(A)+arctan(B) \tag{7.21}$$

Therefore,

$$\varphi_{traj}(\xi) = arctan\left(\frac{v_y}{v_x}\right) = arctan\left(\frac{-4\pi p}{\alpha\beta_0}\right)+arctan(tan(-\xi)) \tag{7.22}$$

So finally the Thiele equation leads to:

$$\varphi_{traj}(\xi) = arctan\left(\frac{-4\pi p}{\alpha\beta_0}\right)-\xi = \varphi_{SkHE}(p,\alpha,\beta_0)-\xi \tag{7.23}$$

From this expression we expect the evolution of the trajectory angles of the skyrmions to be linear with respect to the helicity, shifted by a value known as the skyrmion Hall angle:

$$\varphi_{SkHE} = arctan\left(\frac{-4\pi p}{\alpha\beta_0}\right) \tag{7.24}$$

Many studies on skyrmions are carried out in systems with large DMI values, where pure Néel skyrmions are stabilized, corresponding to helicities $\xi = 0$ or π. In such cases, the dependence of the trajectories on helicity is usually not investigated. Instead, attention is focused mainly on the skyrmion Hall angle. In contrast, this thesis focuses on weak-DMI systems, where intermediate skyrmions appear where the helicity evolves continuously with the DMI strength.

The figure 7.10 shows the trajectory angle of the skyrmions with respect to their helicity value. The red dotted line represents the linear behavior expected from the Thiele equation 7.23

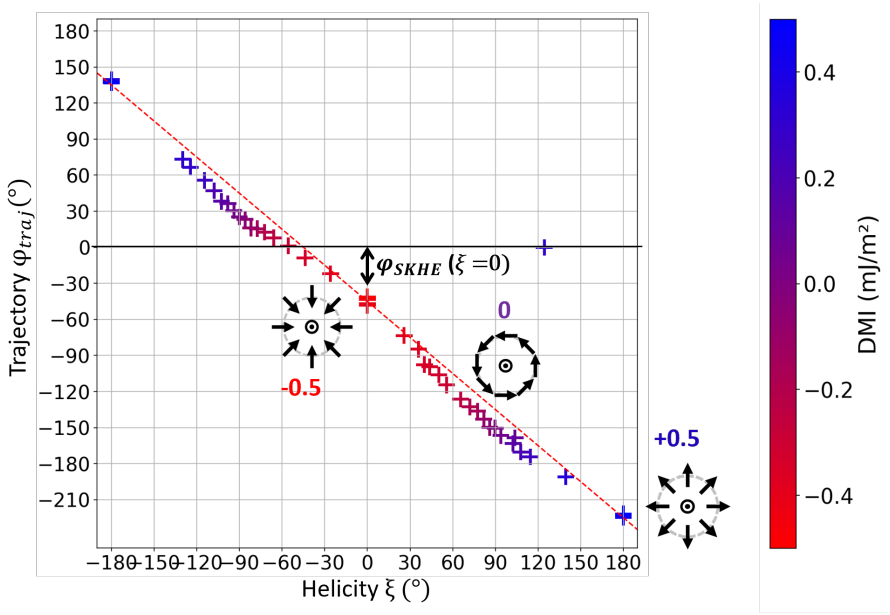

Figure 7.10: Trajectory of the skyrmions plotted with respect to their helicity value. The colored crosses correspond to the simulated values. The red dotted line represents the linear behavior expected from the Thiele equation Eq. 7.7, shifted from a certain value: the skyrmion Hall angle φ_{SkHE}. A scheme of the skyrmion having a DMI of -0.5, 0 and +0.5 is represented.

if the skyrmion Hall angle φ_{SkHE} would be constant. The simulated values of the skyrmion's trajectories follow quite well this linear behavior, however it can be noted that a small discrepancy appears for the smaller values of DMI, i.e close to $D = 0$.

To understand this difference we look at the skyrmion Hall angle φ_{SkHE} as a function of the ratio R/δ_{DW}, the radius of the skyrmion over its domain wall width. Indeed as explain before the β_0 parameter can be decomposed in two terms: the usual exchange term and a curvature exchange term.

The figure 7.11(a) presents the expected behavior of the skyrmion Hall angle, plotted from the equation 7.24 for a damping $\alpha = 0.5$. The model is represented by the straight colored lines.

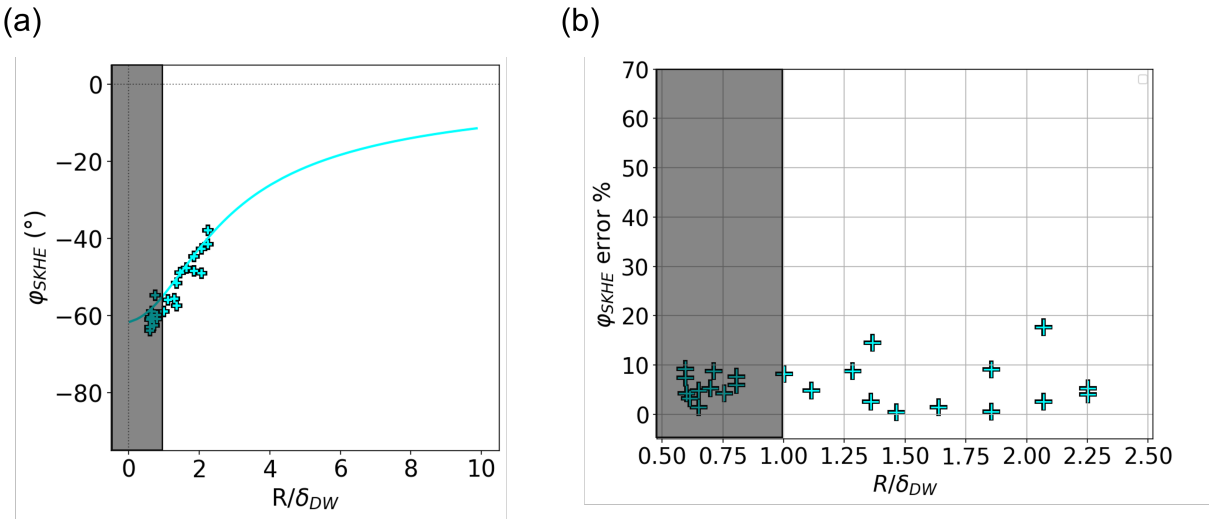

Figure 7.11: (a) Skyrmion Hall angle φ_{SkHE} as function of the ratio of the radius over the domain wall width R/δ_{DW}. The colored solid line represented the model for a damping $\alpha = 0.5$. The corresponding simulated values are represented with the blue crosses. (b) Skyrmion Hall angle φ_{SkHE} error in between the simulated values and the model expressed in percentage (%) and for a damping of 0.5

The simulated values of the skyrmion Hall angle are represented by the blue crosses for a damping constant $\alpha = 0.5$. Overall, the simulations follow the model reasonably well. In the figure 7.11 we plotted the skyrmion Hall angle φ_{SkHE} error percentage in between the simulated values and the model. We see that almost all the values have a difference below 10%. We note here that the values corresponding to $R/\delta_{DW} < 1$ (gray region) should not be considered, since a ratio smaller than one implies a domain wall width larger than the skyrmion radius, which is nonphysical. This is coming from a non accurate extraction of δ_{DW} at small radius.

7.3.2 Large Skyrmion Approximation

We thus focus now on the large skyrmion case, for which the β_0 parameter can be expressed as :

$$\beta_0 = 4\pi \frac{R}{\delta_{DW}} \tag{7.25}$$

Figure 7.12(a) shows the evolution of the parameter β_0 as a function of the ratio R/δ_{DW} for a damping constant $\alpha = 0.5$. The solid line corresponds to the calculated integral from Eq. 7.12, while the black dotted line represents the large-skyrmion approximation from Eq. 7.25. The corresponding error percentage between the full model and the approximation is shown in figure 7.12(b). Although the error is large for small ratios, it decreases rapidly and falls below 10% around $R/\delta_{DW} = 2$.

Thus the skyrmion Hall angle can be expressed:

$$\varphi_{SkHE} = \arctan\left(\frac{-p\delta_{DW}}{\alpha R}\right) \tag{7.26}$$

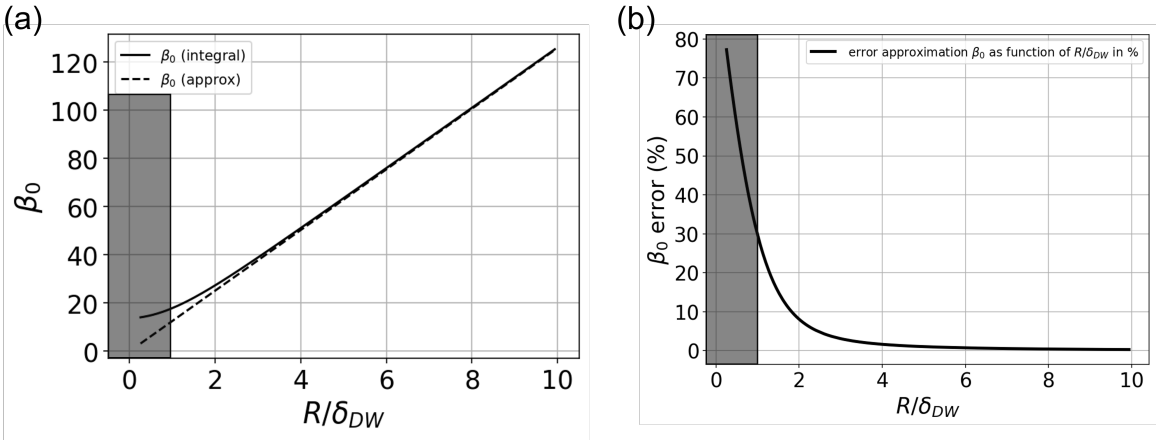

Figure 7.12: (a) The β_0 parameter calculated directly with the integral Eq. 7.12 is represented by the black solid line. The Black dashed line represents the β_0 parameter calculated using the large skyrmion approximation Eq. 7.25. Both are represented with respect to the ratio of the radius over the domain wall width of the skyrmion, ${}^{R}/\delta_{DW}$. (b) Error made by using the approximation for the β_0, expressed in %.

With p the polarity of the skyrmion $p = \pm 1$, α the damping (here $\alpha = 0.5$), R the radius of the skyrmion and δ_{DW} the domain wall width of the skyrmion. Four parameters that are easily determined. Indeed, both the radius and the domain wall width can be extracted from the simulations values. In the figure 7.13 we plot the radius and the domain wall width of the skyrmion with respect to the helicity value.

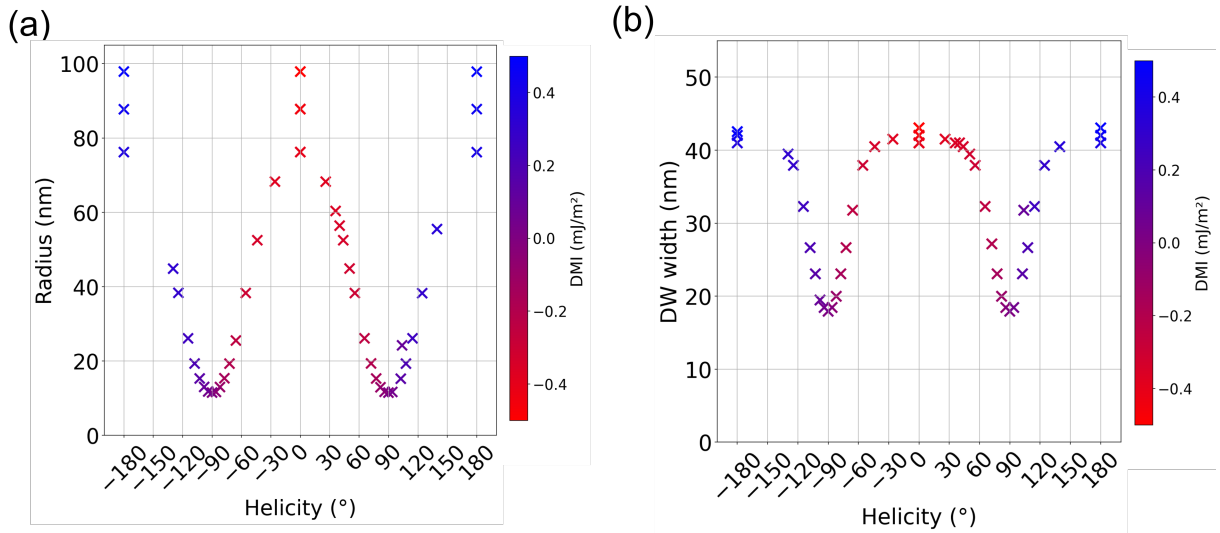

Figure 7.13: (a) Evolution of the radius R (in nm) of the simulated skyrmion with respect to the its helicity value. (b) Evolution of the domain wall width δ_{DW} (in nm) as a function of the helicity of the skyrmion.

The skyrmion Hall angle, using the β_0 approximation can also be plotted, as was previously done for the full model. This is represented in figure7.14(a) by the blue solid line, with the same

simulation data points overlaid. In Figure 7.14(b), we observe an increase in the error percentage between the simulated data and the Skyrmion Hall angle calculated using the approximation at small ratios. This behavior is due to the limitations of the large-skyrmion approximation. However, as before, the physically meaningful regime corresponds to $R/\delta_{DW} > 1$, for which the error remains below 10%, confirming the validity of the large skyrmion approximation model.

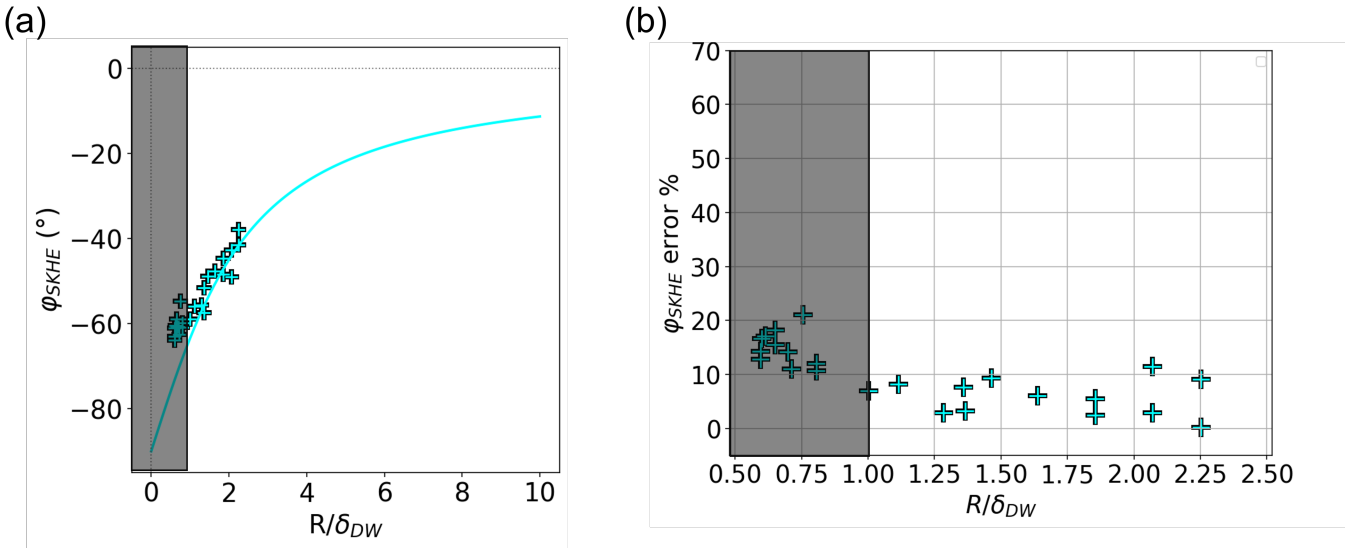

Figure 7.14: (a) Skyrmion Hall angle φ_{SkHE} as function of the ratio of the radius over the domain wall width R/δ_{DW}, calculated using the approximated value of the β_0 parameters (equation 7.25). The blue solid line represented the approximated skyrmion Hall angle a damping $\alpha = 0.5$. The corresponding simulated values are represented with the blue crosses. (b) Skyrmion Hall angle φ_{SkHE} error in between the simulated values and the approximation for a damping of 0.5, expressed in percentage (%).

7.3.3 Effect of the damping on the trajectories

It is now interesting to study the damping value effect in our simulations. To do so we performed the exact same study we just presented for two other values of damping: one smaller $\alpha = 0.05$ and one larger $\alpha = 1$. The figures 7.15 and 7.16 shows the different trajectories of the skyrmions and the evolution of φ_{traj} with the helicity for respectively a damping of $\alpha = 0.05$ and $\alpha = 1$. Both figures 7.15(a) and 7.16(a) already show a strong effect of the damping on the direction of motion of the skyrmions. Indeed we can clearly see that the trajectories are modified with respect to the case of the damping of $\alpha = 0.5$, presented in the figure 7.8(a). Also, we note here that a decrease of the damping has a stronger impact than an increase on the skyrmion Hall angle and thus on the trajectory angle. Indeed as shown in the figures 7.15(b) and 7.16(b) the highest damping is closer to the trajectories obtained for a damping of 0.5 than the small damping. We see that the linear behavior of φ_{SkHE} with the helicity expected from the initial Thiele equation is almost followed for a small damping ($\alpha = 0.05$) while for the larger value ($\alpha = 1$) the simulations data drift from this linear curve (red dotted curve in the figure) as for the initial damping study $\alpha = 0.5$). We can also note here the effect of the damping on the velocity, as we can see by comparing the figures 7.15(a) and 7.16(a), for which the simulations time was as well $120ns$. As expected a smaller damping leads to a faster motion of the skyrmions.

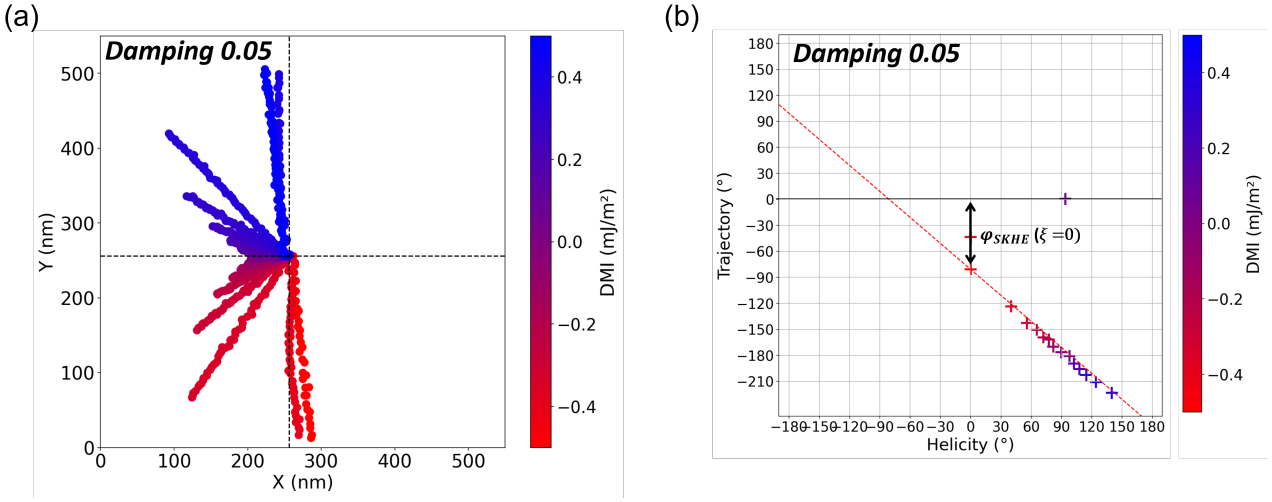

Figure 7.15: (a) Trajectories of skyrmions driven by an electrical current density $j = 10^{10}\mathrm{A/m}^2$ with a damping of $\alpha = 0.05$, for different values of the DMI ranging from -0.5 to $+0.5\mathrm{mJ/m}^2$. The color of each curve corresponds to a specific DMI value. (b) Trajectory of the skyrmions plotted with respect to their helicity value, for a damping of $\alpha = 0.05$. The colored crosses correspond to the simulated values. The red dotted line represents the linear behavior expected from the Thiele equation Eq. 7.7, shifted from a certain value: the skyrmion Hall angle φ_{SkHE}. Only one Bloch chirality is plotted.

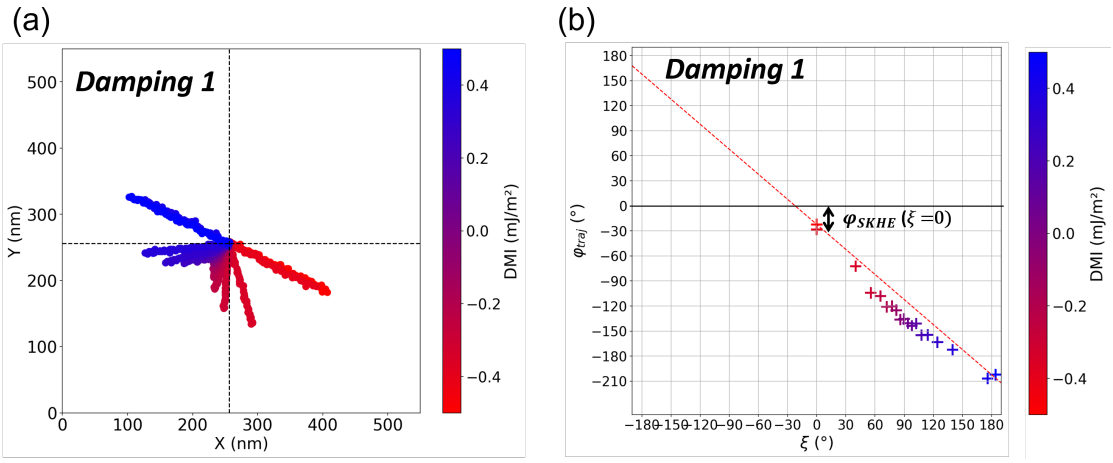

Figure 7.16: (a) Trajectories of skyrmions driven by an electrical current density $j = 10^{10}\mathrm{A/m}^2$ with a damping of $\alpha = 1$, for different values of the DMI ranging from -0.5 to $+0.5\mathrm{mJ/m}^2$. The color of each curve corresponds to a specific DMI value.(b) Trajectory of the skyrmions plotted with respect to their helicity value, for a damping of $\alpha = 1$. The colored crosses correspond to the simulated values. The red dotted line represents the linear behavior expected from the Thiele equation Eq. 7.7, shifted from a certain value: the skyrmion Hall angle φ_{SkHE}. Only one Bloch chirality is plotted.

To go further and understand these different behaviors, we add in the figure 7.17(a) the simulated values of the skyrmion Hall angle φ_{SkHE} with respect to the ratio R/δ_{DW} on top of the full model with β_0 calculated from the integral Eq 7.12. The figure 7.17(b) shows the error in between the simulated values and the φ_{SkHE} calculated using the full model. The effect of the damping on the skyrmion Hall angle stands out: while a small damping value leads to a large and constant skyrmion Hall angle, a large damping value reduces the deviation of the skyrmions, which is more affected by the skyrmions geometry (radius and domain wall width ratio). Then, we also see that the damping value influence the error percentage for small ratio value. While for a small damping the difference in between the simulation and the model are close to 0 for all the ratio studied. When increasing the damping value the difference is increasing as well. It is important to note here that for all the meaningful ratios ($R/\delta_{DW} > 1$) the error in the skyrmion Hall angle is less than 10%.

Then, we plot, in the figure 7.17(c), the evolution of the skyrmion Hall angle, using the large skyrmion approximation of β_0 of Eq 7.25, with the ratio R/δ_{DW}. For comparison we plot in the figure 7.17(d) the difference in between the simulated values and the approximation, expressed in percentage. For small ratios, a small increase can be identified, however, for all the physically meaningful values are below 10% of error for all simulated damping. This result allows us to validate the large skyrmion approximation, for all the damping.

This agreement between the simulated data and the approximated model confirms that the skyrmion Hall angle φ_{SkHE} can be expressed in terms of four parameters: the polarity $p = \pm 1$, the skyrmion radius R, the domain wall width δ_{DW}, and the damping α. Knowing these parameters, the approximated model can predict the skyrmion trajectory. Moreover, this implies that fine tuning of the skyrmion helicity and radius could enable precise control of the trajectory. In

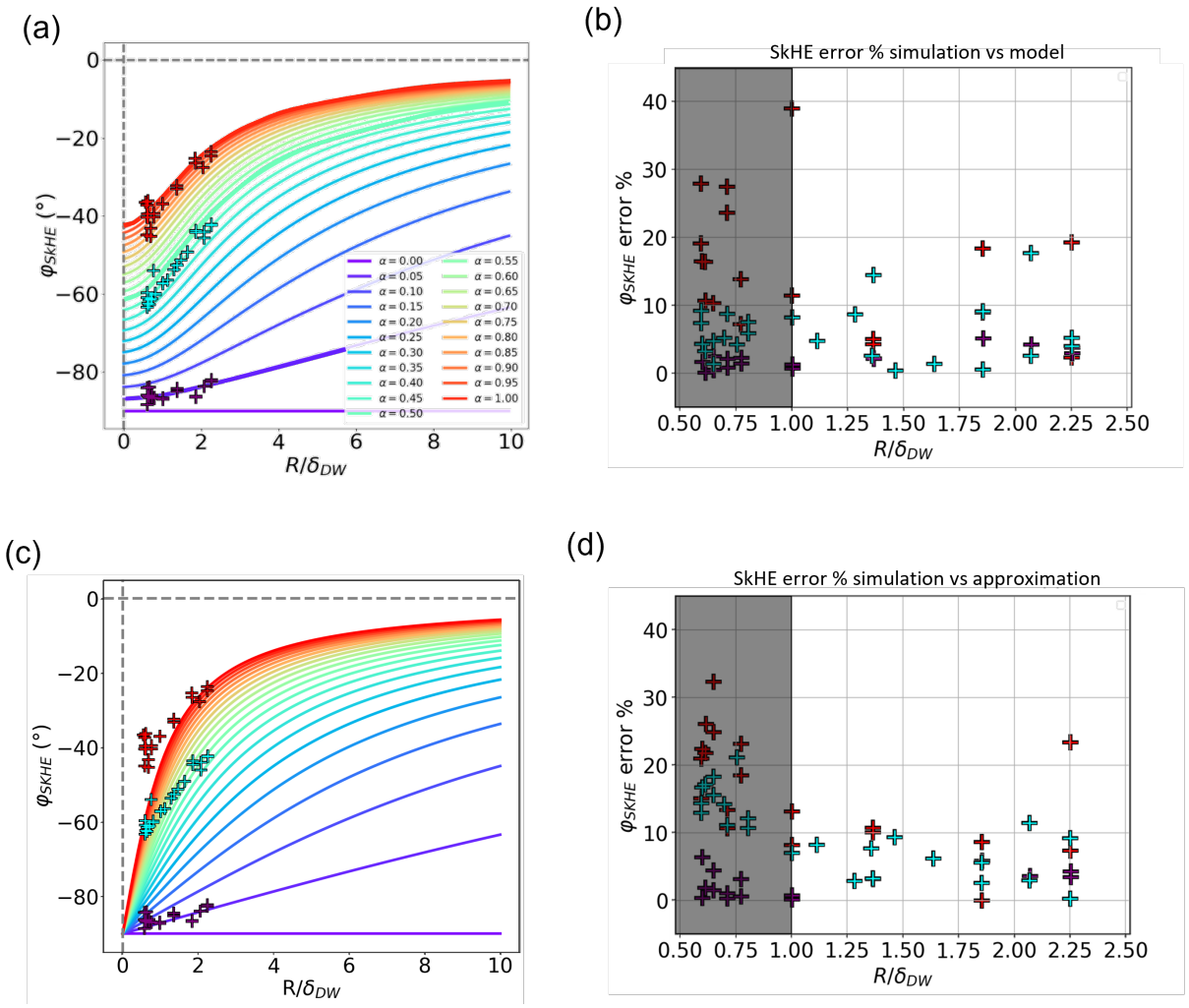

Figure 7.17: (a)-(c) Skyrmion Hall angle φ_{SkHE} as function of the ratio of the radius over the domain wall width R/δ_{DW}. The colored solid lines represented in (a) the model and (c) the approximation for different values of damping α going from 0.00 to 1.00 with a step of 0.05. The simulated values corresponding to a damping of 0.05, 0.5 and 1 are represented with the purple, blue and red crosses. (b)-(d) Skyrmion Hall angle φ_{SkHE} error in between the simulated values and (b) the model or (d) the approximation, for a damping of 0.05, 0.5 and 1, expressed in percentage (%)

particular, a continuous control of the skyrmion parameters and trajectory could be achieved through the application of a gate voltage, since we have already shown experimentally that the DMI may be tuned or even inverted with a gate voltage.

7.4 Motion of skyrmions under high current

We are then interested in the case of a high current application. We performed the same study as before with an electrical current density $J = 10^{11} A/m^2$, the other parameters being the same as in section 7.2. The first important characteristics is the deformation of the skyrmion under this high current. As shown in the figure 7.18 under an high current the skyrmion is elongated in the direction perpendicular to the applied current J, i.e along the injected spin direction.

In this section we call the initial state the first step when the current is applied. It corresponds to the state after 2 nanoseconds of current application. The final state corresponds to the last state, after 120 nanoseconds.

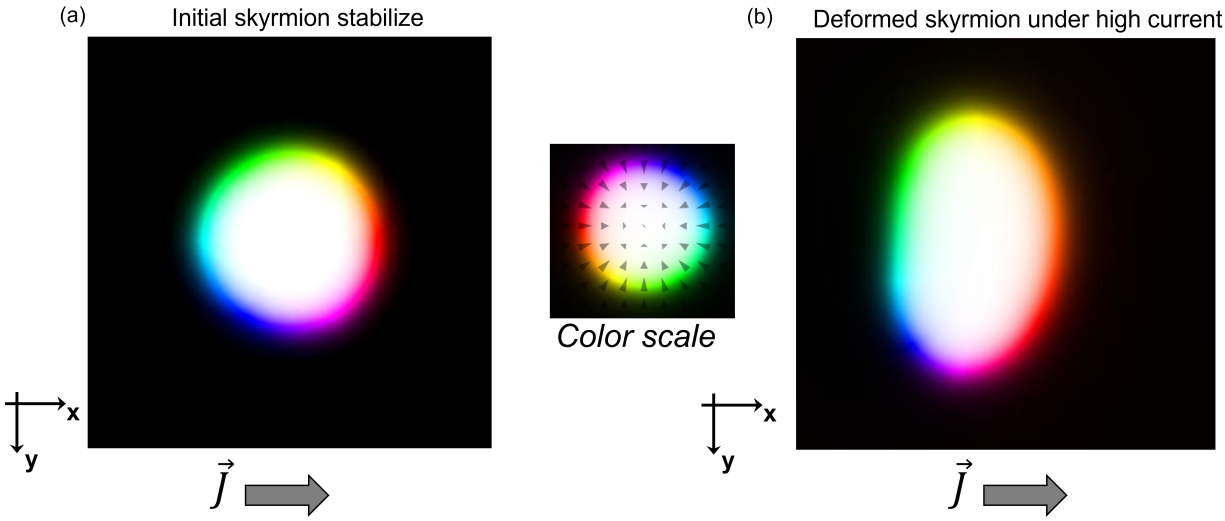

Figure 7.18: (a) Skyrmion stabilize using the simulation parameters described in the table 7.1, before the application of a current density, that we call the initial state. (b) Elongated skyrmion after the application of a current density $\vec{J}$ in the x-direction, called the final state.

The obtained trajectories of skyrmion under a high current density, for a damping of $\alpha = 0.5$, are plotted in the figure 7.19. As for a smaller current, the trajectory of the skyrmion differed for different DMI value, due to an evolution of the helicity with the DMI. We also notice a sudden change in trajectory during the application of the electrical current for some of the studied skyrmions. The difference of the DMI coefficient ΔD between a skyrmion having a straight motion and the next one changing of direction is small, $\Delta D = 20\mu J/m^2$. Therefore this creates four regions where the skyrmions are not going, highlighted with the hatched regions in the figure. We are then expecting that skyrmions stabilized in this specific ranges of DMI will follow one or the other trajectory around the hatched region.

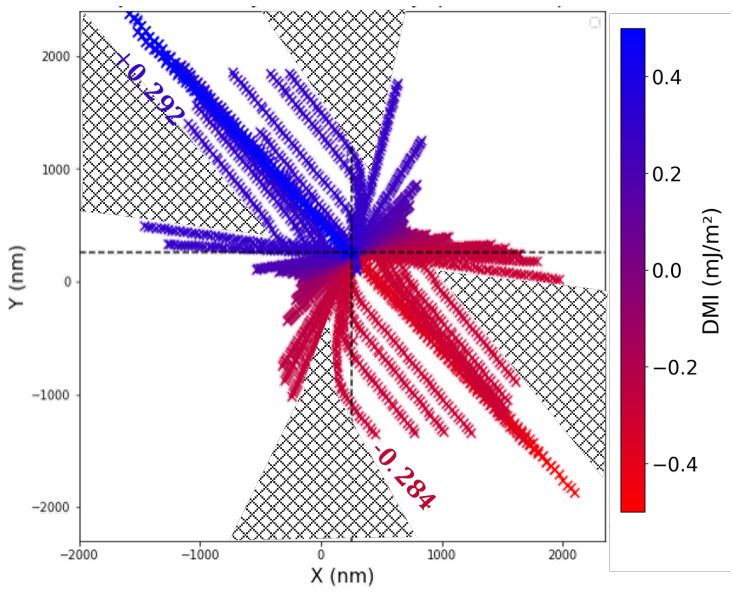

Figure 7.19: Trajectories of skyrmions driven by an electrical current density $j = 10^{11}\mathrm{A/m}^2$, for different values of the DMI ranging from -0.5 to $+0.5\mathrm{mJ/m}^2$. The color of each curve corresponds to a specific DMI value. The hatched regions indicate areas where no skyrmions goes under high current. Two values of DMI are written to highlight two trajectories study in the following: $D = +0.292mJ/m^2$ and $D = -0.284mJ/m^2$

To understand why this change in the direction of motion occurs, we first examine the significant variations in skyrmion parameters under high current.

Measurement method of the skyrmion radius, domain wall width and helicity using python.

For the measurement of these three parameters we use the same technique described in the section 7.2. In addition, due to the deformation of the skyrmion under high current, we measure the parameters all along the skyrmion perimeters for each angle around the skyrmion, between 0° and 360°. An average of each parameter is then calculated and used for the studies.

First, the most intuitive change linked to a deformation is a change in the radius. The value of the skyrmion radius, depending along which radial direction it is measured will not be the same. In the figure 7.20, for both the initial and the final state, we plot the polar representation of the radius as well as the radius value with respect to the angle around the skyrmion, for a DMI value of $D = 0.292mJ/m^2$ corresponding to one of the skyrmion changing its trajectory during the simulation, highlighted in figure 7.19. The figure 7.20(a)-(b) shows the initial state for which the skyrmion radius is not changing for all the measurements done around the skyrmion edge.

After the application of a high current density, the skyrmion starts to deform and the radius change depending on the angle of measurement, as it is shown by both the figures 7.20(c) and (d). In the initial state, a difference in the radius measured of $\Delta R_{max} = 2nm$ can be found, which corresponds to 6% of the average radius measured. For the final state, when the skyrmion is elongated, a difference of $\Delta R_{max} = 35nm$, which corresponds to 38% of the average radius, is measured around the skyrmion. After the application of the current the maximum radius difference measured in between each radial direction increases of 33%.

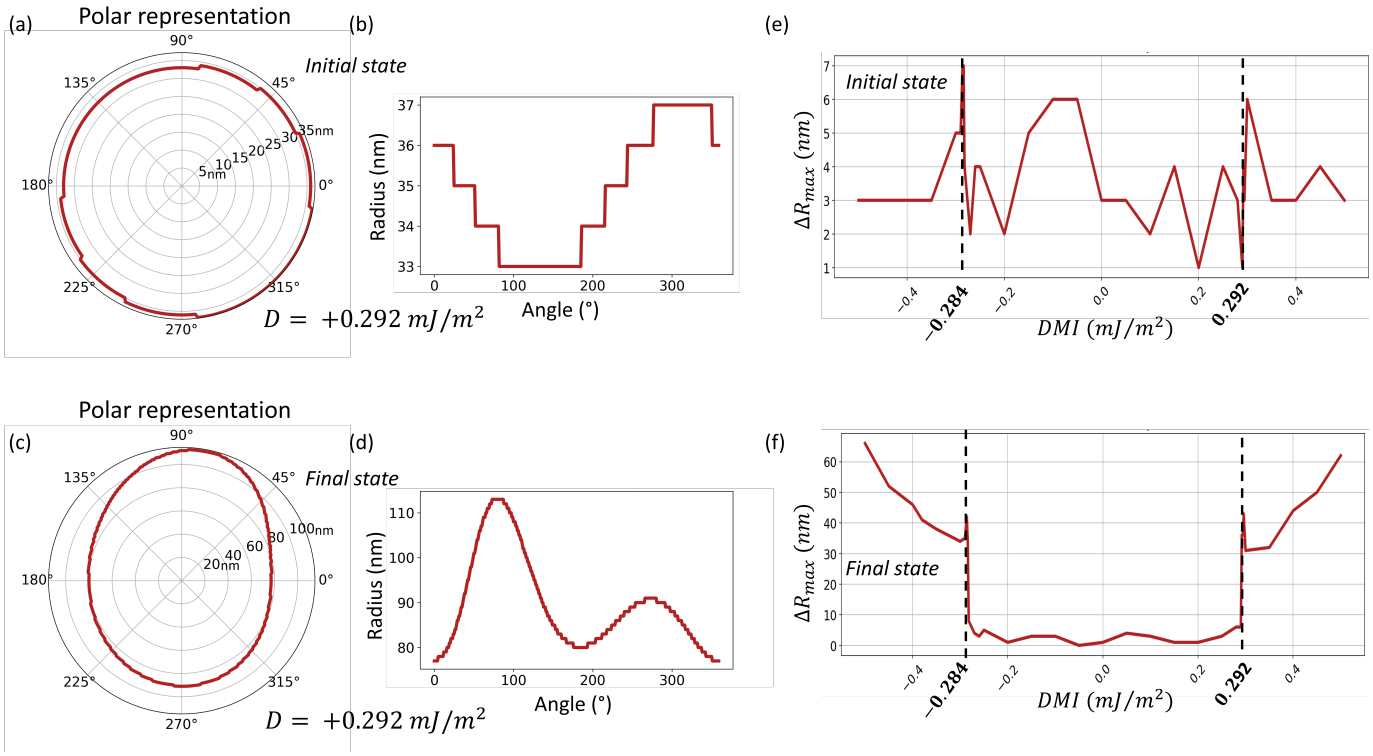

Figure 7.20: Radius measured all around the skyrmion in the initial (a)-(b) and final state (c)-(d) after the application of an electrical current density. (a) and (c) are the polar representation and (b) and (d) the evolution of the radius value with respect to the angle of measurement. (e) and (f) Maximum variation of the radius measured around the skyrmion perimeter as a function of the DMI value in the initial and final state. The vertical dashed lines represent the DMI value for which skyrmions trajectories is changing during the simulation.

Figure 7.20(e)-(f) shows the maximum variation in the skyrmion radius measured around its perimeter for the different DMI values studied, in (e) the initial state and (f) the final state. In the initial state, before applying the current, the maximum difference measured for each angle around the skyrmion edge is in between $1 - 7nm$, which corresponds respectively to 5%- 20% of the average radius measured, while after the application of the current, once the skyrmion is deformed, this difference can reaches up to $65nm$, which corresponds to 55% of the average radius. Also, by comparing both states, we see that after the elongation of the skyrmion the difference in the measured radius depends much more of the DMI value. The difference is higher for the skyrmions closer to Néel skyrmion and drops at almost 0 around a DMI of $D = \pm 0.3 mJ/m^2$.

With the deformation of the skyrmion an evolution of the domain wall width around the skyrmion is also measured. The figure 7.21 shows, both the polar representation of the domain wall width and values measured with respect to each angle, for the initial (a)-(b) and the final state (c)-(d), for the DMI value of $D = 0.292mJ/m^2$. Initially the maximum domain wall width difference measured is $\Delta\delta_{DW} = 0.3nm$ which is less than the resolution as one pixel corresponds to one nm. In the final state this difference increase to reach $\Delta\delta_{DW} \sim 12.5nm$. We also see that after the application of the current the average domain width value change. Initially we measure $\delta^{Av}_{DW_{init}} = 38.9nm$

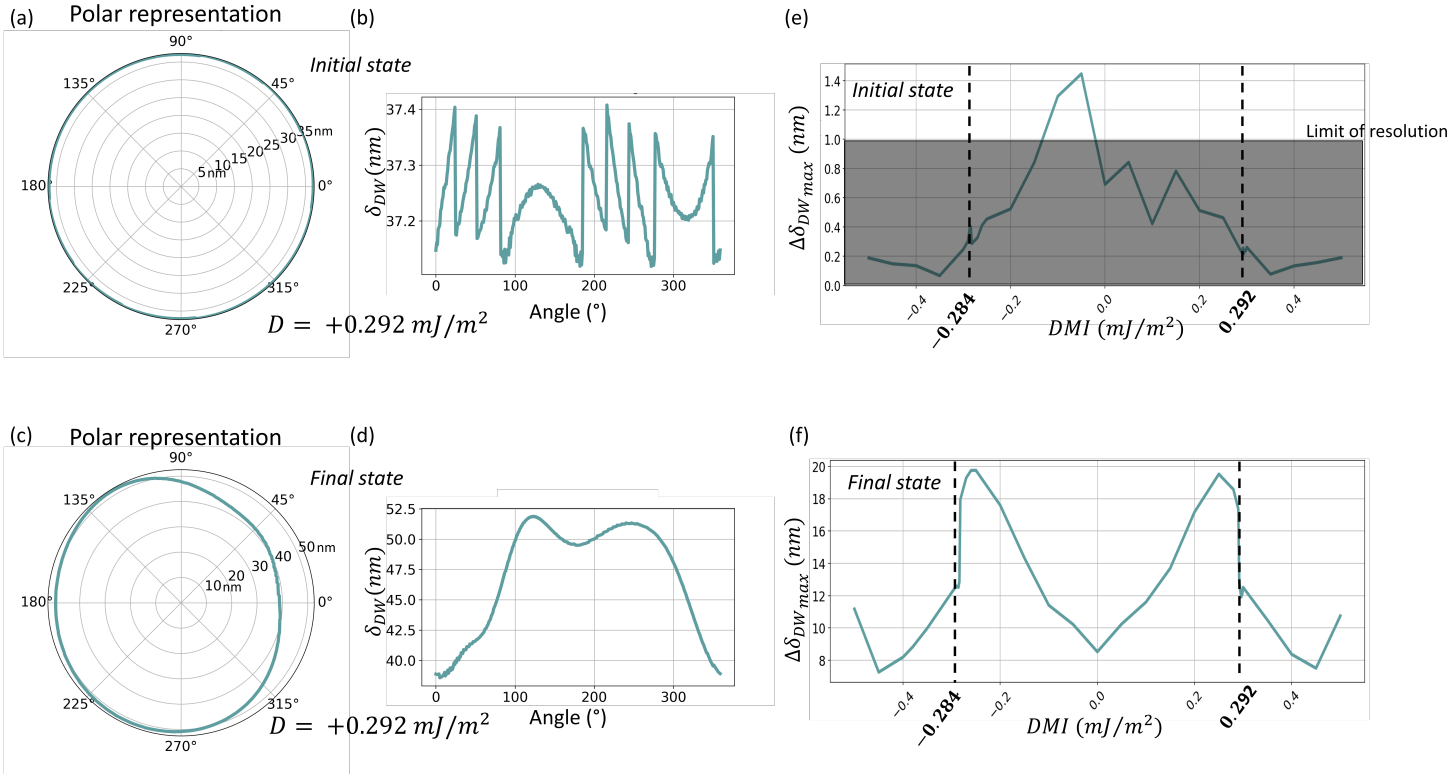

Figure 7.21: Domain wall width δ_{DW} measured all around the skyrmion in the initial (a)-(b) and final state (c)-(d) after the application of an electrical current density. (a) and (c) are the polar representation and (b) and (d) the evolution of the δ_{DW} value with respect to the angle of measurement. (e) and (f) Maximum variation of the domain wall width measured around one skyrmion perimeter as a function of the DMI value in the initial and final state.The vertical dashed lines represent the DMI value for which skyrmions trajectories is changing during the simulation.

As for the radius we show in Figure 7.21(e)-(f) the maximum variation in the domain wall width δ_{DW} measured around its perimeter for the different DMI values studied, in (e) the initial state and (f) the final state. In the initial state, before applying the current, the maximum difference measured for each angle around the skyrmion edge is in between 0 and 1.4 nm, while after the application of the current, once the skyrmion is deformed, this difference can reach up to $20nm$. Also, in the final state, the maximum difference observed all around the skyrmion is the highest for a DMI value around $\pm 0.25mJ/m^2$, close to the values for which the skyrmion

change of trajectories, represented in the figure by the black dashed line.

Finally, the helicity is also affected by the deformation of the skyrmion. The figure 7.22 shows the polar representation and the evolution of the helicity ξ with the angle around the skyrmion in the initial state (a)-(b) and final state (c)-(d). The jump and flat part in the final state graphs are due to the removal of some values out of range due to the handling of the PBC, leading to a bad measurement of the helicity for some angles around the skyrmion. In the initial state the maximum of difference found for the helicity all around the skyrmion is $\Delta\xi \simeq 12°$. In the final state this difference increases up to $\Delta\xi \simeq 100°$ (not taking into account the few points out of range). In the initial state the average helicity measured is $\xi_{init}^{av} \simeq 122.4°$ while in the final state this value increase to $\xi_{init}^{av} \simeq 165°$. For most of the angles around the skyrmion the helicity is higher than in the initial state in addition to the elongation of the skyrmion and the increase in the domain wall width.

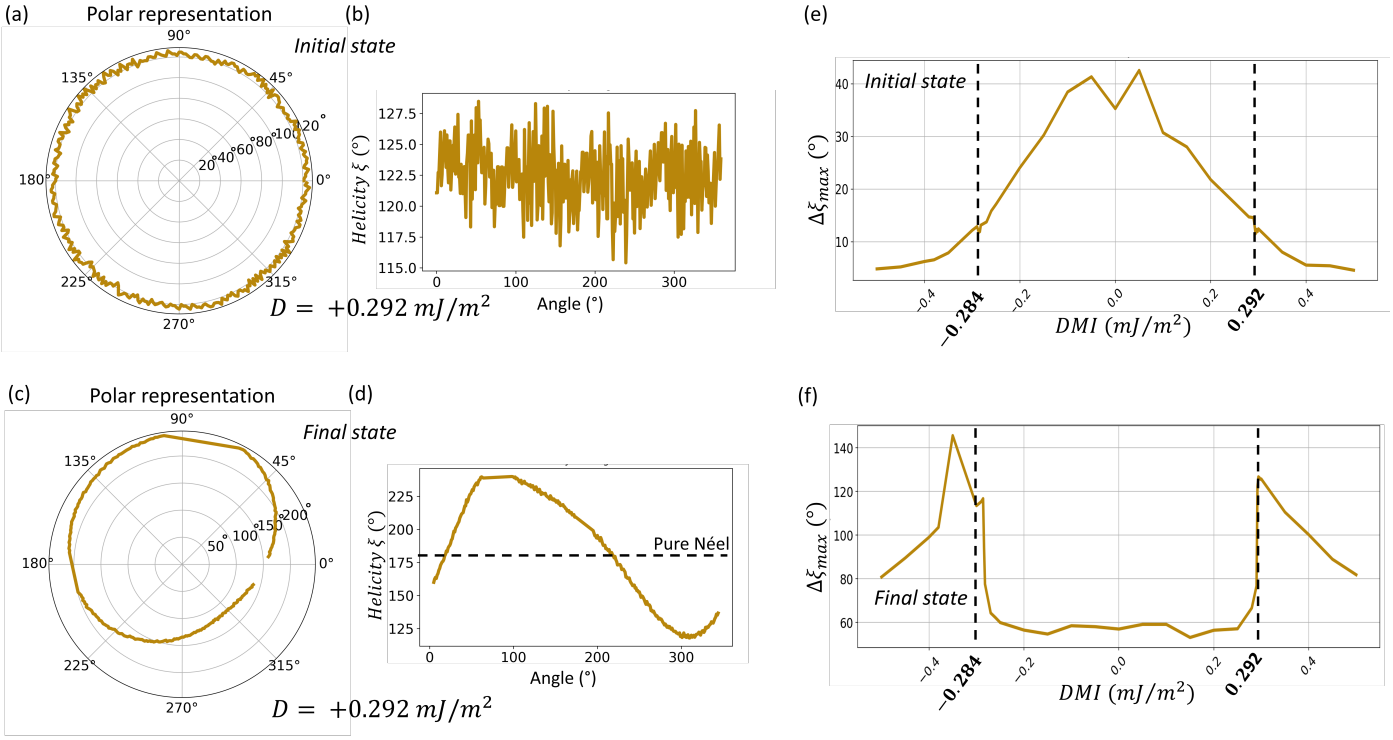

Figure 7.22: Helicity ξ measured all around the skyrmion in the initial (a)-(b) and final state (c)-(d) after the application of an electrical current density. (a) and (c) are the polar representation and (b) and (d) the evolution of the helicity value with respect to the angle of measurement. Jump and flat part in the final state graphs are due to the removal of some values out of range due to the handling of the PBC. (e)-(f) Maximum variation of the domain wall width measured around one skyrmion perimeter as a function of the DMI value in the initial and final state.

The figure 7.22(e)-(f) presents the maximum difference in helicity measured all around the perimeter of the skyrmion in (e) the initial state and (f) the final state. In the initial state, a maximum variation of the helicity, $\Delta\xi_{max} \simeq 40°$ is measured for the DMI values close to 0, corresponding to pure Bloch skyrmions. We attribute this deviation to the current already

beginning to influence the helicity orientation, since the measurements are performed 2ns after the current is applied. This indicates that Bloch skyrmions respond more rapidly to the current than skyrmions closer to the Néel configuration.

However, we see that this tendency is inverted in the final state. The higher variations are found for skyrmions with a DMI value D close to $\pm 0.3 mJ/m^2$, with $\Delta\xi_{max} \simeq 140°$.

When an electrical current is applied, spins polarized along $\overrightarrow{y}$ are injected. At high current densities, this tends to align the spins within the domain walls along the same $\overrightarrow{y}$ direction. Finally, after the application of the current, we observe that the skyrmions exhibiting the largest variations of their parameters (R, δ_{DW}, ξ) along their perimeter are those with a DMI value close to the transition point where the direction of motion changes.

In the following study we consider for these three parameters, an average value along the perimeter of the skyrmion. To understand better the effect of the high current and the deformation on the skyrmion parameters we plot in the figure 7.23 the difference between the initial and final trajectories (a) as well as the average value of the three parameters of the skyrmion: (b) the radius, (c) the domain wall width δ_{DW} and (d) the helicity ξ.

We observe that the most pronounced effect of applying a high current density occurs near the DMI value of $D \simeq \pm 0.3, \mathrm{mJ/m^2}$ for all three parameters. Specifically, the high current density induces changes in the skyrmion radius, domain wall width, and helicity at certain DMI values, close to the critical D_C^N DMI, which in turn could lead to the observed change in direction as seen in the figure 7.23(a).

Indeed, as explained before the motion of skyrmions is dictated by the helicity angle ξ. A change in the direction of the skyrmion would imply a change in the helicity. This is confirmed in the figure 7.24 where we plot the helicity angle with respect to the DMI values for both the initial state (corresponding to the first few points of the trajectories) and the final state (corresponding to the few last points of the trajectory).

A change in the average helicity value is observed between the initial state and the final state for the skyrmions having a change in the trajectory. This means that, in addition to not be constant all around the skyrmion edge, the average helicity is also changing during the application of the electrical current, after an application of current during ~ 30 to $70ns$ depending the DMI value.

In the figure 7.25 we plot the evolution of the three skyrmion parameters, during the time the current is applied, for both DMI values $D = +0.292 mJ/m^2$ [figure 7.25(a)-(c)] and $D = -0.284 mJ/m^2$ [figure 7.25(d)-(f)] corresponding to skyrmions changing their direction of motion. It is important to note here that the two first points on each graphs correspond to the relaxation of the skyrmion with new parameters and does not have to be taken into account in the study, the current starts to be applied at the state 2.

In the figure 7.25(a) and (d) the evolution of the radius shows for both value of DMI a fast increase of the radius measured at the beginning, followed by a smoother increase and a second fast increase, located at the states at which the skyrmion starts to change direction to reach finally a 'plateau' at the end. For the domain wall width, presented in the figure 7.25(b) and (e)

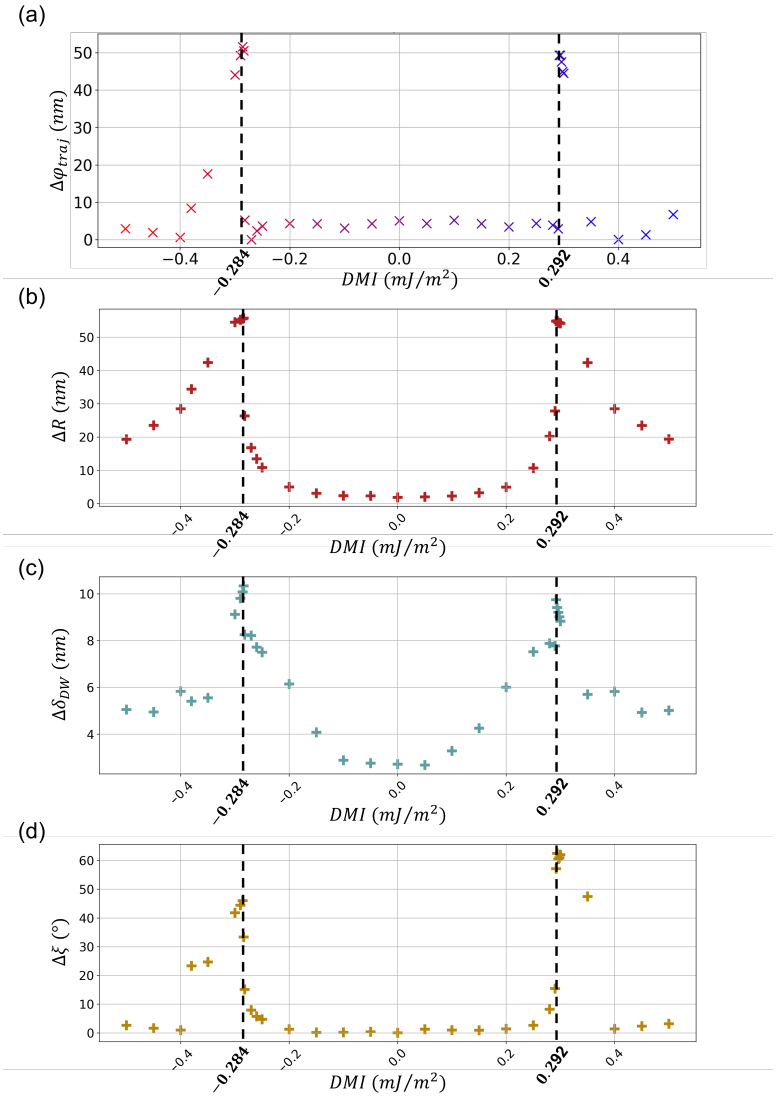

Figure 7.23: Evolution of the difference between the initial and the final state for (a) the trajectories, (b) the average radius, (c) the average domain wall width δ_{DW} and (d) the average helicity ξ, plotted as a function of the DMI value.

only a small variation of $\Delta\delta_{DW} = 4nm$ is measured along the whole simulation. However the increase is located once again at the state where the change of direction starts. Finally we plot in the figure 7.25(c) and (f) the evolution of the helicity. A sharp change is noticeable once again close to the state where the deviation in the direction motion occurs, preceded by a 'plateau'. The length of these 'plateau', for all the three skyrmion parameters, can be explained by the time it takes to accumulate enough energy in order to transition into one or the other skyrmion configuration surrounding the hatched region of figure 7.19.

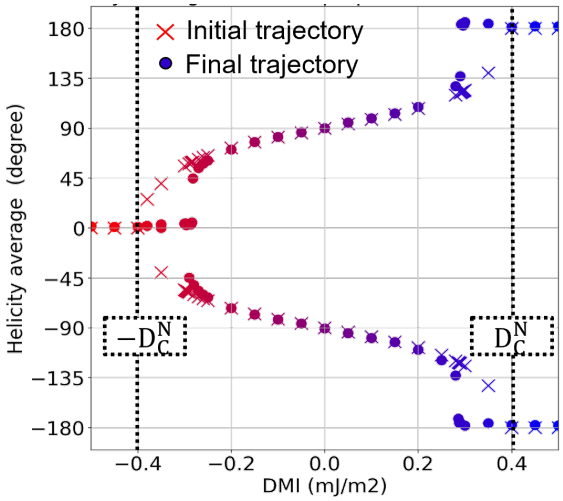

Figure 7.24: Comparison of the average helicity measured in the initial state and in the final state, after the application of the current, as a function of the DMI. Critical value of the DMI $\pm D_N^C$ for which we consider pure Néel skyrmion are represented using black dotted line.

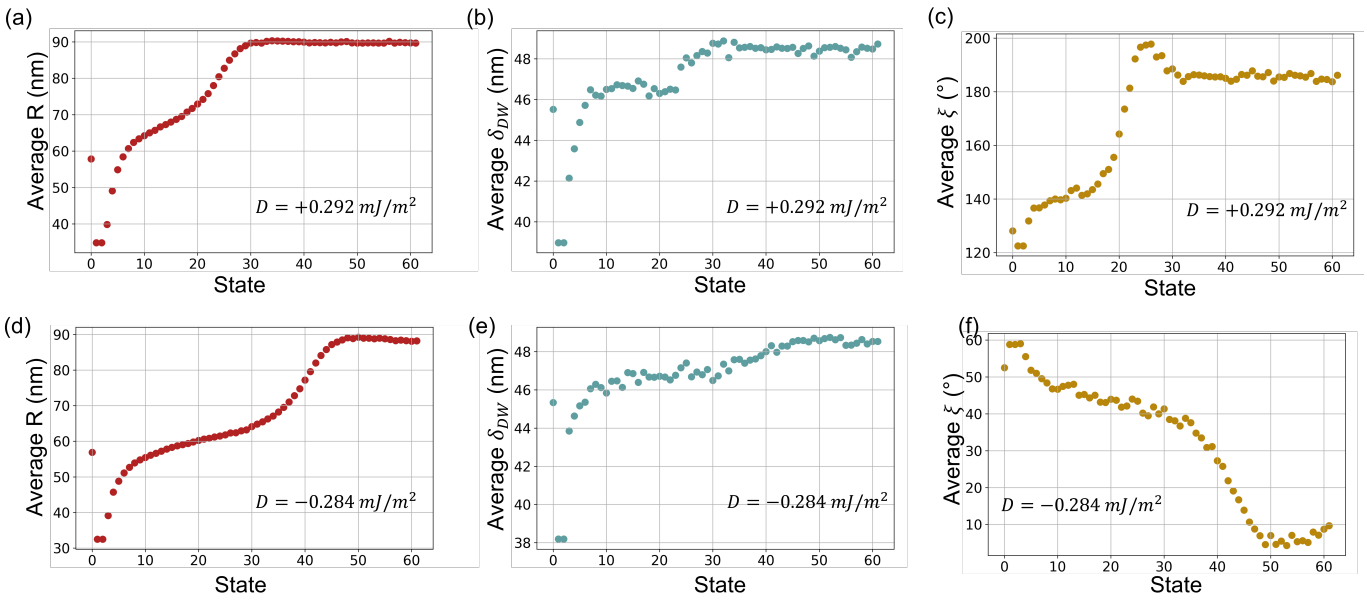

Figure 7.25: Evolution of the average radius R, average domain wall width δ_{DW} and average helicity ξ as a function of the state inside the simulation, corresponding to the time of current injection. The evolution of these three parameters is plotted for both DMI value $D = +0.292 mJ/m^2$ [(a)-(c)] and $D = -0.284 mJ/m^2$ [(d)-(f)], two values for which skyrmions change of direction during the application of the current.

7.5 Conclusion

In conclusion, we demonstrated that the characteristics of skyrmions (radius, domain wall width, and helicity) strongly depend on the DMI strength. A precise control of the interfacial DMI

therefore enables tuning of the skyrmion configuration and helicity. Moreover, adjusting the skyrmion radius and helicity would allow to control their trajectory. Our simulations validate the model predicting skyrmion motion as a function of their intrinsic parameters (R, δ_{DW}, ξ, p) and the damping constant α.

We also identified regions where skyrmions are unable to propagate under large current densities due to helicity changes during current application. In particular, skyrmions stabilized with a DMI value close but lower to the critical threshold for a pure Néel state (D_N^C) behave effectively as pure Néel skyrmions.

Further studies are required to better understand the change in helicity under high current density. A deeper insight could be obtained by revisiting Thiele model and approximation used in the low-current regime, in particular regarding the rigid-core assumption of the model and the evolving helicity around the skyrmion parameter measured in the simulations. Controlling the evolution of skyrmion parameters may enable experimental control of skyrmions under high current densities.

Trajectories of skyrmions in Co based devices should meet the findings described by the simulations presented in this chapter, an experimental study could therefore be done to verify and support simulated results.

In section 2.3.2 we discuss about the field-like torque effect and efficiency: for the whole study we only considered damping-like torque originating from the spin Hall effect. However recent studies highlight the importance of the field-like torque, as well as its possible orbital origin. Field-like torque is generally seen as an in-plane external field, inducing a expansion of the skyrmions. Therefore it could be interesting to add a field-like torque component in our simulations to study its influence on the skyrmion deformation, and therefore on the trajectories, that would probably happen at lower current density.

Chapter 8

Conclusion and perspectives

This chapter first summarizes the different studies and main results obtained during my PhD. In the second part, I discuss the remaining work required to deepen these topics as well as the perspectives of the overall project.

8.1 General Conclusion

In this thesis, we combined experimental, theoretical, and numerical studies to advance the understanding and control of skyrmions. We focused on a heavy metal/ferromagnet/oxide trilayer system composed of Ta/FeCoB/TaOx and investigated both the intrinsic properties of skyrmions and their response to electrical currents.

Using current-induced motion, we mapped the DMI sign in our samples and revealed its dependence on both the oxidation state at the FeCoB/TaOx interface and the ferromagnetic layer thickness. Together with *ab initio* calculations, this study provided an explanation for the observed DMI reversal, highlighting the role of *d*-orbital occupation and the resulting modification of interatomic distances at the interface.

Building on previous work from our group, we confirmed that skyrmion chirality can be tuned by electric fields through oxidation control at the interface. High-energy photoemission spectroscopy (HAXPES) measurements directly evidenced oxygen-ion migration under gating in a similar Pt/Co/AlOx syste. Unambiguously identifying the magneto-ionic origin of the effect. Combined with anisotropy studies, these results confirm that applying a gate voltage can reversibly modify the interfacial oxidation state.

This confirmation of oxygen-ion migration under gate voltage, associated with the previous study on the DMI sign makes possible the chirality change of skyrmions by applying a gate voltage in a region close to zero DMI. Specifically, we investigated the possibility of reversing the chirality of spin textures in a magnetic track. While single-skyrmion control remains challenging, we established that domain wall motion and thus chirality can be efficiently tuned by gate voltage near the zero-DMI region.

Finally we numerically studied skyrmions dynamics under an electrical current using micromagnetic simulations. We showed that skyrmion trajectory strongly depend on the DMI value and helicity, in agreement with analytical models linking motion to intrinsic parameters (R, δ_{DW}, ξ, p) and the damping constant α.

We also identified regions where skyrmions are unable to propagate under large current densities due to a helicity change during current application. In particular, skyrmions stabilized with a DMI value close to the critical threshold for a pure Néel state (D_N^C), then having an intermediate wall type, have their helicity changed to pure Néel and then behave effectively as pure Néel skyrmions.

8.2 Perspectives

The connection between the interatomic distance z and the inversion of the DMI sign opens perspectives for controlling chiral domain walls and skyrmions through strain. In this context, a growing research field explores the potential of nucleating and propagating skyrmions using transient strain induced by surface acoustic waves [142], [143], [90].

Numerically, the skyrmion dynamics study constitutes a large subject. Additional simulations could be performed to deepen our understanding. In continuity with our work, investigating the effect of damping on skyrmion trajectories and intrinsic parameters under high current densities would provide further understanding and bring the analysis closer to experimental conditions. In this idea, it could also be interesting to add a field-like torque component in our simulations to study its influence on the skyrmion deformation, and therefore on the trajectories, that would probably happen at lower current density.

The stability of the skyrmion experiencing a reversal of its chirality is also of interest. By linking both gate voltage control experiments and micromagnetic simulations study a full control of a single skyrmion could be achievable.

Experimentally, a larger spin-orbit torque, associated with an enhanced DMI, can be obtained by replacing the bottom tantalum layer in our trilayer system with tungsten (W). A study of the W/FeCoB/TaOx trilayer will be carried out by a postdoctoral researcher in the team to verify the possible reversal of the DMI sign.

In parallel, both Ta/FeCoB/TaOx and W/FeCoB/TaOx systems will be investigated using ultrafast laser pulses, with the aim of creating more stable skyrmions. This constitutes an important step toward achieving controlled chirality reversal of individual skyrmions.

To increase the efficiency of gate control, Lithium Phosphorus Nitride (LiPON) has been proposed as a substitute for the HfO_2 dielectric layer and has already shown promising results. In [156], the nucleation and annihilation of skyrmions were demonstrated using a LiPON-based solid-state ionic supercapacitor combined with a $Pt/Co_{40}Fe_{40}B_{20}/Pt$ magnetic thin film, as

illustrated in the figure 8.1. The application of a gate voltage induces the accumulation or depletion of Li^+ ions at the magnetic interface, thereby also controlling the skyrmion density.

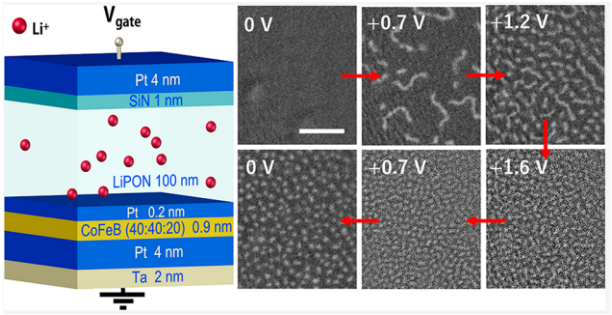

Figure 8.1: *Extracted from [156]*(a) Scheme of the LiPON-based solid-state ionic supercapacitor combined with a $Pt/Co_{40}Fe_{40}B_{20}/Pt$ magnetic thin film. A gate voltage is applied from the top. (b) Polar MOKE microscopy images recorded while sweeping the applied voltage from 1.0 V to +2.0 V and back. The perpendicular magnetic field is +0.7mT.

LiPON-based voltage control of magnetization offers a promising route to tune the DMI via gate voltage in supercapacitor devices, an approach that, to our knowledge, remains unexplored. Such efficient gated devices could facilitate chirality reversal.

Chapter 9

Supplementary

9.1 Supplementary 1: Thickness conversion

The off-axis deposition technique is schematized in the fiure 9.1(a). To convert an (x,y) position on the sample into thicknesses value of the materials (t_{FM};t_{HM}), we consider as a good enough approximation that, in the case of off-axis deposition, the deposition thickness t has a linear variation with the distance from the target to the center of the sample. Hence, the thickness t(d) can be expressed as:

$$t(d) = (ad + b)e_0$$

With d the distance to the target center, a is the slope in m^{-1} representing the rate of material deposition per unit length, b is the intercept from the linear approximation, and e_0 the thickness that would have been deposited under on-axis deposition conditions. The coefficients a and b care material dependent and are determined by the deposition chamber geometry.
The two expressions of thickness of the two materials are therefore:

$$t_{FM} = (a_{FM}d_{FM} + b_{FM})e_0^{FM} \text{ for ferromagnet}$$

$$t_{HM} = (a_{HM}d_{HM} + b_{HM})e_0^{HM} \text{ for heavy metal}$$

The distance d from the center of the sample remains constant along a circle. However, since the two wedges (the ferromagnetic and heavy metal layers) are deposited perpendicular to each other, the distances d_{FM} and d_{HM} are not identical. Considering a reference frame with coordinates (x, y), the circular symmetry for each material's wedge is oriented differently. This is illustrated in Figure 9.1(b). Consequently, the distance expressions for the two materials differ:

$$d_{FM} = \sqrt{(x - \text{deport})^2 + y^2}$$

$$d_{HM} = \sqrt{x^2 + (y - \text{deport})^2}$$

Here, the deport is the same for both cases and equals 100 nm, corresponding to the wafer diameter.

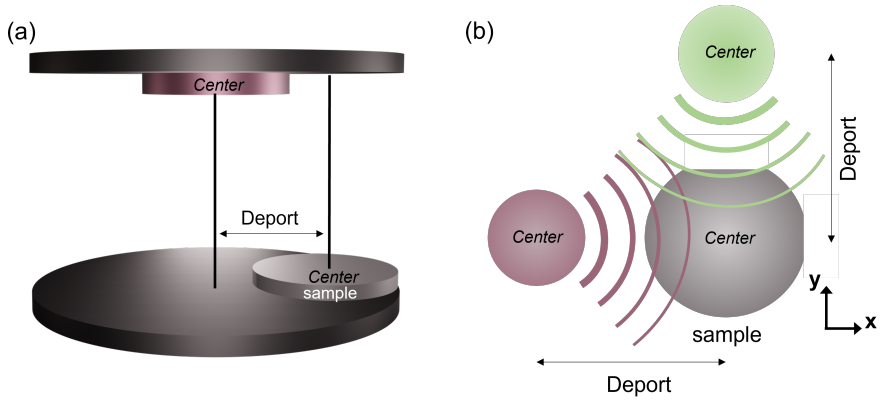

Figure 9.1: (a) 3D Scheme of Off-axis deposition technique. The sample is misaligned with respect to the target by a value "deport". The dotted line represents the conical deposition distribution and the thick pink line represents the thickness of the deposited layer with respect to deport (b) Top view of the off-axis deposition, pink lines represents the iso-thickness lines of the first material to be deposited, green lines correspond to the iso thickness of the second material to be deposited perpendicular to the first one.

9.2 supplementary 2: Inter and intralayer contribution to the DMI

In a bcc structure, the DMI energy can be separated into two components: interlayer E_{DMI}^{inter} and intralayer E_{DMI}^{intra}. The figure 9.2 displays the resulting $d_{kk'}$ DMI coefficients calculated by constructing two spin-spiral in the bilayer k and k'. For the intralayer contributions, only one spin spiral is constructed in the focused layer while the spins of the others are fixed in the y-crystallographic direction.
The highest contributions to the DMI is coming from the intralayer interactions Fe_1Fe_1 and Fe_3Fe_3 exhibiting opposite sign. For the interlayer contributions the large value of the Fe_1Fe_2 interaction is compensate by the combination of the Fe_1Fe_3 with Fe_2Fe_3. Finally in the overall we found $\sum_k E_k^{intra} + \sum_{k,k'} E_{k,k'}^{inter} = -7.84meV$. By comparison with the calculated energy in the section 4.3 ($E_{DMI} = -8.34meV$) we see a slight difference in the resulting value. In fact, calculations with different constrained configuration cannot result in the exact same value; but this difference is small enough (6%) to demonstrates the accuracy of our results.

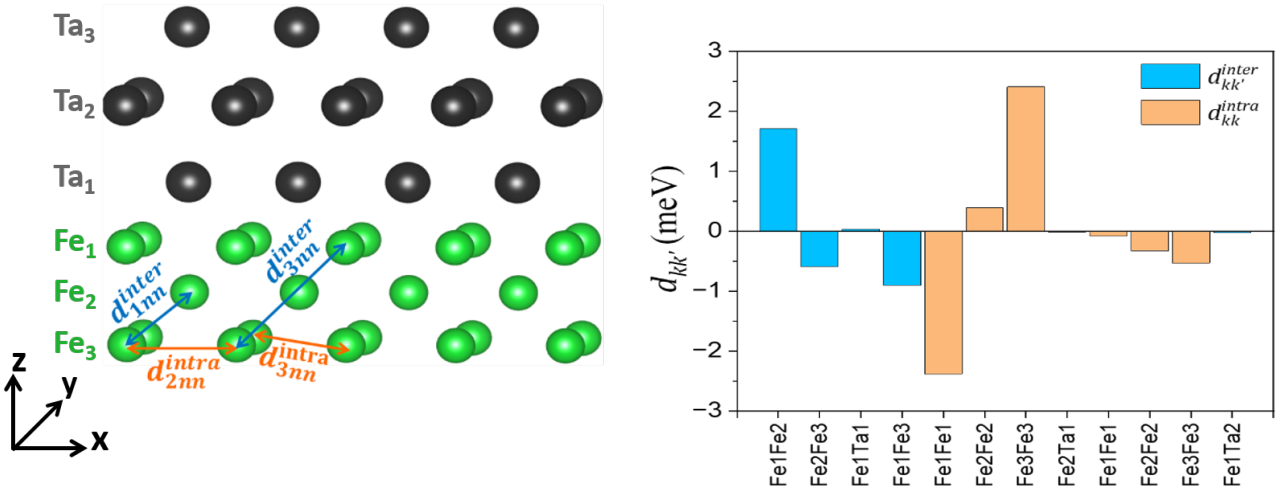

(a) (b)

Figure 9.2: (a) Fe_3Ta_3 structure with the different interactions, between nearest neighbors, represented. Intralayer interaction are displayed in orange while interlayer ones are in blue. (b) Histogram showing the the calculated layer-resolved intra- and interlayer contributions to the DMI energy

9.3 Supplementary 3: Bloch and Néel domain wall energy and profile

1- Bloch domain wall energy per unit area:

We can write the volume energy of a domain wall in the 1D model as :

$$E_{tot} = A[\frac{d\theta}{dx}(x)]^2 + E_a[\theta(x)] \tag{9.1}$$

A being the exchange stiffness and θ a quantity defined at each point, in the case of domain wall it represents the angle of the spin inside the domain wall with respect to the direction out of the plane of the ferromagnetic thin film.

To minimize the energy, we apply the Euler-Lagrange equation 1.28 we obtain:

$$\frac{\partial E_a}{\partial \theta} - \frac{d}{dx}[2A\frac{\partial \theta}{\partial x}] = 0 \tag{9.2}$$

$$\frac{\partial E_a}{\partial \theta} = 2A\frac{d^2\theta}{dx^2} \tag{9.3}$$

$$\frac{\partial E_a}{\partial \theta}\frac{d\theta}{dx} = 2A\frac{d^2\theta}{dx^2}\frac{d\theta}{dx} \tag{9.4}$$

As E_a only depends on x via θ we can write:

$$\frac{dE_a}{dx} = A\frac{d}{dx}[(\frac{d\theta}{dx})^2] \tag{9.5}$$

$$E_a = A(\frac{d\theta}{dx})^2 \tag{9.6}$$

The Bloch domain wall energy per unit area is written :

$$\sigma_{BlochDW} = \int_{-\infty}^{+\infty} \left[A(\frac{\partial\theta}{\partial x})^2 + E_a[\theta(x)] \right] dx \tag{9.7}$$

$$\sigma_{BlochDW} = 2\int_{-\infty}^{+\infty} \left[A(\frac{\partial\theta}{\partial x})^2 \right] dx \tag{9.8}$$

With the equation 9.6 we deduce $\frac{d\theta}{dx} = \sqrt{\frac{E_a[\theta(x)]}{A}}$, by replacing it in the equation 9.8 we obtain:

$$\sigma_{BlochDW} = 2\int_{-\infty}^{+\infty} \left[\sqrt{AE_a[\theta(x)]}\frac{d\theta}{dx} \right] dx = 2\int_{x_A}^{x_B} \left[\sqrt{AE_a[\theta(x)]}\frac{d\theta}{dx} \right] dx \tag{9.9}$$

With $x_a = -\infty$ and $x_B = +\infty$ We want to integrate over θ and not x so we change the variable as $d\theta = dx\frac{d\theta}{dx}$.

$$\sigma_{BlochDW} = 2\int_{\theta(x_A)}^{\theta(x_B)} \left[\sqrt{AE_a[\theta(x)]} \right] d\theta \tag{9.10}$$

In the case of a Bloch domain wall we have: $\begin{cases} E_{tot} = A(\frac{\partial\theta}{\partial x})^2 + K_u sin^2\theta \\ \theta(x_A) = 0 \\ \theta(x_B) = \pi \end{cases}$

So $E_a[\theta(x)] = K_u sin^2\theta$, therefore we have:

$$\sigma_{BlochDW} = 2\int_0^{\pi} \left[\sqrt{AK_u} sin\theta \right] d\theta \tag{9.11}$$

Finally,

$$\sigma_{BlochDW} = 4\sqrt{AK_u} \tag{9.12}$$

2- Domain wall profile
The free energy of a domain is:

$$E_{tot} = E_{ex} + E_{aniso} + E_{DMI} = A(\frac{\partial\theta}{\partial x})^2 + K_{eff}sin^2\theta + D\frac{\partial\theta}{\partial x} \tag{9.13}$$

With θ the angle between the magnetization and the easy axis, A the exchange stiffness, K_{eff} the effective anisotropy coefficient and D the DMI coefficient.
Minimizing this energy is equivalent to resolve the Euler-Lagrange equation:

$$\frac{\partial E_{tot}}{\partial\theta} - \frac{d}{dx}(\frac{\partial E_{tot}}{\partial\theta'}) = 0 \tag{9.14}$$

Where $\theta' = \frac{d\theta}{dx}$. By solving this equation we can define a domain wall profile $\theta(x)$, which defines the spatial variation of the magnetization while crossing the DW along its normal.

$$2K_{eff}cos(\theta)sin(\theta) - \frac{d}{dx}(2A\frac{\partial\theta}{\partial x} + D) = 0 \tag{9.15}$$

$$\frac{d^2\theta}{dx^2} = \frac{K_{eff}}{A}sin(\theta)cos(\theta) = \frac{sin(\theta)cos(\theta)}{\Delta^2} \tag{9.16}$$

Where $\Delta = \sqrt{\frac{A}{K_{eff}}}$ the characteristic domain wall length.

$$\int \frac{d\theta}{dx}\frac{d^2\theta}{dx^2} = \int \frac{d\theta}{dx}\frac{sin(\theta)cos(\theta)}{\Delta^2}dx \tag{9.17}$$

$$\Leftrightarrow \frac{1}{2}\int \frac{d}{dx}(\frac{d\theta}{dx})^2dx = \frac{1}{2}\frac{sin^2(\theta)}{\Delta^2} \tag{9.18}$$

$$\Leftrightarrow (\frac{d\theta}{dx})^2 = \frac{sin^2(\theta)}{\Delta^2} + C_1 \tag{9.19}$$

The integration constant C_1 can be consider zero.

$$\Leftrightarrow \frac{d\theta}{dx} = \pm\frac{sin(\theta)}{\Delta} \tag{9.20}$$

$$\Leftrightarrow \frac{d\theta}{sin(\theta} = \pm\frac{dx}{\Delta} \tag{9.21}$$

For simplification we introduce $t = tan(\frac{\theta}{2})$, therefore $dt = \frac{d\theta}{2}[1 + tan^2(\frac{\theta}{2})] = \frac{d\theta}{2}[1 + t^2]$ and $sin(\theta) = \frac{2t}{1+t^2}$

$$\Leftrightarrow \frac{2dt}{1+t^2} \times \frac{1+t^2}{2t} = \pm\frac{dx}{\Delta} \tag{9.22}$$

$$\Leftrightarrow \frac{dt}{t} = \pm\frac{dx}{\Delta} \tag{9.23}$$

$$\Leftrightarrow ln(t) = \pm\frac{x - x_0}{\Delta} \tag{9.24}$$

$$\Leftrightarrow t = e^{\pm\frac{x-x_0}{\Delta}} \tag{9.25}$$

$$\Leftrightarrow \theta(x) = 2arctan(e^{\pm\frac{x-x_0}{\Delta}}) + k\pi \tag{9.26}$$

3- Néel domain wall energy per unit area : In a Néel domain wall, spinorbit coupling combined with broken inversion symmetry gives rise to an additional energy term: the DzyaloshinskiiMoriya interaction (DMI). Magnetic charges also contribute a dipolar component to the anisotropy energy. It is important to note here that we are neglecting these dipolar contribution for the moment to express the Néel DW energy.

The energy per unit area is thereby written :

$$\varepsilon_{NeelDW} = \int_{-\infty}^{+\infty} A(\frac{\partial\theta}{\partial x})^2 + K_{eff}sin^2(\theta) + D\frac{\partial\theta}{\partial x}dx \tag{9.27}$$

$$= \int_{-\infty}^{+\infty} A(\frac{\partial\theta}{\partial x})^2 + K_{eff}sin^2(\theta)dx + \int_{-\infty}^{+\infty} D\frac{\partial\theta}{\partial x}dx \tag{9.28}$$

For a Néel domain wall with the orientation of the magnetization m_z going from 0 at $x = -\infty$ to $\pm\pi$ at $x = +\infty$ and following the demonstration in the supplementary 9.31 we can write:

$$= 4\sqrt{AK_{eff}} + D[\theta]_0^{\pm\pi} \tag{9.29}$$

$$= 4\sqrt{AK_{eff}} \pm \pi D \tag{9.30}$$

The $\pm$ sign is coming from the two chiralities, CW or CCW, that the domain wall can have to go from a magnetization oriented with an angle 0 to a magnetization oriented with an $\pm\pi$. We recall that in our convention a CW chirality corresponds to a DMI coefficient $D < 0$ and the angle θ go from 0 to $+\pi$ while for a CCW rotation, $D > 0$ and θ goes from 0 to $-\pi$.

9.4 Supplementary 4: Thiele equation - the velocities

Considering a robust skyrmion with a circular geometry in a HM/FM/MOx system, the broken symmetry being along the $\overrightarrow{z}$ direction. The current is applied to induce a motion of the skyrmion in the (x,y) plane and by considering a rotational symmetry in this plane the Thiele equation can be written:

$$\begin{pmatrix} -G_z v_y \\ G_z V_x \\ 0 \end{pmatrix} - \begin{pmatrix} \alpha D v_x \\ \alpha D v_y \\ 0 \end{pmatrix} + \begin{pmatrix} F_{DL,x} \\ F_{DL,y} \\ 0 \end{pmatrix} = 0 \tag{9.31}$$

$$\begin{cases} -G_z v_y - \alpha D v_x + F_{DL,x} = 0 \\ G_z v_x - \alpha D v_y + F_{DL,y} = 0 \end{cases} \tag{9.32}$$

$$\begin{cases} v_x = \frac{F_{DL,x} - G_z v_y}{\alpha D} \\ \frac{G_z F_{DL,x}}{\alpha D} - \frac{G_z^2}{\alpha D} v_y - \alpha D v_y + F_{DL,y} = 0 \end{cases} \tag{9.33}$$

$$\begin{cases} v_x = \frac{F_{DL,x} - G_z v_y}{\alpha D} \\ \frac{G_z F_{DL,x}}{\alpha D} - v_y(\frac{G_z^2 + \alpha^2 D^2}{\alpha D}) + F_{DL,y} = 0 \end{cases} \tag{9.34}$$

$$\begin{cases} v_x = \frac{F_{DL,x} - G_z v_y}{\alpha D} \\ v_y = \frac{G_z F_{DL,x} + \alpha D F_{DL,y}}{G_z^2 + \alpha^2 D^2} \end{cases} \tag{9.35}$$

$$\begin{cases} v_x = \frac{F_{DL,x}}{\alpha D} - \frac{G_z^2 F_{DL,x}}{\alpha D(G_z^2 + \alpha^2 D^2)} - \frac{G_z F_{DL,y}}{\alpha D(G_z^2 + D^2)} \\ v_y = \frac{G_z F_{DL,x} + \alpha D F_{DL,y}}{G_z^2 + \alpha^2 D^2} \end{cases} \tag{9.36}$$

$$\begin{cases} v_x = \frac{\alpha D F_{DL,x} - G_z F_{DL,y}}{G_z^2 + \alpha^2 D^2} \\ v_y = \frac{G_z F_{DL,x} + \alpha D F_{DL,y}}{G_z^2 + \alpha^2 D^2} \end{cases} \tag{9.37}$$

9.5 Supplementary 5: Analytical model of the helicity as a function of the DMI coefficient D

We have seen that by taking into account both the iDMI and the magnetic volume charges contribution the surface energy of the DW can be written:

$$\sigma_{DW} = 4\sqrt{A_{ex}(K_0 + K_d^V cos^2\xi)} + \pi D cos\xi \tag{9.38}$$

By minimizing this expression with respect to ξ we can obtain the expression of the equilibrium helicity as a function of the DMI value.

$$\frac{d\sigma_{DW}}{d\xi} = \frac{d}{d\xi}\left[4\sqrt{A_{ex}(K_0 + K_d^V cos^2\xi)}\right] + \frac{d}{d\xi}\left[\pi D cos\xi\right] = 0 \tag{9.39}$$

We recall the derivative of a square root function :

$$\frac{d}{dx}\left[\sqrt{u(x)}\right] = \frac{u'(x)}{2\sqrt{u(x)}} \tag{9.40}$$

With $u'(x) = \frac{du(x)}{dx}$ the derivative of the function u.

Therefore,

$$\frac{d}{d\xi}\left[4\sqrt{A_{ex}(K_0 + K_d^V cos^2\xi)}\right] = \frac{-4A_{ex}K_d^V sin\xi cos\xi}{\sqrt{A_{ex}(K_0 + K_d^V cos^2\xi)}} \tag{9.41}$$

Then,

$$\frac{d}{d\xi}\left[\pi D cos\xi\right] = -\pi D sin\xi \tag{9.42}$$

Finally we can write:

$$\frac{d\sigma_{DW}}{d\xi} = \frac{-4A_{ex}K_d^V sin\xi cos\xi}{\sqrt{A_{ex}(K_0 + K_d^V cos^2\xi)}} - \pi D sin\xi = 0 \tag{9.43}$$

$$\leftrightarrow \frac{4A_{ex}K_d^V sin\xi cos\xi}{\sqrt{A_{ex}(K_0 + K_d^V cos^2\xi)}} = -\pi D sin\xi \tag{9.44}$$

$$\leftrightarrow 4A_{ex}K_d^V cos\xi = -\pi D\sqrt{A_{ex}(K_0 + K_d^V cos^2\xi)} \tag{9.45}$$

$$\leftrightarrow 16A_{ex}^2 {K_d^V}^2 cos^2\xi = \pi^2 D^2 A_{ex}(K_0 + K_d^V cos^2\xi) \tag{9.46}$$

$$\leftrightarrow cos^2\xi = \frac{\pi^2 D^2 K_0}{16A_{ex}{K_d^V}^2 - \pi^2 D^2 K_d^V} \tag{9.47}$$

$$\leftrightarrow \xi(D) = \pm cos^{-1}\left[-\pi D\sqrt{\frac{K_0}{K_d^V(16A_{ex}K_d^V - \pi^2 D^2)}}\right] \tag{9.48}$$

Critical DMI value D_C^N :

The critical DMI value D_C^N corresponds to the value of DMI for which we consider to have pure Néel skyrmion. In that case the helicity $\xi = 0 + n\pi$. Therefore we can deduce D_C^N from the equation 9.48:

$$\xi(D_C^N) = 0 + n\pi \tag{9.49}$$

$$\leftrightarrow \pm cos^{-1}\left[-\pi D_C^N\sqrt{\frac{K_0}{K_d^V(16A_{ex}K_d^V - \pi^2 (D_C^N)^2)}}\right] \tag{9.50}$$

$$\leftrightarrow -\pi D_C^N\sqrt{\frac{K_0}{K_d^V(16A_{ex}K_d^V - \pi^2 (D_C^N)^2)}} = 1 \tag{9.51}$$

$$\leftrightarrow (D_C^N)^2\frac{K_0}{K_d^V(16A_{ex}K_d^V - \pi^2 (D_C^N)^2)} = \frac{1}{\pi^2} \tag{9.52}$$

$$\leftrightarrow (D_C^N)^2 K_0 = \frac{16A_{ex}(K_d^V)^2}{\pi^2} - K_d^V (D_C^N)^2 \tag{9.53}$$

$$\leftrightarrow (D_C^N)^2(K_0 + K_d^V) = \frac{16A_{ex}(K_d^V)^2}{\pi^2} \tag{9.54}$$

$$\leftrightarrow \left|D_C^N\right|\sqrt{K_0 + K_d^V} = \frac{4}{\pi}\sqrt{A_{ex}(K_d^V)^2} \tag{9.55}$$

$$\leftrightarrow \left|D_C^N\right| = \frac{4}{\pi}\sqrt{\frac{A_{ex}(K_d^V)^2}{K_0 + K_d^V}} \tag{9.56}$$

Finally,

$$\leftrightarrow \left|D_C^N\right| = \frac{4}{\pi}\sqrt{\frac{A_{ex}K_d^V}{K_0/K_d^V + 1}} \tag{9.57}$$

Bibliography

[1] M. N. Baibich, J. M. Broto, A. Fert, et al., "Giant Magnetoresistance of (001)Fe/(001)Cr Magnetic Superlattices," en, Phys. Rev. Lett., vol. 61, no. 21, pp. 2472–2475, Nov. 1988, Publisher: American Physical Society (APS), ISSN: 0031-9007. DOI: 10.1103/physrevlett.61.2472.

[2] G. Binasch, P. Grünberg, F. Saurenbach, et al., "Enhanced magnetoresistance in layered magnetic structures with antiferromagnetic interlayer exchange," en, Phys. Rev. B, vol. 39, no. 7, pp. 4828–4830, Mar. 1989, ISSN: 0163-1829. DOI: 10.1103/PhysRevB.39.4828.

[3] L. Wang, Z. Liu, A. Liu, et al., "Artificial intelligence in product lifecycle management," en, Int J Adv Manuf Technol, vol. 114, no. 3-4, pp. 771–796, May 2021, ISSN: 0268-3768, 1433-3015. DOI: 10.1007/s00170-021-06882-1.

[4] J. Grollier, D. Querlioz, K. Y. Camsari, et al., "Neuromorphic spintronics," en, Nat Electron, vol. 3, no. 7, pp. 360–370, Mar. 2020, ISSN: 2520-1131. DOI: 10.1038/s41928-019-0360-9.

[5] A. Fert, V. Cros, and J. Sampaio, "Skyrmions on the track," en, Nature Nanotech, vol. 8, no. 3, pp. 152–156, Mar. 2013, Publisher: Springer Science and Business Media LLC, ISSN: 1748-3387, 1748-3395. DOI: 10.1038/nnano.2013.29.

[6] X. Zhang, M. Ezawa, and Y. Zhou, "Magnetic skyrmion logic gates: Conversion, duplication and merging of skyrmions," en, Sci Rep, vol. 5, no. 1, p. 9400, Mar. 2015, ISSN: 2045-2322. DOI: 10.1038/srep09400.

[7] D. Pinna, F. Abreu Araujo, J.-V. Kim, et al., "Skyrmion Gas Manipulation for Probabilistic Computing," en, Phys. Rev. Applied, vol. 9, no. 6, Jun. 2018, Publisher: American Physical Society (APS), ISSN: 2331-7019. DOI: 10.1103/physrevapplied.9.064018.

[8] K. M. Song, J.-S. Jeong, B. Pan, et al., "Skyrmion-based artificial synapses for neuromorphic computing," Nature Electronics, vol. 3, no. 3, pp. 148–155, Mar. 2020, ISSN: 2520-1131. DOI: 10.1038/s41928-020-0385-0.

[9] U. Gradmann, "MAGNETIC SURFACE ANISOTROPIES," en,

[10] E. P. Wohlfarth and K. H. J. Buschow, Eds., Ferromagnetic materials: a handbook on the properties o
en. Amsterdam ; New York : New York: North-Holland Pub. Co. ; Sole distributors for the U.S.A. and Canada, Elsevier North-Holland, 1980, ISBN: 978-0-444-89853-1 978-0-444-85313-4 978-0-444-88952-2 978-0-444-51459-2 978-0-444-56371-2 978-0-444-63291-3.

[11] A. Hubert and R. Schäfer, Magnetic domains: the analysis of magnetic microstructures, en. Berlin ; New York: Springer, 1998, ISBN: 978-3-540-64108-7.

[12] S. Blundell, Magnetism in condensed matter (Oxford master series in condensed matter physics), en. Oxford ; New York: Oxford University Press, 2001, ISBN: 978-0-19-850592-1.

[13] J. M. D. Coey, Magnetism and Magnetic Materials. Cambridge University Press, 2010.

[14] A. Aharoni, Introduction to the Theory of Ferromagnetism (International Series of Monographs on Physics). Clarendon Press, 2000, ISBN: 978-0-19-850809-0.

[15] A. Aharoni, "Demagnetizing factors for rectangular ferromagnetic prisms," en, Journal of Applied Physics, vol. 83, no. 6, pp. 3432–3434, Mar. 1998, ISSN: 0021-8979, 1089-7550. DOI: 10.1063/1.367113.

[16] B. Dieny and M. Chshiev, "Perpendicular magnetic anisotropy at transition metal/oxide interfaces and applications," en, Rev. Mod. Phys., vol. 89, no. 2, Jun. 2017, Publisher: American Physical Society (APS), ISSN: 0034-6861, 1539-0756. DOI: 10.1103/revmodphys.89.025008.

[17] J. Kohlhepp, H. J. Elmers, S. Cordes, et al., "Power laws of magnetization in ferromagnetic monolayers and the two-dimensional Ising model," en, Phys. Rev. B, vol. 45, no. 21, pp. 12 287–12 291, Jun. 1992, ISSN: 0163-1829, 1095-3795. DOI: 10.1103/PhysRevB.45.12287.

[18] Y. Li and K. Baberschke, "Dimensional crossover in ultrathin Ni(111) films on W(110)," en, Phys. Rev. Lett., vol. 68, no. 8, pp. 1208–1211, Feb. 1992, ISSN: 0031-9007. DOI: 10.1103/PhysRevLett.68.1208.

[19] I. Dzyaloshinsky, "A thermodynamic theory of weak ferromagnetism of antiferromagnetics," en, Journal of Physics and Chemistry of Solids, vol. 4, no. 4, pp. 241–255, Jan. 1958, Publisher: Elsevier BV, ISSN: 0022-3697. DOI: 10.1016/0022-3697(58)90076-3.

[20] T. Moriya, "Anisotropic Superexchange Interaction and Weak Ferromagnetism," en, Phys. Rev., vol. 120, no. 1, pp. 91–98, Oct. 1960, Publisher: American Physical Society (APS), ISSN: 0031-899X. DOI: 10.1103/physrev.120.91.

[21] M. Fang, W. Zhang, X. Wu, et al., "Recent advances in tunable spinorbit coupling using ferroelectricity," en, APL Materials, vol. 9, no. 6, p. 060 704, Jun. 2021, ISSN: 2166-532X. DOI: 10.1063/5.0052553.

[22] K. V. Shanavas, Z. S. Popovi, and S. Satpathy, "Theoretical model for Rashba spinorbit interaction indelectrons," en, Phys. Rev. B, vol. 90, no. 16, Oct. 2014, Publisher: American Physical Society (APS), ISSN: 1098-0121, 1550-235X. DOI: 10.1103/physrevb.90.165108.

[23] A. Fert and P. M. Levy, "Role of Anisotropic Exchange Interactions in Determining the Properties of Spin-Glasses," en, Phys. Rev. Lett., vol. 44, no. 23, pp. 1538–1541, Jun. 1980, Publisher: American Physical Society (APS), ISSN: 0031-9007. DOI: 10.1103/physrevlett.44.1538.

[24] A. Bogdanov and A. Hubert, "Thermodynamically stable magnetic vortex states in magnetic crystals," en, Journal of Magnetism and Magnetic Materials, vol. 138, no. 3, pp. 255–269, Dec. 1994, Publisher: Elsevier BV, ISSN: 0304-8853. DOI: 10.1016/0304-8853(94)90046-9.

[25] A. Crépieux and C. Lacroix, "DzyaloshinskyMoriya interactions induced by symmetry breaking at a surface," en, Journal of Magnetism and Magnetic Materials, vol. 182, no. 3, pp. 341–349, Mar. 1998, ISSN: 03048853. DOI: 10.1016/S0304-8853(97)01044-5.

[26] A. Manchon, H. C. Koo, J. Nitta, et al., "New perspectives for Rashba spinorbit coupling," en, Nature Mater, vol. 14, no. 9, pp. 871–882, Sep. 2015, Publisher: Springer Science and Business Media LLC, ISSN: 1476-1122, 1476-4660. DOI: 10.1038/nmat4360.

[27] C.-E. Fillion, "Electric control of skyrmions for spintronic applications," en,

[28] Y.-K. Park, D.-Y. Kim, J.-S. Kim, et al., "Experimental observation of the correlation between the interfacial DzyaloshinskiiMoriya interaction and work function in metallic magnetic trilayers," en, NPG Asia Mater, vol. 10, no. 10, pp. 995–1001, Oct. 2018, Publisher: Springer Science and Business Media LLC, ISSN: 1884-4049, 1884-4057. DOI: 10.1038/s41427-018-0090-x.

[29] F. Ajejas, Y. Sassi, W. Legrand, et al., "Interfacial potential gradient modulates Dzyaloshinskii-Moriya interaction in Pt/Co/metal multilayers," en, Phys. Rev. Materials, vol. 6, no. 7, Jul. 2022, Publisher: American Physical Society (APS), ISSN: 2475-9953. DOI: 10.1103/physrevmaterials.6.l071401.

[30] A. Thiaville, S. Rohart, É. Jué, et al., "Dynamics of Dzyaloshinskii domain walls in ultrathin magnetic films," en, EPL, vol. 100, no. 5, p. 57 002, Dec. 2012, Publisher: IOP Publishing, ISSN: 0295-5075, 1286-4854. DOI: 10.1209/0295-5075/100/57002.

[31] A. Fert, N. Reyren, and V. Cros, "Magnetic skyrmions: Advances in physics and potential applications," en, Nat Rev Mater, vol. 2, no. 7, Jun. 2017, Publisher: Springer Science and Business Media LLC, ISSN: 2058-8437. DOI: 10.1038/natrevmats.2017.31.

[32] T. Skyrme, "A unified field theory of mesons and baryons," en, Nuclear Physics, vol. 31, pp. 556–569, Mar. 1962, Publisher: Elsevier BV, ISSN: 0029-5582. DOI: 10.1016/0029-5582(62)90775-7.

[33] A. N. Bogdanov and D. A. Yablonskii, "Thermodynamicallystable "vortices" in magnetically ordered crystals.The mixed state of magnets," en,

[34] S. Mühlbauer, B. Binz, F. Jonietz, et al., "Skyrmion Lattice in a Chiral Magnet," en, Science, vol. 323, no. 5916, pp. 915–919, Feb. 2009, Publisher: American Association for the Advancement of Science (AAAS), ISSN: 0036-8075, 1095-9203. DOI: 10.1126/science.1166767.

[35] X. Z. Yu, Y. Onose, N. Kanazawa, et al., "Real-space observation of a two-dimensional skyrmion crystal," en, Nature, vol. 465, no. 7300, pp. 901–904, Jun. 2010, Publisher: Springer Science and Business Media LLC, ISSN: 0028-0836, 1476-4687. DOI: 10.1038/nature09124.

[36] C. Moreau-Luchaire, C. Moutafis, N. Reyren, et al., "Additive interfacial chiral interaction in multilayers for stabilization of small individual skyrmions at room temperature," en, Nature Nanotech, vol. 11, no. 5, pp. 444–448, May 2016, Publisher: Springer Science and Business Media LLC, ISSN: 1748-3387, 1748-3395. DOI: 10.1038/nnano.2015.313.

[37] O. Boulle, J. Vogel, H. Yang, et al., "Room-temperature chiral magnetic skyrmions in ultrathin magnetic nanostructures," en, Nature Nanotech, vol. 11, no. 5, pp. 449–454, May 2016, Publisher: Springer Science and Business Media LLC, ISSN: 1748-3387, 1748-3395. DOI: 10.1038/nnano.2015.315.

[38] M. Schott, A. Bernand-Mantel, L. Ranno, et al., "The Skyrmion Switch: Turning Magnetic Skyrmion Bubbles on and off with an Electric Field," en, Nano Lett., vol. 17, no. 5, pp. 3006–3012, May 2017, Publisher: American Chemical Society (ACS), ISSN: 1530-6984, 1530-6992. DOI: 10.1021/acs.nanolett.7b00328.

[39] S. Woo, K. Litzius, B. Krüger, et al., "Observation of room-temperature magnetic skyrmions and their current-driven dynamics in ultrathin metallic ferromagnets," en, Nature Mater, vol. 15, no. 5, pp. 501–506, May 2016, Publisher: Springer Science and Business Media LLC, ISSN: 1476-1122, 1476-4660. DOI: 10.1038/nmat4593.

[40] X. Zhang, Y. Zhou, K. Mee Song, et al., "Skyrmion-electronics: Writing, deleting, reading and processing magnetic skyrmions toward spintronic applications," en, J. Phys.: Condens. Matter, vol. 32, no. 14, p. 143 001, Apr. 2020, Publisher: IOP Publishing, ISSN: 0953-8984, 1361-648X. DOI: 10.1088/1361-648x/ab5488.

[41] S. Heinze, K. von Bergmann, M. Menzel, et al., "Spontaneous atomic-scale magnetic skyrmion lattice in two dimensions," en, Nature Phys, vol. 7, no. 9, pp. 713–718, Sep. 2011, Publisher: Springer Science and Business Media LLC, ISSN: 1745-2473, 1745-2481. DOI: 10.1038/nphys2045.

[42] S. L. Zhang, G. van der Laan, and T. Hesjedal, "Direct experimental determination of the topological winding number of skyrmions in Cu2OSeO3," en, Nat Commun, vol. 8, no. 1, Feb. 2017, Publisher: Springer Science and Business Media LLC, ISSN: 2041-1723. DOI: 10.1038/ncomms14619.

[43] A. Bernand-Mantel, L. Camosi, A. Wartelle, et al., "The skyrmion-bubble transition in a ferromagnetic thin film," en, SciPost Phys., vol. 4, no. 5, May 2018, Publisher: Stichting SciPost, ISSN: 2542-4653. DOI: 10.21468/scipostphys.4.5.027.

[44] A. Bogdanov and A. Hubert, "The stability of vortex-like structures in uniaxial ferromagnets," en, Journal of Magnetism and Magnetic Materials, vol. 195, no. 1, pp. 182–192, Apr. 1999, Publisher: Elsevier BV, ISSN: 0304-8853. DOI: 10.1016/s0304-8853(98)01038-5.

[45] A. Manchon, C. Ducruet, L. Lombard, et al., "Analysis of oxygen induced anisotropy crossover in Pt/Co/MOx trilayers," en, Journal of Applied Physics, vol. 104, no. 4, Aug. 2008, Publisher: AIP Publishing, ISSN: 0021-8979, 1089-7550. DOI: 10.1063/1.2969711.

[46] G. H. O. Daalderop, P. J. Kelly, and M. F. H. Schuurmans, "Magnetic anisotropy of a free-standing Co monolayer and of multilayers which contain Co monolayers," en, Phys. Rev. B, vol. 50, no. 14, pp. 9989–10 003, Oct. 1994, Publisher: American Physical Society (APS), ISSN: 0163-1829, 1095-3795. DOI: 10.1103/physrevb.50.9989.

[47] S. Monso, B. Rodmacq, S. Auffret, et al., "Crossover from in-plane to perpendicular anisotropy in Pt/CoFe/AlOx sandwiches as a function of Al oxidation: A very accurate control of the oxidation of tunnel barriers," en, Applied Physics Letters, vol. 80, no. 22, pp. 4157–4159, Jun. 2002, Publisher: AIP Publishing, ISSN: 0003-6951, 1077-3118. DOI: 10.1063/1.1483122.

[48] A. Manchon, S. Pizzini, J. Vogel, et al., X-Ray Analysis of Oxygen-induced Perpendicular Magnetic A arXiv:0709.2581 [cond-mat], Dec. 2007. DOI: 10.1016/j.jmmm.2008.02.131.

[49] D. d. S. Chaves, F. Ajejas, V. Kiáková, et al., "Oxidation dependence of the Dzyaloshinskii-Moriya interaction in Pt/Co/MOx trilayers (M=Al or Gd)," en, Phys. Rev. B, vol. 99, no. 14, Apr. 2019, Publisher: American Physical Society (APS), ISSN: 2469-9950, 2469-9969. DOI: 10.1103/physrevb.99.144404.

[50] M. Arora, J. M. Shaw, and H. T. Nembach, "Variation of sign and magnitude of the Dzyaloshinskii-Moriya interaction of a ferromagnet with an oxide interface," en, Phys. Rev. B, vol. 101, no. 5, Feb. 2020, Publisher: American Physical Society (APS), ISSN: 2469-9950, 2469-9969. DOI: 10.1103/physrevb.101.054421.

[51] R. Kumar, C. Fillion, B. Lovery, et al., "Control of Skyrmion Chirality in Ta/FeCoB/-TaOx Trilayers by TaOx Oxidation and FeCoB Thickness," en, Phys. Rev. Applied, vol. 19, no. 2, Feb. 2023, Publisher: American Physical Society (APS), ISSN: 2331-7019. DOI: 10.1103/physrevapplied.19.024064.

[52] C.-E. Fillion, J. Fischer, R. Kumar, et al., "Gate-controlled skyrmion and domain wall chirality," en, Nat Commun, vol. 13, no. 1, Sep. 2022, Publisher: Springer Science and Business Media LLC, ISSN: 2041-1723. DOI: 10.1038/s41467-022-32959-w.

[53] L. Néel, "Anisotropie magnétique superficielle et surstructures d'orientation," fr, J. Phys. Radium, vol. 15, no. 4, pp. 225–239, 1954, Publisher: EDP Sciences, ISSN: 0368-3842. DOI: 10.1051/jphysrad:01954001504022500.

[54] H. Draaisma, W. de Jonge, and F. den Broeder, "Magnetic interface anisotropy in Pd/Co and Pd/Fe multilayers," en, Journal of Magnetism and Magnetic Materials, vol. 66, no. 3, pp. 351–355, Apr. 1987, Publisher: Elsevier BV, ISSN: 0304-8853. DOI: 10.1016/0304-8853(87)90169-7.

[55] W. B. Zeper, F. J. A. M. Greidanus, P. F. Carcia, et al., "Perpendicular magnetic anisotropy and magneto-optical Kerr effect of vapor-deposited Co/Pt-layered structures," en, Journal of Applied Physics, vol. 65, no. 12, pp. 4971–4975, Jun. 1989, Publisher: AIP Publishing, ISSN: 0021-8979, 1089-7550. DOI: 10.1063/1.343189.

[56] J. Cho, N.-H. Kim, S. Lee, et al., "Thickness dependence of the interfacial DzyaloshinskiiMoriya interaction in inversion symmetry broken systems," en, Nat Commun, vol. 6, no. 1, Jul. 2015, Publisher: Springer Science and Business Media LLC, ISSN: 2041-1723. DOI: 10.1038/ncomms8635.

[57] R. Lo Conte, G. V. Karnad, E. Martinez, et al., "Ferromagnetic layer thickness dependence of the Dzyaloshinskii-Moriya interaction and spin-orbit torques in Pt\Co\AlO$x$," en, AIP Advances, vol. 7, no. 6, Jun. 2017, Publisher: AIP Publishing, ISSN: 2158-3226. DOI: 10.1063/1.4990694.

[58] I. Benguettat-El Mokhtari, D. Ourdani, Y. Roussigné, et al., "Investigation of the correlation between perpendicular magnetic anisotropy, spin mixing conductance and interfacial DzyaloshinskiiMoriya interaction in CoFeB-based systems," en, J. Phys. D: Appl. Phys., vol. 53, no. 50, p. 505 003, Dec. 2020, Publisher: IOP Publishing, ISSN: 0022-3727, 1361-6463. DOI: 10.1088/1361-6463/abb488.

[59] S. Emori, U. Bauer, S.-M. Ahn, et al., "Current-driven dynamics of chiral ferromagnetic domain walls," en, Nature Mater, vol. 12, no. 7, pp. 611–616, Jul. 2013, Publisher: Springer Science and Business Media LLC, ISSN: 1476-1122, 1476-4660. DOI: 10.1038/nmat3675.

[60] M. Weisheit, S. Fähler, A. Marty, et al., "Electric Field-Induced Modification of Magnetism in Thin-Film Ferromagnets," en, Science, vol. 315, no. 5810, pp. 349–351, Jan. 2007, Publisher: American Association for the Advancement of Science (AAAS), ISSN: 0036-8075, 1095-9203. DOI: 10.1126/science.1136629.

[61] J. Zhang, P. V. Lukashev, S. S. Jaswal, et al., "Model of orbital populations for voltage-controlled magnetic anisotropy in transition-metal thin films," en, Phys. Rev. B, vol. 96, no. 1, Jul. 2017, Publisher: American Physical Society (APS), ISSN: 2469-9950, 2469-9969. DOI: 10.1103/physrevb.96.014435.

[62] F. Bonell, Y. T. Takahashi, D. D. Lam, et al., "Reversible change in the oxidation state and magnetic circular dichroism of Fe driven by an electric field at the FeCo/MgO interface," en, Applied Physics Letters, vol. 102, no. 15, Apr. 2013, Publisher: AIP Publishing, ISSN: 0003-6951, 1077-3118. DOI: 10.1063/1.4802030.

[63] T. Kawabe, K. Yoshikawa, M. Tsujikawa, et al., "Electric-field-induced changes of magnetic moments and magnetocrystalline anisotropy in ultrathin cobalt films," en, Phys. Rev. B, vol. 96, no. 22, Dec. 2017, Publisher: American Physical Society (APS), ISSN: 2469-9950, 2469-9969. DOI: 10.1103/physrevb.96.220412.

[64] A. J. Tan, M. Huang, C. O. Avci, et al., "Magneto-ionic control of magnetism using a solid-state proton pump," en, Nature Mater, vol. 18, no. 1, pp. 35–41, Jan. 2019, Publisher: Springer Science and Business Media LLC, ISSN: 1476-1122, 1476-4660. DOI: 10.1038/s41563-018-0211-5.

[65] Q. Zhang, X. Luo, L. Wang, et al., "Lithium-Ion Battery Cycling for Magnetism Control," en, Nano Lett., vol. 16, no. 1, pp. 583–587, Jan. 2016, Publisher: American Chemical Society (ACS), ISSN: 1530-6984, 1530-6992. DOI: 10.1021/acs.nanolett.5b04276.

[66] F. Ibrahim, A. Hallal, B. Dieny, et al., "Establishing characteristic behavior of voltage control of magnetic anisotropy by ionic migration," en, Phys. Rev. B, vol. 98, no. 21, Dec. 2018, Publisher: American Physical Society (APS), ISSN: 2469-9950, 2469-9969. DOI: 10.1103/physrevb.98.214441.

[67] T. da Câmara Santa Clara Gomes, T. Bhatnagar-Schöffmann, S. Krishnia, et al., "Control of the magnetic anisotropy in multirepeat Pt/Co/Al heterostructures using magnetoionic gating," en, Phys. Rev. Applied, vol. 21, no. 2, Feb. 2024, Publisher: American Physical Society (APS), ISSN: 2331-7019. DOI: 10.1103/physrevapplied.21.024010.

[68] A. Fassatoui, J. P. Garcia, L. Ranno, et al., "Reversible and Irreversible Voltage Manipulation of Interfacial Magnetic Anisotropy in Pt/Co/Oxide Multilayers," en, Phys. Rev. Applied, vol. 14, no. 6, Dec. 2020, Publisher: American Physical Society (APS), ISSN: 2331-7019. DOI: 10.1103/physrevapplied.14.064041.

[69] M. Weiler, A. Brandlmaier, S. Geprägs, et al., "Voltage controlled inversion of magnetic anisotropy in a ferromagnetic thin film at room temperature," en, New J. Phys., vol. 11, no. 1, p. 013 021, Jan. 2009, Publisher: IOP Publishing, ISSN: 1367-2630. DOI: 10.1088/1367-2630/11/1/013021.

[70] T. Maruyama, Y. Shiota, T. Nozaki, et al., "Large voltage-induced magnetic anisotropy change in a few atomic layers of iron," en, Nature Nanotech, vol. 4, no. 3, pp. 158–161, Mar. 2009, Publisher: Springer Science and Business Media LLC, ISSN: 1748-3387, 1748-3395. DOI: 10.1038/nnano.2008.406.

[71] U. Bauer, L. Yao, A. J. Tan, et al., "Magneto-ionic control of interfacial magnetism," en, Nature Mater, vol. 14, no. 2, pp. 174–181, Feb. 2015, Publisher: Springer Science and Business Media LLC, ISSN: 1476-1122, 1476-4660. DOI: 10.1038/nmat4134.

[72] T. Nozaki, T. Yamamoto, S. Miwa, et al., "Recent Progress in the Voltage-Controlled Magnetic Anisotropy Effect and the Challenges Faced in Developing Voltage-Torque MRAM," en, Micromachines, vol. 10, no. 5, p. 327, May 2019, Publisher: MDPI AG, ISSN: 2072-666X. DOI: 10.3390/mi10050327.

[73] W.-G. Wang, M. Li, S. Hageman, et al., "Electric-field-assisted switching in magnetic tunnelăjunctions," en, Nature Mater, vol. 11, no. 1, pp. 64–68, Jan. 2012, Publisher: Springer Science and Business Media LLC, ISSN: 1476-1122, 1476-4660. DOI: 10.1038/nmat3171.

[74] Y. Shiota, T. Nozaki, F. Bonell, et al., "Induction of coherent magnetization switching in a few atomic layers of FeCo using voltage pulses," en, Nature Mater, vol. 11, no. 1, pp. 39–43, Jan. 2012, Publisher: Springer Science and Business Media LLC, ISSN: 1476-1122, 1476-4660. DOI: 10.1038/nmat3172.

[75] J. A. Urrestarazu, "Strategies for the nucleation, electric control and detection of magnetic skyrmions for memory and computing applications," en,

[76] M. Williamson, M. de Rozieres, H. Almasi, et al., "Probing VCMA in MTJs with in-plane magnetization," en, AIP Advances, vol. 7, no. 11, Nov. 2017, Publisher: AIP Publishing, ISSN: 2158-3226. DOI: 10.1063/1.5008379.

[77] G. Yu, Z. Wang, M. Abolfath-Beygi, et al., "Strain-induced modulation of perpendicular magnetic anisotropy in Ta/CoFeB/MgO structures investigated by ferromagnetic resonance," en, Applied Physics Letters, vol. 106, no. 7, Feb. 2015, Publisher: AIP Publishing, ISSN: 0003-6951, 1077-3118. DOI: 10.1063/1.4907677.

[78] N. Funabashi, R. Higashida, K.-i. Aoshima, et al., "Magneto-optical light modulation using the VCMA effect in MgO/CoFe/Gd/GdFe layers," en, AIP Advances, vol. 9, no. 3, Mar. 2019, Publisher: AIP Publishing, ISSN: 2158-3226. DOI: 10.1063/1.5080147.

[79] M. Fettizio and C. O. Avci, "Harmonic Hall characterization of voltage-controlled magnetic anisotropy at ferromagnet/oxide interfaces," en, Phys. Rev. B, vol. 111, no. 5, Feb. 2025, Publisher: American Physical Society (APS), ISSN: 2469-9950, 2469-9969. DOI: 10.1103/physrevb.111.054438.

[80] L. Herrera Diez, Y. Liu, D. Gilbert, et al., "Nonvolatile Ionic Modification of the Dzyaloshinskii-Moriya Interaction," en, Phys. Rev. Applied, vol. 12, no. 3, Sep. 2019, Publisher: American Physical Society (APS), ISSN: 2331-7019. DOI: 10.1103/physrevapplied.12.034005.

[81] K. Nawaoka, S. Miwa, Y. Shiota, et al., "Voltage induction of interfacial Dzyaloshinskii-iMoriya interaction in Au/Fe/MgO artificial multilayer," en, Appl. Phys. Express, vol. 8, no. 6, p. 063 004, Jun. 2015, Publisher: IOP Publishing, ISSN: 1882-0778, 1882-0786. DOI: 10.7567/apex.8.063004.

[82] T. Srivastava, M. Schott, R. Juge, et al., "Large-Voltage Tuning of DzyaloshinskiiMoriya Interactions: A Route toward Dynamic Control of Skyrmion Chirality," en, Nano Lett., vol. 18, no. 8, pp. 4871–4877, Aug. 2018, Publisher: American Chemical Society (ACS), ISSN: 1530-6984, 1530-6992. DOI: 10.1021/acs.nanolett.8b01502.

[83] M. Schott, L. Ranno, H. Béa, et al., "Electric field control of interfacial Dzyaloshinskii-Moriya interaction in Pt/Co/AlOx thin films," en, Journal of Magnetism and Magnetic Materials, vol. 520, p. 167 122, Feb. 2021, Publisher: Elsevier BV, ISSN: 0304-8853. DOI: 10.1016/j.jmmm.2020.167122.

[84] L. Landau and E. Lifshits, "ON THE THEORY OF THE DISPERSION OF MAGNETIC PERMEABILITY IN FERROMAGNETIC BODIES," en, vol. 53,

[85] T. Gilbert, "Classics in Magnetics A Phenomenological Theory of Damping in Ferromagnetic Materials," en, IEEE Trans. Magn., vol. 40, no. 6, pp. 3443–3449, Nov. 2004, ISSN: 0018-9464. DOI: 10.1109/TMAG.2004.836740.

[86] S. Azzawi, A. T. Hindmarch, and D. Atkinson, "Magnetic damping phenomena in ferromagnetic thin-films and multilayers," en, J. Phys. D: Appl. Phys., vol. 50, no. 47, p. 473 001, Nov. 2017, ISSN: 0022-3727, 1361-6463. DOI: 10.1088/1361-6463/aa8dad.

[87] J. Ding, X. Yang, and T. Zhu, "The Motion of Magnetic Skyrmions Driven by Propagating Spin Waves," en, IEEE Trans. Magn., vol. 51, no. 11, pp. 1–4, Nov. 2015, ISSN: 0018-9464, 1941-0069. DOI: 10.1109/TMAG.2015.2446516.

[88] L. Huang, G. Burnell, and C. H. Marrows, "Transient retrograde motion of spin wave driven skyrmions in magnetic nanotracks," en, Phys. Rev. B, vol. 107, no. 22, p. 224 418, Jun. 2023, ISSN: 2469-9950, 2469-9969. DOI: 10.1103/PhysRevB.107.224418.

[89] C. Liu, J. Wang, W. He, et al., "Strain-Induced Reversible Motion of Skyrmions at Room Temperature," en, ACS Nano, vol. 18, no. 1, pp. 761–769, Jan. 2024, ISSN: 1936-0851, 1936-086X. DOI: 10.1021/acsnano.3c09090.

[90] T. Yokouchi, S. Sugimoto, B. Rana, et al., "Creation of magnetic skyrmions by surface acoustic waves," en, Nat. Nanotechnol., vol. 15, no. 5, pp. 361–366, May 2020, ISSN: 1748-3387, 1748-3395. DOI: 10.1038/s41565-020-0661-1.

[91] R. Nepal, U. Güngördü, and A. A. Kovalev, "Magnetic skyrmion bubble motion driven by surface acoustic waves," en, Applied Physics Letters, vol. 112, no. 11, p. 112 404, Mar. 2018, ISSN: 0003-6951, 1077-3118. DOI: 10.1063/1.5013620.

[92] Z. Chen, X. Zhang, Y. Zhou, et al., "Skyrmion Dynamics in the Presence of Deformation," en, Phys. Rev. Applied, vol. 17, no. 1, Jan. 2022, Publisher: American Physical Society (APS), ISSN: 2331-7019. DOI: 10.1103/physrevapplied.17.l011002.

[93] Z. Wang, M. Guo, H.-A. Zhou, et al., "Thermal generation, manipulation and thermoelectric detection of skyrmions," Nature Electronics, vol. 3, no. 11, pp. 672–679, Nov. 2020, ISSN: 2520-1131. DOI: 10.1038/s41928-020-00489-2.

[94] E. Raimondo, E. Saugar, J. Barker, et al., "Temperature-Gradient-Driven Magnetic Skyrmion Motion," en, Phys. Rev. Applied, vol. 18, no. 2, p. 024 062, Aug. 2022, ISSN: 2331-7019. DOI: 10.1103/PhysRevApplied.18.024062.

[95] S. Lepadatu, "All-Optical Magnetothermoelastic Skyrmion Motion," en, Phys. Rev. Applied, vol. 19, no. 4, p. 044 036, Apr. 2023, ISSN: 2331-7019. DOI: 10.1103/PhysRevApplied.19.044036.

[96] S. Lemerle, J. Ferré, C. Chappert, et al., "Domain Wall Creep in an Ising Ultrathin Magnetic Film," en, Phys. Rev. Lett., vol. 80, no. 4, pp. 849–852, Jan. 1998, ISSN: 0031-9007, 1079-7114. DOI: 10.1103/PhysRevLett.80.849.

[97] N. L. Schryer and L. R. Walker, "The motion of 180ř domain walls in uniform dc magnetic fields," en, Journal of Applied Physics, vol. 45, no. 12, pp. 5406–5421, Dec. 1974, ISSN: 0021-8979, 1089-7550. DOI: 10.1063/1.1663252.

[98] A. Mougin, M. Cormier, J. P. Adam, et al., "Domain wall mobility, stability and Walker breakdown in magnetic nanowires," en, Europhys. Lett., vol. 78, no. 5, p. 57 007, Jun. 2007, ISSN: 0295-5075, 1286-4854. DOI: 10.1209/0295-5075/78/57007.

[99] P. J. Metaxas, J. P. Jamet, A. Mougin, et al., "Creep and Flow Regimes of Magnetic Domain-Wall Motion in Ultrathin Pt / Co / Pt Films with Perpendicular Anisotropy," en, Phys. Rev. Lett., vol. 99, no. 21, p. 217 208, Nov. 2007, ISSN: 0031-9007, 1079-7114. DOI: 10.1103/PhysRevLett.99.217208.

[100] T. Ha Pham, J. Vogel, J. Sampaio, et al., "Very large domain wall velocities in Pt/-Co/GdOx and Pt/Co/Gd trilayers with Dzyaloshinskii-Moriya interaction," en, EPL, vol. 113, no. 6, p. 67 001, Mar. 2016, ISSN: 0295-5075, 1286-4854. DOI: 10.1209/0295-5075/113/67001.

[101] J. Slonczewski, "Current-driven excitation of magnetic multilayers," en, Journal of Magnetism and Magnetic Materials, vol. 159, no. 1-2, pp. L1–L7, Jun. 1996, ISSN: 03048853. DOI: 10.1016/0304-8853(96)00062-5.

[102] L. Berger, "Emission of spin waves by a magnetic multilayer traversed by a current," en, Phys. Rev. B, vol. 54, no. 13, pp. 9353–9358, Oct. 1996, ISSN: 0163-1829, 1095-3795. DOI: 10.1103/PhysRevB.54.9353.

[103] S. Zhang and Z. Li, "Roles of Nonequilibrium Conduction Electrons on the Magnetization Dynamics of Ferromagnets," en, PHYSICAL REVIEW LETTERS, vol. 93, no. 12, 2004.

[104] J. Zhang, P. Levy, S. Zhang, et al., "Identification of Transverse Spin Currents in Noncollinear Magnetic Structures," en, Phys. Rev. Lett., vol. 93, no. 25, p. 256 602, Dec. 2004, ISSN: 0031-9007, 1079-7114. DOI: 10.1103/PhysRevLett.93.256602.

[105] A. Thiaville, Y. Nakatani, J. Miltat, et al., "Micromagnetic understanding of current-driven domain wall motion in patterned nanowires," en, Europhys. Lett., vol. 69, no. 6, pp. 990–996, Mar. 2005, ISSN: 0295-5075, 1286-4854. DOI: 10.1209/epl/i2004-10452-6.

[106] I. M. Miron, T. Moore, H. Szambolics, et al., "Fast current-induced domain-wall motion controlled by the Rashba effect," en, Nature Mater, vol. 10, no. 6, pp. 419–423, Jun. 2011, ISSN: 1476-1122, 1476-4660. DOI: 10.1038/nmat3020.

[107] P. Gambardella and I. M. Miron, "Current-induced spinorbit torques," en, Phil. Trans. R. Soc. A., vol. 369, no. 1948, pp. 3175–3197, Aug. 2011, Publisher: The Royal Society, ISSN: 1364-503X, 1471-2962. DOI: 10.1098/rsta.2010.0336.

[108] M. Dyakonov and V. Perel, "Current-induced spin orientation of electrons in semiconductors," en, Physics Letters A, vol. 35, no. 6, pp. 459–460, Jul. 1971, ISSN: 03759601. DOI: 10.1016/0375-9601(71)90196-4.

[109] A. V. Khvalkovskiy, V. Cros, D. Apalkov, et al., "Matching domain-wall configuration and spin-orbit torques for efficient domain-wall motion," en, Phys. Rev. B, vol. 87, no. 2, p. 020 402, Jan. 2013, ISSN: 1098-0121, 1550-235X. DOI: 10.1103/PhysRevB.87.020402.

[110] H. L. Wang, C. H. Du, Y. Pu, et al., "Scaling of Spin Hall Angle in 3d, 4d, and 5d Metals from Y 3 Fe 5 O 12 /Metal Spin Pumping," en, Phys. Rev. Lett., vol. 112, no. 19, p. 197 201, May 2014, ISSN: 0031-9007, 1079-7114. DOI: 10.1103/PhysRevLett.112.197201.

[111] L. Liu, O. J. Lee, T. J. Gudmundsen, et al., "Current-Induced Switching of Perpendicularly Magnetized Magnetic Layers Using Spin Torque from the Spin Hall Effect," en, Phys. Rev. Lett., vol. 109, no. 9, p. 096 602, Aug. 2012, ISSN: 0031-9007, 1079-7114. DOI: 10.1103/PhysRevLett.109.096602.

[112] K. Garello, I. M. Miron, C. O. Avci, et al., "Symmetry and magnitude of spinorbit torques in ferromagnetic heterostructures," en, Nature Nanotech, vol. 8, no. 8, pp. 587–593, Aug. 2013, ISSN: 1748-3387, 1748-3395. DOI: 10.1038/nnano.2013.145.

[113] C.-F. Pai, L. Liu, Y. Li, et al., "Spin transfer torque devices utilizing the giant spin Hall effect of tungsten," en, Appl. Phys. Lett., vol. 101, no. 12, p. 122 404, Sep. 2012, ISSN: 0003-6951, 1077-3118. DOI: 10.1063/1.4753947.

[114] L. Liu, C.-F. Pai, Y. Li, et al., "Spin-Torque Switching with the Giant Spin Hall Effect of Tantalum," en, Science, vol. 336, no. 6081, pp. 555–558, May 2012, ISSN: 0036-8075, 1095-9203. DOI: 10.1126/science.1218197.

[115] V. Edelstein, "Spin polarization of conduction electrons induced by electric current in two-dimensional asymmetric electron systems," en, Solid State Communications, vol. 73, no. 3, pp. 233–235, Jan. 1990, ISSN: 00381098. DOI: 10.1016/0038-1098(90)90963-C.

[116] J. C. R. Sánchez, L. Vila, G. Desfonds, et al., "Spin-to-charge conversion using Rashba coupling at the interface between non-magnetic materials," en, Nat Commun, vol. 4, no. 1, p. 2944, Dec. 2013, ISSN: 2041-1723. DOI: 10.1038/ncomms3944.

[117] A. Manchon, J. elezný, I. M. Miron, et al., "Current-induced spin-orbit torques in ferromagnetic and antiferromagnetic systems," en, Rev. Mod. Phys., vol. 91, no. 3, p. 035 004, Sep. 2019, ISSN: 0034-6861, 1539-0756. DOI: 10.1103/RevModPhys.91.035004.

[118] A. V. Khvalkovskiy, K. A. Zvezdin, Y. V. Gorbunov, et al., "High Domain Wall Velocities due to Spin Currents Perpendicular to the Plane," en, Phys. Rev. Lett., vol. 102, no. 6, p. 067 206, Feb. 2009, ISSN: 0031-9007, 1079-7114. DOI: 10.1103/PhysRevLett.102.067206.

[119] A. Manchon and S. Zhang, "Theory of spin torque due to spin-orbit coupling," en, Phys. Rev. B, vol. 79, no. 9, p. 094 422, Mar. 2009, ISSN: 1098-0121, 1550-235X. DOI: 10.1103/PhysRevB.79.094422.

[120] S. Krishnia, Y. Sassi, F. Ajejas, et al., "Large Interfacial Rashba Interaction Generating Strong SpinOrbit Torques in Atomically Thin Metallic Heterostructures," en, Nano Lett., vol. 23, no. 15, pp. 6785–6791, Aug. 2023, ISSN: 1530-6984, 1530-6992. DOI: 10.1021/acs.nanolett.2c05091.

[121] J. Liu, C. Song, L. Zhao, et al., "Manipulation of Skyrmion by Magnetic Field Gradients: A SternGerlach-Like Experiment," en, Nano Lett., vol. 23, no. 11, pp. 4931–4937, Jun. 2023, ISSN: 1530-6984, 1530-6992. DOI: 10.1021/acs.nanolett.3c00731.

[122] S. L. Zhang, W. W. Wang, D. M. Burn, et al., "Manipulation of skyrmion motion by magnetic field gradients," en, Nat Commun, vol. 9, no. 1, p. 2115, May 2018, ISSN: 2041-1723. DOI: 10.1038/s41467-018-04563-4.

[123] K.-W. Moon, D.-H. Kim, S.-G. Je, et al., "Skyrmion motion driven by oscillating magnetic field," en, Sci Rep, vol. 6, no. 1, p. 20 360, Feb. 2016, ISSN: 2045-2322. DOI: 10.1038/srep20360.

[124] A. A. Thiele, "Steady-State Motion of Magnetic Domains," en, Phys. Rev. Lett., vol. 30, no. 6, pp. 230–233, Feb. 1973, Publisher: American Physical Society (APS), ISSN: 0031-9007. DOI: 10.1103/physrevlett.30.230.

[125] R. Juge, S.-G. Je, D. d. S. Chaves, et al., "Current-Driven Skyrmion Dynamics and Drive-Dependent Skyrmion Hall Effect in an Ultrathin Film," en, Phys. Rev. Applied, vol. 12, no. 4, Oct. 2019, Publisher: American Physical Society (APS), ISSN: 2331-7019. DOI: 10.1103/physrevapplied.12.044007.

[126] W. Jiang, X. Zhang, G. Yu, et al., "Direct observation of the skyrmion Hall effect," en, Nature Phys, vol. 13, no. 2, pp. 162–169, Feb. 2017, ISSN: 1745-2473, 1745-2481. DOI: 10.1038/nphys3883.

[127] K. Litzius, I. Lemesh, B. Krüger, et al., "Skyrmion Hall effect revealed by direct time-resolved X-ray microscopy," en, Nature Phys, vol. 13, no. 2, pp. 170–175, Feb. 2017, ISSN: 1745-2473, 1745-2481. DOI: 10.1038/nphys4000.

[128] F. Jonietz, S. Mühlbauer, C. Pfleiderer, et al., "Spin Transfer Torques in MnSi at Ultralow Current Densities," en, Science, vol. 330, no. 6011, pp. 1648–1651, Dec. 2010, ISSN: 0036-8075, 1095-9203. DOI: 10.1126/science.1195709.

[129] J. Iwasaki, M. Mochizuki, and N. Nagaosa, "Current-induced skyrmion dynamics in constricted geometries," en, Nature Nanotech, vol. 8, no. 10, pp. 742–747, Oct. 2013, ISSN: 1748-3387, 1748-3395. DOI: 10.1038/nnano.2013.176.

[130] X. Yu, N. Kanazawa, W. Zhang, et al., "Skyrmion flow near room temperature in an ultralow current density," en, Nat Commun, vol. 3, no. 1, p. 988, Aug. 2012, ISSN: 2041-1723. DOI: 10.1038/ncomms1990.

[131] T. Srivastava, W. Lim, I. Joumard, et al., "Mapping different skyrmion phases in double wedges of Ta/FeCoB/TaOx trilayers," en, Phys. Rev. B, vol. 100, no. 22, Dec. 2019, Publisher: American Physical Society (APS), ISSN: 2469-9950, 2469-9969. DOI: 10.1103/physrevb.100.220401.

[132] T. Srivastava, "Engineering and dynamical control of interfacial properties in ultra-thin films to tune magnetic spin textures," en,

[133] A. Singh, S. Gupta, M. Kuteifan, et al., "Effect of interlayer exchange coupling parameter on switching time and critical current density in composite free layer," en, Journal of Applied Physics, vol. 115, no. 17, p. 17D111, May 2014, ISSN: 0021-8979, 1089-7550. DOI: 10.1063/1.4861215.

[134] F. Ibrahim, A. Hallal, A. Kalitsov, et al., "Unveiling Temperature-Dependence Mechanisms of Perpendicular Magnetic Anisotropy at Fe / Mg O Interfaces," en, Phys. Rev. Applied, vol. 17, no. 5, p. 054 041, May 2022, ISSN: 2331-7019. DOI: 10.1103/PhysRevApplied.17.054041.

[135] A. Belabbes, G. Bihlmayer, S. Blügel, et al., "Oxygen-enabled control of Dzyaloshinskii-Moriya Interaction in ultra-thin magnetic films," en, Sci Rep, vol. 6, no. 1, Apr. 2016, Publisher: Springer Science and Business Media LLC, ISSN: 2045-2322. DOI: 10.1038/srep24634.

[136] G. Kresse and J. Furthmüller, "Efficiency of ab-initio total energy calculations for metals and semiconductors using a plane-wave basis set," en, Computational Materials Science, vol. 6, no. 1, pp. 15–50, Jul. 1996, Publisher: Elsevier BV, ISSN: 0927-0256. DOI: 10.1016/0927-0256(96)00008-0.

[137] G. Kresse and J. Hafner, "*Ab initio*molecular dynamics for liquid metals," en, Phys. Rev. B, vol. 47, no. 1, pp. 558–561, Jan. 1993, Publisher: American Physical Society (APS), ISSN: 0163-1829, 1095-3795. DOI: 10.1103/physrevb.47.558.

[138] G. Kresse and J. Furthmüller, "Efficient iterative schemes for*ab initio*total-energy calculations using a plane-wave basis set," en, Phys. Rev. B, vol. 54, no. 16, pp. 11 169–11 186, Oct. 1996, Publisher: American Physical Society (APS), ISSN: 0163-1829, 1095-3795. DOI: 10.1103/physrevb.54.11169.

[139] H. Yang, A. Thiaville, S. Rohart, et al., "Anatomy of Dzyaloshinskii-Moriya Interaction atCo/PtInterfaces," en, Phys. Rev. Lett., vol. 115, no. 26, Dec. 2015, Publisher: American Physical Society (APS), ISSN: 0031-9007, 1079-7114. DOI: 10.1103/physrevlett.115.267210.

[140] G. Chen, A. Mascaraque, H. Jia, et al., "Large Dzyaloshinskii-Moriya interaction induced by chemisorbed oxygen on a ferromagnet surface," en, Sci. Adv., vol. 6, no. 33, Aug. 2020, Publisher: American Association for the Advancement of Science (AAAS), ISSN: 2375-2548. DOI: 10.1126/sciadv.aba4924.

[141] A. Belabbes, G. Bihlmayer, F. Bechstedt, et al., "Hunds Rule-Driven Dzyaloshinskii-Moriya Interaction at 3 d 5 d Interfaces," en, Phys. Rev. Lett., vol. 117, no. 24, p. 247 202, Dec. 2016, ISSN: 0031-9007, 1079-7114. DOI: 10.1103/PhysRevLett.117.247202.

[142] R. Chen, C. Chen, L. Han, et al., "Ordered creation and motion of skyrmions with surface acoustic wave," en, Nat Commun, vol. 14, no. 1, p. 4427, Jul. 2023, ISSN: 2041-1723. DOI: 10.1038/s41467-023-40131-1.

[143] Y. Yang, L. Zhao, D. Yi, et al., "Acoustic-driven magnetic skyrmion motion," en, Nat Commun, vol. 15, no. 1, p. 1018, Feb. 2024, ISSN: 2041-1723. DOI: 10.1038/s41467-024-45316-w.

[144] C. Balan, J. Fischer, C. Gueneau, et al., "Using hard-x-ray photoelectron spectroscopy to measure the oxidation state of gated Co/AlOx interfaces," en, Phys. Rev. Applied, vol. 21, no. 6, Jun. 2024, Publisher: American Physical Society (APS), ISSN: 2331-7019. DOI: 10.1103/physrevapplied.21.064023.

[145] F. Matsukura, Y. Tokura, and H. Ohno, "Control of magnetism by electric fields," en, Nature Nanotech, vol. 10, no. 3, pp. 209–220, Mar. 2015, Publisher: Springer Science and Business Media LLC, ISSN: 1748-3387, 1748-3395. DOI: 10.1038/nnano.2015.22.

[146] J. Zhang, P. V. Lukashev, S. S. Jaswal, et al., "Elucidating the Voltage Controlled Magnetic Anisotropy," en,

[147] C. Bi, Y. Liu, T. Newhouse-Illige, et al., "Reversible Control of Co Magnetism by Voltage-Induced Oxidation," en, Phys. Rev. Lett., vol. 113, no. 26, Dec. 2014, Publisher: American Physical Society (APS), ISSN: 0031-9007, 1079-7114. DOI: 10.1103/physrevlett.113.267202.

[148] X. Zhou, Y. Yan, M. Jiang, et al., "Role of Oxygen Ion Migration in the Electrical Control of Magnetism in Pt/Co/Ni/HfO_2 Films," en, J. Phys. Chem. C, vol. 120, no. 3, pp. 1633–1639, Jan. 2016, Publisher: American Chemical Society (ACS), ISSN: 1932-7447, 1932-7455. DOI: 10.1021/acs.jpcc.5b10794.

[149] M. C. Biesinger, B. P. Payne, A. P. Grosvenor, et al., "Resolving surface chemical states in XPS analysis of first row transition metals, oxides and hydroxides: Cr, Mn, Fe, Co and Ni," en, Applied Surface Science, vol. 257, no. 7, pp. 2717–2730, Jan. 2011, Publisher: Elsevier BV, ISSN: 0169-4332. DOI: 10.1016/j.apsusc.2010.10.051.

[150] M. Sicot, S. Andrieu, F. Bertran, et al., "Electronic properties of Fe, Co, and Mn ultrathin films at the interface with MgO(001)," en, Phys. Rev. B, vol. 72, no. 14, Oct. 2005, Publisher: American Physical Society (APS), ISSN: 1098-0121, 1550-235X. DOI: 10.1103/physrevb.72.144414.

[151] M. Endo, S. Kanai, S. Ikeda, et al., "Electric-field effects on thickness dependent magnetic anisotropy of sputtered MgO/Co40Fe40B20/Ta structures," en, Applied Physics Letters, vol. 96, no. 21, p. 212 503, May 2010, ISSN: 0003-6951, 1077-3118. DOI: 10.1063/1.3429592.

[152] A. Vansteenkiste, J. Leliaert, M. Dvornik, et al., "The design and verification of Mumax3," AIP Advances, vol. 4, no. 10, p. 107 133, 2014. DOI: 10.1063/1.4899186.

[153] J. Mulkers, B. Van Waeyenberge, and M. V. Miloevi, "Effects of spatially-engineered Dzyaloshinskii-Moriya interaction in ferromagnetic films," Physical Review B, vol. 95, no. 14, p. 144 401, 2017. DOI: 10.1103/PhysRevB.95.144401.

[154] S. Tarasenko, A. Stankiewicz, V. Tarasenko, et al., "Bloch wall dynamics in ultrathin ferromagnetic films," en, Journal of Magnetism and Magnetic Materials, vol. 189, no. 1, pp. 19–24, Oct. 1998, ISSN: 03048853. DOI: 10.1016/S0304-8853(98)00230-3.

[155] A. Vansteenkiste, J. Leliaert, M. Dvornik, et al., "The design and verification of MuMax3," en, AIP Advances, vol. 4, no. 10, Oct. 2014, Publisher: AIP Publishing, ISSN: 2158-3226. DOI: 10.1063/1.4899186.

[156] M. Ameziane, J. Huhtasalo, L. Flajman, et al., "Solid-State Lithium Ion Supercapacitor for Voltage Control of Skyrmions," en, Nano Lett., vol. 23, no. 8, pp. 3167–3173, Apr. 2023, Publisher: American Chemical Society (ACS), ISSN: 1530-6984, 1530-6992. DOI: 10.1021/acs.nanolett.2c04731.